THE LEACHING AND PASSIVATION OF CHALCOPYRITE IN ACID SULFATE MEDIA

by

RALPH PETER HACKL

B.Sc.(Hons.), The University of British Columbia, 1977
M.Sc., The University of British Columbia, 1983

A THESIS SUBMITTED IN PARTIAL FULFILLMENT OF
THE REQUIREMENTS FOR THE DEGREE OF
DOCTOR OF PHILOSOPHY

in

THE FACULTY OF GRADUATE STUDIES

Department of Metals and Materials Engineering

We accept this thesis as conforming
to the required standard

THE UNIVERSITY OF BRITISH COLUMBIA

November 1995

In presenting this thesis in partial fulfillment of the requirements for an advanced degree at the University of British Columbia, I agree that the library shall make it freely available for reference and study. I further agree that permission for extensive copying of this thesis for scholarly purposes may be granted by the head of my department or by his or her representatives. It is understood that copying or publication of this thesis for financial gain shall not be allowed without my written permission.

Department of Metals and Materials Engineering
The University of British Columbia
Vancouver, B.C., Canada

Date: November 20, 1995

ABSTRACT

Sulfate-based leaching processes for chalcopyrite ($CuFeS_2$) are attractive because of their inherent simplicity. Unfortunately, high copper extractions are not attainable in a reasonable residence time unless the leaching temperature exceeds 200°C (oxygen pressure leaching) or chalcopyrite is "activated" by a pretreatment method prior to leaching. In the present work, the oxygen pressure leaching behaviour of chalcopyrite in the temperature range 110-220°C was studied to shed new light on the reasons for the slow leaching.

At temperatures where molten elemental sulfur is stable (120-180°C), the reaction was found to be prematurely stifled by liquid sulfur formed during leaching. The liquid sulfur wetted and agglomerated the unreacted mineral particles, effectively stopping the leach at 40-70% copper extraction. The feasibility of using surfactants to disperse the sulfur and enhance the copper extraction in the temperature range 125-155°C was investigated. Most of the surfactants tested decomposed too rapidly to be of benefit. The best results were obtained with orthophenylenediamine (OPD) when it was added continuously at a low temperature (125°C) and a high dosage (50 kg/t). Under these conditions the surfactant was successful in dispersing liquid sulfur and it effected a modest increase in copper extraction over that obtained at 110°C, but only after prolonged retention times (6 hours). It was found that chalcopyrite leached slowly even if molten sulfur was prevented from wetting the mineral surfaces. This led to the conclusion that the reaction rate is ultimately controlled by a passivating mechanism unrelated to elemental sulfur formation.

Oxidized chalcopyrite mineral surfaces were examined by Auger electron spectroscopy and X-ray photoelectron spectroscopy to identify the presence of any passivating layers that may form during leaching. The results indicated that an iron-deficient, copper-rich sulfide layer forms on the surface of chalcopyrite as a result of solid state changes that occur in the mineral during leaching. This layer is thought to be a copper polysulfide, CuS_n, where $n > 2$. The layer is quite thin (~10-100 nm) and hence is not detectable by conventional electron microscopy. The copper polysulfide is believed to passivate the chalcopyrite.

The addition of silver ions at a temperature below the sulfur melting point (110°C) was found to catalyze the leach, resulting in the copper extraction increasing from 53% to 96% after

3 hours leaching. Silver alone was ineffective at 125°C and 155°C because the leach was stifled by liquid sulfur. However, when silver was used in conjunction with OPD at 125°C the copper extraction was again enhanced significantly, to 91%. The OPD prevented the sulfur from wetting the mineral surfaces, allowing the catalytic effect of the silver ions to be maintained.

A simple mathematical model was formulated to explain the leaching and passivation of chalcopyrite at low temperature (110°C). The reaction kinetics can be explained in terms of a mixed diffusion/chemical reaction model where the reaction rate is initially dependent on the rate at which copper and iron diffuse through the thickening passive layer. The passive layer also leaches, but at a slower rate than the chalcopyrite. Eventually, the passive layer reaches a steady state thickness and the kinetics are then controlled by the rate at which the passivating layer decomposes. The linear rate constant k_l for the decomposition of the passive layer was calculated to be 5.0×10^{-3} μm/min. The low value of k_l explains why inordinately long residence times are required to obtain a high copper extraction from chalcopyrite at 110°C.

TABLE OF CONTENTS

List of Tables

List of Figures

List of Symbols

Interfacial chemistry notation:

γ	surface tension or interfacial tension; by convention the S.I. units are mN/m for liquid-liquid and gas-liquid interfaces and mJ/m^2 for solid-liquid and solid-gas interfaces
γ_{MA}	mineral-aqueous solution interfacial tension; mJ/m^2
γ_{MS}	mineral-sulfur interfacial tension; mJ/m^2
γ_{SA}	sulfur-aqueous solution interfacial tension; mN/m
θ	solid-liquid (mineral-sulfur) contact angle; degrees
$\Delta\rho$	density difference between liquid sulfur and the aqueous solution; g/cm^3
ρ_{sol}	density of the aqueous solution; g/cm^3
ρ_{H_2O}	density of water; g/cm^3
W_{sol}	weight of solution; g
W_{H_2O}	weight of water; g
d_e	equatorial diameter of a pendant drop; cm
d_s	width of a pendant drop at a distance d_e from the bottom of the drop; cm
g	gravitational acceleration constant; 980.7 cm/s^2
S	pendant drop shape factor; dimensionless
H	empirical value that is a function of S; dimensionless
W_a	work of adhesion; mJ/m^2
ΔG	Gibbs free energy, kJ/mol
σ	standard deviation; arbitrary units

Pressure leaching notation:

P	gas pressure; MPa
T	temperature; °C
Eh	redox potential vs. standard hydrogen electrode (SHE); mV
P_{90}	90% passing particle size; μm
K	reaction equilibrium constant; dimensionless
K_a	acid dissociation constant; dimensionless
Me_{calc}	calculated head assay of *Me* (metal); wt. %
W_{Me}^{sol}	weight of *Me* in solution; g

W_{Me}^{res} weight of *Me* in the leach residue; g

W_t weight of the head sample; g

$W_{sulfide}^{head}$ weight of sulfide sulfur in the head sample; g

$W_{sulfide}^{res}$ weight of sulfide sulfur in the leach residue; g

W_{sulfur}^{res} weight of elemental sulfur in the leach residue; g

Surface science notation:

n principal quantum number

l orbital angular momentum quantum number

s spin momentum quantum number

j total angular momentum quantum number

$K,...,N$ electron energy levels (X-ray notation)

$1s,...,4f$ electron energy levels (spectroscopic notation)

E_i binding energy of an electron in the ith atomic energy level; eV

E_B binding energy of an Auger electron or photoelectron; eV

E_K kinetic energy of an Auger electron or photoelectron; eV

$h\nu$ photon (X-ray) energy; eV

ϕ_{sp} spectrometer work function; eV

C_i concentration of element i; atomic percent

I_i Auger electron or photoelectron count intensity for element i; arbitrary units

S_i Auger electron or photoelectron sensitivity factor for element i; dimensionless

α Auger parameter; eV

α' modified Auger parameter; eV

Mathematical modelling notation:

k_r macromodel rate constant; mol m^{-2} min^{-1}

k_l shrinking spherical particle (linear) micromodel rate constant, μm min^{-1}

k_p shrinking core (parabolic) micromodel rate constant, μm^2 min^{-1}

C_i dissolved metal concentration; mol m^{-3}

t leach residence time; minutes

$A_{s/l}$ mineral surface area; m^2 mineral/m^3 leach solution ≡ m^{-1}

V_m mineral molar volume; m^3 mol^{-1}

δ_l particle penetration depth for the shrinking particle micromodel; μm

δ_p	thickness of the passive layer for the shrinking core micromodel; μm
$\delta_{p/l}$	particle penetration depth for the mixed diffusion/chemical reaction model; μm
D	particle size (diameter); μm
D_i	initial particle size; μm
D_t	particle size at time t; μm
ΔD_i	difference in size between particles of size D_i and D_{i+1}; μm
$\overline{D_i}$	arithmetic mean size of particles between size D_i and D_{i+1} μm
$A(D_i)$	fractional surface area of a particle of size D_i lost to leaching; dimensionless
$X(D_i)$	fractional weight of a particle of size D_i lost to leaching; dimensionless
$A(\overline{D_i})$	fractional surface area of particles of size $\overline{D_i}$ lost to leaching, dimensionless
$X(\overline{D_i})$	fractional weight of particles of size $\overline{D_i}$ lost to leaching, dimensionless
$\overline{A_t}$	surface area fraction of feed lost to leaching at time t, dimensionless
$\overline{X_t}$	weight fraction of feed lost to leaching at time t, dimensionless
$F(D)$	cumulative particle size distribution function; dimensionless
$f(\overline{D_i})$	probability density function of a discrete particle size distribution; μm^{-1}
$F(D_i)$	cumulative fraction of particles smaller than size D_i; dimensionless
$F(D_{i+1})$	cumulative fraction of particles smaller than size D_{i+1}; dimensionless
ΔF_i	weight fraction of particles of size $\overline{D_i}$, dimensionless
ΔS_i	surface area fraction of particles of size $\overline{D_i}$, dimensionless
S_o	feed specific surface area; $m^2\ kg^{-1}$
W_o	feed weight; kg
V	leach solution volume; m^3
ρ	feed density; $kg\ m^{-3}$

ACKNOWLEDGEMENTS

I would like to express my sincere gratitude to my supervisor, Dr. David Dreisinger, for his constant guidance and encouragement throughout the course of this study. Dr. Dreisinger was instrumental in securing the funding that enabled me to take a hiatus from the working world to pursue my doctorate. A very heartfelt thank you is also extended to Dr. Ernest Peters for contributing many hours of his time to the numerous constructive discussions we had as the work progressed.

Much of the experimental work was conducted at the research facilities of my Industrial Sponsor, Placer Dome Inc. The guidance, technical assistance and analytical services received from Mr. George Rodger and his staff at the Placer Dome Research Centre are gratefully acknowledged.

I would like to extend my appreciation to the research engineers and my fellow graduate students in the Hydrometallurgy Group for their assistance in implementing certain experimental procedures which facilitated the research greatly.

Dr. Bret Haugrud and Mr. Ken Myrtle of the Surface Physics Group at Simon Fraser University provided valuable assistance in acquiring and interpreting the Auger and XPS spectra, for which I am most appreciative.

I would like to thank Placer Dome Inc., the Science Council of British Columbia and the Natural Sciences and Engineering Research Council of Canada for their financial support of this work.

Finally, I am forever grateful to my wife Evelyn, for her patience, understanding and moral support over the three years it took to complete this study.

CHAPTER 1

INTRODUCTION

Commercial processes for treating copper flotation concentrates are almost exclusively pyrometallurgical despite the concerted efforts of many organizations to develop competitive hydrometallurgical processes. Copper pyrometallurgy has the advantages of being a well developed and efficient technology, and its dominance over hydrometallurgy is not likely to change in the near future. However, increasingly stringent environmental standards have made smelting an unpopular technology in many parts of the world. Copper smelters are perceived to be bad air polluters despite the fact that advances in smelting technology have led to significant reductions in SO_2 emissions. A second disadvantage with copper pyrometallurgy is that copper smelters have a high capital cost, meaning it is usually only economic to build large plants to realize economies of scale. Consequently, small copper concentrate producers have no way of producing their own refined copper and they are forced to sell their concentrates to toll smelters. Shipping costs and smelter charges can be exorbitantly high for the small producer. In theory, the hydrometallurgical processes represent attractive alternatives in that they are non-air polluting and potentially more cost effective on a small scale than the pyrometallurgical processes. Thus, there is continuing interest in copper hydrometallurgy.

An important consideration in developing a copper concentrate hydrometallurgical process is that it should be able to treat chalcopyrite, $CuFeS_2$, the most important copper mineral in the world. The hydrometallurgical processes can be categorized according to the type of lixiviant used, the most common lixiviants being chloride, nitrate, ammine and sulfate. The sulfate-based processes have some advantages over the others in that the leaching chemistry is generally simpler and better understood, and copper recovery from sulfate media (by solvent extraction/electrowinning) is straightforward. Unfortunately, chalcopyrite leaches more slowly in sulfate media than in the other media. The well known difficulty in leaching chalcopyrite in sulfate media is probably the single most important reason why a sulfate-based process for chalcopyrite concentrates has never been commercialized. The reasons for the slow leaching kinetics have never been clearly established; however, there is general agreement that chalcopyrite is passivated in some fashion.

Chalcopyrite will react rapidly in sulfate media if the temperature is raised sufficiently high, i.e. to 200°C or higher. Such temperatures are readily accessible with modern pressure leaching equipment. In fact, the oxygen pressure leaching of sulfide minerals in acid sulfate media is now a well established technology for treating nickel-copper mattes, zinc concentrates and refractory gold concentrates [1]. Its applicability to chalcopyrite copper concentrates is of current interest. The oxygen pressure leaching behaviour of chalcopyrite is the subject of the present study.

The principal leach reactions for the oxygen pressure leaching of chalcopyrite in acid sulfate media can be represented by the following two competing reactions depicting oxidation of the sulfide fraction to elemental sulfur or sulfate [2, 3]:

$$2CuFeS_2 + 10H^+ + \tfrac{5}{2}O_2 \rightarrow 2Cu^{2+} + 2Fe^{3+} + 4S^o + 5H_2O \qquad (1\text{-}1)$$

$$2CuFeS_2 + 2H^+ + \tfrac{17}{2}O_2 \rightarrow 2Cu^{2+} + 2Fe^{3+} + 4SO_4^{2-} + H_2O \qquad (1\text{-}2)$$

The sulfur vs. sulfate yield is dependent mainly on temperature, with increasing temperature favouring the formation of sulfate. The reaction rate is also highly temperature dependent. Ideally, an oxygen pressure leaching process for chalcopyrite should achieve the dual objectives of: (1) a high copper extraction (>98%) in a reasonable residence time (1-3 hours), and (2) a high yield of elemental sulfur, a potentially saleable by-product, instead of sulfate, a waste product. To date this has not been possible. At low leach temperatures, i.e. temperatures below the melting point of sulfur (119°C), the S° yield is high (80-90%) but chalcopyrite leaches slowly and incompletely. Increasing the leach temperature moderately (to 120-160°C) in an attempt to accelerate the kinetics is counter-productive because leaching becomes stifled by molten sulfur, which wets and agglomerates the sulfide particles [2]. Above about 180°C the reactivity of chalcopyrite increases dramatically and high copper extractions are attainable [4, 5]. Unfortunately, at temperatures this high the sulfide fraction is oxidized entirely to sulfate.

The reasons for chalcopyrite's resistance to leaching in sulfate media have never been clearly established. Initial reaction rates have been noted to decline rapidly with time, leading many investigators to conclude that a passivating layer forms on the mineral surface. However, the composition of the passivating layer and the mechanism by which it forms are still the subjects of considerable dispute. Hence the primary goal of the present work was to undertake a fundamental study of how chalcopyrite is passivated under oxygen pressure leaching conditions.

The approach taken was twofold. One, the leaching kinetics of chalcopyrite over a wide temperature range (110-220°C) were studied. Two, the surfaces of leached chalcopyrite specimens were examined by Auger electron spectroscopy (AES) and X-ray photoelectron spectroscopy (XPS) to identify any compositional changes that might signify the formation of a passivating layer. The overall objective was to develop a kinetic model incorporating both a leaching and a passivation mechanism.

A secondary goal of the present work was to investigate the feasibility of using molten sulfur-dispersing surfactants to enhance the oxygen pressure leaching of chalcopyrite in the temperature range where liquid sulfur is most stable, i.e. 125-155°C. There is evidence that sulfur wets and coats the unreacted chalcopyrite mineral surfaces, forming an impermeable barrier that stifles the leach [2]. The sulfur masks the true leaching kinetics (i.e., the leach rate obtained if liquid sulfur did not stifle the reaction) in this temperature range, so it is not known if acceptably fast leach rates could be obtained if sulfur were prevented from wetting the sulfide particles. This sulfur wetting phenomenon stymied commercialization of zinc sulfide pressure leaching for a long time, until researchers discovered that adding certain surfactants to the leach dispersed the liquid sulfur and allowed high zinc extractions to be obtained at 140-150°C [6]. In this temperature range most of the sulfide is oxidized to elemental sulfur and so a high recovery of sulfur can also be obtained. It is of interest to extend the application of surfactants to the chalcopyrite pressure leaching system. If liquid sulfur could be kept off the mineral surfaces during leaching, it might be possible to achieve the dual objectives of a high copper recovery and a high sulfur yield from chalcopyrite with a moderate temperature leach.

CHAPTER 2

LITERATURE REVIEW

2.1 Elemental Sulfur

One of the goals of the research was to shed new light on the effect of liquid elemental sulfur on the kinetics of oxygen pressure leaching of chalcopyrite. To this end the literature on sulfur was reviewed, with the focus being: (1) the physical properties of elemental sulfur and (2) the aqueous chemistry of elemental sulfur under typical oxidative leaching conditions.

2.1.1 Properties of Elemental Sulfur Allotropes

Sulfur has an unusually large number of allotropes. Meyer [7] distinguished between two kinds of allotropy; (1) intramolecular allotropy, which accounts for the different molecular species formed by chemical bonding of sulfur atoms, and (2) intermolecular allotropy, which accounts for the different structural arrangements of the molecules in crystals. At standard temperature and pressure, the only stable sulfur molecule is cyclooctasulfur, S_8, which exists as a puckered ring [7]. The top four and bottom four atoms are positioned in the corners of two parallel squares turned concentrically against each other at a 45° angle (Figure 2-1). The S-S bond distance is 2.059 ± 0.002 Å.

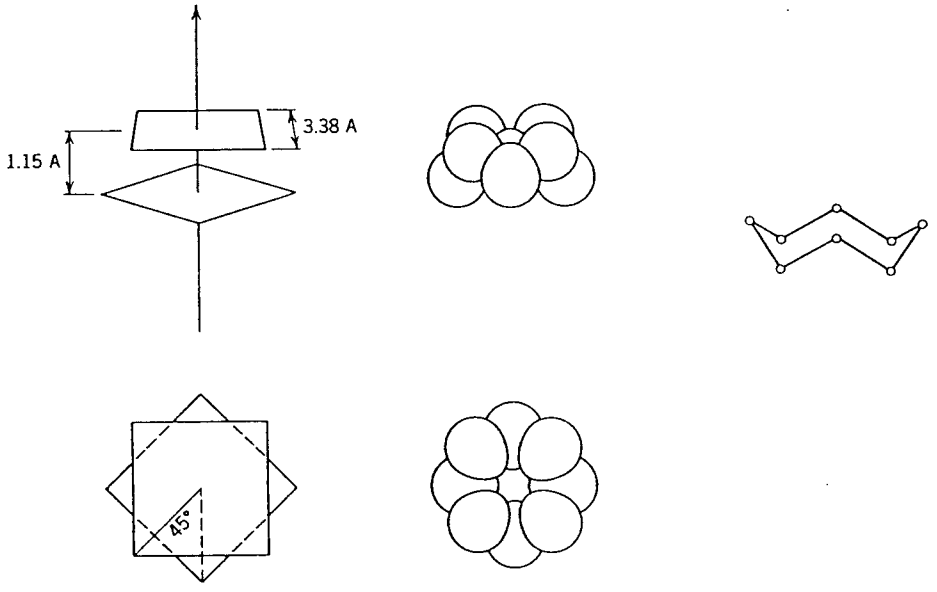

Figure 2-1. Structure of cyclooctasulfur [7]

There are two crystalline allotropes of cyclooctasulfur, orthorhombic sulfur (S_α) and monoclinic sulfur (S_β). Their structures have been completely worked out [8]. The orthorhombic form is stable at atmospheric pressure up to 95.5°C, at which transition to monoclinic sulfur takes place.

The molecular composition of liquid sulfur undergoes significant and reversible changes with temperature variations. Figure 2-2 shows how the viscosity of liquid sulfur changes with temperature [9]. At 159°C the viscosity suddenly rises sharply, increasing by two orders of magnitude over the next 30°C. Above 190°C the viscosity drops off again. This behaviour was explained by Tobolsky and Eisenberg in terms of a sulfur polymerization mechanism [10]. Below 159°C, sulfur consists mainly of S_8 rings, and a normal decrease of viscosity with temperature is observed. However, starting sharply at about 159°C, S_8 rings start to break apart to form linear sulfenyl diradicals. These radicals attack other S_8 rings in a chain reaction which leads to long-chain polymers and the consequent high viscosity. The polymerization reactions can be represented by the following two equations:

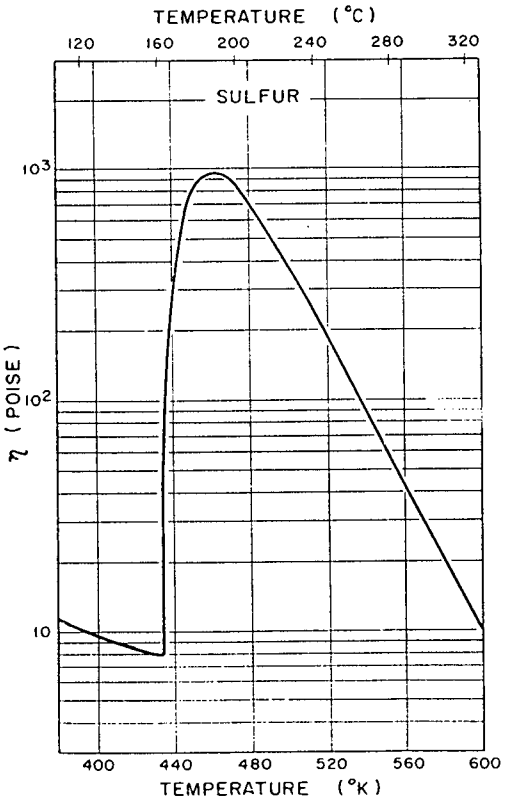

Figure 2-2. Viscosity - temperature curve for liquid sulfur [9].

$$S_8(\text{ring}) \longleftrightarrow \cdot S—S_6—S\cdot \quad \text{(linear diradical)} \tag{2-1}$$

$$\cdot S—S_6—S\cdot + S_8 \longleftrightarrow \cdot S—S_6—S—S_8\cdot \xleftrightarrow{\text{etc.}} \cdot S—S_x—S\cdot \tag{2-2}$$

Above 190°C the viscosity decreases rapidly because of cleavage of the chains. If molten sulfur is heated above 190°C and rapidly cooled to room temperature, a transparent elastic substance is obtained. It is believed that quick quenching of molten sulfur temporarily "freezes" the equilibrium mixture of S_8 rings and polymeric S_x chains [11]. The polymeric form is distinguished by its insolubility in carbon disulfide and is often referred to as amorphous sulfur. Amorphous sulfur reverts slowly back to orthorhombic sulfur at room temperature. Above 90°C the reversion is extremely rapid, taking place within minutes [11].

The melting point of sulfur changes during the melting process [12]. With rapid heating it is possible to melt orthorhombic sulfur before it converts to the monoclinic form. Pure orthorhombic sulfur melts at 112.8°C (referred to as the "ideal" melting point) but the melting point is then depressed to 110.2°C (the "natural" melting point). If orthorhombic sulfur is heated slowly enough to allow the transformation to the monoclinic allotrope to go to completion (about 1 hour at 100°C), then the monoclinic sulfur melts at 119.3°C. The melting point of the monoclinic form is similarly depressed, to 114.5°C. The melting point depression is caused by the presence of trace amounts of sulfur species other than S_8, which are stable in liquid sulfur. From infrared and Raman spectra, Steudel and Mäusle [13, 14] determined that the sulfur melt contains about 95% S_8 and small amounts of S_6, S_7, and S_n ($n > 8$).

Some selected physical constants for sulfur are given in Table 2-1 [15, 16].

2.1.2 Aqueous Oxidation of Elemental Sulfur in Acid Sulfate Media

In discussing the aqueous oxidation of elemental sulfur it is useful to start with the Eh-pH diagram for the sulfur-water system as developed by Peters [17], depicted in Figure 2-3. The diagram considers only those oxy-sulfur species stable in the acid pH range, i.e. HSO_4^- and SO_4^{2-}. The alkaline pH-stable species such as thiosulfate, $S_2O_3^{2-}$, and tetrathionate, $S_4O_6^{2-}$, have been excluded to simplify the diagram.

Table 2-1. Selected physical constants of sulfur (taken from refs. [15] and [16]).

Property	Value	
	Ideal	Natural
Freezing point of solid phase, °C		
orthorhombic	112.8	110.2
monoclinic	119.3	114.5
Density of solid (at 20°C), g/cm^3		
orthorhombic		2.07
monoclinic		1.96
amorphous		1.92
Density of liquid, g/cm^3		
125°C		1.7988
130°C		1.7947
140°C		1.7865
150°C		1.7784
Vapour pressure, P= Pa, T = K		
orthorhombic (20-80°C)	$\log P = 16.557 - 5166/T$	
monoclinic (96-116°C)	$\log P = 16.257 - 5082/T$	
liquid (120-325°C)	$\log P = 19.6 - 0.0062238\ T - 5405.1/T$	
Surface tension, γ = mN/m, T = °C		
< 159°C		$\gamma = 73.4 - 0.105\ T$
> 159°C		$\gamma = 65.7 - 0.0566\ T$

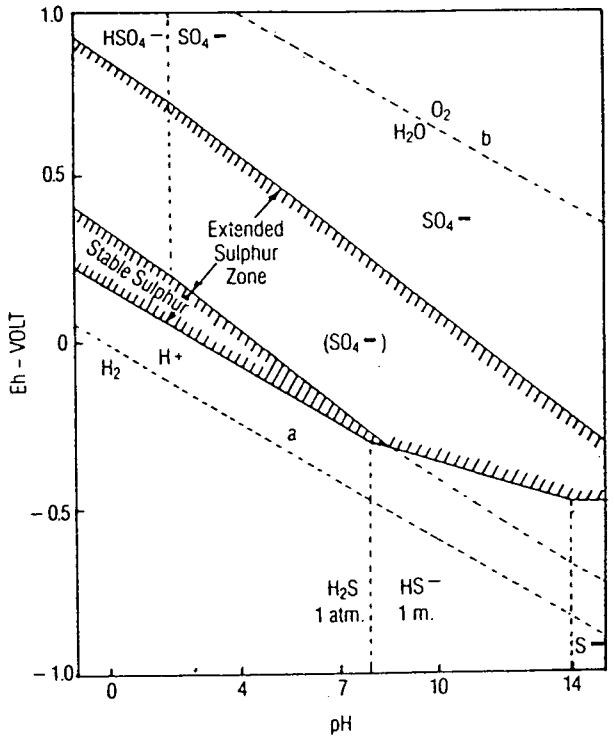

Figure 2-3. The Eh-pH diagram for the S-H_2O system, showing the region of sulfur stability and the extended stability that is realized by a 300 kJ/mol barrier in the formation of sulfate (from Peters [17]).

From the diagram it can be seen that elemental sulfur is thermodynamically stable in a rather narrow potential range at pH values lower than about 9. Peters pointed out that sulfur is known to be far more stable with respect to oxidation than depicted, at least in hydrometallurgical time frames of hours to days. To account for the observed stability, he extended the sulfur stability region by destabilizing the sulfate equilibrium line by 300 kJ/mol sulfate. The extended (metastable) sulfur region is also shown in Figure 2-3. The diagram now reflects more accurately hydrometallurgical observations on the acid side, in that sulfur is not oxidized by Fe^{3+} at a significant rate, but is oxidized slowly by HNO_3 (Eh = 1 V) and rapidly by hypochlorite or chlorine (Eh = 1.35 V).

Literature on the oxidation of elemental sulfur under typical pressure leaching conditions is rather sparse. Habashi and Bauer studied the aqueous oxidation of sulfur in the temperature range 60-170°C, oxygen partial pressure 0.10-0.69 MPa and pulp density 100 g/L [18]. The reaction:

$$S + \tfrac{3}{2} O_2 + H_2O \rightarrow H_2SO_4 \qquad (2\text{-}3)$$

was observed to depend greatly on temperature and oxygen pressure. The rate was appreciable only at temperatures above the sulfur melting point (119°C) and then increased with increasing temperature. The activation energy in the temperature range 130-170°C was 49.2 kJ/mol, which they interpreted as indicative of a chemical rate control mechanism. The initial H_2SO_4 concentration had practically no affect on oxidation rate. The rate was proportional to $P_{O_2}^{3/2}$, thus they argued the reaction takes place in two steps:

$$S + \tfrac{3}{2} O_2 \rightarrow SO_3 \qquad (2\text{-}4)$$

$$SO_3 + H_2O \rightarrow H_2SO_4 \qquad (2\text{-}5)$$

in which the first step is the slowest. Reaction (2-4) was postulated to take place by the following sequence of reactions involving scission of the S_8 ring:

$$S_8 + O_2 \leftrightarrow S_{8-x}O + S_xO \qquad (2\text{-}6)$$

$$S_{8-x}O + O_2 \rightarrow SO_3 + S_{7-x} \qquad (2\text{-}7)$$

$$S_xO + O_2 \rightarrow SO_3 + S_{x-1} \qquad (2\text{-}8)$$

where x may range from 1 to 4. The rate was also affected by the presence of some foreign ions. Cu^{2+} had a catalytic effect at 1 g/L, quadrupling the rate in the first two hours. Zn^{2+} and Ni^{2+} had a lesser effect and Co^{2+} had virtually no affect. Percent conversion of elemental sulfur to sulfuric acid was not reported, but it was not high under the conditions they used. From their data it was calculated that the highest conversion they obtained was 1.6% oxidation of S° to H_2SO_4. For a commercial process they recommended oxidizing sulfur at 300°C and 2.8 MPa oxygen pressure. The slow oxidation rates they obtained may have been partly due to a low sulfur surface area caused by the tendency of liquid elemental sulfur to coalesce, even under conditions of vigorous agitation, as has been observed by researchers at INCO in their studies on the oxygen pressure leaching of nickeliferous pyrrhotite concentrate [19].

Corriou and Kikindai studied the aqueous oxidation of elemental sulfur in the temperature range 125-230°C and oxygen partial pressure range 0.1-5 MPa [20]. They found that below the sulfur melting point, oxidation was negligible, which is consistent with Habashi's findings. The sulfur oxidation kinetics experienced a transition in the 160-175°C region. Between 125°C and 160°C, the activation energy was 119.2 kJ/mol; between 175°C and 230°C the activation energy was significantly lower at 64.9 kJ/mol. They attributed this behaviour to the changing allotropic composition of molten sulfur with temperature. As discussed in Section 2.1.1, sulfur exists primarily as S_8 below 160°C. Above 160°C, the proportion of polymeric sulfur increases rapidly. The authors concluded that the polymeric sulfur is much less reactive than S_8. Their activation energy was higher than Habashi and Bauer's value of 49.2 kJ/mol. This may be attributable to a lack of control over the surface area of liquid sulfur during the tests. Habashi and Bauer carried out their tests in a stirred autoclave whereas Corriou and Kikindai used a shaking autoclave. It is likely that the different agitation methods yielded quite different sulfur surface areas. Moreover, temperature profoundly affects sulfur viscosity so it seems reasonable to assume that temperature would also affect the sulfur surface area and indirectly, the reaction kinetics. Thus it is difficult to draw any meaningful conclusions from activation energies measured from leach tests on molten sulfur. Both authors concluded that sulfur is slow to oxidize under typical oxygen pressure leaching conditions.

2.2 Properties of Chalcopyrite

2.2.1 Crystal Structure

The crystal structure of chalcopyrite is illustrated in Figure 2-4 [21]. The structure belongs to the zincblende (ZnS) group but the tetragonal unit cell of chalcopyrite is twice the volume of the zincblende unit cell. The zinc atoms are replaced by copper and iron atoms which occupy alternate positions along the *c* axis while the positions of the sulfur atoms remain unchanged. Each metal atom is co-ordinated by a tetrahedron of sulfurs and each sulfur atom by a tetrahedron of metal atoms (two iron and two copper). The sulfur atoms are displaced slightly from the centres of the metal tetrahedra towards the iron-iron edge. The average bond distances for Fe-S and Cu-S are 2.257 and 2.302 Å respectively.

The bonding in chalcopyrite is considered to be essentially covalent in nature. Mössbauer spectroscopy was used to determine that copper and iron in chalcopyrite have valencies of one and three respectively, rather than two and two [22]. X-ray photoelectron spectroscopic studies have confirmed that copper in chalcopyrite is univalent [23]. Sulfur is present as monosulfide (S^{2-}).

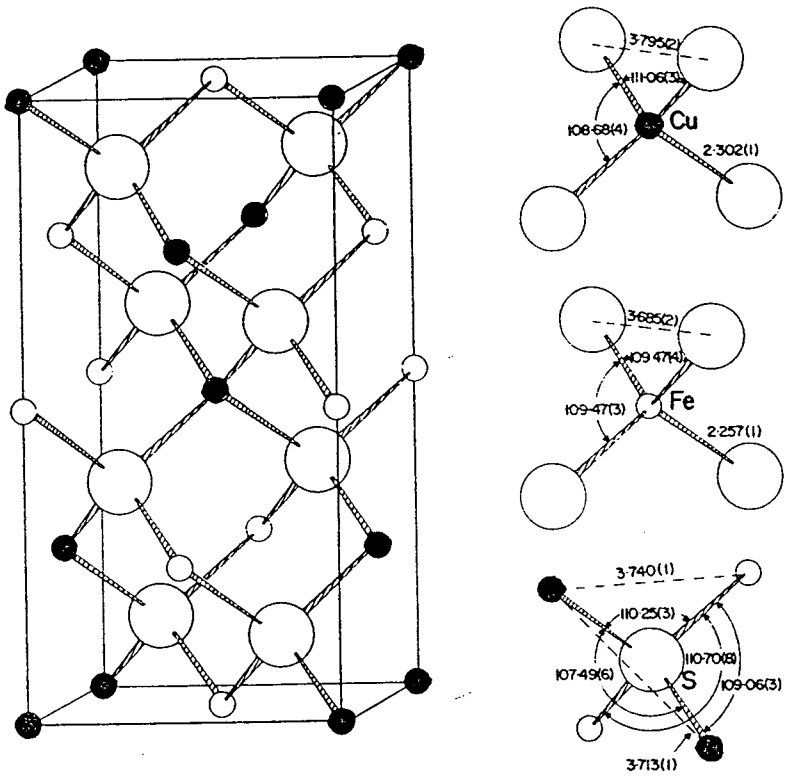

Figure 2-4. Crystal structure and interatomic bond lengths and angles of chalcopyrite [21]

Natural chalcopyrite is an *n*-type semiconductor, with a resistivity varying from $2x10^{-4}$ - $3x10^{-1}$ Ωm and an energy band gap of 0.60 eV at room temperature [24]. Many semiconductor minerals leach by electrochemical mechanisms and in fact, electrochemical phenomena have been implicated in the leaching of chalcopyrite [25, 26]. Some aspects of chalcopyrite electrochemistry will be reviewed in Section 2.4.1.

2.2.2 Thermodynamic Considerations

Thermodynamic domains of stability of sulfide minerals in aqueous media are commonly shown on Eh-pH diagrams. Figure 2-5 shows the Eh-pH diagram for the Cu-Fe-S-H_2O system as drawn by Peters [27], on which the stable zone for chalcopyrite is depicted. The diagram has been simplified in that it includes only those sulfide minerals most commonly found associated with chalcopyrite, i.e. bornite (Cu_5FeS_4), covellite (CuS), chalcocite (Cu_2S), pyrrhotite (~FeS) and pyrite (FeS_2). Also, the diagram considers only the sulfur species SO_4^{2-}, S°, H_2S, HS^- and S^{2-} while neglecting oxy-sulfur species such as $S_2O_3^{2-}$ and $S_4O_6^{2-}$ (which are metastable only at alkaline pH). From Figure 2-5 several predictions can be made concerning the thermodynamic stability of chalcopyrite and the other phases. For the hydrometallurgist it is a useful exercise to see if these predictions have been confirmed experimentally in practical leaching times, i.e. in hours or days. When this is done, discrepancies in what is predicted by the diagram and what is observed experimentally become apparent. Three of the more pertinent discrepancies under acid oxidizing conditions will now be discussed.

First, in acidic media at increasing potentials, chalcopyrite is predicted to oxidize successively to bornite, chalcocite and covellite according to the following sequence of half-reactions:

$$5CuFeS_2 + 2H_2S \rightarrow Cu_5FeS_4 + 4FeS_2 + 4H^+ + 4e^- \quad (2\text{-}9)$$

$$Cu_5FeS_4 + 0.5H_2S \rightarrow 2.5Cu_2S + FeS_2 + H^+ + e^- \quad (2\text{-}10)$$

$$Cu_2S + H_2S \rightarrow 2CuS + 2H^+ + 2e^- \quad (2\text{-}11)$$

In actuality, only covellite has been observed. In the early 1950's McGauley *et al.* [28] patented a process to convert chalcopyrite to CuS by a metathetic-type leach that operates under weakly oxidizing conditions at 160-230°C, according to the reaction:

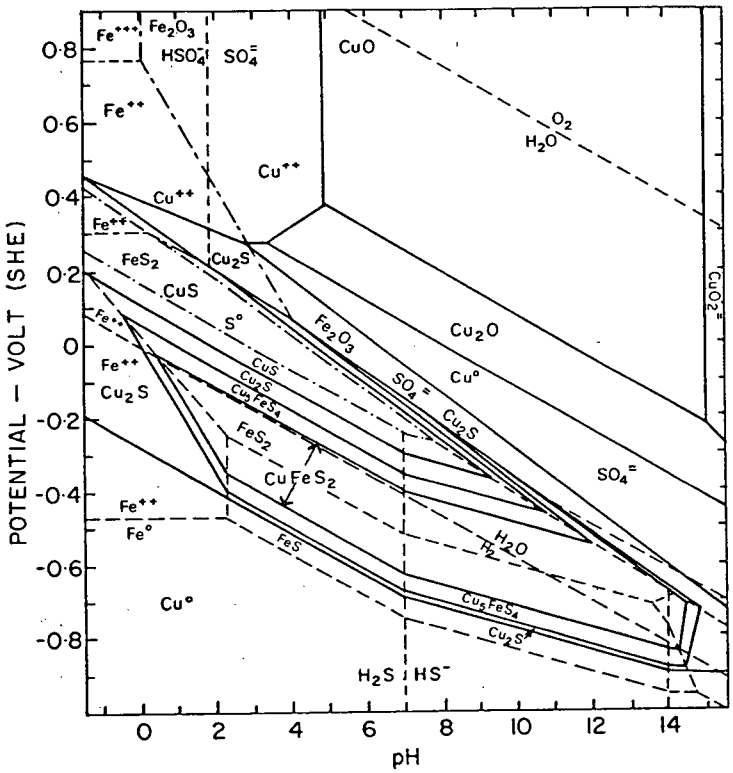

Figure 2-5. The Eh-pH diagram for the Cu-Fe-S-H_2O system at 25°C; all solutes at 0.1 mol/L activity except Cu^{2+} = 0.01 mol/L [27].

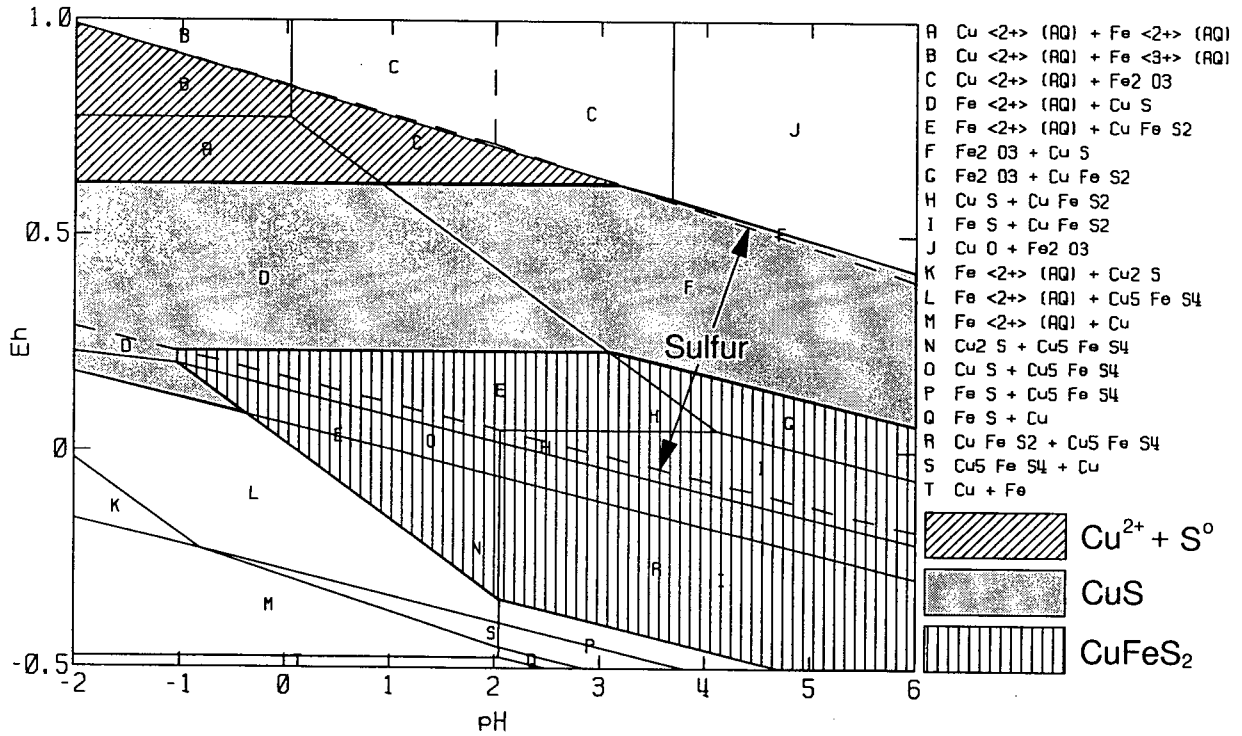

Figure 2-6. The metastable Eh-pH diagram for the Cu-Fe-S-H_2O system at 25°C; all solutes at 1 mol/L activity (adopted from ref. [29] using the CSIRO Thermochemistry program).

$$CuFeS_2 + Cu^{2+} \rightarrow 2CuS + Fe^{2+} \qquad (2\text{-}12)$$

Unfortunately, the reaction is too slow to be commercially useful. Jones observed covellite on the surfaces of chalcopyrite anodized at 130°C [25] and from the morphology of the product he concluded the covellite precipitated out of solution. Under moderate to strongly oxidizing leaching conditions covellite has rarely if ever been seen. Stanczyk and Rampacek did make brief mention of seeing covellite as an intermediate reaction product in their early work on oxygen pressure leaching of chalcopyrite [4].

A second discrepancy is that the diagram predicts covellite oxidizes to chalcocite and sulfate ions via:

$$2CuS + 4H_2O \rightarrow Cu_2S + SO_4^{2-} + 8H^+ + 6e^- \qquad (2\text{-}13)$$

but in fact this reaction occurs only over geologic time [29].

Finally, the diagram indicates that cupric ions co-exist with sulfate or bisulfate ions but not elemental sulfur. However, elemental sulfur is always the predominant sulfur product when chalcopyrite is acid leached at low or moderate temperatures (< 180°C) and moderately oxidizing potentials (< 1 V).

To rationalize these discrepancies Peters introduced the concept of metastable Eh-pH diagrams [27, 29, 30]. In these diagrams, thermodynamically stable phases which do not form except over geologic time are deleted while experimentally observed metastable phases of interest are included. Figure 2-6 shows one such version of a metastable Cu-Fe-S-H_2O diagram, developed by Peters [29], which highlights the new predominance areas for chalcopyrite, covellite and (Cu^{2+} + S°). Two changes were incorporated into the drawing of this diagram. One, pyrite was deleted because it does not nucleate at a measurable rate from reactions involving chalcopyrite (contrary to thermodynamic expectation, see equation (2-9)). Two, to account for the observed stability of elemental sulfur, the sulfur stable range was artificially extended by increasing the free energy of formation for sulfate by 300 kJ/mol. The result is a diagram which is of more use to hydrometallurgists because it resolves the above-mentioned discrepancies. The stable areas for chalcopyrite, covellite and sulfur have increased greatly and there is now considerable overlap between the three. Chalcopyrite oxidation is now depicted by the following reactions:

$$CuFeS_2 \rightarrow CuS + S^\circ + Fe^{2+} + 2e^- \quad (2\text{-}14)$$

$$CuS \rightarrow Cu^{2+} + S^\circ + 2e^- \quad (2\text{-}15)$$

Covellite is the only intermediate sulfide phase. Bornite and chalcocite now appear only as reduction products. There is a common area of stability for Cu^{2+} and S°. Oxidation of the covellite intermediate yields Cu^{2+} plus S° or Cu^{2+} plus SO_4^{2-}, again consistent with hydrometallurgical observation.

2.3 Leaching of Chalcopyrite in Sulfate Media

Chalcopyrite leaching in sulfate media has received extensive study. The majority of the previous work in this area can conveniently be grouped into three major categories: (1) ferric sulfate leaching, (2) oxygen pressure leaching and (3) bioleaching (bacterial leaching). Other more exotic oxidants such as dichromate [31] and ozone [32] have received cursory study, but they will not be discussed here. In addition, there is considerable literature on leaching of chalcopyrite under near-neutral and reducing conditions (see for example refs. [33, 34]), but the present study is concerned with oxidative leaching and as such the literature review will be restricted to the same.

2.3.1 Ferric Sulfate Leaching

The leaching of chalcopyrite with ferric sulfate was first investigated by Sullivan in the 1930's [35]. Reviews covering the literature in this field up to the early 1970's have been prepared by Wadsworth [36], Roman and Benner [37], Dutrizac and MacDonald [38] and Habashi [39]. More recently, kinetic studies have been carried out by Dutrizac [40-43], Jones and Peters [44], Munoz *et al.* [45], Beckstead *et al.* [46] and Majima's group [47, 48].

There is general agreement that ferric sulfate leaching of chalcopyrite can be represented by the following two reactions:

$$CuFeS_2 + 4Fe^{3+} \rightarrow Cu^{2+} + 5Fe^{2+} + 2S^\circ \quad (2\text{-}16)$$

$$CuFeS_2 + 16Fe^{3+} + 8H_2O \rightarrow Cu^{2+} + 17Fe^{2+} + 2SO_4^{2-} + 16H^+ \quad (2\text{-}17)$$

Equation (2-16), which depicts the sulfide sulfur oxidized to the elemental form, is the predominant reaction. Sullivan found that about 75 percent of the chalcopyrite dissolved according to this reaction [35]. Jones and Peters leached pure, massive chalcopyrite specimens

in 1 mol/L ferric sulfate at 90°C for 38 days and found that 82% of the oxidized sulfur reported as the elemental form and 18% as sulfate [44]. Dutrizac leached natural chalcopyrite with ferric sulfate at 95°C and reported about 94% S° formation and less than 6% sulfate generation regardless of leaching time (0-70 h), ferric sulfate concentration (0-2 mol/L Fe^{3+}) and chalcopyrite particle size [43].

Chalcopyrite leaches extremely slowly in ferric sulfate. For example, Munoz *et al.* leached fine (12 μm nominal size) chalcopyrite at 90°C and obtained only 58% copper extraction in 100 hours [45]. Dutrizac leached -14+10 μm chalcopyrite particles in 0.3 mol/L ferric sulfate at 95°C and obtained 90% copper extraction in 50 hours [43].

The kinetic evidence suggests that chalcopyrite becomes passivated during ferric sulfate leaching but there is disagreement regarding the reaction mechanism. Some researchers concluded that leaching follows a parabolic rate law in which the rate is controlled by diffusion of reactants or products through a progressively thickening layer of elemental sulfur [43, 45, 49]. Munoz *et al.* suggested that transport of electrons through the S° reaction product is rate limiting [45]. Wan *et al.* presented evidence showing that if leaching is interrupted and the S° is removed, the initial reaction kinetics are restored [50]. However, Buttinelli *et al.* noted that chalcopyrite still leaches slowly even if S° is removed during the leach with an organic solvent [51]. Linge argued that ferric leaching is far too slow to be controlled by reactant/product diffusion through a porous sulfur layer; instead he proposed that the rate is controlled by a solid state diffusional process [52]. His argument is supported by the magnitude of the measured activation energies, which range from 63 kJ/mol [40, 41] to as high as 88 kJ/mol [48]. These values are too high to be consistent with a pore diffusion process and are more typical of a chemical reaction controlled process or a solid state diffusional controlled process.

Other researchers observed linear kinetics or mixed linear-parabolic kinetics [46, 48, 53] and they concluded that the leach rate was surface reaction controlled for at least part of the leach.

Most of the researchers found a strong dependence of reaction rate on particle size. Munoz *et al.* determined the leaching rate was inversely proportional to the square of the initial particle size, which supports a diffusion controlled mechanism [45]. In contrast, Jones and Peters found that a reduction in particle size below 100 mesh did not improve the rate of leaching or the final extraction [44]. In several studies it was determined that addition of $FeSO_4$ depressed the reaction rate severely [41, 44, 48], although at least one study found that $FeSO_4$

had no effect [53]. Most of the researchers agreed that leaching was virtually insensitive to: (1) initial ferric sulfate concentration, (2) acidity, provided it was sufficient to prevent iron hydrolysis and (3) agitation, as long as the particles were suspended off-bottom.

The reaction rates reported vary widely. In an effort to determine if rates were affected by the presence of impurities in the chalcopyrite, Dutrizac *et al.* leached sintered disks of synthetic chalcopyrite containing known amounts of various sulfide impurities [54]. He found that major concentrations of impurities were necessary to alter materially the chalcopyrite leaching rate. The presence of pyrite accelerated the chalcopyrite dissolution rate whereas galena retarded the dissolution. The results were consistent with a galvanic corrosion mechanism. Dutrizac also leached relatively pure chalcopyrites from eleven different localities and obtained similar leaching rates (± 50%) when the leaching rates were corrected for the amount of $CuFeS_2$ in the samples [42]. He concluded that the chalcopyrite leaching rate was independent of electrical conductivity, *n-p* typing, dislocation density and the presence of minor amounts of other sulfides or solid silver impurities. He thought that the varying reaction rates could be attributed to problems previous researchers had in obtaining a well defined mineral surface area.

In summary, chalcopyrite leaches at an unacceptably slow rate in ferric sulfate media. The reaction rate can be increased by "activating" chalcopyrite; this will be discussed in more detail in Section 2.5.

2.3.2 Oxygen Pressure Leaching

One of the first kinetic studies on the oxygen pressure leaching of chalcopyrite was performed by Warren [55], who carried out tests at 120-180°C and 0.17-2.41 MPa O_2 pressure. He reported an activation energy of 96 kJ/mol and concluded the rate of dissolution was surface reaction controlled. He noticed that elemental sulfur was invariably formed during high acidity leaches. When the leaching temperature exceeded the sulfur melting point, the sulfur caused the mineral particles to cement together, resulting in incomplete leaching.

Researchers at Sherritt Inc. developed a copper process based on the oxygen pressure leaching of chalcopyrite [2, 56]. At moderate temperature (< 150°C) and acidity (1 mol/L H_2SO_4) they reported that the reaction generated primarily elemental sulfur rather than sulfate. The main leach reaction could be represented by:

$$CuFeS_2 + 2H_2SO_4 + O_2 \rightarrow CuSO_4 + FeSO_4 + 2S^\circ + 2H_2O \qquad (2\text{-}18)$$

About 10-15% of the sulfide sulfur was oxidized to sulfate. By proper control of the initial acidity the ferrous iron was oxidized to ferric in the leach and hydrolyzed as a mixture of ferric hydroxide and basic ferric sulfate. The rate of reaction was affected by temperature, oxygen partial pressure and particle size. The leach reaction was severely inhibited at temperatures above about 120°C and this imposed an upper limit on the temperature at which they could operate (see Figure 2-7). They believed the inhibition was due to molten sulfur coating the unreacted chalcopyrite. Ideal conditions were determined to be 116°C, 3.45 MPa O_2 partial pressure, minus 325 mesh particle size and a 2.5 hour residence time. The process had difficulty in achieving a high conversion rate, making it necessary to recycle the partially leached solids back to the leach after removing the S°.

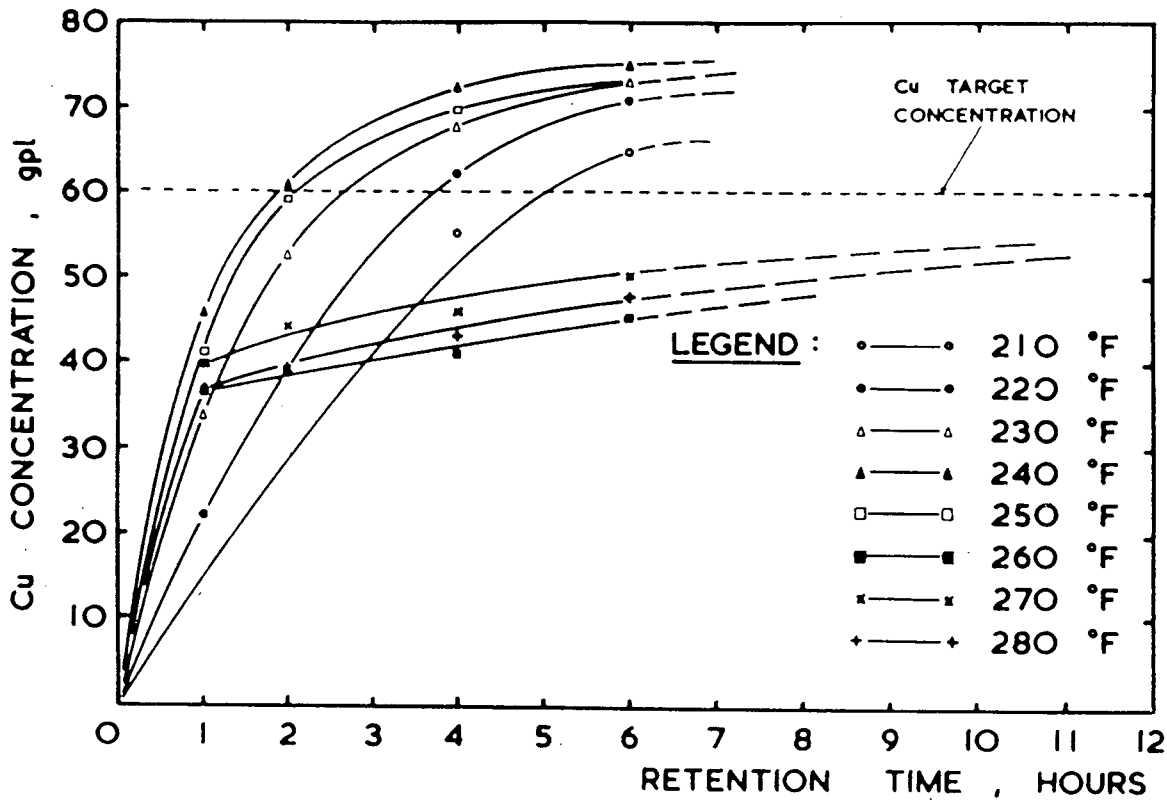

Figure 2-7. Oxygen pressure leaching of chalcopyrite - effect of temperature on rate of copper leaching. Conditions: -325 mesh chalcopyrite, 300 g conc. per L solution, 3.45 MPa O_2 pressure, 95 g/L H_2SO_4 (from data by Vizsolyi *et al.* [2])

Peters and Loewen leached chalcopyrite in dilute perchloric acid under oxygen pressure over the temperature range 105-130°C [57]. The purpose of using perchloric acid was to permit easy sulfate determinations while maintaining essentially the same reaction chemistry as that of the pure sulfate system. They obtained an activation energy of 47.3 kJ/mol over the temperature range 105-120°C. At temperatures in excess of 120°C the reaction appeared to be susceptible to stifling by elemental sulfur. The elemental sulfur vs. sulfate yield varied from 80-90%, depending on the temperature and the initial acidity. The lower the temperature or the higher the acidity, the higher the elemental sulfur yield. Dysinger *et al.* obtained about 90% S° yield in the temperature range 35-95°C as long as the acidity was in stoichiometric excess of that required for equation (2-18) [58].

Yu *et al.* studied the kinetics of chalcopyrite leaching at 125-175°C and 0.52-2.76 MPa oxygen pressure [59]. Most of their tests were conducted at an initial acidity of 0.25 mol/L H_2SO_4. Under these conditions they found that little elemental sulfur was formed. Microscopic examination of partially leached particles showed no observable coatings on the surfaces. The reaction could be expressed by the following stoichiometry:

$$2CuFeS_2 + \tfrac{17}{2}O_2 + H_2SO_4 \rightarrow 2CuSO_4 + Fe_2(SO_4)_3 + H_2O \qquad (2\text{-}19)$$

The reaction followed linear kinetics. The addition of cupric or ferrous ions had no effect on the dissolution rate whereas ferric ions slightly enhanced the rate. The rate increased with increasing acid concentration up to 0.1 mol/L H_2SO_4, remained constant between 0.1-0.25 mol/L H_2SO_4, then decreased somewhat above 0.25 mol/L H_2SO_4. At low acidity Fe_2O_3 precipitated as a coating on the particle surfaces, but it was non-protective and did not interfere with the reaction rate. The linear mechanism was explained in terms of a steady state adsorption of oxygen at the chalcopyrite surface followed by a surface reaction. Their results differ from the findings of Vizsolyi *et al.* [2] and Peters and Loewen [57]. The latter two groups observed parabolic kinetics and, at temperatures above the sulfur melting point, saw evidence of stifling of the reaction by molten sulfur.

Braithwaite and Wadsworth studied the oxygen pressure leaching of chalcopyrite in the temperature range 30-150°C, initial pH range 0.86-5.9 and oxygen pressure range 0.28-11.17 MPa [3]. In contrast to the results of Yu *et al.* [59], they found that chalcopyrite oxidized according to two parallel competing reactions, with a product of one being elemental sulfur

(equation (2-18)) and the other being sulfate (equation (2-19)). The sulfide partitioning to S° and SO_4^{2-} varied with time, temperature and solution pH. Higher temperatures and lower acid concentrations favoured sulfate formation relative to elemental sulfur. At an initial pH of 1.88, the copper leach rate increased with increasing temperature, even at temperatures above the sulfur melting point, because sulfur formation at this pH was minimal at the higher temperatures. The activation energy measured 92.9 kJ/mol for temperatures greater than 118°C and 37.2 kJ/mol for temperatures less than 118°C. The change in activation energy was thought to indicate a probable switch in the reaction mechanism. The rate was quite sensitive to particle size, with finer particles leaching at a much faster rate. A mixed kinetic model involving diffusion of dissolved oxygen through a sulfur-hematite product layer and chemical reaction at the chalcopyrite surface was used to describe the kinetics.

Le Houillier and Ghali studied the kinetics of leaching chalcopyrite in sulfuric acid at low temperature (50-110°C), low oxygen pressure (0.48 MPa O_2) and initial H_2SO_4 concentrations ranging from 0.1-1.8 mol/L [60]. Under these conditions the rate of reaction was very slow. They were only able to extract 80% of the copper from very fine (5 μm) chalcopyrite in 10 hours leaching at 90°C. Both elemental sulfur and sulfate were produced. The kinetics followed a parabolic rate law until the latter stages when the leach rate slowed dramatically, indicative of a passivating mechanism. From initial rate curves the activation energy was calculated to be 46 kJ/mol.

Oxygen pressure leaching of chalcopyrite does not yield a high copper extraction (>96%) in a practical residence time (1-3 hours) unless the temperature is raised to 200°C or higher. Stanczyk and Rampacek leached chalcopyrite under various conditions of temperature, reaction time and oxygen partial pressure [4]. They obtained 98% copper extraction from minus 270 mesh chalcopyrite in 30 minutes leaching at 200°C and 0.69 MPa O_2. King *et al.* leached four different chalcopyrite-copper concentrates and consistently obtained 98-99% copper extraction within 3 hours at 200°C and 0.69 MPa oxygen pressure [5].

2.3.3 Bioleaching

Certain naturally occurring microorganisms have the ability to oxidize many sulfide minerals, including chalcopyrite. The most widely studied of these organisms is called *Thiobacillus ferrooxidans*. *T. ferrooxidans* derives its energy for metabolism and growth from the oxidation of soluble ferrous iron and reduced sulfur species such as sulfide and elemental

sulfur. *T. ferrooxidans* has received considerable interest from the mining industry because of its commercial potential. It has a remarkable ability to leach sulfide minerals while adapting to low pH's and high soluble metal concentrations. A comprehensive review of the literature on bioleaching (bacterial leaching) is beyond the scope of this thesis; rather, the review in this section will be restricted to a brief summary of what is known about bioleaching of chalcopyrite concentrates. Bioleaching kinetics will be compared to the kinetics of the chemical ferric and oxygen pressure leaching systems discussed in the previous two sections.

Bioleaching of chalcopyrite concentrates in stirred tank reactors was pioneered by B.C. Research in the 1960's [61] and has been the subject of numerous papers since then [62-69]. Leaching can be represented by the following series of reactions [67]:

$$CuFeS_2 + 4O_2 \rightarrow CuSO_4 + FeSO_4 \qquad \text{direct bacterial attack} \qquad (2\text{-}20)$$

$$2FeSO_4 + \tfrac{1}{2}O_2 + H_2SO_4 \rightarrow Fe_2(SO_4)_3 + H_2O \qquad \text{bacterial ferrous oxidation} \qquad (2\text{-}21)$$

$$CuFeS_2 + 2Fe_2(SO_4)_3 \rightarrow CuSO_4 + 5FeSO_4 + 2S^\circ \qquad \text{indirect ferric leaching} \qquad (2\text{-}22)$$

$$S^\circ + \tfrac{3}{2}O_2 + H_2O \rightarrow H_2SO_4 \qquad \text{bacterial sulfur oxidation} \qquad (2\text{-}23)$$

Chalcopyrite is oxidized by two mechanisms: (1) directly by the bacteria (equation (2-20)) and (2) indirectly by ferric iron (equation (2-22)). The question as to which mechanism predominates is the subject of considerable controversy. Direct sulfide oxidation is considered to proceed through two enzyme mediated stages [70]. In the first stage, sulfide loses two electrons and polymerization of the resulting sulfur atoms occurs. The polymeric sulfur compounds are then oxidized to sulfate. These processes are thought to occur in the cell membrane. Ferrous iron is oxidized by the bacteria (equation 2-21) and the resulting ferric iron tends to partially re-precipitate as a basic ferric sulfate at the pH's normally employed in bioleaching (pH 1.5-2.5). Any elemental sulfur formed by indirect ferric leaching is oxidized by the bacteria to sulfate (equation 2-23).

Bioleaching of chalcopyrite is influenced by a number of the same factors that affect chemical leaching, e.g., acidity, temperature, mineral particle size, pulp density and availability of oxygen. The optimum pH is in the range 1.5-2.5 and the optimum temperature is about 35°C [62]. The copper leach rate is proportional to mineral surface area with finer grinding yielding faster rates [62, 65]. The leach rate increases linearly with increasing pulp density up to a limit

of about 20 wt. % [65]. The dependence of the chalcopyrite leach rate on dissolved oxygen content does not appear to have been quantified as it has for the biooxidation of ferrous iron [71] or biooxidation of pyrite/arsenopyrite mixtures [72]. In the latter cases it was found that oxygen mass transfer was not rate limiting until the dissolved oxygen content fell below about 1-2 mg/L. It seems reasonable to assume that a similar limiting dissolved oxygen value would prevail for chalcopyrite bioleaching.

Additional considerations for bioleaching are that the bacteria need an adequate supply of nutrients [62] and they are sensitive to the presence of certain mining chemicals such as some solvent extraction reagents [64] and some flotation reagents [73]. The bacteria are able to adapt to high concentrations (60 g/L) of dissolved copper [62].

The kinetics of bioleaching in batchwise mode are marked by three distinct phases which yield a characteristic sigmoidal leach curve. The first phase is a lag period characterized by little leaching because the bacterial population needs time to get established and grow. In the second phase, copper leaches rapidly and rates as high as 725 mg Cu/L-h have been reported [62]. In the third phase of batch bioleaching, leaching slows abruptly and then ceases entirely as the bacteria run out of available substrate. In the case of bioleaching chalcopyrite an unusual feature is that leaching ceases prematurely, usually below 60% copper extraction [62, 65, 66]. The reasons for the poor extraction have not been determined with certainty but the abrupt cessation of leaching suggests the mineral becomes passivated. It has been observed that the sulfide mineral surfaces become coated with insoluble reaction products (mainly iron salts) which are thought to interfere with leaching [63, 65]. A number of procedures have been tried to reactivate the leach residue to further leaching. Only regrinding the residue [62, 63, 66] and heat treatment above 300°C [63] have been successful.

Despite its appeal as an ambient temperature process for chalcopyrite, bioleaching has not been commercialized, mainly because: (1) copper extractions are poor and (2) sulfide sulfur is oxidized to sulfate rather than the more desirable elemental sulfur. A significant breakthrough with respect to these two problems was made when it was discovered that the addition of silver to the leach catalyzes the reaction and yields elemental sulfur rather than sulfate. Silver catalyzed bioleaching will be discussed in Section 2.5.3.

2.4 Passivation of Chalcopyrite

The kinetic leaching studies reviewed in Section 2.3 suggest that chalcopyrite becomes passivated during leaching. Other experimental methods have been used to provide further insight into the passivation phenomenon. These will be reviewed here.

2.4.1 Electrochemical Studies

The electrochemical behaviour of chalcopyrite has received extensive study and an excellent review of the literature in this field has recently been prepared by Hiskey [74]. The electrochemical studies are of interest as they have led to the formulation of some intriguing passivation theories for chalcopyrite leaching.

The application of a positive potential to a chalcopyrite electrode produces an anodic current response due to oxidation of the electrode. Figure 2-8 shows examples of typical anodic polarization curves; these were obtained by Warren *et al.* for different chalcopyrite specimens in 1 mol/L H_2SO_4 at 25°C [75, 76]. The overall shape of the curves is generally the same for each of the samples and shows a large potential range (0.6-0.9 V SHE) where the current does not increase, termed the passive region. This is followed by a rapid increase in current at potentials greater than about 0.9-1 V, called the transpassive region. Constant potential experiments showed that the current decays rapidly with time at potentials less than about 1 V (Figure 2-9). This passive region is of particular interest as it occurs in the potential range typical of oxidants used in leaching. Warren proposed that in the passive region chalcopyrite reacts initially via:

$$CuFeS_2 \rightarrow Cu_{1-x}Fe_{1-y}S_{2-z} + xCu^{2+} + yFe^{2+} + zS^{o} + 2(x+y)e^{-} \qquad (2\text{-}24)$$

to form an intermediate defect structure, $Cu_{1-x}Fe_{1-y}S_{2-z}$, termed S_1. In the initial stages of leaching iron is known to leach preferentially [25, 77-79] so $y > x$. The intermediate S_1 decomposes further to form a second intermediate, CuS_n, termed S_2:

$$Cu_{1-x}Fe_{1-y}S_{2-z} \rightarrow (y-x)CuS_n + (1-y)Cu^{2+} + (1-y)Fe^{2+} + (2+nx-ny-z)S^{o} + 4(1-y)e^{-} \qquad (2\text{-}25)$$

Warren speculated that S_1 and S_2 were bornite and covellite respectively; this is consistent with the Eh-pH diagram. In the transpassive region (1.0-1.2 V) chalcopyrite decomposes according to a combination of the following two overall reactions:

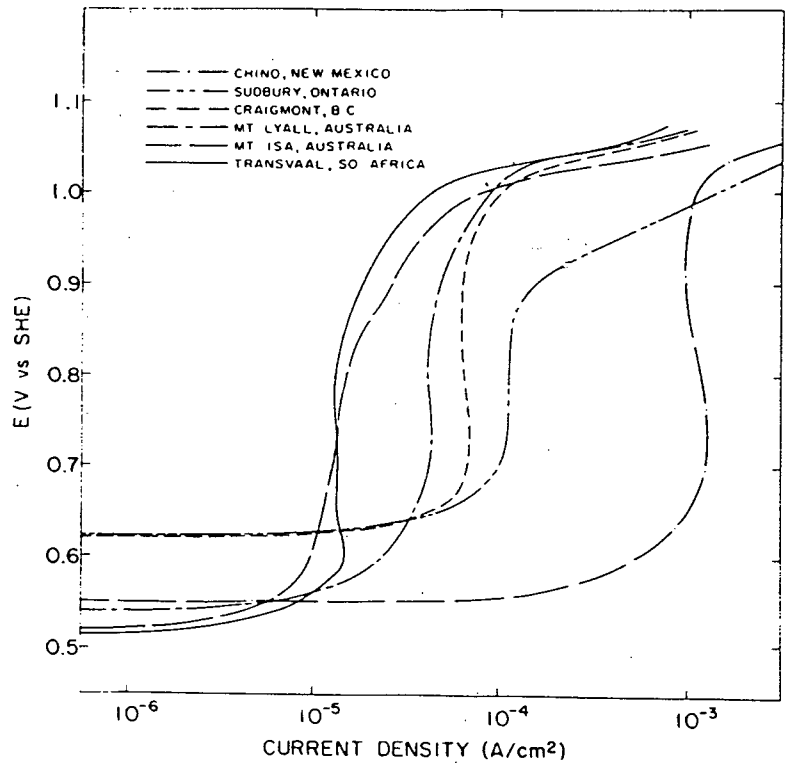

Figure 2-8. Anodic polarization curves for $CuFeS_2$ from six different locations in 1 mol/L H_2SO_4, scan rate 30 mV/min, temperature 25°C (from Warren *et al.* [75, 76]).

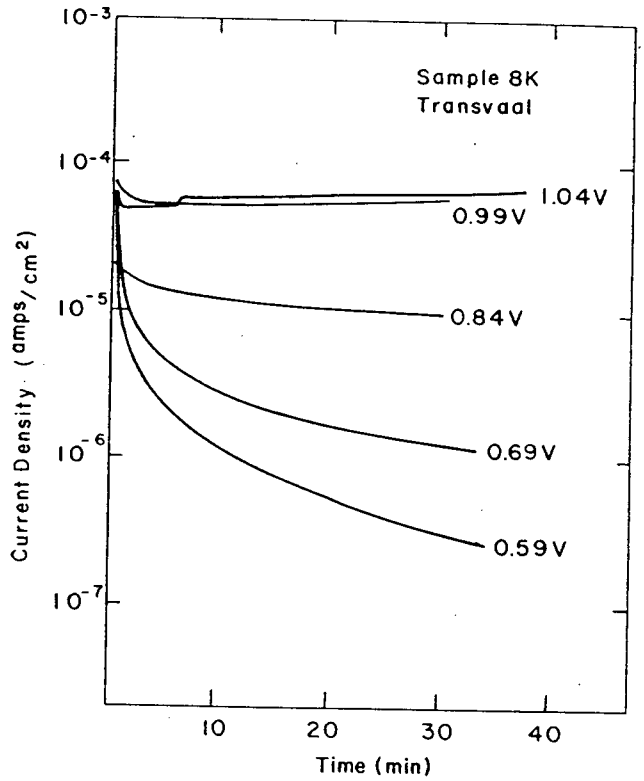

Figure 2-9. Current density vs. time plots for Transvaal $CuFeS_2$ at various anodic potentials in 1 mol/L H_2SO_4, temperature 25°C (from Warren *et al.* [75, 76]).

$$CuFeS_2 \rightarrow Cu^{2+} + Fe^{3+} + 2S^{\circ} + 5e^{-} \quad (2\text{-}26)$$

$$CuFeS_2 + 8H_2O \rightarrow Cu^{2+} + Fe^{3+} + 2SO_4^{2-} + 16H^{+} + 17e^{-} \quad (2\text{-}27)$$

From the amount of copper leached and the charge passed, Warren determined that reaction (2-26) dominates with about 90% of the sulfide sulfur converted to elemental sulfur and 10% to sulfate.

Warren's observation of a passive region has been confirmed by others. Parker *et al.* reported that chalcopyrite was strongly passivated when oxidized at potentials up to 0.7 V SCE at 80-90°C [80, 81]. They ruled out elemental sulfur and basic iron or copper salts as being responsible for passivation. They believed the passivating film was a metal-deficient, copper-rich polysulfide (the exact composition was unknown) with different semiconductor properties from $CuFeS_2$. The polysulfide film was thought to slow transport of ions and electrons during leaching. The film achieved an equilibrium thickness and decomposed thermally.

In similar experiments carried out at 25°C in a variety of different acid media (H_2SO_4, HCl, HNO_3 and $HClO_4$), Biegler *et al.* consistently observed a broad prewave in the 0.2-0.8 V region on the first anodic sweep, which was greatly diminished or absent on subsequent sweeps [82, 83]. This was attributed to a surface oxidation process involving preferential iron dissolution from the sulfide lattice to form a thin passivating film. They suggested the following stoichiometry for the prewave reaction:

$$CuFeS_2 \rightarrow 0.75CuS + 0.25Cu^{2+} + Fe^{2+} + 1.25S^{\circ} + 2.5e^{-} \quad (2\text{-}28)$$

showing covellite and sulfur as solid reaction products. On the basis of this stoichiometry and the amount of charge passed, they calculated the product layer to be about 3 nm thick. From rotating ring-disc electrode experiments Holliday and Richmond [84] determined that the ratio of Fe^{2+} to Cu^{2+} formed during the prewave reaction was about 5/1. They proposed the following stoichiometry for the prewave reaction:

$$CuFeS_2 \rightarrow 0.2Cu^{2+} + Fe^{2+} + Cu_{0.8}S_2 + 2.4e^{-} \quad (2\text{-}29)$$

in which a copper polysulfide of composition close to $Cu_{0.8}S_2$ is formed.

Gardner and Woods performed cyclic voltammetry experiments with chalcopyrite in a range of buffer solutions with pH's varying from 4.6 to 13.0 [85]. They observed a characteristic

anodic wave which was interpreted as representing oxidation of chalcopyrite to covellite and sulfur. However, in follow-up work Hamilton and Woods [86] studied the surface composition of anodized chalcopyrite and decided the initial anodic reaction was more likely to involve formation of a copper sulfide with stoichiometry closer to CuS_2. Surface studies of oxidized chalcopyrite will be discussed in more detail in Section 2.4.2.

Jones and Peters anodized chalcopyrite in a specially designed autoclave which enabled them to study the reactions at elevated temperatures [25, 87]. The anodic behaviour was studied in a variety of solutions, including H_2SO_4, in the temperature range 7-175°C. Their work is particularly relevant as the conditions they used resemble the oxygen pressure leaching conditions employed in the present study. Figure 2-10 shows how the polarization curves of chalcopyrite in 0.1 mol/L H_2SO_4 change with temperature. At lower temperatures (6-98°C) the passive region in the 0.6-1 V potential range was clearly evident. However, at higher temperatures the passive region gradually disappeared until at 175°C it was lost entirely. This would seem to suggest that the intermediate passive layer is unstable at temperatures approaching 175°C. Another interesting feature is that at the lower temperatures, the current density continued to increase with increasing potential in the transpassive region (potentials greater than 1 V), but at higher temperatures the current density saturated at potentials above 1 V. Possibly the saturation at higher temperatures can be attributed to chalcopyrite becoming coated by an insulating layer of liquid elemental sulfur. The current obtained at low potentials i.e., the passive region, was time-dependent (it decayed with time at constant potential), indicative of a rate-controlling diffusional process. The current in the passive region was also dependent on the scan rate, and Peters suggested this indicates the passivating process is probably a superficial phenomenon [88]. At low potentials, i.e. in the passive region, and at higher temperatures (> 125°C), covellite was observed to form on the chalcopyrite surface. The morphology of the covellite product varied from finely crystalline material at 125°C to large well-defined crystals in an ordered matrix at 175°C. The morphology suggested that the covellite was not an alteration product of chalcopyrite but rather, it precipitated out of solution, possibly by disproportionation of a soluble cuprous thiosulfate intermediate species.

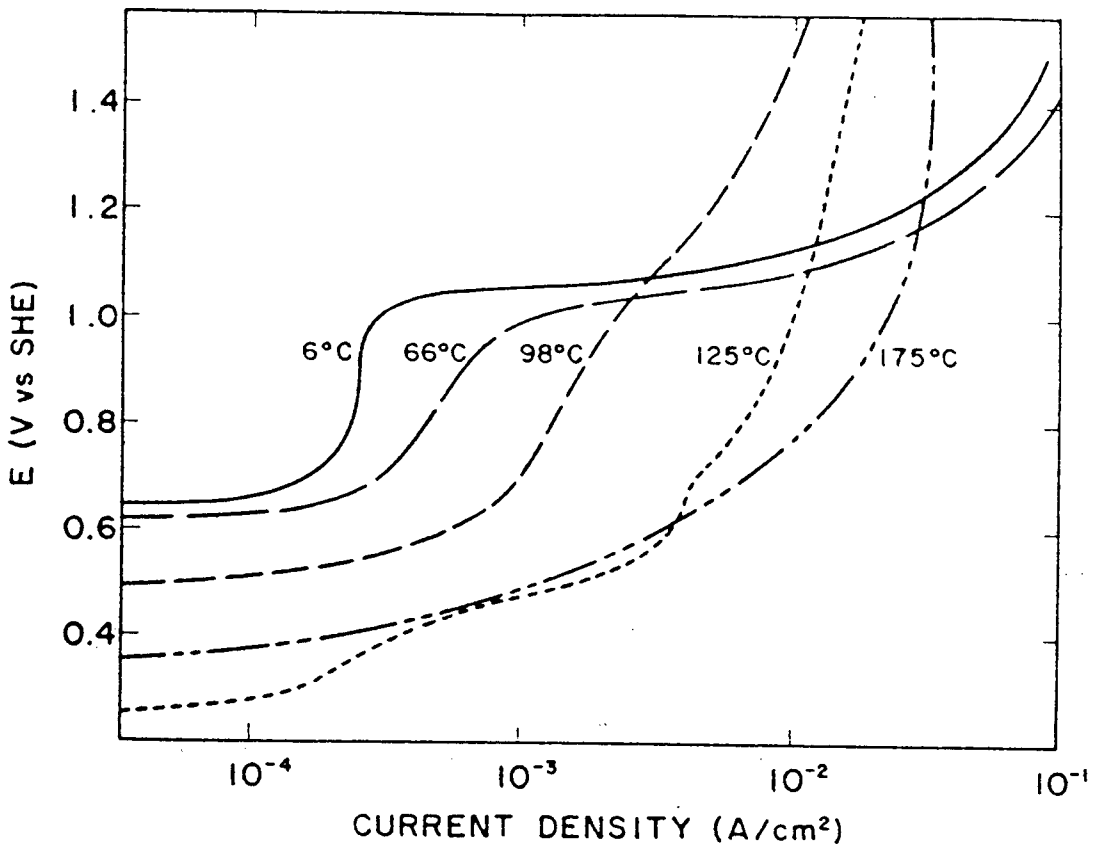

Figure 2-10. Effect of temperature on the polarization curve of $CuFeS_2$ in 0.1 mol/L H_2SO_4 , scan rate 300 mV/min (taken from the work of Jones and Peters [25, 87]).

2.4.2 Surface Studies

In the past 20 years modern surface sensitive analytical techniques have been used to study the compositions of sulfide mineral surfaces, particularly as a means to understand their flotation behaviour [89, 90]. The most popular of these techniques are Auger electron spectroscopy (AES) and X-ray photoelectron spectroscopy (XPS). AES and XPS were employed in the present study to examine the surfaces of oxygen pressure leached chalcopyrite with the objective of identifying the composition of any passivating layers that may form. Previous investigations in which AES and XPS were employed to study chalcopyrite surfaces are reviewed here. The basic theory and application of AES and XPS to the study of mineral surfaces are reviewed in Chapter 3.

Eadington was the first to report on a study of chalcopyrite surfaces [91]. He examined oxidation layers on surfaces of chalcopyrite exposed to air and water, using AES. A sample fractured within the spectrometer sample chamber was exposed to 1 torr of oxygen pressure and quickly showed a peak due to oxygen, the intensity of which corresponded to 11 atomic % oxygen on the surface after just 30 seconds exposure. With continued exposure copper, iron and sulfur concentrations decreased steadily and oxygen and carbon (from adsorption of general organic contaminants) increased. Iron decreased more quickly than copper so that the Cu/Fe atomic ratio increased from 1/1 to 2.2/1 after 90 seconds oxidation time. Eadington thought the increased Cu/Fe ratio indicated the initial adsorption of oxygen was associated with iron rather than copper. After 30 minutes exposure the thickness of the oxidation layer was estimated to be 0.9 nm thick, equivalent to between 1 and 2 monolayers. In comparison, a sample fractured under deionized water in equilibrium with air yielded an oxidation layer 9.5 nm thick after 30 minutes exposure. On this basis Eadington concluded the rate of wet oxidation was about 10 times greater than dry. The first monolayer of the wet-oxidized sample surface consisted mainly of adsorbed carbon; when this layer was removed by argon ion sputtering the immediate subsurface had a Cu/Fe atomic ratio of 5.5/1.

Brion used XPS to study the oxidation of chalcopyrite particles ground in air [92]. He found the surfaces became enriched in iron due to formation of iron hydroxide or oxy-hydroxide initially, with basic iron sulfate formed subsequently. Copper remained unoxidized, as a sulfide. He observed a broadening of the S *2p* peak towards higher binding energy and proposed this was due to formation of S_2 groups in the iron-depleted copper sulfide lattice. Oxidation in water yielded similar results except basic iron sulfate was not observed and surface enrichment of iron over copper was not apparent.

Holloway *et al.* studied the effects of polishing on chalcopyrite surfaces using AES, XPS and microreflectometry [93]. Two polishing media were used; diamond powder dispersed in a silicone oil and chromic oxide dispersed in distilled water. They concluded that polishing in either media oxidized the chalcopyrite surface to yield iron oxide and a copper-rich sulfide. The surface composition could not be conclusively identified, but the oxide was thought to be Fe_3O_4 and/or FeOOH while the sulfide was tentatively identified as Cu_5FeS_4 and/or Cu_2S. From the reflectance data they discounted the presence of other possible compounds, including CuS, Cu_9S_5 and Fe_2O_3. Surface layers were approximately 10 nm thick. In a later, related study Ruzakowski *et al.* used the same techniques to examine the surfaces of polished chalcopyrite

exposed to air at temperatures between 23°C and 300°C [94]. Exposure times varied from a maximum of 1.5 years at 23°C to 1-2 hours at 300°C. They found that in all cases iron oxide formed as the outermost layer. The Auger low energy iron peak at 48 eV was split into two peaks at 45 and 51 eV which they interpreted as indicative of an Fe_3O_4 layer with a small amount of Fe_2O_3 or FeOOH. Underlying the oxide layer was a copper sulfide-rich region. From the reflectance data, they proposed a model in which the $CuFeS_2$ surface becomes covered with three layers, the first being Cu_5FeS_4 followed by Cu_2S and finally Fe_3O_4. Total film thicknesses were 10-35 nm at 23°C and 12-85 nm at 300°C.

Luttrell and Yoon used XPS to study the surface species responsible for the collectorless flotation of chalcopyrite [95]. They washed a freshly fractured chalcopyrite sample with a 5% Na_2S solution to remove oxidation products, then brought the sample back to an oxidizing environment by rinsing it with distilled water adjusted to a pH of 10.5. The sample was vacuum-dried and analyzed immediately. They fitted the S *2p* spectrum reasonably well with three components having the binding energies for S°, CuS and $CuFeS_2$. The results appear to be in agreement with the reaction proposed by Gardner and Woods [85]:

$$CuFeS_2 + 3H_2O \rightarrow Fe(OH)_3 + CuS + S^\circ + 3H^+ + 3e^- \qquad (2\text{-}30)$$

However, the S°/CuS ratio was much less than 1, contrary to what is expected by equation (2-30). One possible explanation is that elemental sulfur was lost by volatilization in the spectrometer vacuum. Buckley and Woods observed that elemental sulfur on the surface of galena disappeared completely after 15 hours at ambient temperature *in vacuo* [96].

Buckley and Woods studied the surface oxidation of chalcopyrite and other sulfide minerals by XPS [97, 98]. To avoid loss of elemental sulfur to the vacuum, samples were cooled to 150 K and spectra were recorded at this temperature. Exposure of a fracture surface to air resulted in a decrease in the surface concentrations of copper and sulfur relative to iron. The Fe *2p* spectrum showed a peak near 711 eV, which increased with time of exposure at the expense of the original peak for $CuFeS_2$ at 708 eV, and was consistent with $Fe_2O_3 \cdot xH_2O$. Their results indicated that iron became concentrated at the surface as a hydroxide/oxide, in agreement with the findings of Brion [92]. The copper spectrum indicated that copper remained bonded to sulfur as Cu(I) in the initial stages of oxidation, but on prolonged exposure (> 10 days) Cu(II) appeared along with sulfate, suggesting copper sulfate formed. A statistically acceptable fit to the S *2p* spectrum was obtained by assuming doublets for $CuFeS_2$, CuS and S°. However, the intensity of

the doublet assigned to S° was always much less than that for CuS even though spectra were recorded at 150 K. Furthermore, the spectra did not change when samples were warmed to ambient temperature *in situ*. From these observations they concluded that elemental sulfur was not present, therefore chalcopyrite oxidizing to CuS plus S° was not likely. An alternative, equally acceptable fit to the S *2p* spectrum was obtained by assuming just two doublets were present - one for $CuFeS_2$ and a doublet shifted by 1.8 eV higher than the one for $CuFeS_2$. A shift this large was interpreted as indicating that the iron-deficient sulfide, which remained after iron diffused to the surface to form an overlayer of oxide, was severely metal-deficient. The altered sulfide contained negligible iron because the intensity of the sulfidic iron peak was no more than sufficient to account for the intensity of the underlying chalcopyrite sulfur peak. On this basis they proposed the altered sulfide has a composition close to CuS_2 with a structure similar to that for chalcopyrite, but with vacancies in the sites previously occupied by the iron atoms. Values for the S *2p* binding energy previously reported for CuS_2 [99, 100], which has the pyrite structure, are significantly less than 1.8 eV relative to chalcopyrite. Thus they concluded that the iron-deficient sulfide does not restructure to form pyritic S_2^{2-} groups. Rather, it retains the original chalcopyrite lattice structure.

2.5 Activation of Chalcopyrite

As the previous sections have shown, chalcopyrite appears to passivate under oxidizing conditions in sulfate media and this results in poor leaching kinetics. The literature refers to several methods by which chalcopyrite can be depassivated, or "activated" to improve its amenability to leaching. The activation methods can be grouped into three categories: (1) mechanical activation, (2) thermal activation and (3) chemical activation with silver ions. These methods will be briefly reviewed in the next three sections.

2.5.1 Thermal Activation

The reactivity of chalcopyrite can be enhanced by thermal treatment. For the purposes of this review thermal treatment is understood to include non-oxidative heat treatment processes and not the classical roasting processes in which the sulfur is oxidized to sulfate or SO_2.

When heated in an inert atmosphere or under vacuum the natural, tetragonal form of chalcopyrite (α-chalcopyrite) loses sulfur until its composition reaches $CuFeS_{1.83}$ at 720°C, after which no more sulfur is lost [101]. The latter compound is called β-chalcopyrite and has a cubic

structure. Under acid oxidizing conditions β-chalcopyrite is attacked much more readily than α-chalcopyrite, losing copper preferentially to iron.

Warren *et al.* subjected chalcopyrite to two types of heat treatment: (1) calcination of the material at 825°C in the absence of oxygen and (2) treatment of the mineral with elemental sulfur at 475°C [102]. The untreated and treated materials were ground to minus 325 mesh and leached with H_2SO_4 at 90°C under 0.48 MPa oxygen pressure. After five hours leaching, copper extractions were 49.5% from untreated material, 83% from calcined material and 98.5% from sulfur-treated material. The improved extraction from calcined chalcopyrite was undoubtedly due to its transformation to the more leachable β form. The authors believed the improved extraction from the sulfur-treated chalcopyrite was due to a change in mineralogical composition brought about by sulfidation, i.e.,

$$CuFeS_2 + S^\circ \rightarrow CuS + FeS_2 \qquad (2\text{-}31)$$

to produce covellite and pyrite, leading to rapid and preferential leaching of the copper.

Subramanian and Kanduth determined the optimum conditions for preferential leaching of copper over iron from sulfidized chalcopyrite [103]. The initial molar H_2SO_4/Cu ratio was important; with a 2/1 ratio they obtained 97.6% copper extraction and only 18% iron extraction when the sulfidized material was leached at 110°C and 0.35 MPa O_2 for one hour. They commented that above 110°C the reaction was slow, which they believed was due to coating of the activated concentrate particles by a film of liquid sulfur.

Parker *et al.* found that when chalcopyrite is sulfidized the mineral is converted to idaite (Cu_5FeS_6) or bornite (Cu_5FeS_4) under sulfur-deficient conditions [104]. They also roasted chalcopyrite/covellite mixtures to produce bornite and pyrite, as follows:

$$3CuFeS_2 + 2CuS \rightarrow Cu_5FeS_4 + 2FeS_2 \qquad (2\text{-}32)$$

All of the activated products were more amenable to copper leaching in their tests than the untreated chalcopyrite.

Adam and Neumeier studied the sulfidation reactions for chalcopyrite in detail [105]. They reported that, above the boiling point of sulfur (445°C), with adequate sulfur present (13.9 wt. %), $CuFeS_2$ will partition by sulfidation to idaite plus pyrite. Below the boiling point of sulfur, however, with adequate sulfur (17.4 wt. %) present, $CuFeS_2$ will partition to covellite and

pyrite. The partitioned products were more amenable to leaching in ferric chloride and cupric chloride than the untreated chalcopyrite under the same conditions [106]. Another advantage they cited for leaching the partitioned products is that very little iron is solubilized.

The S.C. Copper Process, developed by Sherritt Gordon and Cominco in the early 1970's [107-109], makes use of a thermal activation step that involves heating the chalcopyrite to 650°C to drive off some sulfur, which is burned to form SO_2, followed by a reduction roast with hydrogen to produce H_2S. Most of the chalcopyrite is converted to bornite and any pyrite is converted to pyrrhotite. The pyrrhotite is decomposed in a non-oxidative acid leach,

$$FeS + H_2SO_4 \rightarrow FeSO_4 + H_2S \tag{2-33}$$

while the iron in bornite is selectively solubilized by a metathetic leach at 156°C:

$$Cu_5FeS_4 + CuSO_4 \rightarrow 2CuS + 2Cu_2S + FeSO_4 \tag{2-34}$$

The copper-enriched residue is then oxygen pressure leached to recover copper. Conditions of 100°C, 1 MPa oxygen pressure and 7.5 hour retention time yielded 98.4% copper extraction. The S.C. Copper Process was never commercialized.

Thermal activation appears to be an effective means of improving the reactivity of chalcopyrite feeds to acid oxidative leaching, but it involves a pyrometallurgical step which is objectionable because of potential air pollution problems from gaseous sulfur species.

2.5.2 Mechanical Activation

Chalcopyrite can be mechanically activated by several fine grinding methods to induce deformations or crystal lattice defects, and this improves its leachability. Gerlach *et al.* ground chalcopyrite in a vibrating impact mill and then leached the material for two hours at 100°C, 200 g/L solids density, 0.67 mol/L H_2SO_4 and 2 MPa oxygen pressure [110]. Copper extraction was improved from 15% for unground concentrate to 98% after grinding for three hours. The elemental sulfur yield was 80-85%. Beckstead *et al.* used attrition grinding to reduce the median particle size of chalcopyrite down to 0.5 μm, in which case 90% copper extraction was obtained by leaching in ferric sulfate for three hours at 93°C [46]. This fine grinding concept formed the basis for a patent [111]. The U.S. Bureau of Mines has recently studied simultaneous grinding and ferric sulfate leaching of chalcopyrite in a turbomill [112, 113]. They were able to obtain 95-97% copper extraction in three hours at 90°C. Tkacova and Balaz leached chalcopyrite

treated by dry vibration milling with ferric sulfate and attributed the increased leaching rate to the increased chalcopyrite surface area and to distortion of the chalcopyrite crystalline structure [114]. Tiwari *et al.* ground chalcopyrite concentrate to 50% minus 1.2 μm in an attrition mill, then leached the material in ferric sulfate which was regenerated in situ with O_2 [115]. They obtained over 80% copper extraction after three hours leaching at 93°C.

High copper extractions from chalcopyrite can be achieved in a reasonable time frame by ultra-fine grinding. The main disadvantages with the size reduction methods are that they are energy intensive and they exacerbate downstream solid/liquid separation problems.

2.5.3 Chemical Activation with Silver Ions

Chalcopyrite can be chemically activated with silver ions to improve its leachability under acid oxidizing conditions. The silver appears to act as a catalyst. Snell showed that the addition of small amounts (50-500 mg/L) of Ag as an initially soluble salt increased the copper extraction by ferric sulfate leaching from 46% to over 90% after three hours leaching at 91°C [116, 117]. Pawlek obtained a similar beneficial effect when Ag was added to attritor-ground chalcopyrite and leached at 110°C in acid under oxygen pressure [118, 119]. At temperatures above the sulfur melting point they noted a reduction in copper extraction due to inclusion of sulfides in liquid sulfur.

Miller *et al.* studied the kinetics of silver catalyzed ferric sulfate leaching of chalcopyrite [120, 121]. The enhanced rate of leaching was thought to be due to the formation of an intermediate silver sulfide film which forms on the $CuFeS_2$ surface by an exchange reaction:

$$CuFeS_2 + 4Ag^+ \rightarrow 2Ag_2S_{(surface)} + Cu^{2+} + Fe^{2+} \qquad (2\text{-}35)$$

Under these conditions, they observed that elemental sulfur forms a porous reaction product on the mineral surface, in contrast to the smooth tenacious sulfur layer formed in uncatalyzed leaching. They concluded that in silver catalyzed leaching the reaction rate is not controlled by diffusion through the elemental sulfur layer. Instead, the rate is controlled by an electrochemical reaction of Ag_2S with Fe^{3+}:

$$Ag_2S_{(surface)} + 2Fe^{3+} \rightarrow 2Ag^+ + 2Fe^{2+} + S^\circ \qquad (2\text{-}36)$$

This explains their finding that the reaction is dependent on the initial Fe^{3+} concentration but not the initial Cu^{2+} concentration. However, their results are in contrast to those of Mateos *et al.*

who presented evidence indicating that elemental sulfur has no effect on the uncatalyzed or catalyzed ferric sulfate leaching of chalcopyrite [122]; they concluded that the passivating layer consists of a sulfide or polysulfide product arising from a transformation of the chalcopyrite.

Peters and Doyle theorized that the reason silver is such an effective catalyst is that the solid state diffusivity of silver in sulfide minerals is very fast [123], so silver can easily enter into exchange reactions (equation (2-35)) and silver sulfide can readily abstract electrons, by ferric iron for instance (equation (2-36)).

Silver also has a catalytic effect in bioleaching of chalcopyrite. B.C. Research scientists discovered that silver dramatically enhanced copper leach rates and extractions, and resulted in quantitative conversion of the sulfide portion to elemental sulfur rather than sulfate [124-126]. To ensure that elemental sulfur was produced consistently in high yield, it was found necessary to activate the concentrate by mixing it with a solution containing silver, thiosulfate ions and cupric ions prior to bioleaching [125, 126]. As with the silver catalyzed chemical leaching processes, the silver precipitates as silver sulfide on chalcopyrite mineral surfaces and this enhances chalcopyrite oxidation. The chemistry of silver catalyzed bioleaching can be represented by the following reaction [126]:

$$CuFeS_2 + O_2 + 2H_2SO_4 \rightarrow CuSO_4 + FeSO_4 + 2S^\circ + 2H_2O \qquad (2\text{-}37)$$

Note that this is the same reaction given by Vizsolyi *et al.* [2] (equation (2-18), page 17) for the oxygen pressure leaching of chalcopyrite , i.e., the overall chemistry is the same. The reason for the switch in chemistry from sulfate producing to sulfur producing has not been determined for certain. Several theories have been advanced. Trace amounts of soluble silver are known to be toxic or inhibitory to the bacteria [127]. It is possible that silver interferes with the bacterial sulfide oxidizing mechanism but not the ferrous oxidation mechanism, so that the leach is essentially a catalyzed ferric leach with the bacterial role reduced to regenerating the spent ferric iron. Another possibility is that the silver causes the bacterial sulfide to sulfate oxidation pathway to stop at elemental sulfur. It has been observed that the redox potential during catalyzed bioleaching is in the range 620-680 mV [126] which is about 100 mV lower than the Eh during non-catalyzed bioleaching. The lower Eh would be expected to favour the formation of sulfur over sulfate. The lower Eh may also explain why pyrite is not attacked during catalyzed bioleaching.

Sukla *et al.* studied the kinetics of silver catalyzed and uncatalyzed bioleaching of chalcopyrite [128]. They reported that uncatalyzed bioleaching exhibits parabolic kinetics with diffusion through a smooth jarosite-sulfur reaction product thought to be the likely rate limiting step. In contrast, with catalyzed bioleaching the product layer was much more porous and the kinetics reverted to chemical reaction control. Their conclusions are similar to the conclusions of Miller *et al.* [120, 121] for the silver catalyzed ferric sulfate leaching of chalcopyrite.

The main problem with silver catalyzed leaching processes is that recovery of the silver from the residue is difficult because much of it is tied up as a silver jarosite from which it is difficult to recover. Recycling the silver is essential because of its high cost. Other ions have been tested in an effort to come up with a less expensive catalyst. Mercury [122] and tin and bismuth [129] are also catalytic but the results are not as good as with silver.

In summary, the chemical activation of chalcopyrite by silver ions yields much higher copper extractions under acid oxidizing conditions at low to moderate temperatures, i.e., temperatures below the sulfur melting point of 119°C. Copper extractions in excess of 90% are possible in silver catalyzed ferric sulfate leaching, oxygen pressure leaching and bioleaching. The silver catalyzed mechanism is not well understood, but it has been shown that silver precipitates as silver sulfide on the mineral surface and this has a depassivating effect.

2.6 Use of Sulfur Dispersing Surfactants in Leaching

One aspect of the research program was concerned with investigating the potential benefit of using sulfur-dispersing surfactants in the oxygen pressure leaching of chalcopyrite. This appears to be a novel concept as a search of the literature failed to turn up any information on this particular application of surfactants. However, surfactants have been used successfully in other leaching systems. In this section a brief overview of surfactant properties as they apply in mineral-aqueous media will be given, followed by a review of surfactant applications in leaching systems.

2.6.1 Overview of Surfactant Properties in Mineral-Aqueous Media

Myers defined surfactants as "those compounds which, when present in relatively low concentrations, will preferentially adsorb at available interfaces, replacing the higher energy bulk phase molecules and resulting in a net reduction in the free energy of the system as a whole" [130]. In aqueous systems all surfactant molecules possess two structurally dissimilar groups: (1) a group with little attraction for water, called the hydrophobic group, and (2) a group with a

strong attraction for water, called the hydrophilic group. The hydrophobic group is generally a long-chain hydrocarbon radical, although there are examples of halogenated or oxygenated hydrocarbon or siloxane chains. The hydrophilic group is an ionic or highly polar group that can impart some water solubility to the molecule.

When a surfactant is dissolved in water, the hydrophobic group causes a distortion of the water structure, which increases the overall energy of the system and means that less work is required to transport a surfactant molecule to a surface or interface. The surfactant will therefore tend to concentrate or preferentially adsorb at those locations. Since less work is required to bring surfactant molecules to the available interfaces, the presence of the surfactant decreases the work required to increase the interfacial area. The work per unit area required to form that new interface is the surface free energy or surface tension of the system, γ, which has S.I. units of millinewtons per metre (mN/m). For solid surfaces, the convention is to use millijoules per square metre (mJ/m^2). Adsorption of surfactants at interfaces will always lead to a reduction in the interfacial/surface tension.

Surfactants are classified depending on the charge of the surface-active moiety, usually the larger part of the molecule. The four general groups of surfactants are defined as follows:

1. Anionic, with the hydrophilic group carrying a negative charge such as carboxyl ($RCOO^-M^+$), sulfonate ($RSO_3^-M^+$), or sulfate ($ROSO_3^-M^+$).

2. Cationic, with the hydrophile bearing a positive charge, for example, the quaternary ammonium halides ($R_4N^+Cl^-$).

3. Nonionic, where the hydrophile has no charge, but derives its water solubility from the highly polar groups such as polyoxyethylene ($-OCH_2CH_2O-$).

4. Amphoteric (and zwitterionic), in which the molecule contains, or can potentially contain, both a negative and a positive charge, e.g. the sulfobetaines ($RN^+(CH_3)_2CH_2CH_2SO_3^-$).

Surfactants are widely used in many industries, ranging from primary processes such as the recovery and purification of raw materials in the mining and petroleum industries, to enhancing the quality of finished products such as paints, detergents, cosmetics, pharmaceuticals

and foods. By far the largest class of surfactants in use are the anionics, which constitute approximately 70-75% of total consumption [131].

Hydrometallurgical systems give rise to interfaces, such as gas/liquid, liquid/liquid and solid/liquid. Osseo-Asare has reviewed the fundamental importance of interfacial phenomena in some hydrometallurgical systems [132]. He points out that adsorption and wetting phenomena occurring at interfaces play important roles in many aqueous metallurgical processes, including leaching, flocculation of leach residues, electrowinning and solvent extraction.

When finely divided mineral particulates are immersed in water, they acquire a surface charge, the presence of which controls much of their interfacial behaviour. The charging of the solid surface gives rise to a separation of electrical charge such that the solid and solution acquire opposite charges at their phase boundary. This is the electrical double layer. The double layer arises because in order to preserve electroneutrality, the surface charge on the solid must be balanced by ions of opposite charge, i.e., the counter ions.

Both ionic and nonionic species are capable of adsorbing at the solid/aqueous interface. In the case of an organic surfactant adsorbing on a solid, the free energy of adsorption, ΔG_{ads}, is of the general form [132]:

$$\Delta G_{ads} = \Delta G_{coul} + \Delta G_{cc} + \Delta G_{cs} + \Delta G_{chem} \qquad (2\text{-}38)$$

where ΔG_{coul} is the electrostatic energy, ΔG_{cc} is the free energy change due to hydrophobic interactions of the organic groups of surfactant molecules with each other (chain-chain interaction), ΔG_{cs} is the free energy change due to hydrophobic interactions of the organic groups with the solid surface (chain-solid interaction), and ΔG_{chem} accounts for the formation of chemical bonds between the solid surface and the adsorbing species. The process of adsorption is termed physical (physisorption) if the electrostatic and hydrophobic interactions constitute the driving force for adsorption. The process is termed chemisorption when the adsorbing species form chemical bonds with ions or atoms in the solid surface. The hydrophobic bonding contributions to ΔG_{ads} depend on the organic chain length. The greater the number of CH_2 groups, the larger the negative value of the chain interaction terms.

In this study we are concerned with the behaviour of liquid sulfur on the chalcopyrite mineral surface. If a liquid is placed on a solid, it may either spread so as to completely wet the solid or remain as a drop having a definite angle of contact. The angle of contact is the angle between the solid surface and a tangent drawn to the liquid surface at the point of contact with

the solid. Owusu [133, 134] has shown how in the zinc sulfide-liquid sulfur-zinc sulfate system, the liquid sulfur-mineral contact angle increases markedly in the presence of sulfur-dispersing surfactants, as depicted in Figure 2-11. The contact angle that a liquid makes when it is in equilibrium with other phases in contact with it is related to interfacial tensions by Young's equation [135]:

$$\gamma_{MA} = \gamma_{MS} + \gamma_{SA}\cos\theta \tag{2-39}$$

or

$$\gamma_{MA} - \gamma_{MS} = \gamma_{SA}\cos\theta \tag{2-40}$$

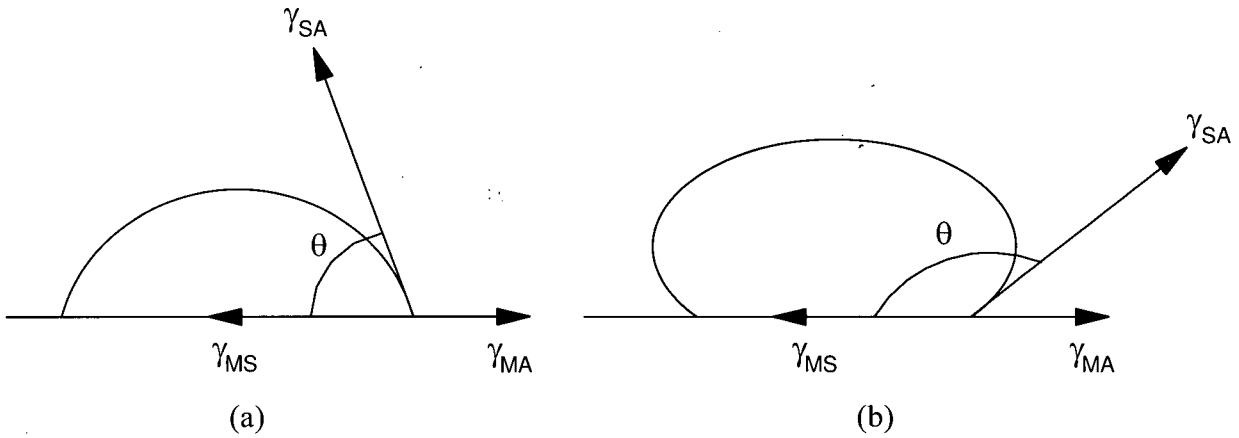

Figure 2-11. Liquid sulfur-mineral contact angles (θ): (a) in the absence of surfactant and (b) in the presence of a sulfur-dispersing surfactant [133, 134].

where the mineral-aqueous solution interfacial tension, γ_{MA}, is balanced by the sum of the mineral-liquid sulfur interfacial tension, γ_{MS}, plus the component of the liquid sulfur-aqueous solution interfacial tension, γ_{SA}, resolved parallel to the solid surface, $\gamma_{SA}\cos\theta$. A zero contact angle is the condition for complete wetting of the mineral by liquid sulfur. With a contact angle greater than 90° the liquid sulfur should move freely about the surface and be easily removed as a result of slurry agitation. A contact angle of 180° represents no wetting at all, which is not attainable in practice.

Owusu showed that the liquid sulfur-zinc sulfate interfacial tension, γ_{SA}, is usually reduced in the presence of certain surfactants [133, 134]. Thus by measuring liquid-liquid interfacial tensions and liquid-solid contact angles in the presence and absence of a particular

surfactant, a prediction can be made as to the ability of the surfactant to disperse elemental sulfur under pressure leaching conditions.

2.6.2 Surfactants in Oxygen Pressure Leaching of Zinc Concentrates

Early work on oxygen pressure leaching of zinc sulfide concentrates was restricted to temperatures below the melting point of sulfur because molten sulfur coated the partially reacted sulfides and prevented reaction beyond 60-70% zinc extraction [136]. The overall reaction for zinc sulfide is:

$$ZnS + H_2SO_4 + \tfrac{1}{2}O_2 \rightarrow ZnSO_4 + S^\circ + H_2O \qquad (2\text{-}41)$$

At temperatures below the sulfur melting point retention times are unacceptably long (6-8 hours). Thus commercialization of zinc pressure leaching was stymied until it was discovered that the addition of sulfur-dispersing surfactants to the leach greatly improved zinc extractions at temperatures above the sulfur melting point [6, 137]. Surfactants that were found to be beneficial were:

- lignin derivatives such as sodium and calcium lignosulfonate
- tannin compounds, particularly tree bark extracts such as quebracho
- alkylaryl sulfonates, particularly sodium alkylbenzene sulfonates

Results given by Sherritt in their patent [6] show that at surfactant dosages of 0.1-0.3 g/L, zinc extraction was improved from 63% to 96-98% when zinc sulfide concentrate ground to minus 325 mesh was leached for 100 minutes at 150°C. The precise manner in which the surfactants functioned was not known at the time but it was believed that they prevented the coating of unreacted zinc sulfides with molten elemental sulfur, allowing the reaction to go to completion.

As a result of this discovery there are now several commercially operating zinc pressure leach plants. Personnel at the Canadian operations were interviewed to obtain information on their surfactant usage. Cominco's plant in Trail, B.C. presently uses about 0.6 kg calcium lignosulfonate per tonne concentrate [138]. Falconbridge's Kidd Creek plant in Timmins, Ontario uses about 1.4 kg/t sodium lignosulfonate [139]. Hudson Bay Mining and Smelting Company's new plant in Flin Flon, Manitoba, which commenced operation in August 1993, uses about 1.2 kg/t quebracho plus 0.8 kg/t calcium lignosulfonate in a two-stage pressure leach process [140]. The reason for the relatively high surfactant consumption is not known but it may

be related to the presence of a minor amount of copper in the feed. There is speculation that the copper may lower the effectiveness of the surfactant by accelerating its degradation [141]. The Hudson Bay leach solution contains about 2 g/L copper [140]. Bolton *et al.* reported that a second, high-acid leaching stage is required to effect high copper recovery from zinc concentrates containing a small amount of copper, due to the refractory nature of the chalcopyrite [142]. They noted that as the copper grade increased above 3%, the copper recovery decreased because of preferential pelletization of chalcopyrite with pyrite and elemental sulfur during the leach, despite the presence of lignosulfonate. This suggests that lignosulfonate is not a particularly good surfactant for chalcopyrite leaching.

Recently, Owusu carried out a comprehensive study of the role played by lignosulfonate and other surfactants in the zinc pressure leach system [133, 134]. He measured the effect of the surfactants on the liquid sulfur-aqueous solution interfacial tensions and on the liquid sulfur-mineral contact angles using a high temperature-high pressure apparatus. He reported that most of the surfactants studied tended to adsorb at the liquid sulfur-aqueous solution interface, and all of them adsorbed at the solid mineral-aqueous solution interface. In most cases the liquid sulfur-aqueous solution interfacial tensions decreased substantially, from 54-55 mN/m in the absence of surfactant to as low as 20-22 mN/m in the presence of 0.1-0.3 g/L surfactant. Also, the liquid sulfur-mineral contact angles increased from 80° to as high as 155°. This resulted in a marked reduction in the work of adhesion between the liquid sulfur-mineral phase which increased the tendency for the liquid sulfur to be dispersed. He concluded that the ability of a surfactant to reduce the interfacial tension did not necessarily mean it was an effective leaching aid in the zinc pressure leach system. Some of the surfactants he studied reduced the sulfur-solution interfacial tension yet were ineffective in enhancing zinc extraction. It was postulated that their ineffectiveness may have been due to their rapid decomposition under pressure leach conditions, as they are known to be susceptible to oxidative degradation. Orthophenylenediamine (OPD) did not reduce the sulfur-solution interfacial tension yet it was one of the most efficient dispersants of elemental sulfur under leaching conditions, enabling very high zinc extractions to be obtained. It was thought to be quite resistant to degradation. Owusu concluded the most important characteristics for the surfactant to possess are: (1) an ability to increase the liquid sulfur-mineral contact angle and (2) reasonable stability under pressure leaching conditions. Of the surfactants studied, the most effective in terms of their ability to enhance zinc extractions were the lignosulfonates and the phenylenediamines (Table 2-2). Infrared spectral analysis

indicated the lignin sulfonate ions are adsorbed both physically and chemically by the mineral. The chemically adsorbed species forms a Zn(II)-based complex. OPD is adsorbed chemically through the interaction of the C-N functional group with the metal ions, forming a metal-amine complex.

Table 2-2. Effect of lignosulfonate and phenylenediamine surfactants on zinc and iron extraction during the oxygen pressure leaching of zinc sulfide concentrate. Conditions: 67 g/L solids density, 97% minus 170 mesh feed, 140°C, 1.1 MPa O_2 pressure, 1 hour leach time, initial leach solution contained 109 g/L H_2SO_4, 1.27 mol/L Zn^{2+}, 0.14 mol/L Fe^{2+} and 0.1 g/L surfactant (taken from Owusu's work [133]).

Surfactant	Zinc Extr. (%)	Iron Extr. (%)
None	48.9	40.5
Lignosol	93.6	69.4
Orthophenylene Diamine	99.8	80.1
Metaphenylene Diamine	98.4	69.5

2.6.3 Surfactants in Oxygen Pressure Leaching of Nickeliferous Pyrrhotite Concentrates

Oxygen pressure leaching of natural pyrrhotite and artificial pyrrhotite (produced by thermal decomposition of pyrite) in sulfate media was studied by workers at Sherritt Gordon in the 1960's [143]. Sulfide is oxidized primarily to elemental sulfur. The reactions were presumed to be:

$$FeS + H_2SO_4 \rightarrow FeSO_4 + H_2S \quad (2\text{-}42)$$

$$H_2S + \tfrac{1}{2}O_2 \rightarrow S^\circ + H_2O \quad (2\text{-}43)$$

$$FeS + Fe_2(SO_4)_3 \rightarrow 3FeSO_4 + S^\circ \quad (2\text{-}44)$$

The optimum temperature was 110°C. Exposure of the leach slurry to temperatures above about 118°C, even for a short period, adversely affected the oxidation rate due to coating of the solid particles with molten elemental sulfur. The researchers made the interesting discovery that at temperatures below the melting point of sulfur, surfactants increased significantly the oxidation rate, but not the ultimate extent of reaction. It is not known if they investigated the use of surfactants above the sulfur melting point.

Falconbridge researchers investigated the pressure leaching of nickeliferous pyrrhotite concentrate as a way to recover the nickel and sulfur by a non-pyrometallurgical route [144]. The temperature was controlled at 110°C to ensure that the sulfur melting point was not exceeded. They reportedly failed to develop a viable process scheme, apparently because the oxidized slurry was unfilterable due to the fine, slimy nature of the iron residue produced.

In the 1970's researchers at INCO also worked on a pyrrhotite leach process. They discovered that the addition of certain surfactants to the leach allowed them to operate at temperatures above the sulfur melting point [19, 145, 146]. The advantages over leaching at low temperature were twofold: (1) sulfide oxidation rates and nickel and sulfur recoveries were much improved and (2) slurries were readily filterable, probably because hematite rather than ferric hydroxide was formed. They constructed a glass autoclave [19] in order to observe the leach in progress. In the absence of surfactants, large elongated globules of molten sulfur were observed to form, which occluded the sulfides. The globules settled and rolled around the bottom of the autoclave and were not dispersed despite vigorous agitation. Addition of surfactants resulted in the sulfur becoming completely dispersed into small droplets, resulting in minimal occlusion of the sulfides. Initially the surfactant INCO used was a di-stearyl amine; some of their results using this amine are reproduced in Table 2-3. The amine appeared to be stable under the conditions employed.

The amine surfactant worked well but at $1.60 per kilogram (1976 Canadian dollars) it was considered to be too expensive as the pyrrhotite concentrate contained only 1% nickel. Fatty acids such as stearic and oleic acid were tried and found to be equally effective [19] but still deemed too expensive ($0.50-0.60/kg). Interestingly, they found that lignosulfonate and quebracho were ineffective for nickeliferous pyrrhotite concentrate. INCO finally settled on tall oil pitch, which is a product of the Kraft pulping processing of pine trees and contains about 25% rosin acids and 8% fatty acids. It cost only $0.12/kg (1978 Canadian dollars). Some of INCO's results with tall oil pitch are reproduced in Table 2-4.

INCO never commercialized the process but still views it as an attractive option should nickel prices rise sufficiently [147].

Table 2-3. Effect of di-stearyl amine surfactant on oxygen pressure leaching of INCO pyrrhotite concentrates. Conditions: 30% solids density, 2.0 MPa O_2 pressure, initial leach solution was water [145].

Leach Temp. (°C)	Leach Time (h)	Surfactant Addition (kg/t conc.)	Nickel Extr. (%)	Sulfide Oxid. (%)
120	1	0	70	93
120	1	2.5	83	92
160	1	0	56	82
160	1	2.5	94	99

Table 2-4. Effect of tall oil pitch surfactant on oxygen pressure leaching of INCO pyrrhotite concentrates. Conditions: 20% solids density, 1.7 MPa O_2 pressure, initial leach solution was water [19].

Leach Temp. (°C)	Leach Time (h)	Surfactant Addition (kg/t conc.)	Nickel Extr. (%)
110	1.5	0	84
130	1.5	0	51
130	1.5	1.5	91
140	2	2.5	94
150	2	2.5	89

Oxygen pressure leaching of nickeliferous pyrrhotite has been practiced commercially by the Noril'sk Mining and Metallurgy Corporation in Russia since 1979 [148, 149]. The process operates at 125-135°C and uses a "concentrated sulfite pulp", evidently containing primarily lignosulfonate, as a surfactant. The apparent effectiveness of lignosulfonate for pyrrhotite is contrary to the findings of Jones and Krause [19].

2.6.4 Surfactants in Pressure Oxidation of Refractory Gold Ores and Concentrates

Pressure oxidation of refractory gold ores and concentrates is practiced commercially to oxidize sulfide minerals such as pyrite, pyrrhotite and arsenopyrite, which encapsulate gold. Some of these operations suffer from sulfur agglomeration problems. Sulfur agglomeration is a particular nuisance with pyrrhotite-containing feeds. The sulfur tends to occlude unreacted sulfides and cause plugging problems. Many of these operations use, or have used, surfactants,

but the use of surfactants alone is not always satisfactory. Sherritt Gordon advocates partial recycling of the oxidized solids to increase the proportion of inert, non-sulfide solids in the feed; apparently this helps to suspend and disperse the elemental sulfur [150].

Refractory gold concentrate produced at the Sao Bento gold mine in Brazil contains substantial pyrrhotite in addition to pyrite and arsenopyrite. The concentrate is pressure oxidized at 190°C by the Sherritt process [151]. To minimize sulfur agglomeration, the original process configuration included recycling a portion of the oxidized solids and adding sodium lignosulfonate to the unoxidized feed. Apparently the use of lignosulfonate has been discontinued [152], perhaps because a biooxidation preleach was recently implemented to oxidize the bulk of the pyrrhotite and the more readily oxidizable sulfide fraction ahead of pressure oxidation [153]. This may have reduced the amount of elemental sulfur formed.

The Porgera gold mine in Papua New Guinea employs Sherritt pressure oxidation technology to treat their refractory gold ore. They initially added 0.5 kg/t calcium lignosulfonate to the leach, however its use was discontinued when no clear benefit was observed [152]. The Porgera ore contains about 7% sulfide, primarily in the form of pyrite which does not generate much elemental sulfur when oxidized. Hence, sulfur agglomeration does not appear to be a significant problem and in this operation surfactants were not required.

Placer Dome's Campbell gold mine in Balmertown, Ontario recently installed a pressure oxidation plant to treat a refractory gold concentrate, also using Sherritt technology [154]. The sulfide mineral composition of the concentrate is about 42% pyrite, 41% pyrrhotite and 17% arsenopyrite [155]. The sulfide sulfur content is about 9.5%. The leach operates at 190-195°C. Standard practice is to recycle a portion of the oxidized solids back to the leach and to add calcium lignosulfonate in the amount 0.15 kg/tonne concentrate. The effect of lignosulfonate on process performance was apparently not studied [155].

The Nerco Con Mine in the Northwest Territories also recently installed a pressure oxidation plant [156]. The feed is a mixture of refractory pyrite-arsenopyrite concentrate, arsenic trioxide sludge and old roaster calcine waste. The purpose of pressure oxidation is to liberate encapsulated gold and to fix arsenic as the relatively stable ferric arsenate. They add 0.9 kg/t calcium lignosulfonate to the feed, which they believe reduces the elemental sulfur content (elemental sulfur is a bad cyanicide), although they are not sure [157]. Recycle of oxidized solids is not practiced. The leach temperature is 210°C which is probably high enough to ensure virtually complete oxidation of sulfide to sulfate.

Barrick Gold Corp. treats refractory gold ore at their Goldstrike Mine in Nevada by pressure oxidation. The sulfide mineralization is primarily pyrite and marcasite. Surfactants in the leach are not required as they do not have a problem with elemental sulfur [158]. The absence of elemental sulfur is attributed to the high operating temperature, which is in the range 210-225°C. Presumably the sulfur is completely oxidized to sulfate.

In summary, there does not seem to be a clear benefit in using surfactants in the pressure oxidation of refractory gold ores and concentrates. Most of the operations run at temperatures in excess of 190°C, at which little elemental sulfur survives, making the use of surfactants unnecessary.

2.7 Conclusions and Focus of the Present Study

Previous research on the chemistry and kinetics of leaching of chalcopyrite clearly shows that regardless of the method used (ferric leaching, oxygen pressure leaching or bioleaching), chalcopyrite is extremely resistant to leaching in sulfate media. In fact, the studies have shown that the options available for achieving a high copper extraction from chalcopyrite in a reasonable time frame are few:

1. Leach at temperatures exceeding 200°C (oxygen pressure leaching);
2. Grind the chalcopyrite very fine, to 1 μm or less;
3. Activate the chalcopyrite by thermal, mechanical or chemical means.

The leaching of chalcopyrite in sulfate media has received considerable study, yet there is still uncertainty regarding the leaching mechanism. The reaction kinetics have been variously described as being under diffusion control (parabolic), chemical reaction control (linear) and mixed diffusion-chemical reaction control. It is generally agreed that the difficulty in leaching chalcopyrite is related to the formation of a passivating layer on the mineral surface. However the identity of this passivating layer and the mechanism by which it forms have not been reliably established. Many of the researchers involved in the leaching studies have theorized that leaching is impeded by elemental sulfur (either solid or liquid sulfur, depending on the leach temperature), or a basic iron sulfate. On the other hand, the researchers involved in the electrochemical and surface studies tend to favour the idea that chalcopyrite is passivated by a sulfide layer.

The intent of the present study was to shed new light on the chalcopyrite passivation phenomenon. To accomplish this, the research focussed on three different areas. One, the oxygen pressure leaching behaviour of chalcopyrite in acid sulfate media was re-examined. In particular, the potential benefits of using sulfur-dispersing surfactants at moderate temperatures (125-155°C) were studied. Two, the surfaces of leached chalcopyrite specimens were examined by AES and XPS to characterize the composition of any passivating layers that may form as a result of leaching. Finally, the results of the leaching and surface characterization studies were incorporated into a kinetic model to explain the leaching and passivation of chalcopyrite.

CHAPTER 3

BASIC PRINCIPLES OF AUGER ELECTRON SPECTROSCOPY AND X-RAY PHOTOELECTRON SPECTROSCOPY

3.1 Introduction

To gain insight into the mechanism by which chalcopyrite is passivated during oxygen pressure leaching, a method of examining chalcopyrite mineral surfaces for evidence of leaching-induced, surface-specific compositional changes was required. The traditional approach for studying leached mineral particles has been to use electron microprobe techniques such as scanning electron microscopy (SEM) in conjunction with energy dispersive X-ray spectroscopy (EDX). For example, as was discussed in Section 2.3, Dutrizac [43] and Le Houillier and Ghali [60] used SEM to study the morphology of the sulfur layer formed on chalcopyrite during ferric sulfate leaching and oxygen pressure leaching, respectively. SEM/EDS is relatively fast and easy to use, and it is capable of providing semi-quantitative to quantitative information. However, SEM/EDX suffers from the disadvantage of having poor analytical spatial and depth resolution capabilities. The depth of electron stimulated X-ray production as well as the X-ray source size (which are dependent mainly on the excitation energy of the particular X-ray line used and the sample density), are typically in the micron to several micron range [159]. Thus SEM/EDX is not suited for the analysis of surface films if the films are less than several microns thick. As was shown in the reviews on chalcopyrite electrochemistry (Section 2.4.1) and chalcopyrite surface studies (Section 2.4.2), there is evidence that chalcopyrite can form extremely thin surface films, on the order of 1-100 nm thick. These films would not be detected by SEM/EDX. Thus, for the purposes of this study a more surface-sensitive analytical technique was required. To this end, Auger electron spectroscopy (AES) and X-ray photoelectron spectroscopy (XPS) were employed in an attempt to obtain compositional information on any surface layers that may form on chalcopyrite during oxygen pressure leaching in sulfate media.

In the past 20 years AES and XPS have emerged as powerful tools for studying the surface compositions of a wide variety of materials. Their applications in corrosion science [160], sulfide mineral flotation [161] and geochemistry [162, 163] have recently been reviewed. This chapter provides an overview of the fundamental theory and application of AES and XPS to

the study of solid surfaces. As pointed out by Hochella [162], surface scientists consider the true "surface" of a solid to mean the top monolayer of atoms. AES and XPS typically obtain their information from the top several monolayers of the solid, more accurately defined as the "near-surface". For convenience the term "surface" is used throughout this thesis, but is understood to actually mean "near-surface".

3.2 Notation used in AES and XPS

The notation used for naming the principal spectral lines in AES and XPS (Table 3-1 [162]) is based on the description of orbital motion of an electron around an atomic nucleus, given by the so-called *j-j* coupling scheme [162, 164]. In the *j-j* coupling scheme, the total angular momentum of a single isolated electron is obtained by summing vectorially the individual electronic spin and angular momenta. The principal quantum number, n, takes on the values 1, 2, 3, 4..., and is designated K, L, M, N..., respectively. The orbital angular momentum quantum number, l, can take on the values 0, 1, 2, 3...n - 1 (designated s, p, d, and f respectively) for each level n. Adding the spin momentum quantum number, s, which takes on the values of $\pm 1/2$, the total electron angular momentum, j, is equal to $l + s$, i.e. 1/2, 3/2, 5/2, 7/2, etc. for the various sublevels as shown in Table 3-1. The various combinations of n, l and j quantum numbers describe the different subatomic levels from which Auger and photoelectrons originate.

By convention, AES peaks are named after the three atomic levels involved in the Auger process (discussed in Section 3.3.1), using the X-ray notation. Conversely, XPS peaks are named by the atomic level from which the photoelectron is ejected (discussed in Section 3.4.1), using the spectroscopic notation. For example, the state labelled L_3 in the X-ray notation is written as $2p_{3/2}$ in the spectroscopic notation.

3.3 Auger Electron Spectroscopy

3.3.1 The Auger Process

The Auger process is depicted in the simplified energy diagram shown in Figure 3-1 [164]. The diagram shows the core (K, L, M) and valence (V) energy levels of electrons in an atom. In this example, the K level is ionized by an incident electron whose energy E_p is greater than the binding energy E_K of an electron in K. This leaves the atom in an excited state (Figure 3-1b), and it relaxes by filling the vacancy with an electron from a higher-energy outer level, in this example the L_1 level (Figure 3-1c). As a result of this transition the energy difference

Table 3-1. Comparison of the X-ray and spectroscopic notation used for the first four principle atomic levels (from Hochella [162]).

Principal shell	Total electrons in shell	Quantum numbers (*j-j* coupling)			X-ray (Auger) notation	Spectroscopic (XPS) notation	Electrons in each level
		n	*l*	*j*			
K	2	1	0	1/2	*K*	$1s_{1/2}$	2
L	8	2	0	1/2	L_1	$2s_{1/2}$	2
		2	1	1/2	L_2	$2p_{1/2}$	2
		2	1	3/2	L_3	$2p_{3/2}$	4
M	18	3	0	1/2	M_1	$3s_{1/2}$	2
		3	1	1/2	M_2	$3p_{1/2}$	2
		3	1	3/2	M_3	$3p_{3/2}$	4
		3	2	3/2	M_4	$3d_{3/2}$	4
		3	2	5/2	M_5	$3d_{5/2}$	6
N	32	4	0	1/2	N_1	$4s_{1/2}$	2
		4	1	1/2	N_2	$4p_{1/2}$	2
		4	1	3/2	N_3	$4p_{3/2}$	4
		4	2	3/2	N_4	$4d_{3/2}$	4
		4	2	5/2	N_5	$4d_{5/2}$	6
		4	3	5/2	N_6	$4f_{5/2}$	6
		4	3	7/2	N_7	$4f_{7/2}$	8

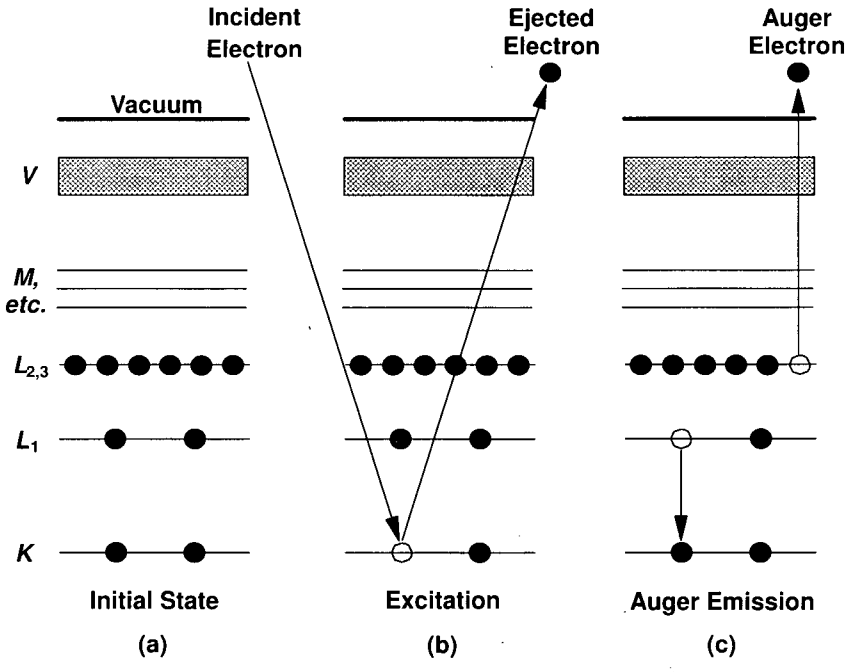

Figure 3-1. Schematic diagram depicting the Auger process (adopted from ref. [164]).

$\left(E_K - E_{L_1}\right)$ becomes available as excess kinetic energy. This excess energy can be dissipated in one of two ways, either through emission of an X-ray photon at that energy, or it can be given up to a second electron from the same level or from a higher-energy level; this electron is then ejected. The first process is the basis of X-ray fluorescence and electron probe microanalysis; the second process, shown in Figure 3-1c, is called Auger emission. In the example depicted in Figure 3-1, the Auger electron is ejected from the $L_{2,3}$ level and the Auger transition is called the $KL_1L_{2,3}$ transition.

It can be seen that after emission of the Auger electron, the atom lacks two electrons and hence has become a doubly-charged ion. A minimum of three electrons are associated with the production of an Auger electron. Thus, the process does not occur in hydrogen or helium, but Auger electrons are generated from all other elements.

3.3.2 Properties of Auger Electrons

In the Auger transition depicted in Figure 3-1c, the energy of the ejected Auger electron is:

$$E_{KL_1L_{2,3}} = E_K - E_{L_1} - E^*_{L_{2,3}} \tag{3-1}$$

where E_i are the binding energies of the ith atomic energy levels. $E^*_{L_{2,3}}$ is starred because it is the binding energy of the $L_{2,3}$ level in the presence of a vacancy in level L_1, and is therefore different from $E_{L_{2,3}}$, the ground state binding energy. From equation (3-1) it can be seen that Auger energies are independent of the incident electron energy. In fact, Auger energies are functions only of atomic energy levels, so that each element has a unique set of Auger energies. Thus Auger energies can be used unambiguously to identify the elements from which the Auger electrons originate.

The characteristic low energies of Auger electrons (generally 20-2000 eV) means that only those Auger electrons generated within the first few monolayers (approximately 5 nm) escape the solid to be detected. The depth of analysis depends on the distance that the Auger electrons travel through the sample without losing energy. Electrons in solids typically lose energy through inelastic collisions with other electrons. The electron *attenuation length* is defined as the distance at which the probability of electron escape from a solid without the occurrence of an inelastic scattering event drops to e^{-1} (36.8%) [162]. To give an example of the

typical range of Auger electron attenuation lengths in minerals, Hochella determined that the attenuation lengths in silicate minerals are between 1.5-3 nm [162]. The electron *escape depth* has the same meaning as attenuation length, except that it is defined for electrons travelling normal to the surface. Therefore, the attenuation length times the cosine of the angle between the direction of electron travel and the sample surface normal is equal to the escape depth. The probability of electron escape falls off exponentially from the depth of origin. More specifically, 63% ($1 - e^{-1}$) of the signal originates from less than one times the escape depth, 86% ($1 - e^{-2}$) is from less than two times the escape depth and 95% ($1 - e^{-3}$) is from less than three times the escape depth. Three times the escape depth is often called the *information depth*.

3.3.3 Generation and Interpretation of Auger Spectra

The basic components of an AES instrument are an electron gun to irradiate the sample surface, a sample/support system, and an electron energy analyzer to collect and analyze the electron distribution. Ultra-high vacuum (~10^{-8} Pa) conditions are maintained to ensure minimum attenuation of the Auger signal and minimal contamination of the sample surface during analysis.

Auger spectra are usually displayed as derivative spectra, dN/dE vs. E, where N is the signal intensity (in arbitrary units) and E is the Auger electron kinetic energy (in eV). The reason for using derivative spectra is that the large background of inelastically scattered electrons is largely eliminated and the Auger peaks are enhanced. By convention, the energies of the differentiated peaks are taken at the peak minimum. The individual peaks are identified with the aid of tabular and graphical data provided in various reference books, for example the handbook by Davis *et al.* [165]. Details regarding the Auger transitions, peak positions and sensitivity factors of interest in this study have been compiled in Appendix 3.

Atomic compositional information is obtained by measuring the distance between the peak maximum and peak minimum of the strongest peak for a particular element. The atomic percentage, C_i, of an element i can be calculated from the following formula [165]:

$$C_i = \frac{I_i / S_i}{\sum_j \left(I_j / S_j \right)} \cdot 100\% \qquad (3\text{-}2)$$

where I_i is the Auger intensity (peak-to-peak amplitude) of element i, S_i is the sensitivity factor for i, and j runs from 1 to the number of elements present at the surface. The summation is

carried out over all elements observed in the Auger spectrum. Sensitivity factors for the various elements have been compiled from reference spectra [165] and their use is considered to be valid for semiquantitative analysis (20-30% error [166]), provided: (1) the peak shapes are the same in the analysis and the reference spectra, (2) the electron beam energies used for both spectra are the same, (3) the analyzers used for both spectra have the same resolution, and (4) the same modulation or differentiating algorithm is used [167]. This method suffers from the fact that elemental sensitivity factors may vary from one matrix to the next. More accurate, quantitative information (~5% error) can be obtained by using a standard with a composition similar to the unknown.

3.3.4 Strengths and Limitations of AES

The major strength of AES lies in its high spatial (lateral) resolution capabilities. In this study a variation of AES known as Scanning Auger Microscopy (SAM) was used. In SAM the incident electron beam is focused electromagnetically to a fine spot, which can be rastered over the analysis area of interest. Presently available commercial SAM instruments offer a spatial resolution in the range 50-200 nm [166]. This makes it ideal for analyzing very small areas.

The most prevalent problem with AES when analyzing mineral surfaces, is that samples which are poor conductors or insulators may cause charging, which will deflect the electron beam onto adjacent areas and prohibit data collection. To minimize sample charging problems, Hochella *et al.* [168] recommended: (1) using a beam voltage of 3 keV or lower, (2) keeping the beam current low, below 10 nA if possible, and (3) keeping the angle between the surface normal and the primary beam between 40° and 60° to increase backscattered and secondary electron emission efficiency.

Another problem with AES is the potential for electron beam damage of the surface. Electron induced damage can include electron stimulated desorption and adsorption and electric field or thermally induced ion migration [162]. To minimize the likelihood of these occurrences, the beam energy and current should be kept low and the beam should be rastered or defocussed whenever possible.

The sensitivity of AES is limited. Elements present at less than 0.1 to 0.5 atomic percent generally cannot be detected and for quantitative analysis, usually at least 1-2 atomic % of the element should be present [163]. Also, with rare exceptions AES provides purely elemental information; it does not provide chemical information on covalency, bonding or oxidation state of the element. The Auger electron does contain some chemical information but

since it results from a three-electron process the information is often too subtly convoluted in the spectral peaks to be deciphered. XPS was used to provide complementary chemical information.

3.4 X-ray Photoelectron Spectroscopy

3.4.1 The XPS Process

In the XPS process (Figure 3-2) the sample surface is irradiated with X-rays of known energy, $h\nu$, (usually Al$K\alpha$ or Mg$K\alpha$ X-rays), causing the ejection of photoelectrons with binding energy, E_B, where $E_B < h\nu$ [169]. Those electrons which are excited and escape without energy loss contribute to the characteristic peaks in the spectrum, whereas the electrons which undergo inelastic scattering and suffer energy loss contribute to the background of the spectrum. The electrons have energy ranges comparable to Auger electrons and hence have similar escape depths and similar surface specificity. Like AES, XPS can detect all elements except hydrogen and helium.

Once a photoelectron has been emitted, the ionized atom must relax in some way. This can be achieved either by emission of an X-ray photon or by ejection of an Auger electron. Thus Auger electrons are also produced as a consequence of the XPS process, and Auger peaks are present in XPS spectra.

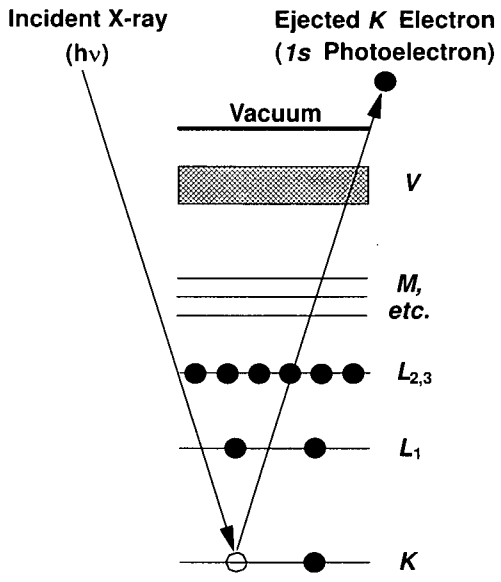

Figure 3-2. Schematic diagram of the XPS process, showing photoionization of an atom by the ejection of a *1s* electron (adopted from ref. [164]).

The major strength of XPS is its ability to provide chemical information in addition to elemental information. In this study it was anticipated that XPS would be able to distinguish between species such as Fe^{2+} and Fe^{3+}, Cu^{+} and Cu^{2+}, and different sulfur species, such as S^{2-} (monosulfide), S_2^{2-} (disulfide), S_n^{2-} (polysulfide), S° (elemental sulfur) and SO_4^{2-} (sulfate), on the surfaces of leached chalcopyrite specimens. The chemical state information derived from XPS was expected to assist in characterizing any passivating layers which may form.

3.4.2 Properties of Photoelectrons

The kinetic energy of an ejected photoelectron is dependent on the energy of the X-ray source employed, unlike Auger electrons, whose energies are independent of the incident electron beam energy. The photoelectron kinetic energy, E_K, is expressed by the following equation:

$$E_K = h\nu - E_B - \phi_{sp} \tag{3-3}$$

where $h\nu$ and E_B are as defined in Section 3.4.1, and ϕ_{sp} is the work function of the spectrometer. The work function can be compensated for electronically, leaving:

$$E_K = h\nu - E_B \tag{3-4}$$

or:

$$E_B = h\nu - E_K \tag{3-5}$$

Each characteristic X-ray will give rise to a series of photoelectron peaks which reflect the discrete binding energies of the electrons present in the solid. Thus by measuring the kinetic energies of the photoelectrons, equation (3-5) can be used to translate this energy into the binding energies of the electrons.

3.4.3 Generation and Interpretation of XPS Spectra

The essential components necessary for performing XPS are an X-ray source, a sample/support system, and an electron energy analyzer, all maintained under ultra-high vacuum. The most popular X-ray source materials are aluminum and magnesium; these elements provide Al$K\alpha$ and Mg$K\alpha$ photons of energy 1486.6 eV and 1253.6 eV respectively. With these X-ray sources, photoelectrons have the same kinetic energy range as Auger electrons and hence the

same escape depth from a solid surface. Another reason that Al and Mg are used is that the X-ray line widths (0.85 eV for Al$K\alpha$ and 0.70 eV for Mg$K\alpha$) are narrow enough to provide good resolution of the XPS peaks. To improve the resolution further, the X-rays can be monochromatized to reduce the X-ray line widths to about 0.2 eV [162]. However, the improved resolution is achieved at the expense of greatly reduced X-ray intensity, which means much longer counting times are required.

XPS spectra are depicted as plots of peak intensity, N (in arbitrary units) vs. E_B, electron binding energy. There are three basic types of peaks [164]: (1) peaks due to photoemission from core levels, (2) peaks due to photoemission from valence levels and (3) peaks due to X-ray-excited Auger emission. Type (2) peaks occur at very low binding energies (0-20 eV) and were not evaluated in this study, hence they will not be considered in the following discussion.

3.4.3.1 Core Level Emission Peaks

The most diagnostically important peaks are those arising from core level emissions. The reason XPS can provide chemical state information is that placing a particular atom in a different chemical environment, or a different oxidation state, on in a different lattice site, etc., gives rise to a change in binding energies of the core level electrons [169]. This binding energy variation manifests itself as a measurable shift of the spectral peaks. This shift is referred to as the chemical shift. For example, in the case of the S *2p* emission, the binding energy changes from S^{2-} to S° to SO_4^{2-} from 161 eV to 169 eV. A great many of these shifts have been documented for reference and are compiled in various handbooks, for example ref. [170]. Details of the core level emissions of a number of reference materials used to aid in the assignment of peaks in this study are compiled in Appendix 4. In many cases there are overlapping chemically shifted peaks. The overlapping peaks can be deconvoluted into their individual components by computerized curve fitting techniques. A number of mathematical functions have been used for this purpose, the most common being a mixed Gaussian/Lorentzian function [171].

An important diagnostic feature of core level emissions is that emissions from non-*s*-levels give rise to doublets because of spin-orbit (*j-j*) coupling (discussed previously in Section 3.2). The magnitude of the doublet energy separation can be many electron volts. The separation increases with increasing atomic number for a given subshell (constant n, l), and also

increases as l decreases for constant n. The relative intensities (areas) of the doublet peaks are given by the ratio of their respective degeneracies ($2j + 1$), summarized in Table 3-2 [164]. Thus a knowledge of doublet separation distances and their area ratios makes their assignment to a particular element, and its oxidation state, quite straight forward and unambiguous.

Table 3-2. Spin-orbit splitting parameters for core level emission peaks [164].

Subshell	j values	Area ratio
s	1/2	-
p	1/2, 3/2	1:2
d	3/2, 5/2	2:3
f	5/2, 7/2	3:4

3.4.3.2 X-ray-Excited Auger Emission Peaks

X-ray-excited Auger electrons give rise to strong peaks in the photoelectron spectrum. Changes in chemical states which cause photoelectron peaks to shift also cause the Auger peaks to shift, although Auger peak shifts are not as well understood. However, the differences between Auger and photoelectron chemical shifts can often provide useful chemical information. The differences are expressed in terms of the Auger parameter, α, defined originally as [162, 172]:

$$\alpha = E_K(A) - E_K(P) \tag{3-6}$$

where $E_K(A)$ is the kinetic energy of an X-ray induced Auger line and $E_K(P)$ is the kinetic energy of a photoelectron line for the same element in the same spectrum. Referring to equation (3-4), it can be seen that equation (3-6) is equivalent to:

$$\alpha = E_K(A) + E_B(P) - h\nu \tag{3-7}$$

where $E_B(P)$ is the binding energy of the photoelectron line and $h\nu$ is the energy of the exciting radiation. Equations (3-6) and (3-7) can produce negative values of α and therefore a modified Auger parameter, α', was subsequently introduced:

$$\alpha' = \alpha + h\nu = E_K(A) + E_B(P) \tag{3-8}$$

The Auger parameter is an empirical measure with a unique value for each chemical state. It can provide additional chemical information which may not be available from the photochemical lines alone.

3.4.3.3 Secondary Peaks

Besides the principal peaks discussed above, the typical XPS spectrum may have numerous secondary peaks, some of which can provide additional chemical information. A discussion of the basic theories behind the origin of these secondary peaks is beyond the scope of this thesis; further information on this subject can be found in ref. [164]. Here, brief mention will only be made of the peaks arising from multiplet splitting and the so-called "shake-up" satellite peaks. The former are evident in Fe *2p* spectra and the latter are important in the interpretation of Cu *2p* spectra.

Multiplet splitting of core level peaks can occur when the system has unpaired electrons in the valence levels. Consider the case of the Fe^{3+} ion. In the ground state the five *3d* electrons are all unpaired and with parallel spins. After ejection of a *2p* electron a further unpaired electron is present. The spin of this electron can be parallel or anti-parallel to that of the *3d* electrons, leading to interactions that give rise to multiple energy states and splitting of the Fe $2p_{3/2}$ and Fe $2p_{1/2}$ peaks. This multiplet splitting causes broadening (with asymmetry) of the peaks and complicates their deconvolution. In contrast, multiplet splitting is not observed in Cu *2p* spectra for Cu^{+} species, because the *3d* shell is completely filled.

Shake-up satellite peaks occur because, to the valence electrons associated with an atom the loss of a core electron by photoemission appears to increase the nuclear charge. This perturbation gives rise to a substantial reorganization of the valence electrons which may involve excitation of one of them to a higher unfilled level (termed "shake-up"). The energy required for this transition is not available to the photoelectron. This results in a reduction in its kinetic energy, or equivalently an increase in the apparent binding energy, leading to satellite peaks on the high binding energy side of the photoelectron peak. Very strong satellites are observed for certain transition and rare earth compounds which have unpaired electrons in *3d* or *4f* shells respectively. In the present study, the presence or absence of shake-up satellite peaks was used to differentiate between Cu^{+} and Cu^{2+} species. Cu^{+} species have a closed-shell configuration ($3d^{10}$) and do not exhibit shake-up satellite peaks, whereas Cu^{2+} species ($3d^{9}$) do.

3.4.3.4 Quantification

Photoelectron peak intensities are used to obtain semi-quantitative to quantitative surface analyses. The peak intensity is taken to be the integrated area under the peak following subtraction of a background. As in AES, the atomic percentage C_i of a particular element or ion i is calculated by dividing the peak intensity by the sensitivity factor S_i (derived from standard materials) and expressing as a fraction of the summation of all normalized intensities:

$$C_i = \frac{I_i/S_i}{\sum_j (I_j/S_j)}(100\%) \tag{3-9}$$

3.4.4 Strengths and Limitations of XPS

As has already been discussed, the major strength of XPS is its ability to provide chemical state information in addition to elemental information. Another advantage with XPS compared to AES is that an X-ray beam is much less destructive (to the sample) than an electron beam [169]. Also, static charging of the sample is less of a problem with XPS than with AES and it is much easier to analyze insulating samples with the former method.

The major limitation of XPS is its low spatial resolution capability. X-rays are not easily focussed into small spots; conventional XPS instruments (such as the one used in the present study) produce a spot size of 1-3 mm. Unlike SAM, the input beam is not rastered over the surface, and only a single selected area is analyzed at a given time. The impetus for better spatial resolution has recently led to the development of small-spot XPS instruments which provide spot sizes as small as 100 μm, and in the future instruments capable of 10 μm spatial resolution are expected to become available [173]. This limitation in spatial resolution means XPS is not suited to the analysis of very small, localized areas (as is SAM); it is considered to be more of an area-averaging analytical technique.

3.5 Sputter Depth Profiling

Often the experimenter is interested in determining the thickness of a surface layer, or how the composition of a surface layer changes with depth. This can be accomplished by alternately sputtering and analyzing the sputtered surface. Most AES and XPS instruments are equipped with ion sputtering guns for this purpose.

Sputtering is a destructive method; the sample is bombarded with inert gas ions (usually argon) accelerated in an ion gun to an energy typically in the range 0.5-5 keV. The ions collide with the surface and effectively peel away the surface atoms. The ion beam is usually rastered over an area of several mm^2 to produce an evenly eroded crater that is larger than the area to be analyzed. The sputtering rate is dependent on the operating conditions and on the sample being sputtered. By way of example, Hochella reported that modern ion guns operating between 1 and 4 keV accelerating potential over an area of up to a few mm^2 will sputter away amorphous SiO_2 at a rate of 1-10 nm/min [162].

There are problems associated with sputtering that can make interpretation of the results complicated and prone to error. Well known sputtering-induced phenomena are [174]:

1. Surface chemistry changes, including chemical reduction of surface species and the promotion of chemical reactions as a result of surface heating.

2. Preferential sputtering of multicomponent samples, in which certain constituents or elements will sputter faster than others, yielding an altered surface that does not reflect the original surface composition.

3. Ion-enhanced diffusion, including knock-on effects where small ions are driven back from the surface.

4. An increase in surface roughness, which reduces the depth resolution attainable by depth profiling.

One application where argon ion sputtering is used routinely is to "clean" the surface prior to analysis by AES. Sample surfaces inevitably become contaminated by adsorption of adventitious elements such as carbon from the atmosphere. The surface is sputtered lightly (for less than 1 minute) to remove the adsorbed contaminants.

CHAPTER 4

EXPERIMENTAL PROCEDURES

The experimental program developed for this study can be divided into three phases:

1. A study of the effect of surfactants on the interfacial chemistry in the chalcopyrite-liquid sulfur-cupric/ferric sulfate system;
2. Oxygen pressure leaching experiments to study the leaching kinetics of chalcopyrite;
3. Examination of chalcopyrite mineral surfaces to characterize the surface-specific compositional changes that occur during leaching.

4.1 Interfacial Experiments

4.1.1 Reagents

The reagents used in the interfacial experiments were: sulfur (99.99% purity), cupric sulfate ($CuSO_4 \cdot 5H_2O$, 98% purity), ferric sulfate ($Fe_2(SO_4)_3 \cdot 5H_2O$, 97% purity), sulfuric acid (H_2SO_4, 95-98% purity). Aqueous acidic cupric/ferric sulfate solutions were made up with deionized water.

4.1.2 Surfactants

Surfactants tested for their interfacial properties were three different lignosulfonate derivatives and orthophenylenediamine (OPD). A list of the surfactants, their trade names and their suppliers is given in Table 4-1.

Owusu has thoroughly reviewed the properties of these surfactants [133]. Briefly, the lignosulfonates are complex, high molecular weight anionic surfactants derived from lignins during the wood pulping process. Georgia-Pacific's depiction of the lignosulfonate structure is shown in Figure 4-1 [175]. Orthophenylenediamine (OPD) is an aromatic amine with two NH_2 groups attached to a benzene ring (Figure 4-2). One of the NH_2 groups is readily protonated in acid media [176] and hence OPD can be classified as a cationic surfactant.

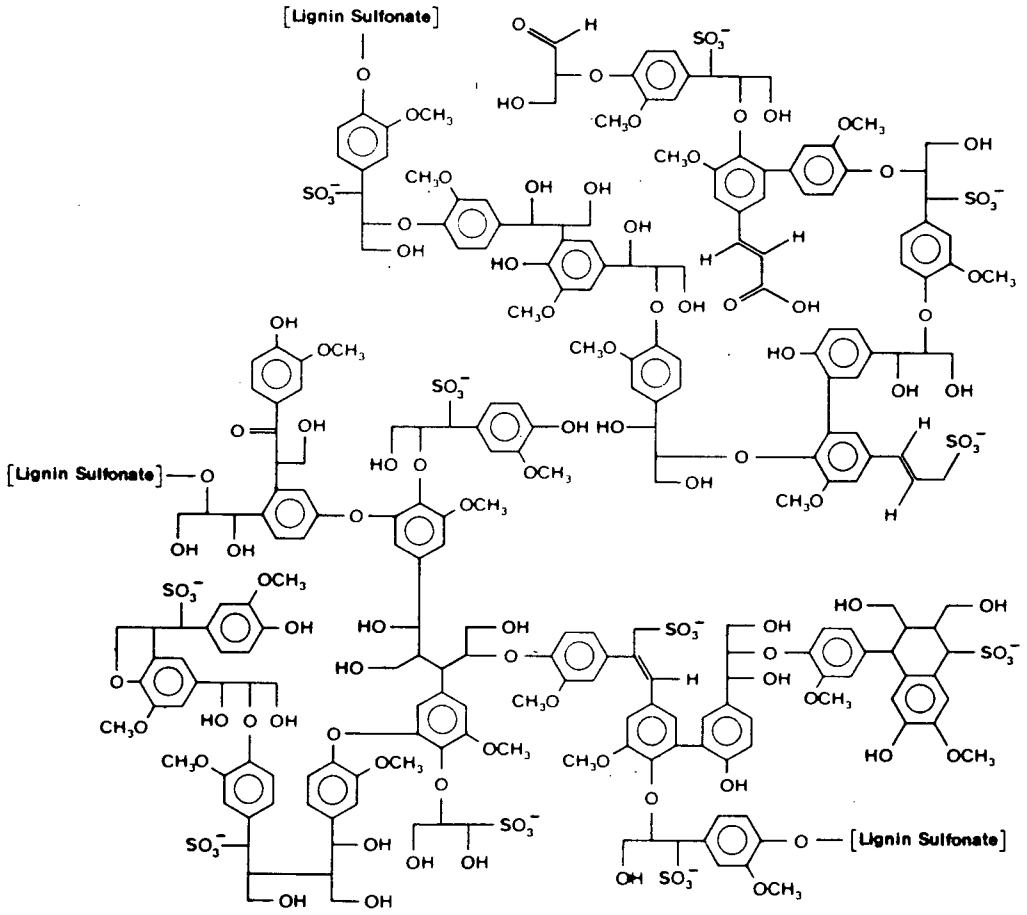

Figure 4-1. Molecular structure of lignosulfonate.

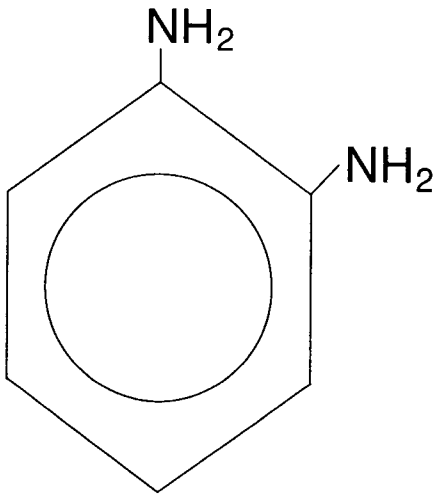

Figure 4-2. Molecular structure of orthophenylenediamine.

Table 4-1. List of surfactants evaluated in the interfacial experiments.

Generic Name	Trade Name	Supplier
Calcium lignosulfonate	Lignosite 100	Georgia-Pacific
Sodium lignosulfonate	Lignosite 458	Georgia-Pacific
Sodium lignosulfonate[1]	Kelig 100	LignoTech USA
Orthophenylenediamine	OPD	DuPont Canada

[1]LignoTech's sodium lignosulfonate, Kelig 100, is more highly sulfonated and hence is claimed to be a "stronger" surfactant than Georgia-Pacific's Lignosite 458.

4.1.3 Chalcopyrite Mineral

Museum grade chalcopyrite mineral specimens originating from Messina, South Africa, were obtained through Wards Natural Science Ltd., St. Catharines, Ontario. A small cube (8 mm length) was cut out of one of the pieces. One face was ground smooth with 600 grit SiC paper and wet-polished with a 1 μm alumina/water suspension. The polished face was examined closely with an optical microscope to ensure that no impurities were visible. Wavelength dispersive X-ray analysis of the sample confirmed it had a composition corresponding to $CuFeS_2$.

4.1.4 Apparatus

Interfacial experiments were performed using a slightly modified version of Owusu's bomb apparatus [133, 134]. A cross-sectional view of Owusu's apparatus is shown in Figure 4-3. The apparatus allows one to form pendant and sessile drops of liquid sulfur at the elevated temperatures and pressures typically used in pressure leaching. The bomb is heated externally with heating tape wrapped around the body, and pressurized with nitrogen gas. The temperature is monitored with a chromel-constantan thermocouple wire inserted into a thermowell (T in Figure 4-3). The temperature is controlled with a Variac transformer which regulates the power to the heating tape. Sulfur drops are formed with the top-mounted syringe (A), equipped with a replaceable pyrex tip (V). The tip is immersed in an aqueous solution held in an optical glass cell (O). The bomb is fitted with two sapphire windows (S), which allows the sulfur drops to be illuminated (L) and photographed with a 35 mm camera (C).

Some modifications were made to the apparatus to improve its performance. The bomb and syringe were originally constructed out of stainless steel. In the present work it was found that a small amount of the aqueous medium always migrated into the interior of the syringe during warm-up. The acidic medium tended to corrode the syringe. A new syringe was

constructed out of titanium which was found to be much more corrosion resistant. The second modification consisted of improving the temperature control, which was ±5°C at best. This was accomplished by adding a PID temperature controller (Omron model #E5CX equipped with RTD probe). The PID controller virtually eliminated temperature overshoot and improved the temperature control to ±0.5°C. Finally, a shorter pathlength optical cell (10 mm pathlength) was substituted for the original cell used by Owusu (40 mm pathlength). This was necessary because one of the surfactants tested (OPD) coloured the aqueous solution a dark reddish-brown, making it difficult or impossible to see the sulfur drops in the original cell. In the shorter pathlength cell the solution remained sufficiently transparent to view and photograph the sulfur drops.

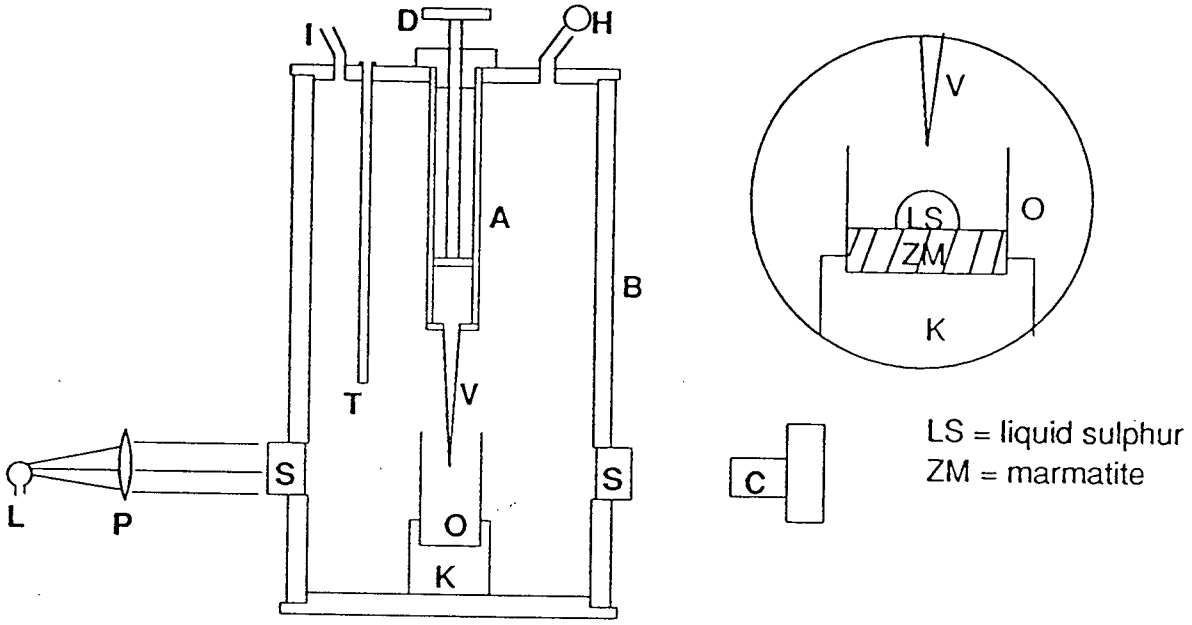

P: converging lens ; I: gas inlet
L: light source for backlightening
B: stainless-steel bomb, (7.6 x 20.3 cm)
T: thermowell (for thermocouple)
C: camera for taking pictures
O: rectangular optical glass cell

A: drive-screw syringe with plunger D
V: replaceable pyrex glass tubing tip (for creating liquid sulphur drops)
S: sapphire windows (1.3 cm diameter)
K: adjustable height seat
H: pressure gauge

Figure 4-3. Cross-sectional view of Owusu's high temperature-high pressure apparatus for generating pendant and sessile drops of liquid sulfur [133].

In order to check for inaccuracies in the measured interfacial parameters that may arise as a result of possible optical distortion effects, the apparatus was tested by measuring the surface tension, γ, of deionized water at room temperature (22°C), using the procedures outlined in Sections 4.1.5 and 4.1.8. The results are given in Table 4-2. The measured values agree well with the literature value of 72.44, indicating that the apparatus was functioning properly.

Table 4-2. Results of surface tension measurements on water at room temperature. The literature value is 72.44 mN/m.

Drop No.	Photograph No.	Surface Tension γ (mN/m)	Average γ (mN/m)	Standard Deviation (mN/m)
1	1	72.5	72.4	0.4
	2	72.3		
	3	72.1		
	4	73.1		
	5	72.1		
2	1	72.5	72.7	0.3
	2	73.1		
	3	72.5		
3	1	72.1	72.1	0.1
	2	72.1		
	3	72.2		

4.1.5 Formation of Pendant Drops

The methodology developed by Owusu [133, 134] for generating pendant and sessile drops was followed. Pendant drop experiments were performed at a temperature of 140°C and a total gauge pressure of 0.69 MPa. The aqueous solution contained 30 g/L Cu^{2+}, 10 g/L Fe^{3+} and 98 g/L H_2SO_4. In tests with surfactants the appropriate amount of surfactant was dissolved in the solution immediately prior to starting the test. The syringe tip diameter was accurately measured (±0.01 mm) with a micrometer. The tips used had diameters varying from 0.9 to 1.2 mm.

Refer to Figure 4-3 for the following discussion regarding the test procedures. To start a test, the optical cell (O) was filled with about 3 mL of aqueous solution and the cell was mounted into position in the seat (K) located on the base of the bomb. The base was then carefully screwed into the bomb. The syringe (A) was partially filled with sulfur and screwed into the bomb head. The tip height was adjusted so that the tip (V) was immersed in the aqueous medium. The RTD probe was inserted into the thermowell, the bomb was pressurized with

nitrogen and heating was initiated. The light (L) and camera (C) were positioned in preparation for viewing and photographing the drops.

A 20 minute warm-up time was typically required to stabilize the operating temperature at 140°C. Once the temperature had stabilized, the syringe plunger (D) was screwed downwards until a pendant drop of sulfur formed at the tip immersed in the solution. The drop was made as large as possible without detaching from the tip. The drop was then photographed at least three times within a 1-2 minute period to determine the reproducibility of the resulting interfacial tension values. In some tests where the effect of time on interfacial tension was of interest, as many as 10 drops were formed and photographed over periods lasting as long as 60 minutes.

To terminate a test, power to the heating tape was shut off, the bomb was allowed to cool, then depressurized. The syringe and cell were cleaned in 10% w/v HNO_3 and rinsed in deionized water to prepare for the next run.

4.1.6 Formation of Sessile Drops

Sessile drop experiments were performed under the same test conditions used for the pendant drop experiments. The procedure was similar to that employed for the pendant drop experiments, with the following variations. Immediately prior to each test, the top face of the $CuFeS_2$ sample was carefully polished with a 1 μm alumina/water suspension and rinsed with deionized water. The mineral was then mounted in the optical cell, the cell was filled with the aqueous solution and the set up was completed as for the pendant drop tests. Sulfur drops were formed and allowed to detach from the syringe tip and spread onto the mineral surface, forming an advancing front until the drop movement ceased. In this way the advancing contact angle was measured[1]. Once the drop movement had ceased the drop was photographed. Several photographs of the drop were taken over a 1-2 minute period to determine the reproducibility of the resulting contact angle values.

To terminate a test, power to the heating tape was shut off, the bomb was allowed to cool, then depressurized. The syringe and cell were cleaned in 10% w/v HNO_3 and rinsed in deionized water to prepare for the next run.

---

[1]For a given liquid-solid system, a number of stable angles can be measured. Two relatively reproducible angles are the largest and smallest, called the advancing angle, θ_a, and the receding angle, θ_r, respectively. They derive their names from the fact that the advancing angle is often measured by advancing the periphery of a drop over a surface and the receding angle is measured by pulling it back. The difference, θ_a - θ_r, is called the hysteresis, which can be significant. Therefore, the type of contact angle being measured should be noted.

4.1.7 Determination of the Aqueous Solution Density at Elevated Temperature

The procedure for calculating the interfacial tension and contact angle values requires knowledge of $\Delta\rho$, the density difference between liquid sulfur and the aqueous medium for the test conditions employed. The density of liquid sulfur at 140°C and atmospheric pressure was obtained from the literature [15] and the value was assumed not to change significantly with pressure up to 0.69 MPa (the pressure at which the interfacial tests were carried out). Density information on the aqueous medium used in the present study was not available from the literature. Owusu estimated the elevated temperature densities of aqueous media by assuming the solutions had the same coefficient of expansion as water [133]. However, for the purposes of this study a method of measuring the solution density was desired. To this end the following procedure was employed.

A 25 cm^3 pyknometer bottle was filled with leach solution and placed inside the interfacial test apparatus. The apparatus was pressurized and heated to 140°C in the usual fashion, and held at temperature for 10 minutes. Excess solution resulting from the expansion of the liquid was expelled via the small capillary opening in the stopper. The apparatus was then cooled to room temperature, depressurized and the bottle was weighed to 0.1 mg accuracy. This procedure was repeated twice to check for reproducibility and the average weight obtained from the three tests was recorded. The procedure was then repeated another three times using deionized water and the average weight was recorded. The density of the leach solution at 140°C was calculated as follows:

$$\rho_{sol} = \left(\frac{W_{sol}}{W_{H_2O}} \right) \rho_{H_2O} \tag{4-10}$$

where ρ_{sol} is the density of the leach solution, W_{sol} and W_{H_2O} are the average weights of the leach solution and deionized water respectively, and ρ_{H_2O} is the density of water at 140°C. The latter value was obtained from the CRC Handbook [177] and was assumed not to change significantly with pressure. This method has the advantage that the glass expansion (due to the increased temperature) is cancelled out by ratioing W_{sol} and W_{H_2O}.

4.1.8 Determination of Interfacial Tensions and Contact Angles

4.1.8.1 Interfacial Tensions by the Method of the Selected Plane

A common procedure for determining interfacial tensions from pendant drop images is to use the Method of the Selected Plane (MSP) [178]. This procedure was used by Owusu to calculate sulfur-solution interfacial tensions in the zinc sulfide-sulfur-zinc sulfate system [133, 134]. Briefly, as applied by Owusu the method consists of taking three measurements from the magnified photographic image of a pendant drop (Figure 4-4): (1) the equatorial diameter of the drop, d_e, (2) the width of the drop, d_s, at a position d_e above the bottom of the drop, and (3) the capillary tip diameter. The latter measurement is used to calculate the magnification factor (the true tip diameter is known) so that the true values of d_e and d_s can be calculated. The interfacial tension is then calculated from the following formula [178]:

$$\gamma = \frac{\Delta\rho g d_e^2}{H} \tag{4-11}$$

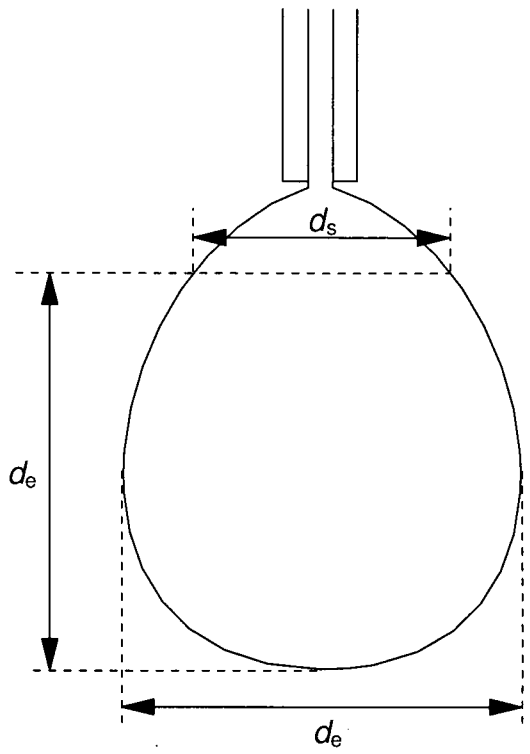

Figure 4-4. Profile of a pendant drop, showing d_e and d_s, the dimensions required to compute the interfacial tension by the Method of the Selected Plane [178].

where $\Delta\rho$ = the density difference between the liquid sulphur and the aqueous solution, g = acceleration due to gravity, d_e = equatorial diameter of the drop, and H is a function of drop shape, $S = d_s/d_e$. Tables of values of H as a function of S are available [178].

The Method of the Selected Plane has the advantage of being rapid and simple, but the precision and accuracy of the results are very sensitive to how accurately the parameters d_s and d_e, and the magnified tip diameter, are measured. This method was used to a limited extent in this study. Using a graduated ruler, the dimensions could be measured to an accuracy of about 0.1-0.2 mm. It was found that a variation of this magnitude for any one of the three parameters changed the computed interfacial tension result by 5-10%. Consequently an alternative method was sought for determining interfacial tensions with a greater degree of precision and accuracy. This led to the use of the Axisymmetric Drop Shape Analysis (ADSA) method, described in Sections 4.1.8.3 and Appendix 1.

4.1.8.2 Manual Measurement of Contact Angles

The most widely used technique for determining contact angles is to measure the angle directly from a sessile drop, by aligning a tangent with the drop profile at the point of contact with the surface (Figure 4-5). The measurement of θ can be performed on a photograph by using a protractor. This procedure is extremely simple but prone to error because aligning the tangent is a very subjective procedure. Owusu used this procedure [133, 134], but recognizing the inherent error, he quoted contact angles to an accuracy of ±4-5%. This method was used to a limited extent in this study. In addition, an alternative method was sought for determining contact angles with a greater degree of precision and accuracy.

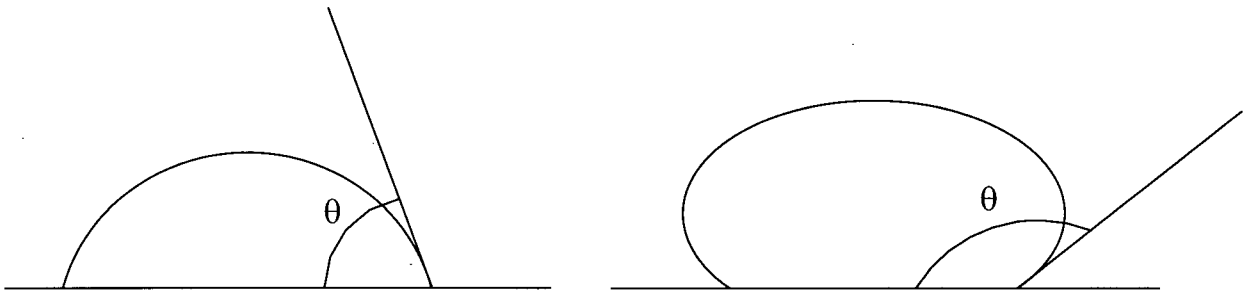

Figure 4-5. Examples of how to manually measure the contact angle (θ) between a liquid and a solid surface, by aligning a tangent with the drop profile at the point of contact with the surface: (a) $\theta < 90°$ and (b) $\theta > 90°$.

In this study the Axisymmetric Drop Shape Analysis method was used to determine contact angles as well as interfacial tensions. This method is described in Section 4.1.8.3 and Appendix 1.

4.1.8.3 Axisymmetric Drop Shape Analysis

Sulfur-solution interfacial tensions and chalcopyrite-sulfur contact angles were determined using the Axisymmetric Drop Shape Analysis-Profile (ADSA-P) program developed by Rotenberg *et al.* [179]. The ADSA-P program automatically digitizes the drop profile from negative or positive photographic images, then fits the drop profile curve to a curve satisfying the Laplace equation of capillarity. The equation is solved numerically to obtain the interfacial tension and contact angle. An overview of the theory behind the method, summarized from ref. [179], is given in Appendix 1.

The ADSA-P program requires as input: (1) coordinate points along the drop profile, (2) the value of the density difference, $\Delta\rho$, between the bulk phases, (3) the value of the local gravitational constant, g (g is assigned positive for sessile drops and negative for pendant drops), and (4) the unmagnified and magnified capillary tip diameters. The solution of the ADSA-P program yields interfacial tension, contact angle, volume, surface area, radius of curvature at the origin, and contact radius of the drop. To use the ADSA-P program, negative or positive photographic images of drops were first enlarged on a computer monitor by means of a video camera. Next, values for $\Delta\rho$, the tip diameter and the magnified tip diameter were input. The drop profile was then digitized using the automatic digitizing feature of the ADSA-P program [180]. The program allows one to input the number of coordinate points desired for the digitizing process; 40 was generally found to be a satisfactory number. After digitizing the drop profile, the program computed the interfacial tension and contact angle, as well as the drop volume, surface area, radius of curvature at the origin and the contact radius of the drop. The program can be run on both pendant drops and sessile drops, although the contact angle and contact radius values calculated for pendant drops are meaningless.

One of the advantages of ADSA-P is that it is capable of calculating the interfacial tension and the contact angle simultaneously from sessile drops. In theory, this would eliminate the requirement for pendant drops. However, Cheng *et. al.* have shown that interfacial tensions computed from pendant drops are more accurate than those computed from sessile drops [180]. This is due to the extreme sensitivity of the interfacial tension values to the shape of the sessile drop, which should be perfectly axisymmetric to obtain the most accurate results. A slightly

uneven surface can distort the drop and render it non-axisymmetric. Apparently, the contact angle values are less sensitive to slight imperfections in the drop shape. Therefore, interfacial tension values were determined from pendant drops and contact angles were determined from sessile drops.

The primary incentive for using the ADSA-P program in the present study was that it allowed for more precise determinations of interfacial tension and contact angle values than were possible by conventional methods (such as the Method of the Selected Plane and the manual measurement of contact angles) [180]. In the present study, repeated measurements of interfacial tensions from pendant drop photographs using ADSA were reproducible to within 3-5% (1-2 mN/m). The precision of contact angle measurements from sessile drops was even better - contact angles were reproducible to within 1-2% (1-2 degrees) with ADSA.

The main disadvantage with ADSA is that the procedure is fairly tedious and time consuming. The automated digitizing feature of the ADSA-P program will only function properly if the drop profile is sharp and clear. The program allows for manual digitizing but this reduces the accuracy of the results [180].

4.1.9 Determination of Work of Adhesion Values

The work of adhesion, W_a, is a direct measure of the reversible work required to separate a unit area of liquid from a solid. In the case of liquid sulfur wetting a mineral surface, W_a can be computed from the following equation [181]:

$$W_a = \gamma_{SA}\left(1+\cos\theta\right) \tag{4-12}$$

once the sulfur-aqueous solution interfacial tension γ_{SA} , and the contact angle θ are known. It can be seen from equation (4-12) that a reduction in γ_{SA} and/or an increase in θ will lower W_a, i.e. reduce the tendency for liquid sulfur to wet the mineral surface.

4.2 Oxygen Pressure Leaching Experiments

4.2.1 Reagents

The reagents used in the pressure leaching experiments were: sulfur (99.99% purity), cupric sulfate ($CuSO_4 \cdot 5H_2O$, 98% purity), ferric sulfate ($Fe_2(SO_4)_3 \cdot 5H_2O$, 97% purity), sulfuric acid (H_2SO_4, 95-98% purity) and cylinder grade pressurized oxygen (minimum 99.5% purity). Aqueous cupric/ferric sulfate leach solutions were made up with deionized water.

4.2.2 Mineral Samples

4.2.2.1 Gibraltar Copper Concentrate

A 100-kg bulk sample of copper concentrate was obtained from the Gibraltar Mine, McLeese Lake, B.C. The as-received concentrate had a moisture content of 6.5%. The sample was thoroughly blended by repeated coning and quartering, then split into 10-kg sub-samples and stored (without drying) in sealed plastic bags for use as required.

An estimation of the mineral content of the Gibraltar concentrate was supplied by Gibraltar Mine's personnel. The concentrate contained approximately 60 wt. % chalcopyrite with lesser amounts of pyrite (17%), chalcocite (8%), copper/iron oxides (5%) and siliceous gangue (10%).

A sieve analysis of the as-received concentrate indicated 90% passing (P_{90}) 105 µm. Prior to using the concentrate for the pressure leach tests, 2-kg samples were re-ground in a rodmill to reduce the particle size to a P_{90} of 38 µm. (More information on the particle size distributions of all the mineral samples is given in Section 4.2.3). The re-ground samples were filtered and allowed to air dry at room temperature.

Table 4-3 summarizes the results of chemical analyses performed on the as-received and re-ground Gibraltar concentrate.

Table 4-3 Results of chemical analyses for the as-received and reground Gibraltar copper concentrate.

Sample	Cu (%)	Fe (%)	S_T (%)	S^{2-} (%)	S_{SO4} (%)	S° (%)
As-received conc.[1]	28.0	26.3	33.3	32.4	0.31	<0.01
Reground conc.[2]	28.3	28.0	32.6	32.0	0.61	0.03

[1]Assay results are average values obtained from duplicate analyses.
[2]Assay results are average values obtained from analyses of four 2-kg grinds.

4.2.2.2 Messina Chalcopyrite

Museum grade chalcopyrite specimens originating from Messina, South Africa, were obtained through Wards Natural Science Ltd., St. Catharines, Ontario. The sample was combined, then crushed and rodmilled to produce about 2 kg of feed for the leach tests. Chemical analysis of the feed revealed the presence of substantial pyrite and silica, therefore the

sample was upgraded by flotation to reject these impurities. The sample underwent one rougher and two cleaning flotation stages in a Denver D12 flotation unit, using Cyanamid's Aerophine 3418A as a collector and methylisobutylcarbinol (MIBC) as a frother. This procedure was quite successful, yielding about 0.6 kg of a relatively pure $CuFeS_2$ concentrate with a $P_{90} < 25$ µm (as determined by sieving). Table 4-4 compares the chemical composition of the Messina chalcopyrite concentrate to the composition expected for pure $CuFeS_2$. It can be seen that the copper, iron and sulfide sulfur values agree quite well with the theoretical values. X-ray diffraction analysis of the concentrate revealed only $CuFeS_2$.

Table 4-4. Results of chemical analysis of the Messina chalcopyrite flotation concentrate.

Sample	Cu (%)	Fe (%)	S_T (%)	S^{2-} (%)	Insol.[2] (%)
Messina conc.[1]	35.0	31.7	34.7	34.7	0.28
$CuFeS_2$ (theoretical)	34.6	30.4	34.9	34.9	0.00

[1]Assay results are average values obtained from duplicate analyses.
[2]Acid insoluble content, indicative of siliceous gangue.

4.2.2.3 Covellite

Museum grade covellite of unknown origin was obtained from Wards Natural Science Ltd., St. Catharines, Ontario. To prepare the sample for leaching, a 2-kg sample was crushed and rodmilled, then filtered and allowed to air dry at room temperature. Sieve analysis of the ground sample indicated a P_{90} of 53 µm. Table 4-5 summarizes the results of chemical analyses performed on the ground covellite sample. The sample contained minor amounts of iron and silica impurities. X-ray diffraction analysis of the sample confirmed it was substantially covellite; no other copper minerals were detected. The sample was considered to be sufficiently pure that further upgrading was not required.

Table 4-5. Results of chemical analysis of the museum grade covellite sample.

Sample	Cu (%)	Fe (%)	S_T (%)	S^{2-} (%)	Insol.[2] (%)
Covellite[1]	62.6	3.40	30.5	30.5	2.59
CuS (theoretical)	66.5	0.00	33.5	33.5	0.00

[1]Assay results are average values obtained from duplicate analyses.
[2]Acid insoluble content, indicative of siliceous gangue.

4.2.3 Particle Size Analyses of the Mineral Samples

4.2.3.1 Sieve Analyses

The ground mineral samples were screened using Tyler sieves #100 (149 μm aperture size), #150 (105 μm), #200 (74 μm), #270 (53 μm), #400 (38 μm) and #500 (25 μm). 100 g portions were first wet-screened through the #500 mesh sieve to remove most of the fines. The plus 500 fraction was dried and dry-screened for 20 minutes on a Rotap shaker. The cumulative particle size distributions determined by sieving are plotted in Figure 4-6. It can be seen that the chalcopyrite concentrate is the finest, followed by the reground Gibraltar concentrate and the covellite.

Sieving was not a very satisfactory method for determining the particle size distributions of these samples, because a substantial proportion of the particles were finer than the finest available sieve (25 μm). For the purposes of modelling the reaction kinetics (Chapter 6) a more accurate size distribution for the $CuFeS_2$ and CuS feeds was desired. Therefore, other methods capable of measuring finer particles were investigated.

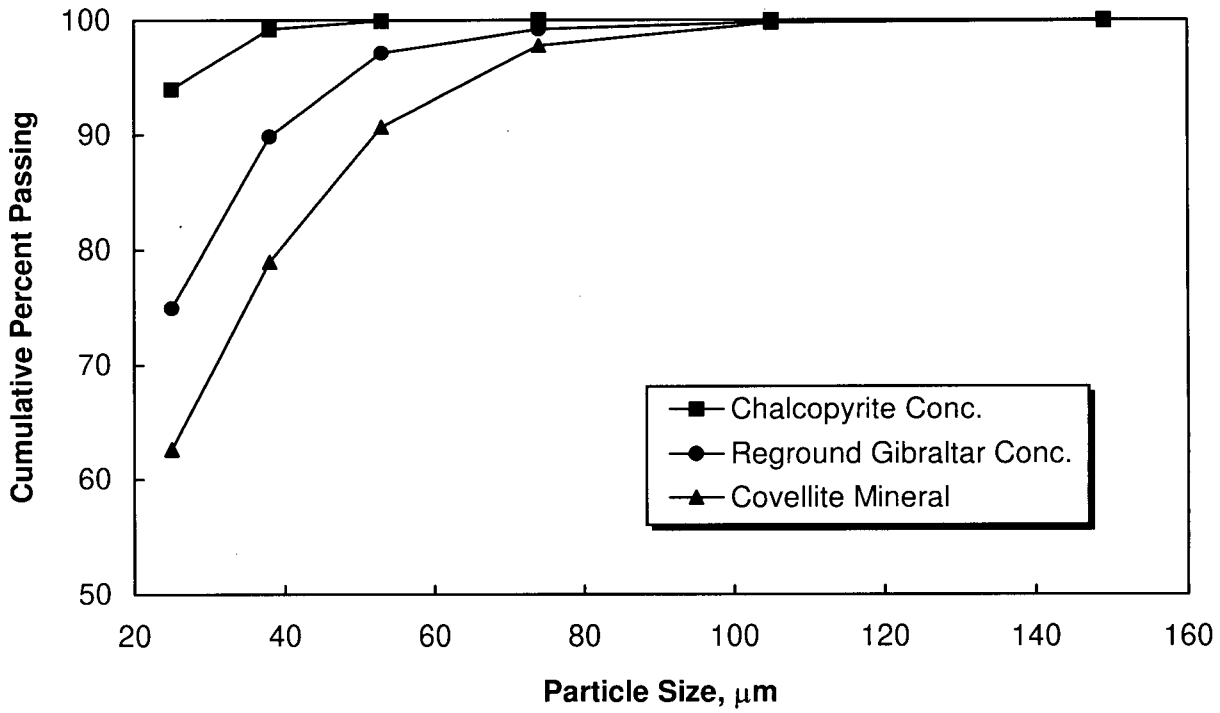

Figure 4-6. Cumulative particle size distributions of the mineral samples as determined by screening with Tyler sieves.

4.2.3.2 Particle Size Analysis with the Elzone Particle Size Counter

The size analyses of the $CuFeS_2$ and CuS feeds were repeated using an Elzone 280PC particle size counter (Particle Data Inc., Elmhurst, Illinois). This instrument is capable of measuring subsieve-size particles. The method involves passing particles suspended in an electrolyte through a small aperture having an immersed electrode on either side [182]. As each particle passes through the aperture, it momentarily changes the resistance value between the electrodes. This change produces a voltage pulse having a magnitude proportional to the particle volume. The instrument counts and measures particle volumes and reports the equivalent spherical diameter. The data output can be either the differential or cumulative volume fraction passing a certain size increment. The magnitude of the size increment is set by the operator. For homogenous materials where all particles have essentially the same density, as was the case with the samples tested here, the volume fraction is equivalent to the weight fraction.

To prepare samples for introduction to the instrument, dilute slurries were made up in a 100 mL beaker using a dispersant solution consisting of 10% w/v Calgon (sodium hexametaphosphate) in deionized water. An ultrasonic probe was applied to break up any agglomerates and thoroughly disperse the solids. A portion of the slurry was then further diluted with an electrolyte solution. Two electrolytes were used depending on the size range being measured. For the coarse size range (10-200 μm), determined using a 300 μm aperture tube, the electrolyte consisted of 0.75% w/v NaCl and 0.5% w/v $Na_4P_2O_7$. For the fine size range (~1.5-25 μm), determined using a 48 μm tube, the electrolyte consisted of 4% w/v NaCl. Particles were kept suspended with an overhead stirrer during measurement. The instrument is equipped with software which blends the two data sets to obtain the overall particle size distribution.

The Elzone instrument has the advantage of being able to measure particle diameters over a wide size range, from ~1.5-1000 μm. The maximum size measurable in this range is dependent on the ability to keep the particles in uniform suspension.

4.2.3.3 Particle Size Analysis with the Horiba Photosedimentation Instrument

The size analysis of the $CuFeS_2$ feed was also carried out using a Horiba CAPA-700 centrifugal photosedimentation instrument (Horiba Instruments Inc., Cameron Park, California). This instrument is based on the principle of liquid-phase sedimentation using Stokes' law for centrifugal sedimentation [183, 184]. A centrifuge is used to accelerate the sedimentation rate of the fine particles. The degree of sedimentation is determined by measuring the amount of light

transmitted over time. The absorbance is related to the size and number of particles. This method can measure particles in the size range ~0.01-50 μm. Prior to analysis the operator inputs the following information: feed density, suspension density, minimum particle size, maximum particle size and the desired size increment.

To prepare samples for introduction to the instrument, dilute slurries were made up in deionized water in a 250 mL beaker, and the particles were thoroughly dispersed with an ultrasonic wand. The correct solids density was determined by trial and error; the density was adjusted until the initial absorbance value was slightly less than 1. A sample was then quickly transferred into the optical cuvette with a pipette. The cuvette was capped, inverted several times to maintain the coarser particles in uniform suspension, inserted into the instrument and the measurement of absorbance with time was initiated. The data output can be either the differential or cumulative volume fraction passing a certain size increment.

The Horiba instrument has the advantage over the Elzone instrument of being able to measure ultra-fine particle sizes, down to 0.1 μm or less. This was considered important for the purposes of modelling the leach, as the ultra-fine particles comprise a disproportionately large amount of the mineral surface area (discussed in Chapter 6). One disadvantage of the Horiba is that it can only be used on homogeneous samples where all particles have the same density. Thus it was suitable for measuring the particle size distribution of the pure $CuFeS_2$ concentrate but it would not have been suitable for, say, the Gibraltar concentrate.

The size analysis results obtained by the Elzone and Horiba instruments are discussed in Chapter 6.

4.2.4 Surfactants

A list of the surfactants evaluated in pressure leaching tests is given in Table 4-6. Samples were supplied by the companies indicated in the table.

4.2.5 Pressure Leaching Apparatus and Procedures

A schematic diagram of the autoclave setup and the monitoring equipment used for the pressure leaching experiments is shown in Figure 4-7. The tests were carried out on a 1 L scale in a standard 2 L Parr titanium autoclave equipped with a PID temperature controller, internally mounted cooling coil and a variable speed stirrer. All wetted parts as well as the magnetic drive were made of grade 4 titanium. All valves and the autoclave head were made of type 316 stainless steel. The temperature was controlled to ±1°C. Agitation was provided by two 58 mm

diameter 45° pitched blade impellers, one situated 25 mm off-bottom and the other located 25 mm below the solution level. The stirring speed was maintained at 800 min^{-1}; at this speed oxygen was dispersed sufficiently fast to ensure the reaction rate was not limited by gas-liquid mass transfer. Leach progress was followed by monitoring oxygen consumption with a mass flowmeter (Omega Instruments) and computerized data acquisition system, according to Grewal *et al.*'s procedure [185].

The accuracy of the oxygen mass flowmeter was periodically checked by oxidizing a solution containing 1 mol/L $FeSO_4$ and 1 mol/L H_2SO_4 at 130°C and 1.38 MPa O_2 pressure. The measured oxygen consumption was compared to the theoretical consumption predicted by the reaction:

$$2FeSO_4 + \tfrac{1}{2}O_2 + H_2SO_4 \rightarrow Fe_2(SO_4)_3 + H_2O \qquad (4\text{-}13)$$

Typically, the reaction was carried out for 30 minutes, after which the solution was analyzed for Fe^{3+} and free H_2SO_4 to determine the percent Fe^{2+} to Fe^{3+} conversion. The predicted oxygen consumption value always agreed to within ±2% of the measured value; this was considered to be adequate.

Table 4-6. List of surfactants evaluated in the pressure leaching study.

Surfactant			Rationale for Study
Generic Name	Trade Name	Supplier	
Calcium lignosulfonate Sodium lignosulfonate	Lignosite 100 Lignosite 458	Georgia-Pacific	Effective in zinc pressure leaching [6, 133, 134]
Sodium lignosulfonate	Kelig 100	LignoTech USA	More highly sulfonated than other lignosulfonate products
O-phenylenediamine M-phenylenediamine P-phenylenediamine	OPD MPD PPD	DuPont Canada	Effective in zinc pressure leaching [133, 134]
Dihydrogenated tallowalkylamine	Armeen 2HT	Akzo Chemicals	Effective in pyrrhotite leaching [19]
Tall oil pitch	Pamak CTP	Hercules Canada	Effective in pyrrhotite leaching [19]
Disulfonated diphenyl oxide	Dowfax 3BO	Dow Chemical	Stable in acid oxidizing electrolyte solutions [186]
Perfluoroalkyl Sulfonate	Fluorad FC-95	3M Company	Stable in copper electrolytes [187]

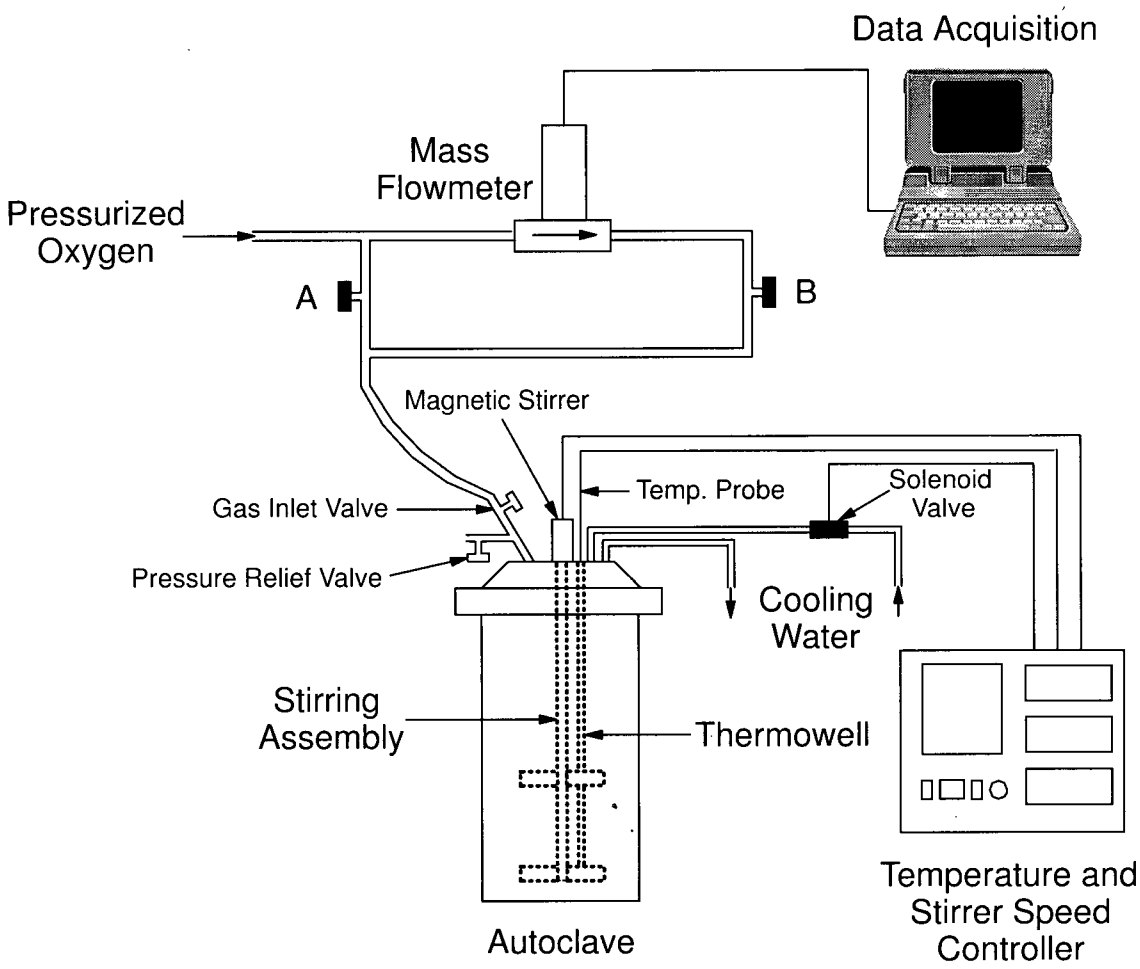

Figure 4-7. Schematic representation of the pressure leaching setup.

Leach tests on the Gibraltar concentrate were carried out at "high" (100 g conc./L solution) and "low" (10 g/L) pulp density. Leach tests on the $CuFeS_2$ concentrate were carried out only at low pulp density due to the scarcity of sample. The starting leach solution always contained cupric/ferric ions and sulfuric acid in order to mimic industrial practice as well as to ensure that an oxidizing environment was maintained during warm-up. The leach solution for the high pulp density tests contained 10 g/L Cu^{2+}, 5 g/L Fe^{3+} and 98 g/L H_2SO_4 while the low pulp density leach solution consisted of 1 g/L Cu^{2+}, 0.5 g/L Fe^{3+} and 98 g/L H_2SO_4.

Most leach tests were performed according to the following procedure: 10 or 100 g of concentrate plus 1 L of leach solution were added to the autoclave, the autoclave was sealed, heating and stirring was initiated and residual nitrogen was vented once the temperature exceeded 100°C. When the desired operating temperature was reached, oxygen was introduced

to the autoclave by opening valve A (Figure 4-7). Once the autoclave was pressurized, valve A was quickly closed, valve B was opened and acquisition of the oxygen flow data was started. This marked the start of the test. During leaching the oxygen partial pressure was maintained at either 0.69 or 1.38 MPa.

In some of the low pulp density tests with surfactants, the concentrate was prevented from contacting the leach solution during warm-up by sealing the solids in a small internal titanium chamber suspended just below the autoclave head. Upon reaching the operating temperature the chamber was forced open by the oxygen gas stream, expelling the solids into solution. In this way the concentrate did not have the opportunity to react with the starting leach solution during the warm-up time, which varied from 15-25 minutes.

In tests with surfactants the surfactants were added either batchwise or continuously. Batchwise addition was accomplished by adding the desired amount of surfactant to the leach solution prior to sealing the autoclave, or by pumping a stock surfactant solution into the autoclave when the desired reaction temperature was reached. Continuous addition was accomplished by pumping a stock surfactant solution into the autoclave throughout the run.

After leaching for the desired residence time, a test was terminated by cooling and depressurizing the autoclave. The autoclave contents were suction filtered and the residue was washed thoroughly with deionized water and allowed to dry at room temperature.

4.2.6 Analytical Methods

Solid and solution samples were analyzed by local Vancouver analytical laboratories or by personnel at the Placer Dome Research Centre, Vancouver, B.C.

Pregnant and wash solutions were routinely analyzed for Cu and Fe and on occasion, S, free H_2SO_4 and Ag (for the silver-catalyzed tests). Cu, Fe and Ag were measured by atomic absorption spectrophotometry (AAS), S was determined gravimetrically as $BaSO_4$, and free H_2SO_4 was analyzed by titration with NaOH after adding excess potassium oxalate to complex the hydrolyzable metals. Solution redox potentials (Eh's) were measured with a platinum electrode (Ag/AgCl reference) and the values corrected to the standard hydrogen reference.

Head samples and most leach residue samples were analyzed for Cu, Fe and S species (S_T, S°, S^{2-}, S_{SO4}). Copper and iron in solids were analyzed by AAS after digesting in aqua regia/bromine. The sulfur species were determined by a sequential leach/digestion procedure. Total sulfur was determined gravimetrically as $BaSO_4$ after digesting in a $KBr\text{-}Br_2/HNO_3$ solution. The other sulfur species were determined gravimetrically after carrying out the

following procedure on a separate sample. First, elemental sulfur was dissolved in boiling perchloroethylene (b.p. = 121°C), then the perchloroethylene leach residue was boiled with 10% Na_2CO_3 solution to selectively dissolve sulfate; finally the Na_2CO_3 leach residue was digested in a KBr-Br_2/HNO_3 solution to dissolve the remaining sulfur, which was assumed to be sulfide. The (S° + S_{SO4} + S^{2-}) sum was usually within 2-3% of the S_T analysis. If not, the analyses were repeated.

4.2.7 Calculation of Metal Extractions and Sulfide Oxidation Extents

Copper and iron mass balances were conducted for most leach tests to ensure the calculated copper and iron extractions were reasonably accurate. If the metal out/metal in mass ratio did not fall within the target range 0.97-1.03, the solution and/or residue analyses were repeated to check for analytical errors, and in some cases the test was repeated. The mass balance yielded a calculated head assay, Me_{calc} (Me = Cu or Fe), defined by:

$$Me_{calc} = \left(\frac{W_{Me}^{sol} + W_{Me}^{res}}{W_t} \right) \cdot 100\% \qquad (4\text{-}14)$$

where W_{Me}^{sol} is the weight of metal (Cu or Fe) solubilized, W_{Me}^{res} is the weight of metal in the leach residue and W_t is the total starting weight of the head sample. The percent metal extraction was based on the calculated head assay:

$$\text{Percent metal extraction} = \frac{W_{Me}^{sol}}{(Me_{calc}/100)(W_t)} \cdot 100\% \qquad (4\text{-}15)$$

Metal extractions determined in this way were considered to be accurate to ± 1%, based on the reproducibility obtained for duplicate test runs.

Head and leach residue sulfur species analyses were used to calculate percent sulfide oxidation extents, using the following formulas:

$$\text{Total } S^{2-} \text{ oxidation (to } S^\circ + SO_4^{2-}) = \left(\frac{W_{sulfide}^{head} - W_{sulfide}^{res}}{W_{sulfide}^{head}} \right) \cdot 100\% \qquad (4\text{-}16)$$

$$S^{2-} \text{ oxidation to } S^\circ = \left(\frac{W_{sulfur}^{res}}{W_{sulfide}^{head}} \right) \cdot 100\% \qquad (4\text{-}17)$$

$$S^{2-} \text{ oxidation to } SO_4^{2-} = (\text{total sulfide oxidation}) - (S^{2-} \text{ oxidation to } S^{\circ}) \qquad (4\text{-}18)$$

where $W_{\text{sulfide}}^{\text{head}}$ is the weight of sulfide sulfur in the head sample, $W_{\text{sulfide}}^{\text{res}}$ is the weight of sulfide in the leach residue and $W_{\text{sulfur}}^{\text{res}}$ is the weight of elemental sulfur in the leach residue. Sulfide oxidations were considered to be accurate to ± 2%, based on the reproducibility obtained for duplicate test runs.

4.3 Analysis of Chalcopyrite Surfaces

The surfaces of unleached and leached massive samples of the Messina chalcopyrite were examined by Auger electron spectroscopy (AES) and X-ray photoelectron spectroscopy (XPS). The use of the term "surface" here is understood to indicate the ~10 nm near-surface region from which Auger electrons or photoelectrons originate.

4.3.1 Sample Preparation

Sample surface preparation was dictated somewhat by the spatial resolution capabilities of the two methods. AES uses a finely focused electron beam and has excellent spatial resolution (30 nm or less), thus it was simple and convenient to analyze fracture surfaces of small fragments. With XPS the resolution is much poorer due to the large size of the X-ray beam (1x3.5 mm in this case); hence larger, relatively smooth surfaces were analyzed from 10x10x2 mm sections.

To obtain reference spectra from unleached chalcopyrite, a sample was fractured (for AES) or a face was sanded with 600 grit SiC paper (for XPS) and quickly inserted into the spectrometer sample chamber and evacuated, limiting the air exposure time to about 1 minute. To prepare a surface for leaching, a small chip sample was fractured (AES) or a face was sanded (XPS) in a nitrogen glove bag, then immediately immersed in the starting leach solution (while still in the glove bag). The sample was allowed to rest on the autoclave bottom during leaching (the bottom impeller was removed to ensure the sample would not be suspended and damaged by the impeller). After leaching, the samples were carefully rinsed with deionized water and vacuum dried at room temperature, then stored under argon overnight prior to analysis. All samples were analyzed within 24 hours of completing the leach test.

4.3.2 Auger Electron Spectroscopy Procedures

Auger electron spectroscopy was used to acquire quantitative elemental information on the composition of chalcopyrite surfaces. Auger spectra were acquired with a Perkin Elmer Model PHI 595 scanning Auger microprobe, property of the Surface Physics Group at Simon Fraser University, Burnaby, B.C. The primary electron beam energy was set at 3 kV with a beam current of 0.2-0.3 μA. The beam was rastered over the analysis area of interest, which varied from 0.9x0.65 mm (200x magnification) to 0.12x0.09 mm (1500x mag.). Prior to analysis surfaces were usually sputtered for 5-10 seconds to lower the carbon contamination resulting from adsorption of atmospheric carbon contaminants. Sputtering was accomplished with a 3 kV, 35 $\mu A/cm^2$ argon ion beam rastered over a 3x3 mm area, with the pressure in the sample chamber adjusted to ~10^{-3} Pa by backfilling the chamber with argon.

Spectra were collected in the differentiated survey scan mode, i.e. dN/dE vs. E, where N is the signal intensity (in arbitrary units) and E is the Auger electron kinetic energy (in eV). Peaks were assigned to their respective elements by referring to reference spectra contained in Davis *et al.*'s handbook [188]. Information on the Auger transitions, peak positions and relative sensitivity factors (for the most intense peaks) for the elements of interest in this study has been tabulated in Appendix 3. Surface compositions (Cu, Fe, S and O) were calculated using peak-to-peak heights and applying Davis *et al.*'s elemental sensitivity factor corrections [165], according to the method described in Section 3.3.3.

AES sputter depth profiling was tried in an attempt to ascertain how surface compositions varied with depth. This was accomplished by alternately sputtering and analyzing the sputtered surface. Sputtering was carried out as described above for cleaning the surfaces, except that the surface was sputtered for 30-60 second intervals between analyses. The total sputtering time varied from 15-60 minutes, depending on the test. The AES depth profiles were collected with reference to sputter time rather than depth as the sputter rate was not known.

4.3.3 X-ray Photoelectron Spectroscopy Procedures

X-ray photoelectron spectroscopy was used to obtain chemical information on the composition of chalcopyrite surfaces. XPS measurements were carried out on an instrument assembled by the Surface Physics Group at Simon Fraser University, Burnaby, B.C. The instrument is equipped with an unmonochromatized Mg K_α X-ray (1253.6 eV) source which was operated at 15 kV and 18 mA. The base pressure of the analytical chamber was on the order of

10^{-7} Pa. Broad survey scans over the binding energy range 0-1000 eV were acquired with the pass energy of the hemispherical analyzer set at 200 eV. Binding energies were referenced to the C *1s* binding energy at 285.0 eV. High resolution narrow-scan spectra were acquired with an analyzer pass energy of 25 or 50 eV. Surfaces were not sputter cleaned prior to analysis to ensure that sputter-induced alterations of the surface chemistry did not occur [162].

Details of the core level emissions of a number of reference materials used to aid in the assignment of peaks in this study are compiled in Appendix 4.

The narrow scan sulfur and oxygen spectra were deconvoluted and fit using a Gaussian-Lorentzian function (Voigt function). Commercially available software (Microcal's Origin™ peak-fitting module) was used for this purpose. Prior to fitting, a linear background correction was applied. Integrated peak areas were used to determine the relative amounts of the different species present.

CHAPTER 5

RESULTS AND DISCUSSION

5.1 Interfacial Experiments

5.1.1 Effect of Surfactants on the Sulfur-Solution Interfacial Tension

The effect of surfactants on the liquid sulfur-aqueous solution interfacial tension at 140°C is summarized in Table 5-1. The aqueous solution contained 30 g/L Cu^{2+}, 10 g/L Fe^{3+} and 98 g/L H_2SO_4. In the absence of surfactant, the sulfur-solution interfacial tension was 56 mN/m. In the presence of 0.1 g/L calcium lignosulfonate (Lignosite 100), the interfacial tension was reduced to 40 mN/m. Increasing the calcium lignosulfonate concentration to 0.3 g/L lowered the interfacial tension further, to 30 mN/m. The use of 0.3 g/L sodium lignosulfonate (either Lignosite 458 or Kelig 100) effected similar reductions in the interfacial tension.

The results indicate that lignosulfonate adsorbs at the sulfur-solution interface. These results are similar to those obtained by Owusu with lignosulfonate in the zinc sulfate system [133, 134]. He found that 0.1 g/L and 0.3 g/L calcium lignosulfonate reduced the interfacial tension from 54-55 mN/m in the absence of surfactant, to 39 mN/m and 27 mN/m respectively at 135±5°C.

In the presence of 0.1 g/L OPD, the sulfur-solution interfacial tension was reduced to 41 mN/m. Increasing the OPD concentration to 0.2 g/L did not lower the interfacial tension any further. Thus, it was concluded that OPD also adsorbs at the sulfur-solution interface but it does not reduce the interfacial tension to the same extent as do the lignosulfonate surfactants. These results are in marked contrast to the results Owusu obtained for OPD in the zinc sulfate system [133, 134]. He found that OPD did not reduce the sulfur-solution interfacial tension. The reason for the differing behaviour of OPD in the two systems is not known for certain. The major difference between the two systems is the substitution of zinc ions for copper, ferric and hydrogen ions (acid) in the aqueous medium, in this study. OPD is known to strongly complex cupric ions to form the ionic species $Cu(OPD)^{2+}$ and $Cu(OPD)_2^{2+}$ [176]:

$$Cu^{2+} + OPD \rightarrow Cu(OPD)^{2+} \qquad \log K_1 = 4.55 \qquad (5\text{-}1)$$

$$Cu(OPD)^{2+} + OPD \rightarrow Cu(OPD)_2^{2+} \qquad \log K_2 = 3.17 \qquad (5\text{-}2)$$

In acid solutions OPD is strongly mono-protonated via one of the NH_2 functional groups [176]:

$$HOPD^{+} \Leftrightarrow H^{+} + OPD \qquad pK_a = 4.63 \qquad (5\text{-}3)$$

Possibly, a Cu-OPD complex or protonated OPD adsorbs at the sulfur-solution interface whereas a Zn-OPD complex (or uncomplexed OPD) is incapable of adsorbing.

Tests with OPD presented some problems because the OPD coloured the aqueous solution a reddish-brown. On heating, the solution became progressively darker in colour, which made it difficult to illuminate the sulfur drop sufficiently for photographing. If the OPD concentration exceeded 0.2 g/L, the solution became too dark to observe the sulfur drop, therefore the maximum OPD concentration tested was 0.2 g/L. After about 15 minutes at temperature (140°C) a voluminous brown precipitate formed, indicating that OPD was being lost from solution (a precipitate did not form in tests where no surfactant was used). It is believed that the OPD was oxidized in the aqueous cupric/ferric medium and formed an insoluble decomposition product. The composition of the decomposition product was not determined. This observed breakdown and loss of OPD from solution suggests that OPD may be too unstable to retain its interfacial activity under copper pressure leaching conditions.

Table 5-1 Effect of surfactants on the liquid sulfur-aqueous solution interfacial tension. Test conditions: 140°C and 0.69 MPa total pressure (nitrogen). The aqueous solution contained 30 g/L Cu^{2+}, 10 g/L Fe^{3+} and 98 g/L H_2SO_4. The interfacial tensions are considered to be accurate to within ± 2 mN/m (± 1σ).

Surfactant	Surfactant Concentration (g/L)	Interfacial Tension, γ_{SA} (mN/m)
None	0	56
Calcium lignosulfonate (Lignosite 100)	0.1	40
Calcium lignosulfonate (Lignosite 100)	0.3	30
Sodium lignosulfonate (Lignosite 458)	0.3	32
Sodium lignosulfonate (Kelig 100)	0.3	31
Orthophenylenediamine (OPD)	0.1	41
Orthophenylenediamine (OPD)	0.2	41

5.1.2 Effect of Surfactants on the Sulfur-Chalcopyrite Contact Angle

The effect of surfactants on the liquid sulfur-chalcopyrite contact angle at 140°C is summarized in Table 5-2. The aqueous solution contained 30 g/L Cu^{2+}, 10 g/L Fe^{3+} and 98 g/L H_2SO_4. In the absence of surfactant, the contact angle was 69 degrees. In the presence of 0.1

g/L calcium lignosulfonate (Lignosite 100), the contact angle increased dramatically, to 146°. Increasing the calcium lignosulfonate concentration to 0.3 g/L resulted in only a slight additional increase in contact angle, to 148°. Figure 5-1a and Figure 5-1b show photographs of liquid sulfur resting on chalcopyrite in the absence and presence of 0.3 g/L Lignosite 100, respectively. The increase in contact angle effected by the surfactant can clearly be seen.

The use of sodium lignosulfonate caused a similar sharp increase in the sulfur-chalcopyrite contact angle. The contact angle increased to 157° with 0.3 g/L Lignosite 458 and to 151° with 0.3 g/L Kelig 100.

In the presence of 0.1 g/L and 0.2 g/L OPD the sulfur-chalcopyrite contact angle was increased to 92° and 133° respectively. The magnitude of the contact angle increase was not as high as that obtained with the lignosulfonate surfactants.

The results indicate that the lignosulfonate and OPD surfactants adsorb at the chalcopyrite-sulfur-solution interface and effect large increases in the sulfur-chalcopyrite contact angle. In addition, it can be concluded that the lignosulfonate surfactants are more effective than OPD at increasing the contact angle. Owusu observed similar sulfur-mineral contact angle increases when using lignosulfonate and OPD in the zinc sulfide-sulfur-zinc/ferric sulfate system [133, 134]. He found that 0.15 g/L calcium lignosulfonate and OPD increased the contact angle from 98° in the absence of surfactant, to 146° and 136° respectively at 135±5°C. Increasing the OPD concentration above 0.15 g/L did not effect any further increase in the contact angle. Increasing the lignosulfonate concentration to 0.3 g/L increased the contact angle only slightly, to 148°.

Table 5-2 Effect of surfactants on the liquid sulfur-chalcopyrite contact angle. Test conditions: 140°C and 0.69 MPa total pressure (nitrogen). Test conditions as for Table 5-1. The contact angles are considered to be accurate to within ± 2° (± 1σ).

Surfactant	Surfactant Concentration (g/L)	Contact Angle θ (degrees)
None	0	69
Calcium lignosulfonate (Lignosite 100)	0.1	146
Calcium lignosulfonate (Lignosite 100)	0.3	148
Sodium lignosulfonate (Lignosite 458)	0.3	157
Sodium lignosulfonate (Kelig 100)	0.3	151
Orthophenylenediamine (OPD)	0.1	92
Orthophenylenediamine (OPD)	0.2	133

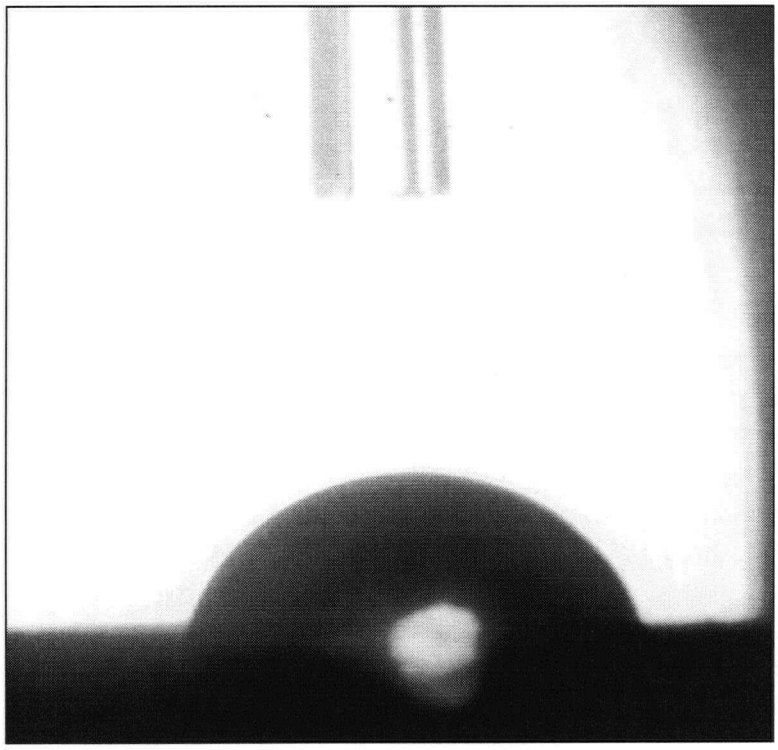

(a)

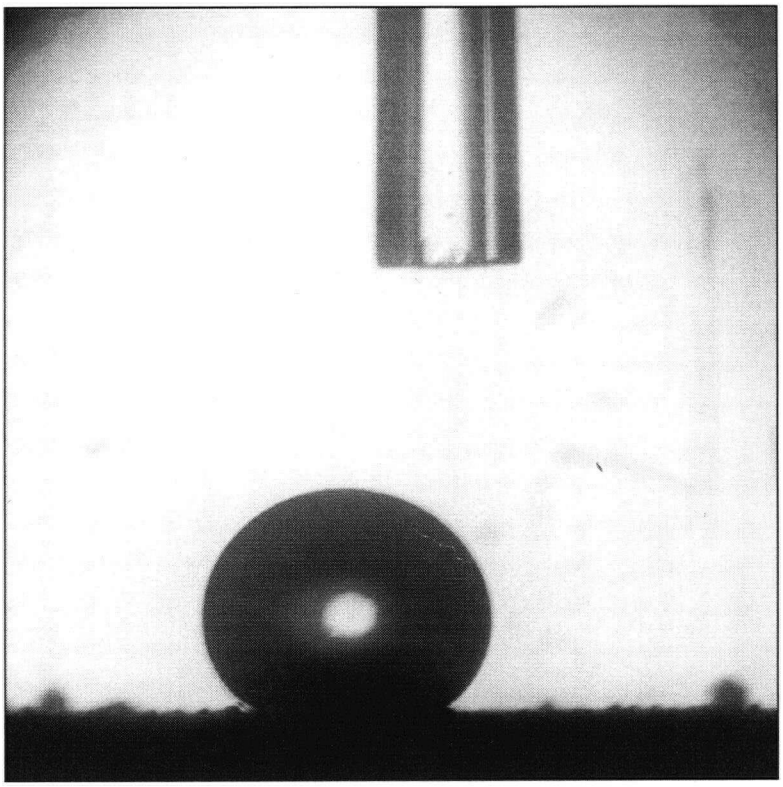

(b)

Figure 5-1. Photographs of liquid sulfur resting on chalcopyrite: (a) in the absence of surfactant and (b) in the presence of 0.3 g/L calcium lignosulfonate (Lignosite 100). Test conditions as for Table 5-1.

5.1.3 Effect of Surfactants on the Work of Adhesion

The work of adhesion, W_a, for liquid sulfur in contact with the chalcopyrite mineral substrate is a measure of the reversible work required to separate a unit area of sulfur from the chalcopyrite. W_a can be computed from the following formula [181]:

$$W_a = \gamma_{SA}(1+\cos\theta) \tag{5-4}$$

if the sulfur-solution interfacial tension, γ_{SA}, and the sulfur-chalcopyrite contact angle, θ, are known. It is evident from equation (5-4) that a surfactant will lower W_a if it decreases γ_{SA} and/or increases θ.

Table 5-3 shows the effect of surfactants on the work of adhesion. It can be seen that the surfactants tested lowered W_a dramatically. The lignosulfonates had a more pronounced effect than OPD, with the former surfactants reducing W_a by more than a factor of 10. This means that in the presence of lignosulfonate, the work required to displace sulfur from the chalcopyrite mineral surface is reduced by over 10 times. OPD had a lesser effect on the work of adhesion, but it still lowered W_a by a factor of two at 0.1 g/L, and by a factor of 6 at 0.2 g/L.

Based on these results the lignosulfonates are predicted to be more effective than OPD at dispersing liquid sulfur during the elevated temperature/pressure leaching of chalcopyrite in acid cupric/ferric sulfate media.

Table 5-3. Effect of surfactants on the sulfur-chalcopyrite work of adhesion. Test conditions as for Table 5-1.

Surfactant	Surfactant Concentration (g/L)	Work of Adhesion, W_a (mJ/m^2)
None	0	76
Calcium lignosulfonate (Lignosite 100)	0.1	6.8
Calcium lignosulfonate (Lignosite 100)	0.3	4.6
Sodium lignosulfonate (Lignosite 458)	0.3	2.5
Sodium lignosulfonate (Kelig 100)	0.3	3.9
Orthophenylenediamine (OPD)	0.1	40
Orthophenylenediamine (OPD)	0.2	13

5.1.4 Discussion

5.1.4.1 Surfactants and Sulfur-Solution Interfacial Tensions

When a surfactant is dissolved in water, the hydrophobic group causes a distortion of the water structure, which increases the overall energy of the system and means that less work is required to transport a surfactant molecule to a surface or interface. The surfactant will therefore tend to preferentially adsorb at those locations, such that its concentration at the interface/surface is greater than its concentration in the bulk solution. Since less work is required to bring surfactant molecules to the available interfaces, the presence of the surfactant decreases the work required to increase the interfacial area. The work per unit area required to form that new interface is the surface free energy or surface tension of the system, γ, which has S.I. units of millinewtons per metre (mN/m). For solid surfaces, the convention is to use millijoules per square metre (mJ/m^2). Adsorption of surfactants at interfaces will always lead to a reduction in the interfacial/surface tension. Thus if the interfacial/surface tension is reduced in the presence of surfactants, it confirms that the surfactant has adsorbed at the interface.

The measurements of sulfur-solution interfacial tensions conducted in this study have shown that both lignosulfonate and OPD lower the interfacial tension under operating conditions similar to those found in copper pressure leaching. Therefore, it can be concluded that these surfactants preferentially adsorb at the sulfur-solution interface and lower the work required to increase the interfacial area. In oxygen pressure leaching, work is supplied by agitation, and the surfactants will increase the efficiency with which the agitator generates additional interfacial area. This principle was aptly demonstrated by INCO in their studies on the oxygen pressure leaching of nickeliferous pyrrhotite concentrates [146]. They showed that as liquid sulfur was formed during oxidation of the sulfide component, the sulfur tended to form drops that coalesced into large globules and settled to the autoclave bottom, despite vigorous agitation. However, when a surfactant was added, the sulfur was dispersed into fine droplets that were uniformly suspended in solution. Similarly, from the results obtained here it can be predicted that the addition of lignosulfonate or OPD to a system containing acidic cupric/ferric sulfate and sulfur under typical pressure leaching conditions (i.e., elevated temperature and pressure) should markedly increase the ability of the agitator to disperse the liquid sulfur into fine droplets. This presumes that the surfactant is sufficiently stable to maintain its interfacial activity under pressure leaching conditions. The stability of OPD is a matter of some concern as a brown

precipitate was observed to form in tests with OPD, suggesting that OPD may be susceptible to oxidative decomposition.

As the surfactant concentration is increased, the amount of surfactant adsorbed at the sulfur-solution interface increases, accompanied by a decrease in the interfacial tension. Eventually, a limiting condition is reached where the interface is completely covered with a layer or layers of the surfactant, and further increases in the surfactant concentration do not lower the interfacial tension any further. With OPD, under the conditions studied here, this limiting condition corresponds to ≤ 0.1 g/L OPD in solution. With lignosulfonate, this limiting condition was not determined precisely but it is probably in the 0.1-0.3 g/L range. Lignosulfonate was able to effect a greater reduction in the interfacial tension than OPD, therefore, under identical agitation conditions, the former is predicted to be more effective than the latter at increasing the sulfur-solution interfacial area.

5.1.4.2 Surfactants and Sulfur-Chalcopyrite Contact Angles

If liquid sulfur is placed on a mineral surface, it may either spread so as to completely wet the surface or remain as a drop having a definite angle of contact. The angle of contact is the angle between the mineral surface and a tangent drawn to the liquid sulfur surface at the point of contact with the solid. The contact angle that liquid sulfur makes when it is in equilibrium with other phases in contact with it is related to interfacial tensions by Young's equation [135]:

$$\gamma_{MA} = \gamma_{MS} + \gamma_{SA}\cos\theta \tag{5-5}$$

or

$$\gamma_{MA} - \gamma_{MS} = \gamma_{SA}\cos\theta \tag{5-6}$$

The mineral-aqueous solution interfacial tension, γ_{MA}, is balanced by the sum of the mineral-liquid sulfur interfacial tension, γ_{MS}, plus the component of the liquid sulfur-aqueous solution interfacial tension, γ_{SA}, resolved parallel to the solid surface, $\gamma_{SA}\cos\theta$. A zero contact angle is the condition for complete wetting of the mineral by liquid sulfur. A contact angle of 180° represents no wetting at all, which is not attainable in practice.

As the sulfur-mineral contact angle increases, the mineral surface becomes more and more accessible to the leaching solution. When the contact angle is greater than 90° the liquid

sulfur should move freely about the surface. Thus, increasing the contact angle lowers the inhibiting effect of sulfur on leaching in two ways: (1) more mineral surface area becomes available for leaching and (2) there is a greater tendency for sulfur to detach from the mineral surface.

The measurements of sulfur-chalcopyrite contact angles conducted in this study have shown that both lignosulfonate and OPD markedly increase the contact angle under operating conditions similar to those found in copper pressure leaching. Therefore, it can be concluded that these surfactants adsorb at the sulfur-chalcopyrite-solution interface. As the surfactant concentration is increased, the amount of surfactant adsorbed at the sulfur-chalcopyrite-solution interface increases, accompanied by an increase in the sulfur-chalcopyrite contact angle. Eventually, a limiting condition is reached where the interface is completely covered with a layer or layers of the surfactant, and further increases in the surfactant concentration do not increase the contact angle any further. With lignosulfonate, this limiting condition was not determined precisely but it is in the 0.1-0.3 g/L range. With OPD, this limiting condition was not reached due to the necessity in limiting the maximum OPD concentration to 0.2 g/L. However, it can be concluded that the lignosulfonates are more efficient at increasing the contact angle, as 0.1 g/L calcium lignosulfonate increased the contact angle from 69° to 146°, whereas the same concentration of OPD increased the contact angle to only 92°.

A quantitative measure of surfactant interfacial activity is the work of adhesion, W_a, which is the reversible work required to separate a unit area of sulfur from the chalcopyrite (equation (5-4)). Calculation of the work of adhesion requires values for the sulfur-solution interfacial tension and the contact angle, demonstrating the relevance of both these values. As shown in Table 5-3, both lignosulfonate and OPD reduced W_a significantly. The lignosulfonates effected a greater reduction in W_a than did OPD, hence the former are predicted to be more effective than the latter at preventing sulfur from wetting chalcopyrite. This again presumes that the surfactants are stable under the leaching conditions employed. The stability of these surfactants was tested in pressure leaching experiments, to be discussed subsequently (Sections 5.2.3-5.2.6).

5.1.4.3 Possible Surfactant-Chalcopyrite and Surfactant-Sulfur Bonding Interactions

Owusu used Fourier transform infrared spectroscopy (FTIR) to gain insight into the nature of the surfactant-mineral bonding interactions in the zinc sulfide-sulfur-zinc/ferric sulfate system [133]. This area of investigation was beyond the scope of the present study and was not attempted here. However, it is instructive to briefly discuss the possible interactions that may be operative in the chalcopyrite-sulfur-cupric/ferric sulfate system, in light of Owusu's findings.

From the FTIR studies Owusu concluded that the surfactants interact with zinc sulfide through the hydrophilic groups. In the case of lignosulfonate the active hydrophilic groups were believed to be the hydroxyl and sulfonate functional groups, which interact chemically and physically to form a Zn(II)-surfactant complex, while the hydrophobic organic portion of the surfactant interacts with the aqueous phase through hydrogen bonding. In the case of OPD the active hydrophilic group was believed to be the C-N functional group, which forms a chemical bond with the metal ions of the sulfide mineral lattice, while the hydrogen atoms interact with the aqueous phase by forming hydrogen bonds. Both surfactants render the mineral surface more hydrophilic than "sulfophilic".

It seems reasonable to speculate that these surfactants interact with chalcopyrite in a similar fashion. In the case of lignosulfonate the hydroxyl and sulfonate functional groups could bond with copper and/or iron in the chalcopyrite lattice, while the hydrophobic portion interacts with the aqueous phase through hydrogen bonding. In the case of OPD, the C-N functional group could also bond with the copper and/or iron in chalcopyrite.

An additional consideration which Owusu did not address is that the surfactants are likely to be chelated by the metal ions in solution. For example, it is well known that OPD forms strong complexes with the cupric ion (equations (5-1) and (5-2)). Ferric/ferrous ions and Zn^{2+} may also complex OPD as well as lignosulfonate (although no information on complexes of these types was found in the literature). Thus, the actively adsorbing species could be a metal-surfactant complex.

A major difference between the results of this study and Owusu's results is that in this study OPD was found to adsorb at the sulfur-solution interface, whereas Owusu found that OPD did not adsorb at the sulfur-solution interface. The reason for the differing results is not known, but a possible explanation can be ventured when one considers the different aqueous media employed. The solution used in this study contained 0.47 mol/L $CuSO_4$, 0.09 mol/L $Fe_2(SO_4)_3$

and 1.00 mol/L H_2SO_4. The solution used by Owusu (to measure the sulfur-solution interfacial tension in the presence of OPD) contained only 1.2 mol/L $ZnSO_4$ and no acid. It is possible that a Cu-OPD complex and/or an Fe-OPD complex and/or protonated OPD adsorbs at the sulfur-solution interface whereas a Zn-OPD complex (or uncomplexed OPD) does not.

5.2 Pressure Leach Experiments

5.2.1 Effect of Temperature on Chalcopyrite Reaction Kinetics and Sulfur Yield

The Gibraltar concentrate was leached at temperatures varying from 110-220°C to ascertain the effect of temperature on reaction rate for this particular feed, as well as to identify a temperature range over which elemental sulfur is produced in high yield. Test conditions were 100 g/L pulp density, 0.69 MPa oxygen pressure and a 3 hour residence time. The oxygen pressure was lower than the usual pressure of 1.38 MPa adopted for most of the subsequent runs, in order to ensure that the total pressure (steam plus oxygen) at the higher temperatures was within safe operating limits for the autoclave. The initial leach solution contained 10 g/L Cu^{2+}, 5 g/L Fe^{3+} and 98 g/L H_2SO_4.

The results are presented showing the effect of temperature on:

- oxygen consumption rate (Figure 5-2);
- copper/iron dissolution and sulfide oxidation extent (Figure 5-3a);
- relative proportion of sulfide oxidized to elemental sulfur vs. sulfate (Figure 5-3b);
- pregnant solution free H_2SO_4 concentration (Figure 5-4);
- leach residue composition (Table 5-4).

At low temperatures, i.e. 110-120°C, the rate of reaction was slow, as indicated by the low oxygen consumption (8.8-11.0 L), low copper extraction (43-47%) and low total sulfide oxidation (42-46%). The proportion of sulfide sulfur oxidized to elemental sulfur (sulfur yield) was 72% at 110°C, lower than the 85-90% yield expected for pure chalcopyrite. The lowered sulfur yield was likely due at least partly to the sulfate generated by oxidation of the pyrite in the Gibraltar concentrate. The sulfur yield from pyrite oxidation under these conditions is only about 40% [189]. The pregnant solution free H_2SO_4 (acid) concentration was 57-61 g/L, or about 60% of the original acid concentration. The leach residue contained essentially no sulfate

sulfur (0.03%), indicating that the acidity level remained high enough to prevent ferric iron hydrolysis (as a basic ferric sulfate such as jarosite).

At moderate temperatures, 130-170°C, the initial oxygen consumption rate increased with increasing temperature, but the rate then slowed dramatically or stopped entirely before the end of the run, signalling a premature cessation in sulfide oxidation. Oxygen consumption (12.8-18.4 L), copper extraction (44-56%), iron extraction (50-58%) and total sulfide oxidation (51-63%) increased only slightly with increasing temperature in this temperature range. The elemental sulfur yield showed a slight decline, from 63% at 130°C to 52% at 170°C. The pregnant solution free acid level remained relatively constant at 58-61 g/L. Leach residue sulfate levels were low and increased only slightly with increasing temperature (from 0.26% to 0.84%), indicating minimal ferric iron hydrolysis occurred. Leach residues were extensively agglomerated, in contrast to the finely disseminated nature of the 110-120°C residues. It was concluded that leaching became stifled by molten sulfur, whereby the sulfur wetted and agglomerated the unreacted sulfide mineral particles. This would explain the relative insensitivity of the results to leach temperature.

At 180°C the reaction rate was still relatively slow, then the rate increased sharply with further temperature increases. A rapid increase in oxygen consumption was noted, which coincided with similar increases in copper extraction, sulfide oxidation, the proportion of sulfide oxidized to sulfate and the solution acidity. At temperatures of 200°C or higher oxygen consumption reached a maximum of about 45 L and 100% sulfide oxidation was achieved within 3 hours. The elemental sulfur yield declined from 35% at 180°C to nil at 210 and 220°C. The pregnant solution acidity increased with increasing temperature and reached a high of 99 g/L at 220°C. Copper dissolution was 98.6% at 200°C and 99.3% at 220°C. The leach residue copper content reached a low of 0.21% at 220°C. The sulfide content of the 200-220°C residues was virtually nil (0.01-0.05%) so the insoluble copper was not unreacted chalcopyrite but rather, copper which must have co-precipitated with the iron. Iron extraction peaked at 61.7% at 180°C, then declined to a low of 10% at 220°C due to ferric iron hydrolysis. The well-oxidized residues from the 190-220°C runs had molar Fe/SO_4 ratios close to 1, suggesting that the iron precipitate had a composition close to $Fe(OH)SO_4$.

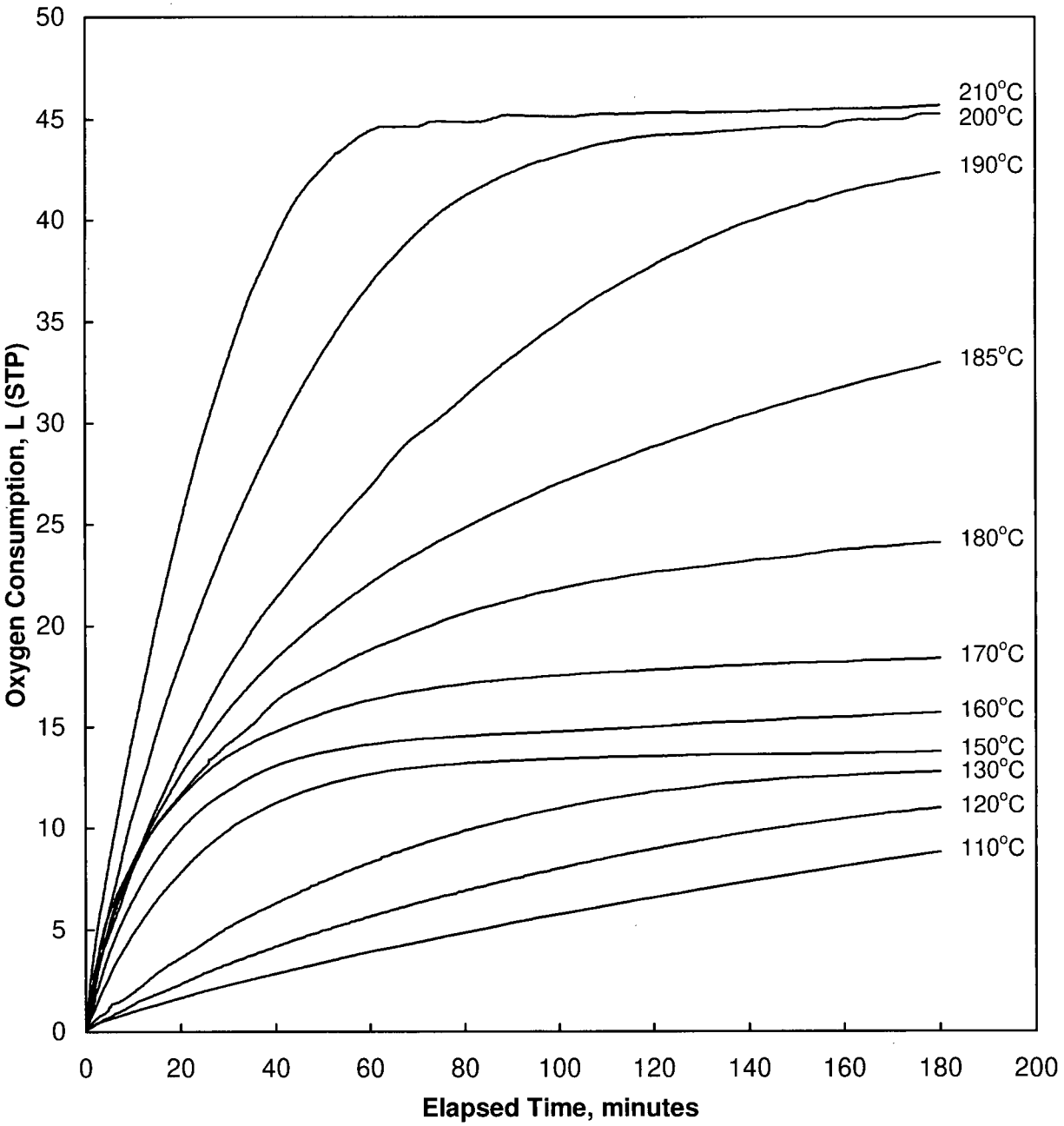

Figure 5-2. Effect of leach temperature on oxygen consumption rate for the oxygen pressure leaching of the Gibraltar concentrate. Test conditions: 100 g/L pulp density and 0.69 MPa oxygen pressure. The initial leach solution contained 10 g/L Cu^{2+}, 5 g/L Fe^{3+} and 98 g/L H_2SO_4.

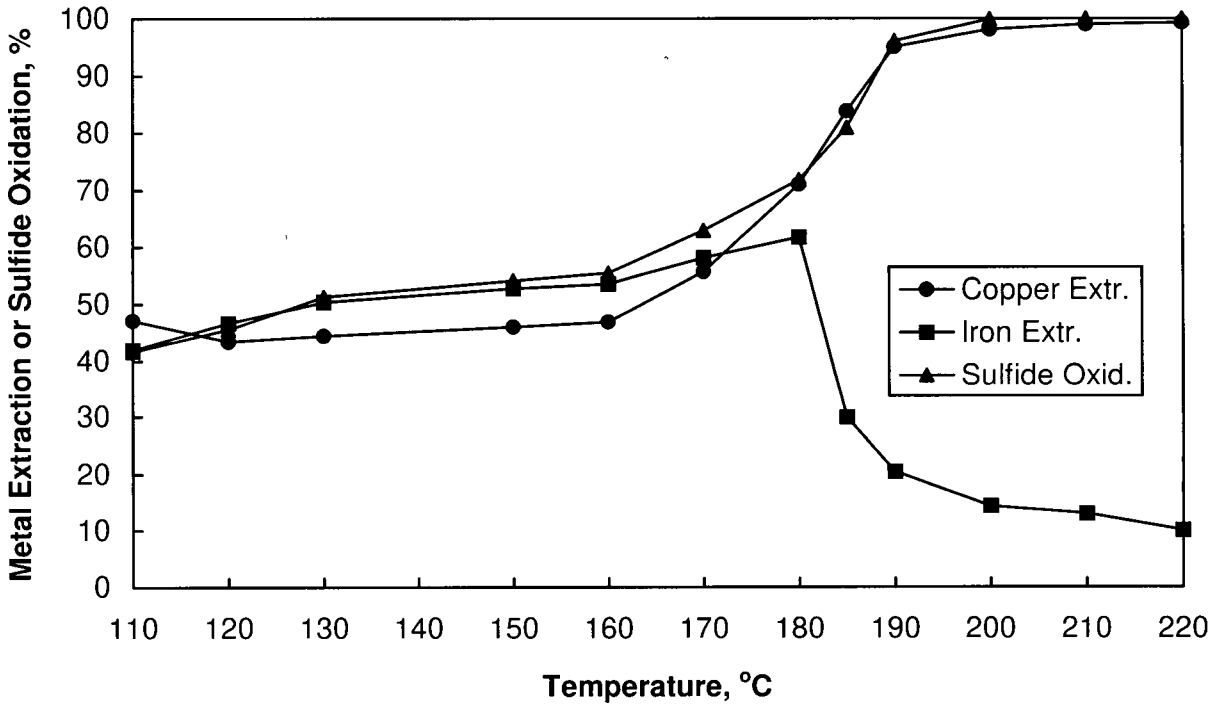

(a)

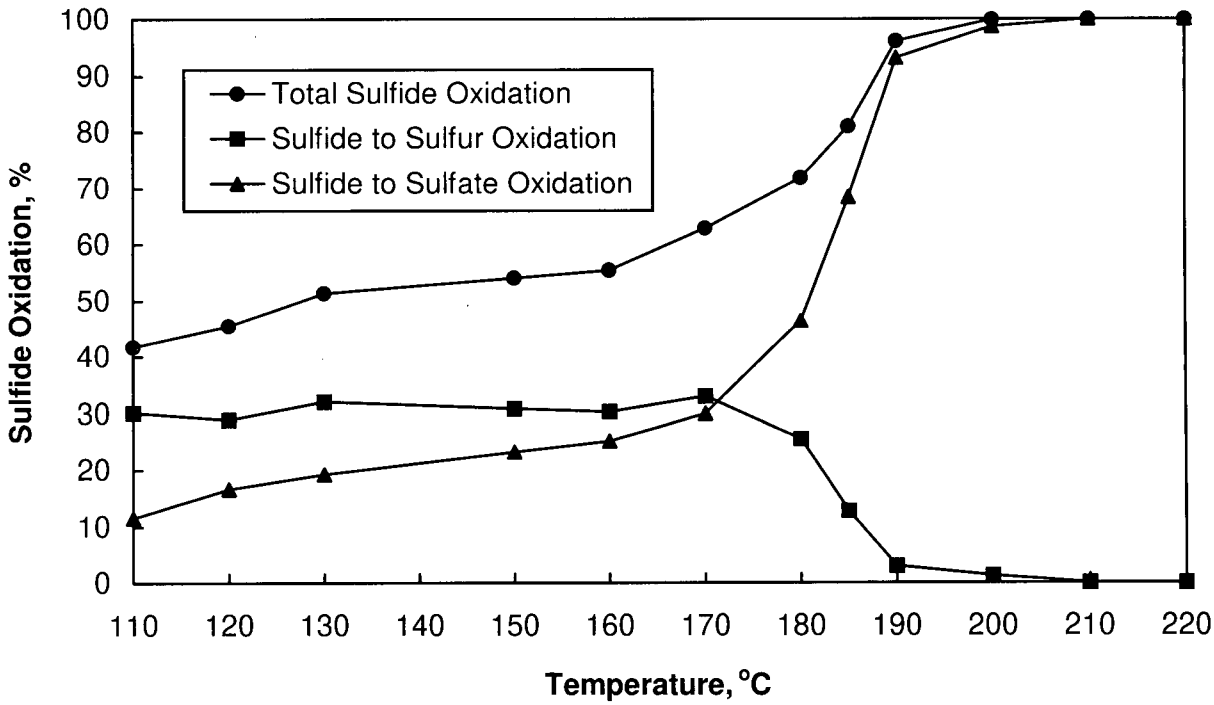

(b)

Figure 5-3. Effect of leach temperature on: (a) copper/iron dissolution and total sulfide oxidation, and (b) sulfide oxidation to elemental sulfur vs. sulfate, for the oxygen pressure leaching of the Gibraltar concentrate. Test conditions as for Figure 5-2 except the residence time was fixed at 3 hours.

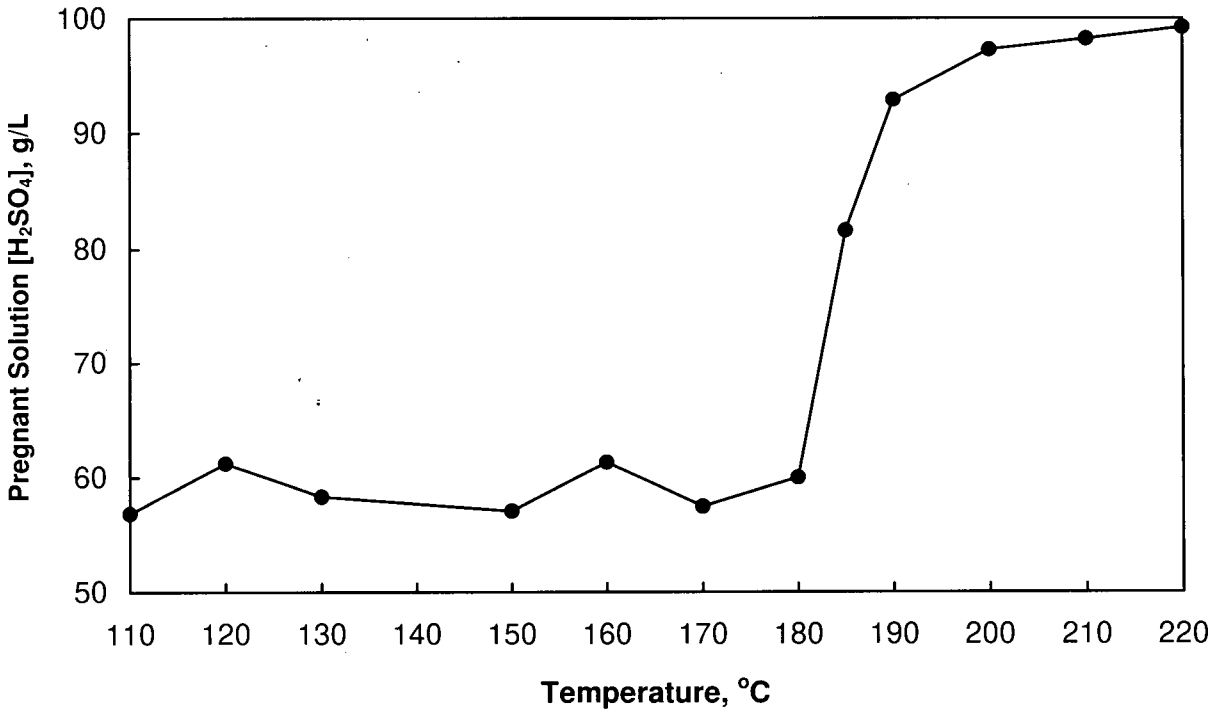

Figure 5-4. Effect of leach temperature on the pregnant solution free H_2SO_4 concentration, for the oxygen pressure leaching of the Gibraltar concentrate. Test conditions as for Figure 5-3.

Table 5-4. Effect of leach temperature on the composition of the Gibraltar leach residue, for the oxygen pressure leaching of the Gibraltar concentrate. Test conditions as for Figure 5-3.

Leach Temp. °C	Leach Residue Composition							
	Wt. g	Cu %	Fe %	S_T %	S^{2-} %	S° %	S_{SO4} %	Fe/SO_4 Molar Ratio
110	65.25	22.24	24.27	43.01	28.14	14.57	0.03	465
120	64.04	24.78	23.77	41.29	26.81	14.20	0.03	455
130	62.23	24.69	21.88	41.80	24.67	16.21	0.26	48.3
150	60.00	24.88	21.61	41.13	24.14	16.17	0.45	27.6
160	60.17	24.85	21.76	40.37	23.34	15.84	0.59	21.2
170	54.32	22.60	21.12	41.81	21.52	19.11	0.82	14.8
180	45.42	17.39	22.62	39.67	19.61	17.62	2.17	5.99
185	72.10	6.02	27.89	25.37	8.32	5.51	11.14	1.44
190	75.54	1.71	29.27	19.05	1.64	1.21	15.73	1.07
200	81.39	0.63	29.65	17.52	0.05	0.48	16.47	1.03
210	79.12	0.32	30.18	17.74	0.01	0.01	17.12	1.01
220	85.57	0.21	30.09	17.50	0.01	0.01	17.14	1.01
Feed	100.00	28.19	27.54	32.17	31.49	0.03	0.61	25.9

These results confirm the findings of others that chalcopyrite is quite resistant to oxidation by oxygen pressure leaching (Section 2.3.2). At low temperatures, i.e. below the sulfur melting point, the elemental sulfur yield was highest but the reaction rate was slow. At temperatures above the sulfur melting point of 119°C to about 170-180°C, the initial reaction rate increased with increasing temperature, but leaching became stifled as a result of liquid sulfur wetting and agglomerating the unreacted sulfides. At temperatures of 200°C or higher complete oxidation of chalcopyrite was achieved within 3 hours, with the sulfide fraction oxidized entirely to sulfate.

5.2.2 Effect of Liquid Sulfur on Chalcopyrite Oxidation

The effect of liquid sulfur on chalcopyrite oxidation was investigated further by comparing the leaching kinetics at a temperature slightly below (110°C) and above (125°C) the sulfur melting point. Low pulp density (10 g/L) leach tests were conducted on both the Gibraltar concentrate and the chalcopyrite concentrate, using a starting leach solution containing 1 g/L Cu^{2+}, 0.5 g/L Fe^{3+} and 98 g/L H_2SO_4. The experimental procedures were identical at the two temperatures with the following exception. For the 110°C tests, the concentrate feed was added to the solution at the start of the 15 minute warm-up period (prior to sealing the autoclave). For the 125°C tests, the same procedure used for the 125°C low pulp density tests with surfactants (Section 5.2.5) was followed in order to be consistent. In this procedure, the feed was initially contained in the internally mounted solids addition chamber, hence it was isolated from the leach solution during warm-up. When the temperature reached 125°C oxygen was added; this forced open the solids chamber and expelled the solids into solution. Thus the feed in the 110°C tests had the opportunity to react with the starting solution during the 15 minutes required to raise the temperature to 110°C, while the feed in the 125°C tests did not.

Figure 5-5a and Figure 5-5b depict the 110°C and 125°C copper leach profiles for the Gibraltar and $CuFeS_2$ concentrates respectively. With the Gibraltar concentrate at 110°C, 15.3% of the copper was solubilized during the 15 minute warm-up period (prior to adding O_2). This is not surprising, as the concentrate contains copper oxide and chalcocite, which would readily react with the acid and ferric iron in the starting solution. In contrast, copper dissolution from the $CuFeS_2$ concentrate during warm-up was minimal (2.2% Cu extraction).

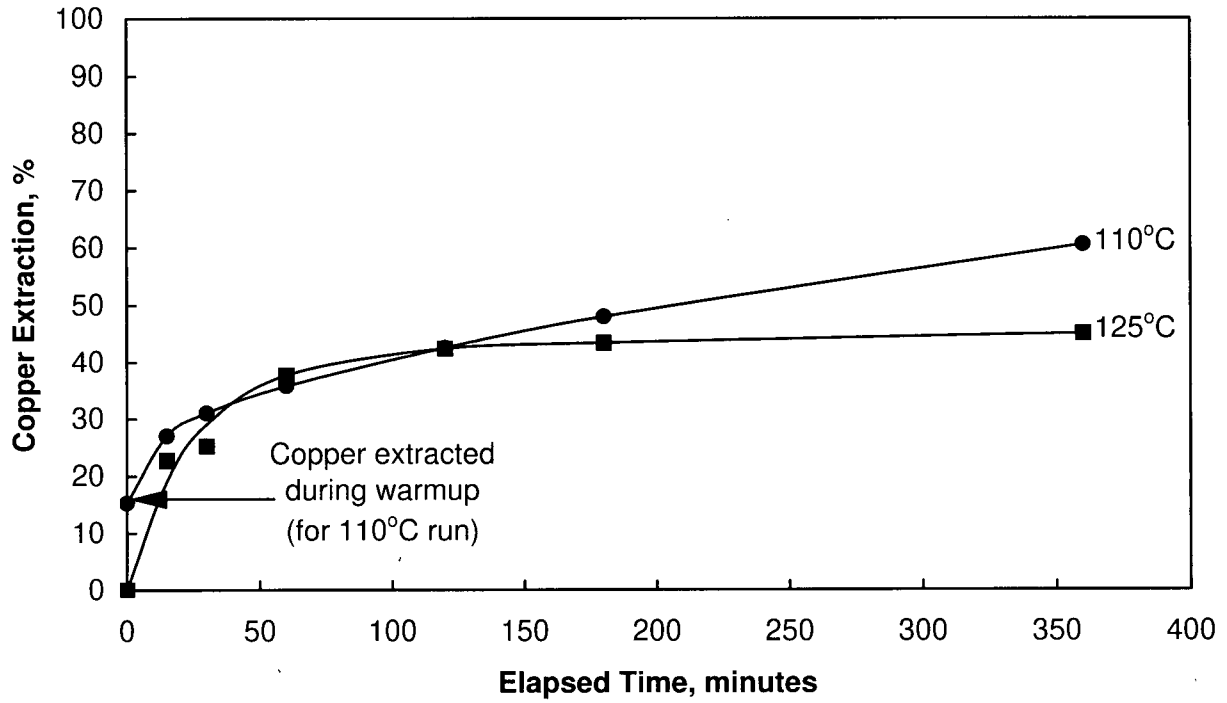

(a)

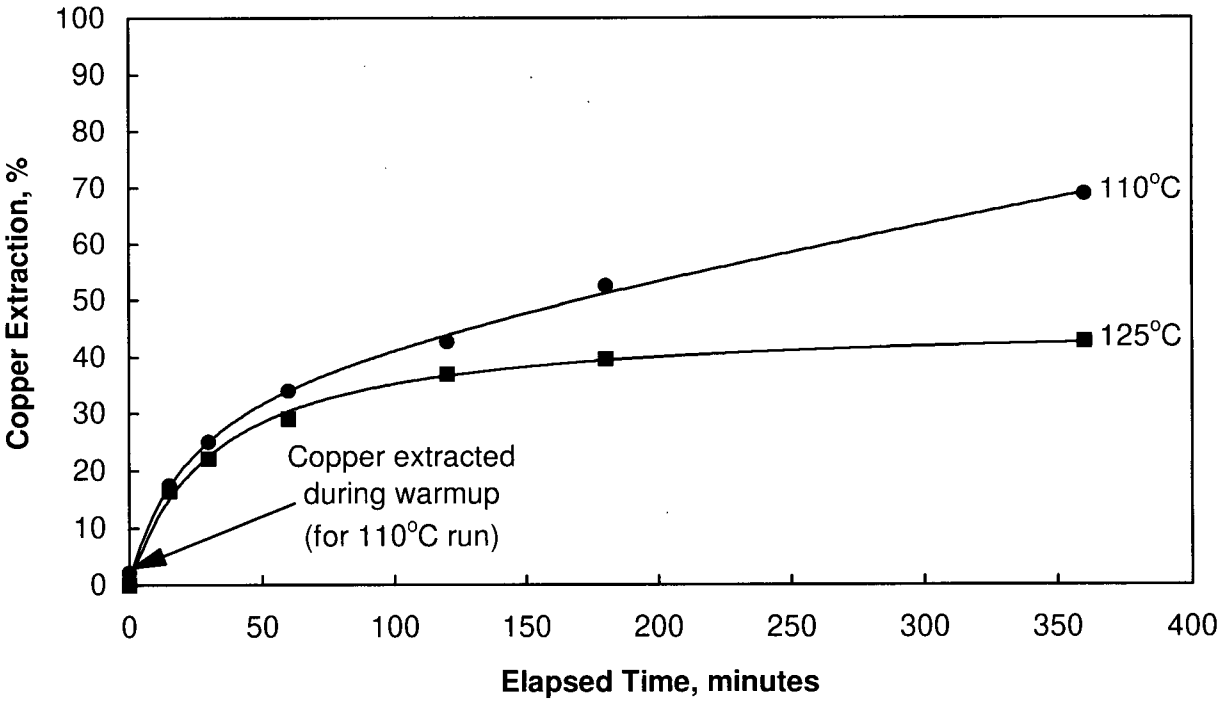

(b)

Figure 5-5. Comparison of the copper extraction profiles obtained when: (a) the Gibraltar concentrate and (b) the $CuFeS_2$ concentrate were leached at a temperature slightly below (110°C) and above (125°C) the sulfur melting point. Test conditions: 10 g/L pulp density and 1.38 MPa oxygen overpressure. The initial leach solution contained 1 g/L Cu^{2+}, 0.5 g/L Fe^{3+} and 98 g/L H_2SO_4. The feed for the 110°C runs was exposed to the starting solution during warm-up, whereas the feed for the 125°C runs was not.

Upon adding oxygen, the copper leach profiles for both concentrates differed markedly at the two temperatures. At 110°C, copper leached slowly but steadily from both the Gibraltar and $CuFeS_2$ concentrates; the copper extractions reached 60.5% and 69.1% respectively after 6 hours. In contrast, at 125°C there was an abrupt and almost complete cessation of leaching after 2-3 hours, indicative of the leach becoming stifled by molten sulfur. The copper extractions had reached only 45.0% and 42.8% for the Gibraltar and $CuFeS_2$ concentrates respectively after 6 hours leaching at 125°C. Thus, the amount of copper extracted from both concentrates was significantly higher at 110°C than at 125°C.

A quantitative measure of the effect of liquid sulfur on the copper leach rate was determined for the $CuFeS_2$ concentrate in the following way. The 110°C and 125°C copper extraction vs. time data were fitted to hyperbolic functions using commercially available software (The details of the function fitting procedures used are given in Appendix 2). The function-fitted data are depicted by the solid lines in Figure 5-5b; as can be seen, the fits are quite good. The functions were then differentiated to obtain the instantaneous copper leach rates (in units of %Cu/min). Figure 5-6 shows the 110°C and 125°C copper leach rates plotted as a function of (a) time and (b) copper extraction. In the early stages of leaching the leach rates were virtually identical, suggesting that liquid sulfur exerted a negative effect even in the initial stages (if liquid sulfur did not affect the kinetics the initial leach rate at 125°C should be higher than the initial rate at 110°C). After about 40 minutes leaching or 25% copper extraction, the 125°C leach rate started to decline much faster than the 110°C leach rate, with the result that after 6 hours the 110°C leach rate was an order of magnitude higher than the corresponding rate at 125°C. In fact the 110°C leach rate appeared to almost level off. The significance of this will be addressed in the kinetic model developed in Chapter 6.

Figure 5-7a and Figure 5-7b depict the 110°C and 125°C iron leach profiles for the Gibraltar and $CuFeS_2$ concentrates respectively. The results were similar to those obtained for copper. With the Gibraltar concentrate, iron leached steadily with time at 110°C and ultimately reached 62.1% extraction after 6 hours. At 125°C iron extractions were significantly higher in the early stages of leaching than at 110°C, due to the increased pyrite oxidation rate at the higher temperature. However, after about 2-3 hours iron leaching virtually stopped. As a result, the iron extraction after 6 hours (57.7%) ended up being slightly lower than the comparable iron

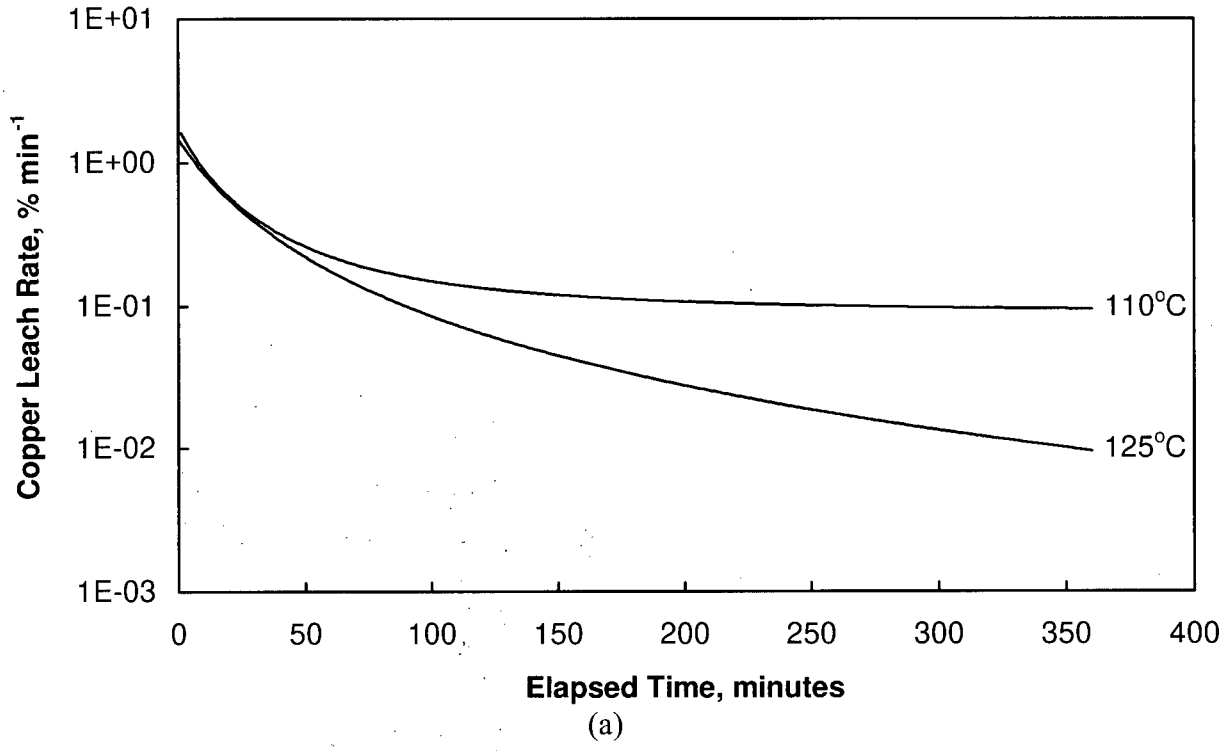

(a)

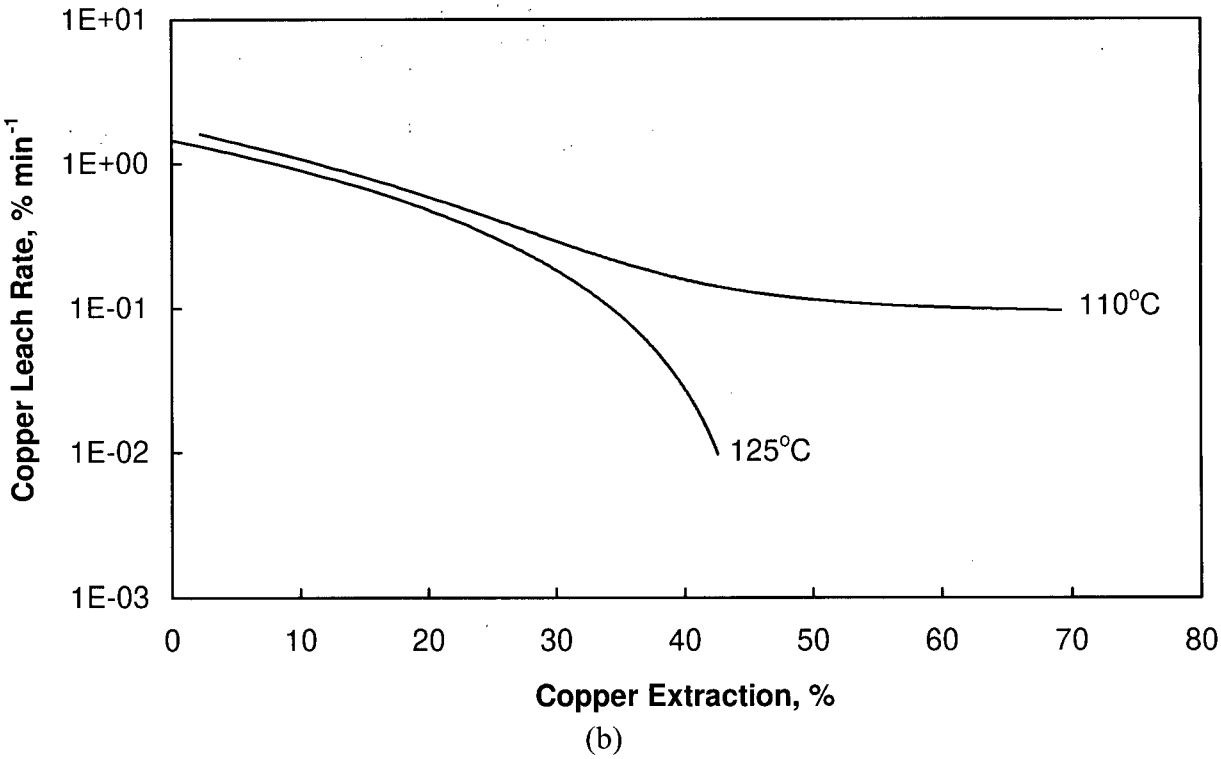

(b)

Figure 5-6. Comparison of the 110°C and 125°C copper leach rates vs. (a) time and (b) copper extraction, for the oxygen pressure leaching of the $CuFeS_2$ concentrate. The leach rates were calculated by differentiating the function-fitted copper extraction plots (Figure 5-5b).

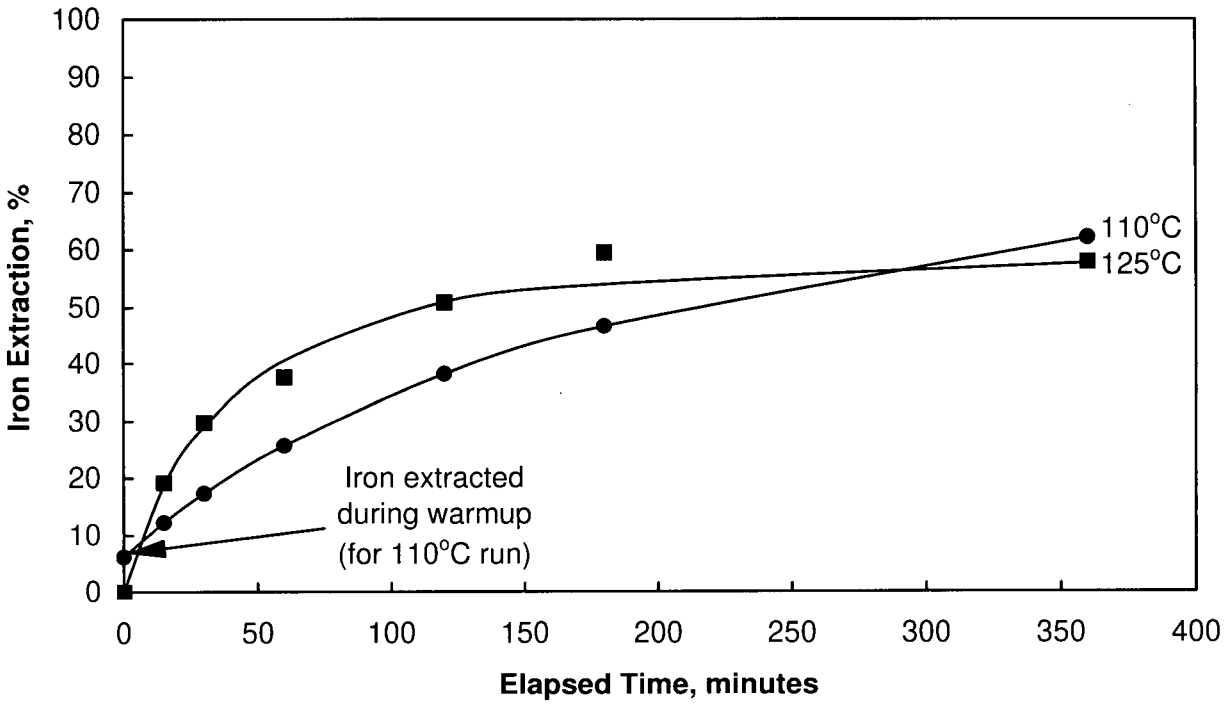

(a)

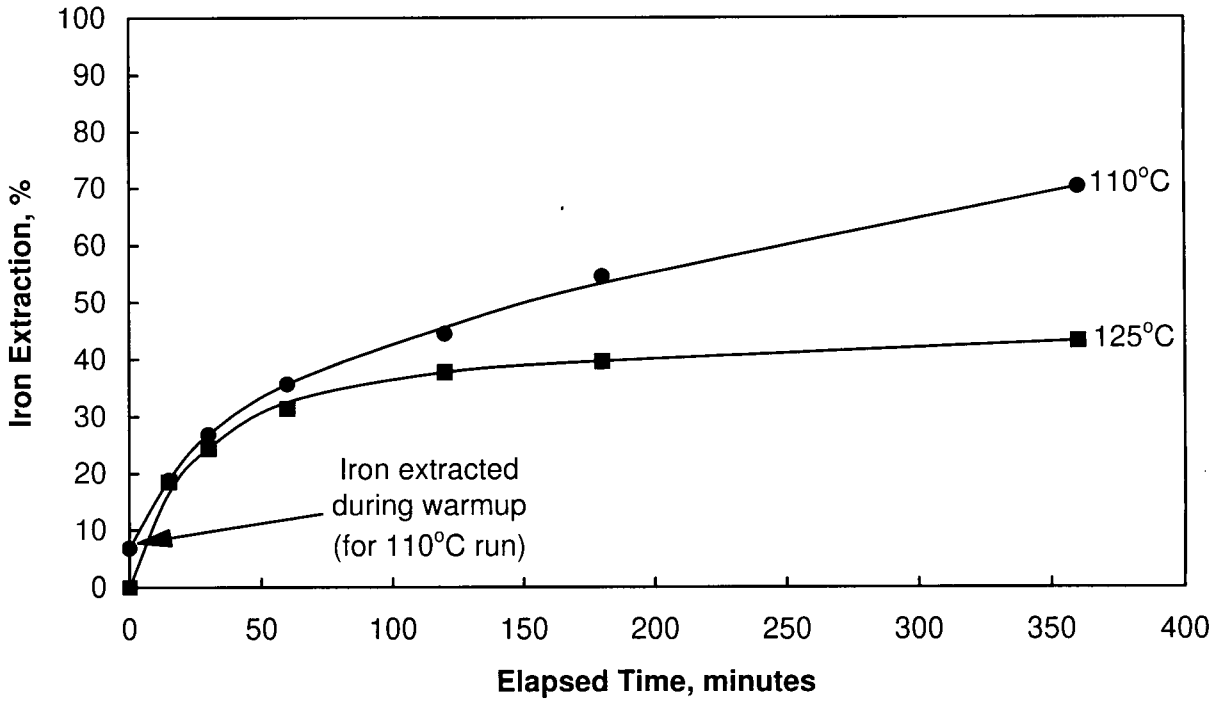

(b)

Figure 5-7. Comparison of the iron extraction profiles obtained when: (a) the Gibraltar concentrate and (b) the $CuFeS_2$ concentrate were leached at a temperature slightly below (110°C) and above (125°C) the sulfur melting point. Test conditions as for Figure 5-5.

extraction at 110°C. With the $CuFeS_2$ concentrate, the iron leach profiles were virtually identical to the copper leach profiles.

Analysis of the $CuFeS_2$ leach residues for sulfur species revealed that the S° yield was about 88% at 110°C regardless of the residence time. This is in good agreement with the results obtained by Vizsolyi *et al.* under comparable conditions [2]. At 125°C the S° yield declined slightly, to 79%.

Figure 5-8a and Figure 5-8b show the effect of liquid sulfur on the morphology of the $CuFeS_2$ leach residues after leaching for 30 minutes and 120 minutes respectively at 125°C. After 30 minutes leaching, most of the particles were still quite finely disseminated but some agglomerates were evident. In contrast, after 120 minutes leaching the particles were extensively agglomerated. The 30-minute residue contained 11.2% S° whereas the S° concentration of the 120-minute residue was considerably higher at 18.9% S°. It was concluded the extent of particle agglomeration is probably related to the concentration of S° in the leach residue, with the agglomeration extent increasing with increasing S° concentration. The 110°C leach residues were all finely disseminated.

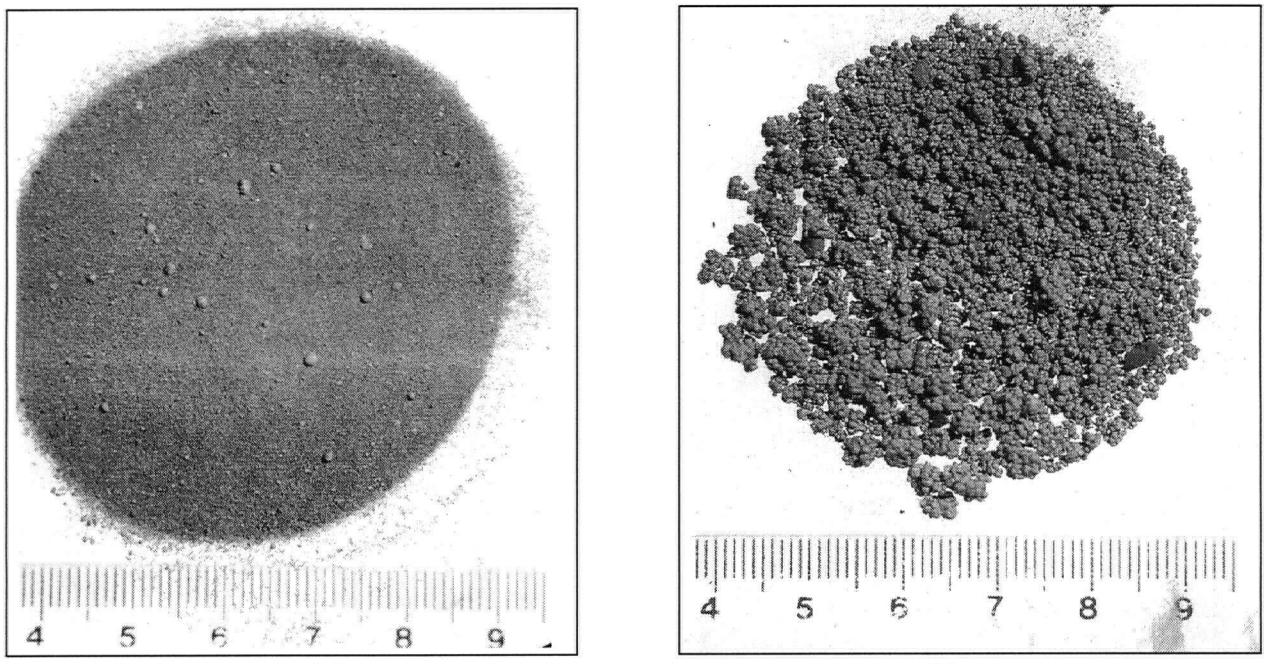

(a) (b)

Figure 5-8. Photographs of $CuFeS_2$ concentrate residue particles after leaching at 125°C for: (a) 30 minutes and (b) 120 minutes, showing the effect of liquid sulfur on particle morphology. The ruler scale is in cm.

The 110°C and 125°C kinetic results combined with observations of the leach residue morphologies provide convincing evidence that liquid sulfur stifles leaching at 125°C. Under the conditions used here, the stifling effect was quite pronounced, with the result that copper and iron extractions after 6 hours leaching were considerably lower at 125°C than at 110°C.

Figure 5-9 shows the copper and iron dissolution plots obtained when the Gibraltar concentrate was leached at high pulp density (100 g/L) at 125°C. The results are very similar to the results obtained at low pulp density (Figure 5-5a and Figure 5-7a). Copper and iron dissolution ceased after about two hours due to the stifling effect of liquid sulfur. The copper extraction after 3 hours (44.9%) was virtually identical to the 3-hour copper extraction obtained at low pulp density (43.4%). The 3-hour iron extraction (48.1%) was slightly lower than the 3-hour iron extraction obtained at low pulp density (54.0%), suggesting that pyrite dissolution was increased slightly at the lower pulp density. The results indicate that oxidation of the Gibraltar concentrate at 125°C is largely independent of pulp density in the range tested (10-100 g/L).

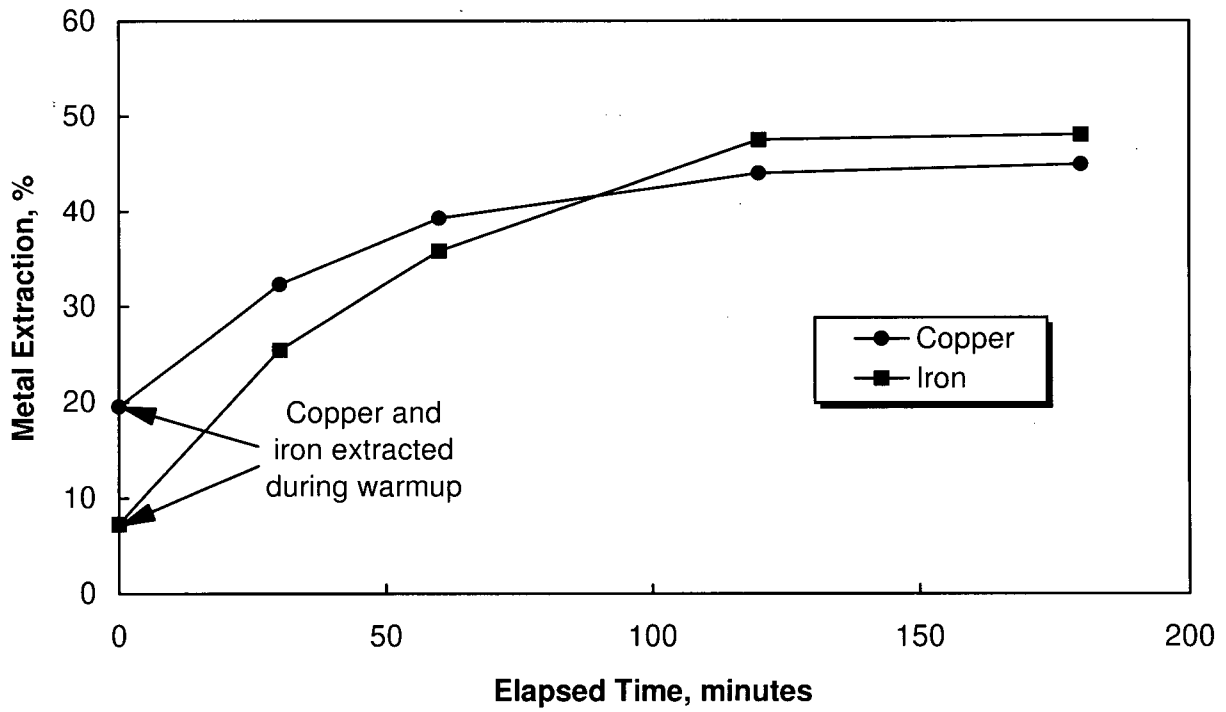

Figure 5-9. Copper and iron dissolution vs. time for the oxygen pressure leaching of the Gibraltar concentrate at high pulp density at 125°C. Test conditions: 100 g/L pulp density and 1.38 MPa oxygen overpressure. The initial leach solution contained 10 g/L Cu^{2+}, 5 g/L Fe^{3+} and 98 g/L H_2SO_4.

5.2.3 Preliminary Evaluation of Surfactants in Pressure Leaching Tests

The results of previous tests (Section 5.2.1) indicated that liquid elemental sulfur was produced in high yield at 125-155°C, hence surfactants were evaluated in leach tests conducted in this temperature range. Initial screening tests were carried out on the Gibraltar concentrate at high pulp density (100 g/L) at 155°C, 1.38 MPa oxygen overpressure and a 1 hour residence time. Surfactants were added batchwise at a dosage of 0.5 g/L, equivalent to 5 kg surfactant per tonne concentrate. In one test, a combination of 0.5 g/L calcium lignosulfonate (Lignosite 100) and 0.5 g/L quebracho was tried (these two surfactants are used in concert in some zinc pressure leaching operations, hence it was of interest to see if there was any benefit to be gained by combining the two surfactants).

Table 5-5 summarizes the copper and iron extraction results obtained and gives a brief description of the morphological characteristics of the leach residues. In the absence of surfactant, copper and iron extractions reached 45.8% and 52.5%, respectively. None of the surfactants tested proved particularly effective in increasing copper extraction; in fact, some surfactants actually depressed the extraction. Surfactants which depressed copper extraction were Armeen 2HT (32.4% copper extraction) and Pamak CTP (27.9%). It was noted that these surfactants caused extensive frothing of the slurry upon adding oxygen. As a result the bulk of the sulfides ended up caked on the autoclave wall above the solution level and had no opportunity to react.

The addition of the lignosulfonate and phenylenediamine surfactants resulted in no improvement or only a slight improvement in copper and iron extraction. The highest copper extraction obtained was 53.5% when a combination of Lignosite 100 and quebracho was used. In most cases the leach residues were extensively agglomerated, indicating that the surfactants had been ineffective in dispersing elemental sulfur during leaching. Agglomerates tended to be quite uniformly shaped spheres, varying in diameter from 0.5-3 mm. Unagglomerated residues were obtained only in the tests with OPD and MPD.

To determine if the extent of oxidation could be increased by increasing the surfactant dosage, the tests with calcium lignosulfonate (Lignosite 100) and OPD were repeated using 15 kg/t surfactant. Table 5-6 shows the results obtained. Increasing the lignosulfonate dosage to 15 kg/t yielded only a slight increase in copper extraction - 52.4% vs. 49.2% obtained with 5 kg/t. The higher OPD dosage had no effect - copper extraction was essentially unchanged at 47.0% vs. 47.5% obtained with 5 kg/t OPD.

Table 5-5. Effect of batchwise surfactant additions on the leaching of Gibraltar concentrate at high pulp density. Test conditions: 100 g/L pulp density, 155°C, 1.38 MPa oxygen pressure and a 1 hour residence time. The starting leach solution contained 10 g/L Cu^{2+}, 5 g/L Fe^{3+} and 98 g/L H_2SO_4. The surfactant dosage was 5 kg/tonne conc.

Surfactant	Cu Extr. %	Fe Extr. %	Leach Residue Morphology
None	45.8	52.5	Agglomerated, 1-2 mm dia. pellets
Lignosite 100	49.2	56.3	Agglomerated, 1-2 mm dia. pellets
Lignosite 458	45.2	52.0	Agglomerated, 0.5-2 mm dia. pellets
Kelig 100	43.6	50.6	Agglomerated, 0.5-2 mm dia. pellets
Quebracho	48.5	55.4	Agglomerated, 1-3 mm dia. pellets
Lignosite 100 + Quebracho	53.5	59.7	Agglomerated, 1-3 mm dia. pellets
OPD	47.5	54.8	Mainly finely disseminated, some pellets
MPD	49.5	56.2	Mainly finely disseminated, some pellets
PPD	44.6	53.0	Agglomerated, 0.5-1 mm dia. pellets
Armeen 2HT	32.4	16.1	Sulfide froth, some pellets[1]
Pamak CTP	27.9	15.4	Sulfide froth, some pellets[1]
Dowfax 3BO	47.0	52.5	Agglomerated, 0.5-1 mm dia. pellets
Fluorad FC-95	45.1	48.1	Agglomerated, 1-3 mm dia. pellets

[1]These surfactants caused extensive frothing of sulfides. The froth coated the auotoclave wall above the solution level; as a result the sulfides remained largely unreacted.

Table 5-6. Effect of varying the surfactant dosage on the leaching of the Gibraltar concentrate. Test conditions as for the runs in Table 5-5.

Surfactant Type	Surfactant Dosage (g/L)	Cu Extr. (%)	Fe Extr. %	Total S^{2-} Oxid. (%)	S° Yield (%)
None		45.8	52.5	55.3	47.7
Lignosite 100	5	49.2	56.3	57.4	48.1
Lignosite 100	15	52.4	58.3	60.1	47.7
OPD	5	47.5	54.8	57.1	39.4
OPD	15	47.0	54.4	56.1	29.1

It was concluded that the surfactants were either not interfacially active or they decomposed too quickly to be effective. The previously discussed interfacial test results (Section 5.1) showed that OPD and the lignosulfonates (at least) should be capable of preventing liquid sulfur from wetting chalcopyrite in acid cupric/ferric solutions. From the agglomerated nature of the leach residues it was concluded that the lignosulfonates decomposed too quickly to be effective. Interestingly, OPD and MPD yielded finely disseminated residues, which indicates they remained interfacially active during leaching, yet copper extractions were not improved significantly. From this it can be inferred that another mechanism unrelated to sulfur wetting

may be at least partly responsible for the low reaction rate. To investigate this possibility further it was decided to conduct leach tests under conditions specifically designed to prolong surfactant life and hopefully prevent wetting of chalcopyrite by liquid sulfur. Attempts to accomplish this and the results obtained are discussed in the next two sections.

5.2.4 Effect of Continuous Surfactant Addition at High Pulp Density

Most of the surfactants appeared to be susceptible to rapid decomposition under pressure leaching conditions, therefore continuous surfactant addition was tried in an attempt to replenish surfactant faster than it decomposed. Tests were carried out at 100 g/L pulp density on the Gibraltar concentrate. The leach temperature was 125°C or 155°C, the oxygen pressure was 1.38 MPa and the residence time was 3 hours. The concentrate was first pre-conditioned with 0.1 g of surfactant which was added to the starting leach solution. During the run, freshly prepared OPD or lignosulfonate stock solution was pumped into the autoclave at a rate set to deliver 0.5 g surfactant over the course of the run, equivalent to an addition rate of 0.028 kg/t-min. The total surfactant dosage was therefore 0.6 g/L or 6 kg/t concentrate. The surfactants tested were OPD and two types of lignosulfonate, Lignosite 100 and Kelig 100.

Table 5-7 shows the results obtained. There was only a slight benefit gained by adding the surfactants continuously. Continuous addition of Lignosite 100 yielded 56.4% copper extraction at 125°C and 54.8% copper extraction at 155°C, compared to 48.2% copper extraction obtained with no surfactant at 125°C. Similarly, continuous OPD addition yielded only 56.8% and 53.6% copper extraction at 125°C and 155°C, respectively. The use of Kelig 100 at 155°C resulted in no improvement in copper extraction.

The 125°C leach residues were mainly finely disseminated, suggesting that continuous surfactant addition was successful in maintaining excess surfactant in solution at this temperature, yet copper extractions did not increase appreciably. In contrast, the 155°C residues were extensively agglomerated, indicating that at the higher temperature, the surfactants decomposed faster than they were being added.

Table 5-7. Effect of continuous surfactant addition on the leaching of the Gibraltar concentrate at high pulp density. Conditions: 100 g/L pulp density, 125°C or 155°C, 1.38 MPa oxygen pressure and 3 hour retention time. The starting leach solution contained 10 g/L Cu^{2+}, 5 g/L Fe^{3+} and 98 g/L H_2SO_4.

Leach Temp. (°C)	Surfactant	Cu Extr. (%)	Fe Extr. (%)	Total S^{2-} Oxid. (%)	S° Yield (%)	Leach Residue Morphology
125	None	44.9	48.1	53.0	55.1	Agglomerated, 1-2 mm pellets
125	Lignosite 100	56.4	58.0	60.2	59.3	Mainly finely disseminated, with 5-10% as 1 mm pellets
155	Lignosite 100	54.8	58.7	59.3	50.3	Agglomerated, 2-4 mm pellets
155	Kelig 100	48.0	56.4	ND	ND	Agglomerated, 2-3 mm pellets
125	OPD	56.8	54.1	55.9	54.2	Finely disseminated, no pellets
155	OPD	53.6	57.2	ND	ND	Agglomerated, 0.5-1 mm pellets

ND = not determined.

5.2.5 Effect of Batch and Continuous Surfactant Additions at Low Pulp Density

In an attempt to ensure that excess surfactant was maintained in solution during leaching, low pulp density (10 g/L) leach tests were carried out at low temperature (125°C) and a high surfactant dosage (0.5 g or 50 kg/t concentrate). Tests were carried out on both the Gibraltar and $CuFeS_2$ concentrates. Two surfactants were tested, calcium lignosulfonate (Lignosite 100) and OPD. Batch and continuous surfactant additions were tried. In these runs the concentrate was isolated from the leach solution during warm-up by storing the feed in the internally mounted chamber. When the operating temperature of 125°C was reached, the autoclave was pressurized and 50 kg/t surfactant was then pumped in, either quickly in the first few minutes (batch additions) or slowly over the duration of the run (continuous additions). Consequently each run received the same surfactant dosage, regardless of residence time. Therefore, the surfactant addition rate varied depending on the residence time, and was as high as 3.33 kg/t-min for the 15 minute run to as low as 0.14 kg/t-min for the 360 minute run.

Figure 5-10a and Figure 5-10b show the effect of batch and continuous surfactant additions on the copper dissolution profiles for the Gibraltar and $CuFeS_2$ concentrates, respectively. The dissolution profiles are somewhat unusual in that the surfactants depressed copper extractions initially, particularly for the $CuFeS_2$ concentrate when OPD was used. The reason for this "induction period" is not known for certain. One possibility is that an excessively

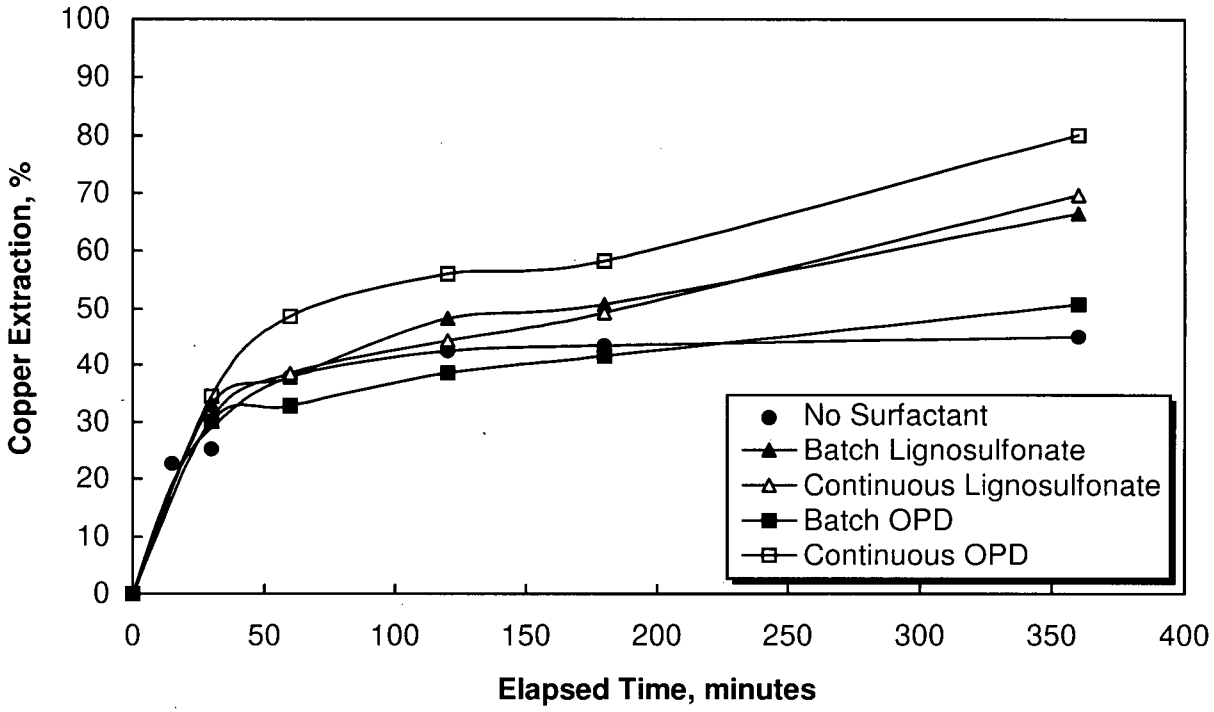

(a)

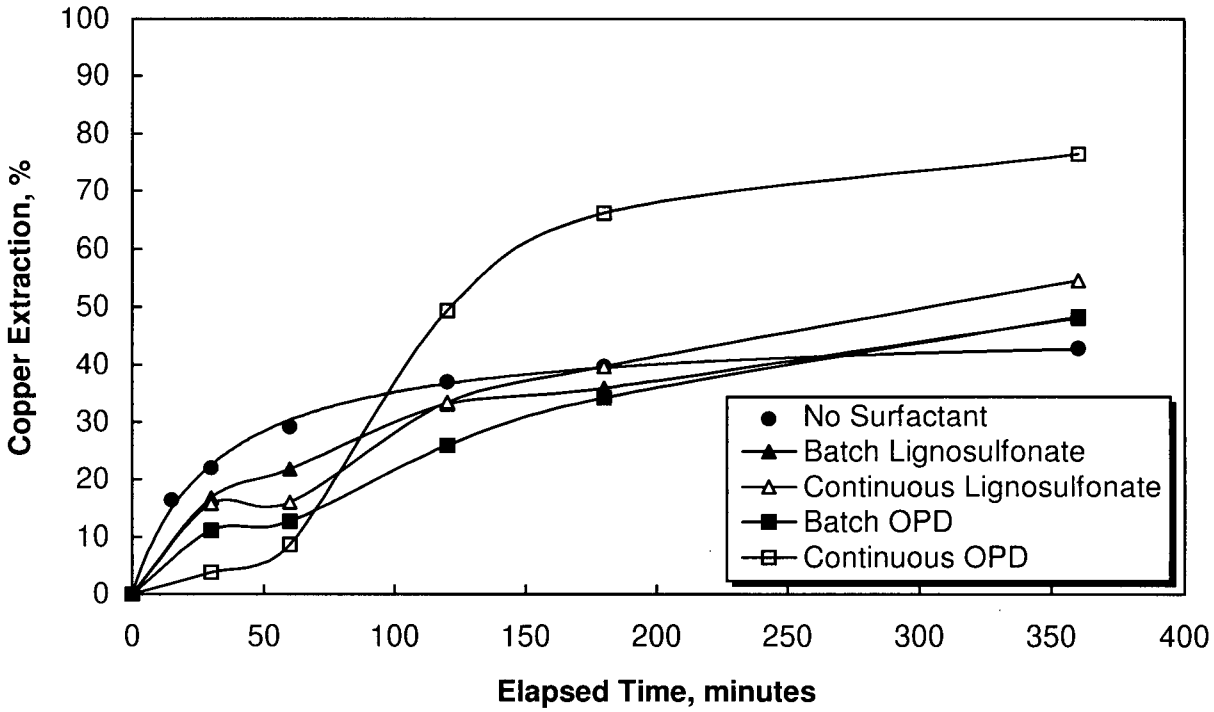

(b)

Figure 5-10. Effect of the surfactants lignosulfonate and OPD on copper extraction during the oxygen pressure leaching of: (a) the Gibraltar concentrate and (b) the $CuFeS_2$ concentrate at low pulp density. Test conditions: 10 g/L pulp density, 125°C and 1.38 MPa oxygen pressure.

high surfactant dosage may impede transfer of oxygen to the mineral surface, slowing the reaction rate. If so, the effect would be more pronounced in the shorter duration runs as they received the full surfactant dose in a short period of time. Despite this induction period, after 3-6 hours leaching copper extractions were ultimately higher when surfactants were used.

The best results were obtained with continuous OPD addition, which increased the copper extraction from 45.0% to 80.1% for the Gibraltar concentrate and from 42.8% to 76.4% for the $CuFeS_2$ concentrate, after 6 hours leaching. This can be compared to the 6-hour copper extractions obtained at low pulp density at 110°C (Section 5.2.2), which were 60.5% and 69.1% for the Gibraltar and $CuFeS_2$ concentrates respectively. Examination of the 125°C leach residues showed them to be finely disseminated. It was concluded that continuous, high-dosage OPD addition was successful in dispersing sulfur, allowing leaching to proceed unimpeded by liquid sulfur. For the Gibraltar concentrate, this resulted in a modest increase in copper extraction, about 18%, over that obtained at 110°C. However, for the $CuFeS_2$ concentrate, the increase in copper extraction at 125°C was minimal, only about 7% over that obtained at 110°C. Therefore, even when a surfactant was successful in dispersing liquid sulfur, the chalcopyrite leaching rate was still relatively slow. This provides support for the theory that chalcopyrite is passivated by a mechanism unrelated to sulfur wetting.

Continuous lignosulfonate addition was not as effective as OPD, yielding copper extractions of 69.6% and 54.5% for the Gibraltar and $CuFeS_2$ concentrates respectively, after 6 hours. Examination of the leach residues revealed that they were partly agglomerated, indicating the lignosulfonate had degraded too quickly to prevent sulfur wetting even when it was added continuously at a high dosage. It would appear that lignosulfonate is more susceptible to oxidative decomposition than OPD. The decomposition of lignosulfonate or OPD does not appear to be a problem in zinc pressure leaching, leading to the hypothesis that surfactant decomposition may be copper-catalyzed.

5.2.6 Effect of Surfactants In Silver Catalyzed Oxygen Pressure Leaching

In the previously discussed leach tests in which surfactants were evaluated, conclusions regarding the success or failure of the surfactants in dispersing sulfur were based largely on a qualitative measure - the appearance of the leach residues. If the residues were finely disseminated the surfactant was judged a success (in dispersing sulfur). If the residues were agglomerated the surfactant was ruled a failure, i.e. the surfactant was concluded to be

interfacially inactive or it decomposed too quickly to disperse sulfur. The rate and extent of chalcopyrite oxidation was generally not a good indicator of the sulfur-dispersing capabilities of a particular surfactant (except in some of the low pulp density tests with high-dosage, continuous surfactant additions, Section 5.2.5) because chalcopyrite leached slowly even when surfactants appeared to disperse sulfur.

A method of increasing the reactivity of chalcopyrite was required to provide a better measure of a surfactant's effectiveness in dispersing sulfur. Silver catalysis was adopted for this purpose. The ability of silver ions to catalyze the oxidative leaching of chalcopyrite has been well documented and this topic was reviewed in Section 2.5.3. Miller and Portillo proposed a mechanism to explain the silver catalyzed ferric sulfate leaching of chalcopyrite [120]. They suggested that the silver ions react with chalcopyrite to form a silver sulfide film on the $CuFeS_2$ surface:

$$CuFeS_2 + 4Ag^+ \rightarrow 2Ag_2S_{(surface)} + Cu^{2+} + Fe^{2+} \qquad (5\text{-}7)$$

with the silver catalyst regenerated by ferric oxidation of the silver sulfide:

$$Ag_2S + 2Fe^{3+} \rightarrow 2Ag^+ + 2Fe^{2+} + S^o \qquad (5\text{-}8)$$

They proposed that the Ag_2S alters the morphology of the solid S° product layer, making it more porous so that the reaction rate is no longer controlled by reactant/product diffusion through S°. Instead, the silver catalyzed rate was thought to be controlled by the rate at which reaction (5-8) occurs.

The effect of surfactants on the silver catalyzed oxygen pressure leaching of chalcopyrite was investigated. Leach tests were conducted on the Gibraltar concentrate at 100 g/L pulp density and on the $CuFeS_2$ concentrate at 110°C. The leach temperature was 110°C, 125°C or 155°C for the tests on the Gibraltar concentrate. The leach temperature was 110°C for the tests on the $CuFeS_2$ concentrate. The oxygen pressure for all tests was 1.38 MPa. The silver dosage was 0.2 g/L (2 kg/t concentrate) for the tests on the Gibraltar concentrate, and 0.05 g/L (5 kg/t concentrate) for the tests on the $CuFeS_2$ concentrate. Silver was added as $AgNO_3$ salt.

5.2.6.1 Effect of Silver in the Absence of Surfactants

Figure 5-11a and Figure 5-11b portray the oxygen consumption vs. time plots obtained at 110°C and 125°C/155°C respectively, for the uncatalyzed and silver catalyzed leach tests performed on the Gibraltar concentrate in the absence of surfactants. Table 5-8 summarizes the leach results obtained.

At 110°C silver had a dramatic effect, increasing the leach rate, as measured by the oxygen consumption (Figure 5-11a). After 3 hours leaching, total oxygen consumption was 9.50 L for the uncatalyzed test and 14.12 L for the catalyzed test. The copper extraction was increased from 52.6% to 95.9%. Iron extraction (82.4%) and total sulfide oxidation (84.7%) were not as high as the copper extraction, indicating that pyrite in the concentrate was not oxidized to nearly the same extent. The use of silver also had the effect of increasing the overall elemental sulfur yield (from 58.3% to 76.4%) and reducing the pregnant solution free acid concentration (from 61.2 g/L to 16.7 g/L). Based on these results it was concluded that under silver catalyzed conditions at 110°C, chalcopyrite leaches primarily according to the acid-consuming, sulfur-generating reaction:

$$CuFeS_2 + 2H_2SO_4 + O_2 \rightarrow CuSO_4 + FeSO_4 + 2S^o + 2H_2O \qquad (5\text{-}9)$$

The pregnant solution contained only 4.2 mg/L Ag, indicating that most of the added silver precipitated during leaching. It would seem likely that silver precipitated as Ag_2S on the chalcopyrite mineral surfaces during leaching, by a mechanism similar to that proposed by Miller and Portillo for the silver catalyzed ferric sulfate leaching of chalcopyrite [120].

At 125°C and 155°C the results were markedly different - silver did not enhance chalcopyrite oxidation. Copper extraction (45-48%), iron extraction (51-53%), and total sulfide oxidation (51-55%) were all essentially unchanged. Examination of the oxygen consumption plots (Figure 5-11b) shows that in all cases oxygen consumption essentially levelled off prior to terminating the tests, indicative of premature stifling of the leach by liquid sulfur. The oxygen consumptions for the silver catalyzed tests were slightly lower than for the uncatalyzed tests. This can be explained by the higher elemental sulfur yields (and correspondingly lower sulfate yields) achieved in the silver catalyzed tests, which would have the effect of lowering the oxygen consumption.

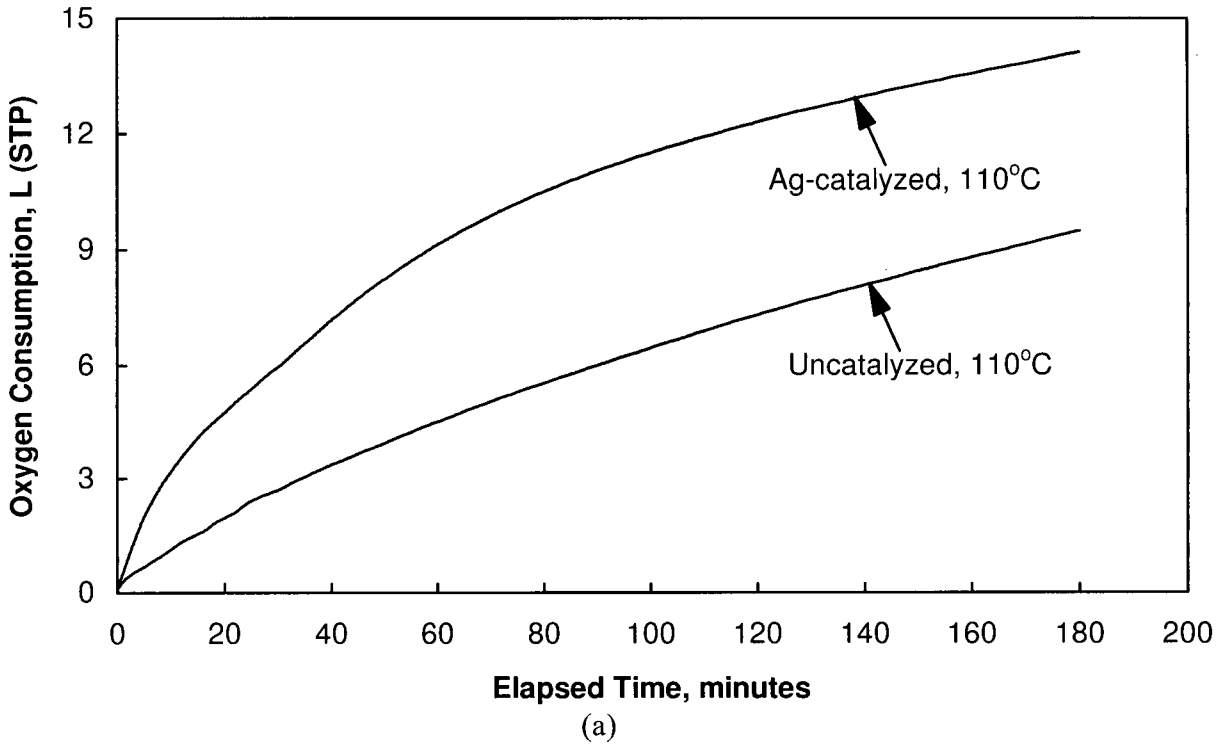

(a)

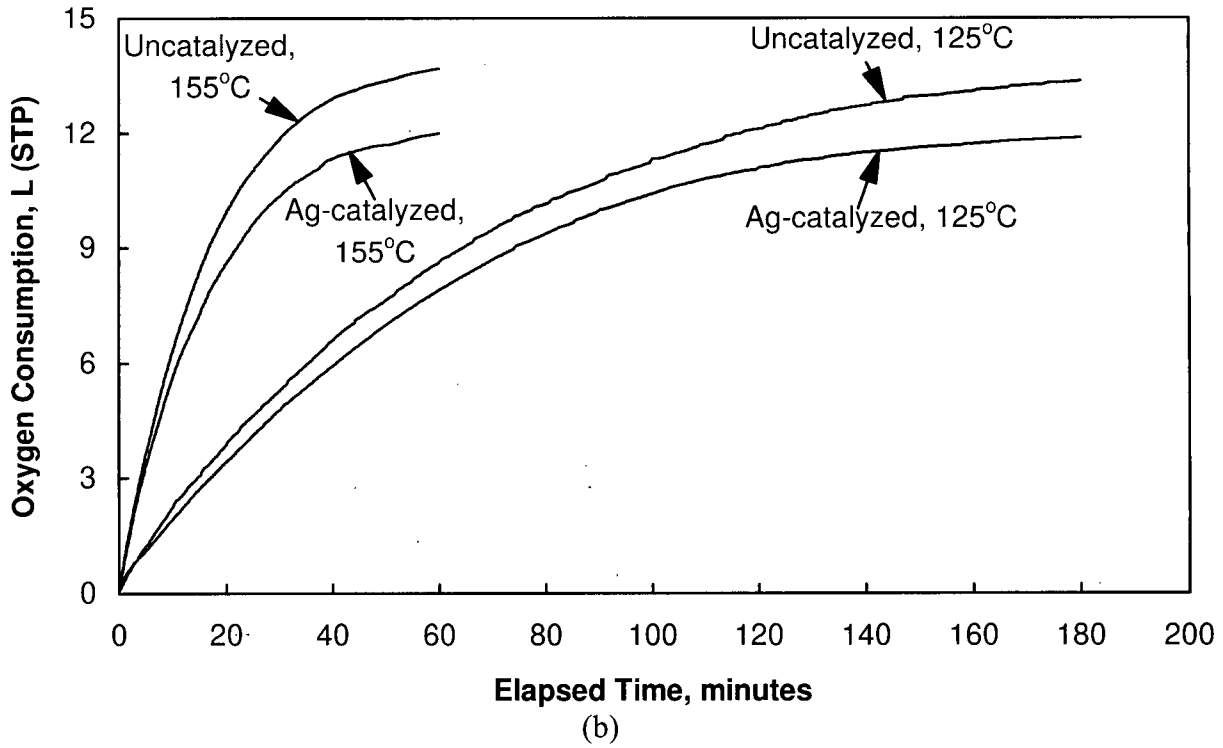

(b)

Figure 5-11. Effect of silver on oxygen consumption at (a) 110°C and (b) 125°C and 155°C, for the oxygen pressure leaching of the Gibraltar concentrate in the absence of surfactants. Test conditions: 100 g/L pulp density and 1.38 MPa oxygen pressure. The initial leach solution contained 10 g/L Cu^{2+}, 5 g/L Fe^{3+} and 98 g/L H_2SO_4. For the silver catalyzed tests, 200 mg/L Ag was added as $AgNO_3$.

Table 5-8. Effect of silver on the oxygen pressure leaching of Gibraltar concentrate in the absence of surfactants. Test conditions as for Figure 5-11.

Leach Temp. (°C)	Leach Time (h)	Ag Added ?	Cu Extr. (%)	Fe Extr. (%)	Total S^{2-} Oxid. (%)	S° Yield (%)	O_2 Cons. (L)	Pregnant Sol'n Free H_2SO_4 (g/L)	Pregnant Sol'n Ag (mg/L)
110	3	no	52.6	48.3	50.8	58.3	9.50	61.2	
110	3	yes	95.9	82.4	84.7	76.4	14.12	16.7	4.2
125	3	no	44.9	48.1	53.0	55.1	13.35	60.8	
125	3	yes	46.1	51.2	51.2	67.7	11.87	54.9	94
155	1	no	45.8	52.5	55.3	47.7	13.68	63.7	
155	1	yes	44.8	53.3	54.3	55.4	11.99	64.7	129

Interestingly, pregnant solution silver levels were much higher in the 125°C (94 mg/L Ag) and 155°C (129 mg/L) tests than in the 110°C test (4.2 mg/L). Assuming that the catalysis chemistry can be explained by equations (5-7) and (5-8), it would seem that at the higher temperatures (i.e., temperatures above the sulfur melting point) there are fewer active mineral sites for the silver ions to react with, possibly because liquid sulfur blocks the reaction sites. In contrast, at 110°C solid sulfur is formed, which obviously is not protective enough to prevent the silver ions from reacting with chalcopyrite (equation (5-7)).

Figure 5-12 compares the silver catalyzed and uncatalyzed copper extraction profiles for the $CuFeS_2$ concentrate at 110°C. As with the Gibraltar concentrate, silver increased the initial leach rate (over the first 2 hours) markedly. After 3 hours leaching, the copper extraction was improved from 51% to 79%, a significant improvement but not as high as that obtained for the Gibraltar concentrate (96%). The dissolved silver concentration for the silver catalyzed test is also plotted in Figure 5-12. Initially, the dissolved silver concentration was close to zero, presumably because the added silver precipitated quantitatively on the mineral surface as Ag_2S. However, as leaching progressed the dissolved Ag concentration increased steadily, indicating the precipitated silver was re-dissolving. After 6 hours 50% of the original amount was in solution. It would appear that as the $CuFeS_2$ surface area is depleted during leaching, there are progressively fewer available sites for the silver to precipitate according to equation (5-7), with the result that more and more silver remains in solution.

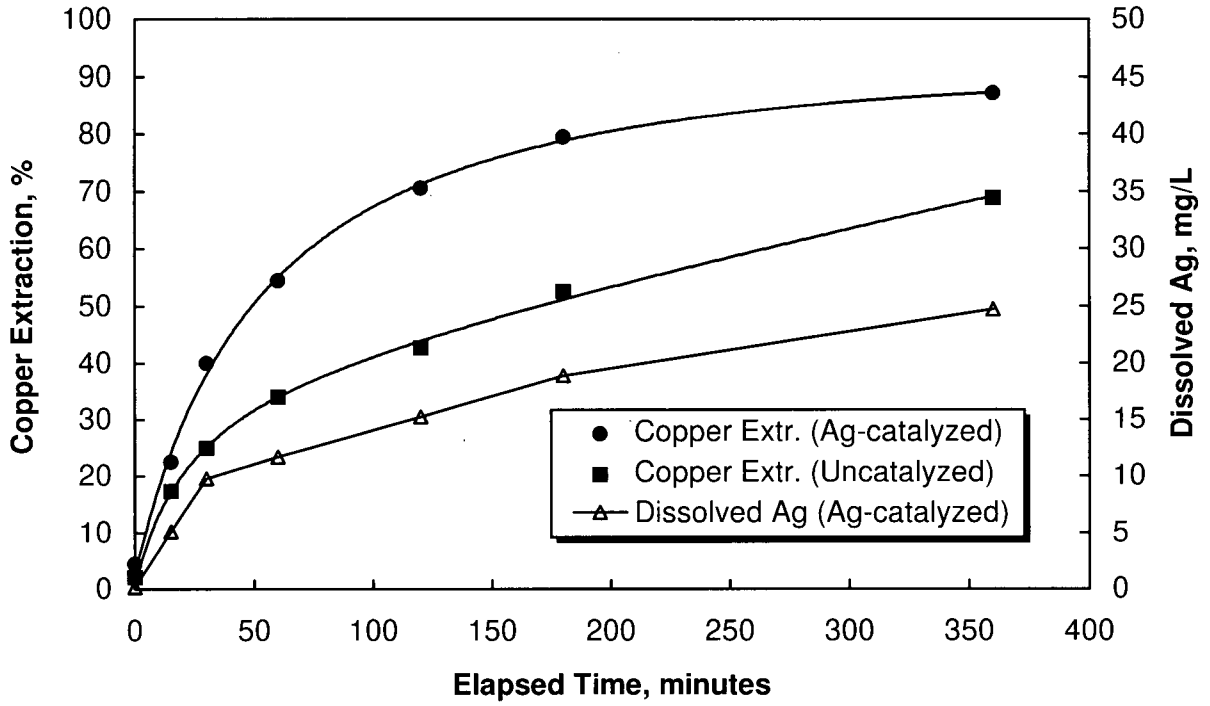

Figure 5-12. Comparison of the copper extraction profiles obtained for the silver catalyzed and uncatalyzed oxygen pressure leaching of the $CuFeS_2$ concentrate at 110°C. The dissolved Ag concentration vs. time for the silver catalyzed test is also shown. Test conditions: 10 g/L pulp density and 1.38 MPa oxygen pressure. The initial leach solution contained 1 g/L Cu^{2+}, 0.5 g/L Fe^{3+} and 98 g/L H_2SO_4. For the silver catalyzed test, 50 mg/L Ag was added as $AgNO_3$.

The results confirm that at 110°C, silver has a catalytic effect and is capable of significantly enhancing the rate and extent of chalcopyrite oxidation. However, silver is ineffective at 125°C and 155°C because the reaction kinetics at these temperatures are controlled primarily by liquid sulfur wetting the sulfides.

5.2.6.2 Effect of Silver in the Presence of Surfactants

Table 5-9 compares the results obtained when silver was used in combination with continuous surfactant addition on the Gibraltar concentrate at 125°C and 155°C. The surfactants used were calcium lignosulfonate (Lignosite 100) and OPD, at a dosage of 0.6 kg/t concentrate (0.1 kg/t was added during pre-conditioning and 0.5 kg/t was pumped in continuously during the run). Some of the previously discussed results obtained in the absence of silver or surfactant are included for comparison.

The use of silver and continuous surfactant addition resulted in enhanced oxidation of chalcopyrite at 125°C. Silver plus continuous lignosulfonate gave 74.3% copper extraction after

3 hours leaching, compared to 56.4% copper extraction obtained with lignosulfonate alone. As was noted previously (Section 5.2.6.1), silver also had the effect of increasing the elemental sulfur yield (from 59.3% to 75.6%). However, the copper extraction obtained with silver plus continuous lignosulfonate at 125°C was considerably lower than that obtained with silver alone at 110°C (95.9% Cu extraction after 3 hours leaching, see Table 5-8). Examination of the leach residues from the tests with lignosulfonate revealed that they were extensively agglomerated. It was concluded that the lignosulfonate decomposed at a faster rate than it was being added, therefore it was unable to prevent liquid sulfur from wetting and agglomerating the sulfides. A higher lignosulfonate addition rate may have kept the sulfur dispersed and yielded a higher copper extraction, at least for the silver catalyzed test.

The use of silver plus continuous OPD at 125°C gave even better results - 90.5% copper extraction and a 75.1% S° yield vs. 56.8% copper extraction and a 54.2% S° yield obtained with OPD alone. The leach residues from both tests were quite finely disseminated, indicating that sufficient surfactant was maintained in solution to prevent or minimize the tendency for liquid sulfur to wet and agglomerate the mineral particles. Dispersion of the sulfur allowed the silver ions unimpeded access to the chalcopyrite mineral surfaces, resulting in the effective depassivation of the chalcopyrite. It should be noted that the copper extraction was not quite as high as the extraction obtained at 110°C, suggesting that some sulfur wetting may still have occurred.

Table 5-9. Effect of continuous surfactant additions on the silver catalyzed oxygen pressure leaching of the Gibraltar concentrate. Test conditions: 100 g/L pulp density, 1.38 MPa oxygen pressure and 3 hour residence time. The starting leach solution contained 10 g/L Cu^{2+}, 5 g/L Fe^{3+} and 98 g/L H_2SO_4. For the silver catalyzed tests, 200 mg/L Ag was added as $AgNO_3$.

Leach Temp. (°C)	Surfactant	Ag Added ?	Cu Extr. (%)	Fe Extr. (%)	Total S^{2-} Oxid. (%)	S° Yield (%)	O_2 Cons. (L)	Pregnant Sol'n Free H_2SO_4 (g/L)	Pregnant Sol'n Ag (mg/L)
125	None	no	44.9	48.1	53.0	55.1	13.35	60.8	
125	None	yes	46.1	51.2	51.2	67.7	11.87	54.9	94
125	Lignosite 100	no	56.4	58.0	60.2	59.3	14.28	46.9	
125	Lignosite 100	yes	74.3	76.1	74.7	75.6	15.22	26.2	48
125	OPD	no	56.8	54.1	55.9	54.2	14.08	48.7	
125	OPD	yes	90.5	80.4	83.3	75.1	15.97	17.6	0.40
155	OPD	yes	62.8	64.7	67.9	59.7	15.87	45.0	13.1

When silver plus continuous OPD addition was tried at 155°C, the copper extraction was only 62.8%, considerably lower than the extraction obtained at 125°C. The leach residue was agglomerated, indicating that OPD degraded too quickly at 155°C to prevent sulfur from wetting the sulfides. Thus the stability of OPD appears to be quite temperature dependent.

5.2.7 Discussion

The results of the leaching studies have confirmed the findings of previous investigators that the oxygen pressure leaching of chalcopyrite is generally slow and incomplete. The slow leaching kinetics tend to support the notion that a surface layer forms on chalcopyrite during leaching, and that this surface layer passivates chalcopyrite. Of all the experimental techniques tried, two methods were identified which appear to overcome this passivating phenomenon: (1) leaching at temperatures of ~200°C or higher, and (2) adding silver to catalyze the leach.

In considering the results of previous investigators in conjunction with the results obtained in this study, it is hypothesized that the passivating layer may consist of one or more of the following:

1. Solid sulfur if the leach temperature is less than 119°C, or liquid sulfur if the temperature is greater than or equal to 119°C;

2. An iron oxide - type phase, Fe_xO_y, or a basic ferric sulfate-type phase, $Fe(SO_4)_x(OH)_y$

3. A $Cu_xFe_yS_2$ - type phase, where $y < x$ (indicative of preferential leaching of iron), the extreme case being a phase approaching CuS_2 in composition;

4. A $Cu_xFe_yS_2$ - type phase, where $x < y$ (indicative of preferential leaching of copper), the extreme case being a phase approaching FeS_2 in composition.

The surface studies to be discussed in subsequent sections in this chapter are concerned with identifying and characterizing this passive layer. However, at this point it is instructive to summarize the insights provided by the leach results. First, let us consider whether sulfur may be passivating chalcopyrite. The results have proven conclusively that in the temperature range where liquid sulfur is stable (~120-180°C), liquid sulfur will inhibit and prematurely stifle leaching. The use of sulfur-dispersing surfactants, a technique that is so successful in oxygen

pressure leaching of zinc concentrates, was largely ineffective for copper concentrates. The surfactants tended to rapidly decompose, which caused problems in evaluating their performance. However, even when leaching was conducted under conditions where the most stable surfactant, OPD, was sufficiently stable to disperse sulfur (short-duration runs at high pulp density or continuous surfactant addition at low pulp density), copper extraction was enhanced only marginally or not at all over the extraction obtained under identical conditions at 110°C. This lends support to the theory that a passivating mechanism unrelated to elemental sulfur formation is ultimately controlling the leaching kinetics, and that liquid sulfur only serves to mask the passivation.

At temperatures below the sulfur melting point, passivation has often been attributed to a layer of solid sulfur. The results obtained here do not support this theory. If solid sulfur was passivating chalcopyrite at 110°C, then the use of OPD under conditions where it successfully dispersed sulfur at temperatures above the sulfur melting point, should have led to a dramatically increased copper extraction. This did not happen. Solid sulfur does tend to coat the mineral surfaces but, as pointed out by Peters [17], the volume of sulfur formed on oxidizing chalcopyrite (31.0 cm^3/mol $CuFeS_2$ assuming 100% conversion of S^{2-} to S°) is considerably less than the molar volume of chalcopyrite (45.1 cm^3/mol $CuFeS_2$). Therefore, the volume shrinkage involved in going from $CuFeS_2$ to S° would be expected to produce a cracked and/or porous sulfur morphology that does not impede reactant/product diffusion to a sufficient extent to account for the extremely slow leach rates observed.

Next, let us consider whether an iron oxide - type phase, Fe_xO_y, or a basic ferric sulfate-type phase, $Fe(SO_4)_x(OH)_y$, may be passivating chalcopyrite. These phases can form due to solid state changes in the mineral structure, i.e., iron in chalcopyrite may diffuse to the surface, react with oxygen and form an iron oxide surface layer that is insoluble in the acid sulfate medium employed for leaching. Alternatively, these phases may form as a result of dissolved iron precipitating in the bulk solution and depositing on the mineral surface. Under the conditions used in this study, dissolved iron did not re-precipitate to a measurable extent until the leach temperature exceeded 170-180°C. Above 180°C, the extent of iron precipitation increased with increasing temperature. At 200°C, most (~85%) of the iron had re-precipitated to form a compound close in composition to $FeOH(SO_4)$. Despite the extensive iron precipitation, copper leached rapidly and completely at this temperature, indicating that the iron precipitate did not interfere with leaching. Thus it seems unlikely that iron compounds precipitating out of the bulk

solution could be responsible for passivating chalcopyrite. The possibility that chalcopyrite is passivated by an iron oxide-type layer formed by solid state diffusional processes, too thin to be detected by conventional chemical analysis of leach residues, cannot be ruled out at this stage, however.

Finally, let us consider the possibility that chalcopyrite is passivated by a $Cu_xFe_yS_2$ - type layer, where $y < x$ or $y > x$. Certainly, the literature on chalcopyrite electrochemistry (Section 2.4.1) and chalcopyrite surface studies (Section 2.4.2) provides support that layers of this type can form, and it seems possible that this layer, although almost certainly metastable, may be less reactive than chalcopyrite in short-term leaching experiments. If such layers do form and persist under commercial leaching conditions, they are likely to be extremely thin (< 1μm) or conventional SEM and electron microprobe studies would have identified them by now.

To summarize, of the four types of passivating surface layers hypothesized above, a thin $Cu_xFe_yS_2$ - type layer or Fe_xO_y - type layer would seem to be the most likely possibilities. In addition, given the high reactivity of chalcopyrite at elevated temperatures and under silver catalyzed conditions, it can be deduced that the passivating layer must be thermally unstable as well as reactive to silver ions. The surface characterization experiments discussed in the next section were carried out in an attempt to prove the existence of this layer and provide additional information regarding its composition.

5.3 Surface Characterization Experiments

5.3.1 Auger Electron Spectroscopy Results

5.3.1.1 Spectral Features

For the purpose of discussing the general features of the Auger spectra collected in this study, we refer to Figure 5-13, which shows an example of a typical Auger spectrum. This particular spectrum was taken from the surface of a chalcopyrite sample that had previously been leached at 110°C and 1.38 MPa oxygen pressure for 3 hours. The spectrum was taken in the derivative mode and portrays elemental peak-to-peak amplitudes vs. electron kinetic energy. The elements identified were Cu, Fe, S, C and O. Details regarding the Auger transitions, peak positions and relative sensitivity factors for these elements have been compiled in Appendix 3.

The most prominent feature of the spectrum is the extremely intense sulfur $L_3M_{2,3}M_{2,3}$ peak at 152 eV. This peak was always the strongest peak evident in the Auger spectra collected

in this study. Copper has 4 major peaks, the strongest of which is the L_3VV transition at 917 eV. Similarly iron also has 4 major peaks with the L_3VV transition at 703 eV being the most intense. In comparing the relative intensities of the Cu and Fe L_3VV peaks, it can be seen that the former peak is more intense than the latter. Since the copper and iron L_3VV transitions have almost identical sensitivity factors (see Appendix 3), it is immediately apparent that the surface of this particular sample has a higher copper concentration than iron concentration. In fact, the Cu/Fe atomic ratio was calculated to be 1.6/1, which is a significant deviation from the 1/1 ratio expected for pure $CuFeS_2$.

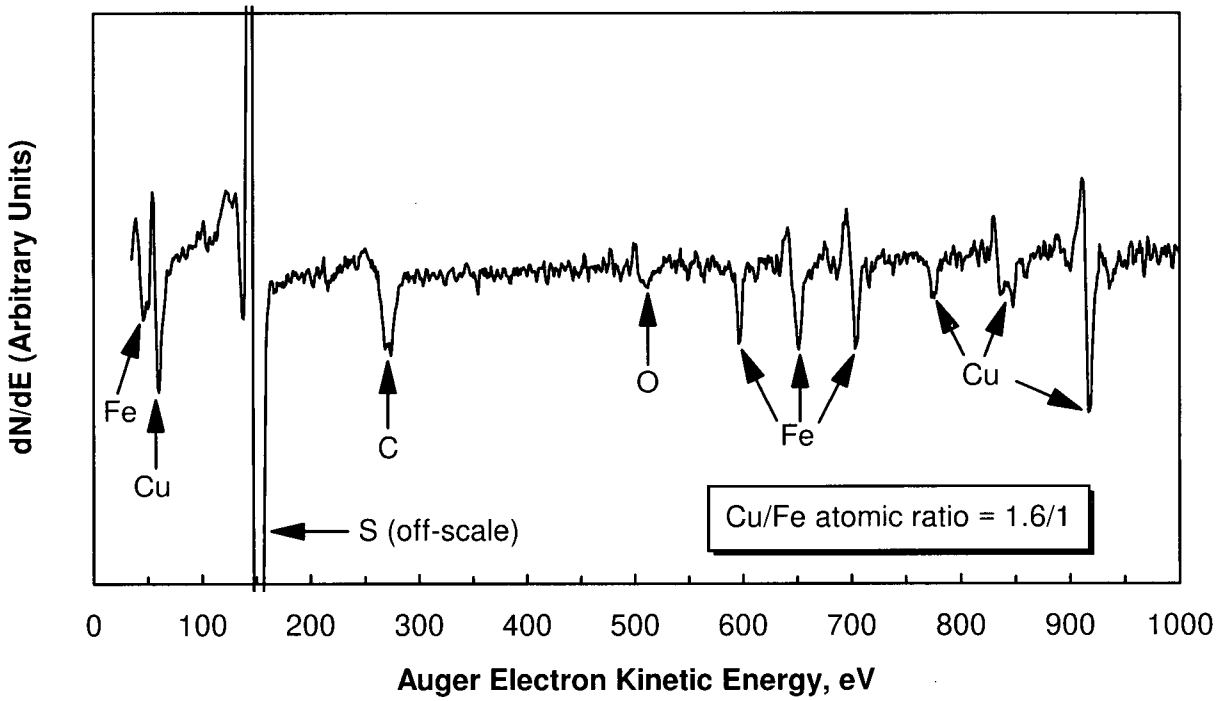

Figure 5-13. A typical Auger spectrum obtained from the surface of a $CuFeS_2$ sample leached for 3 hours at 110°C and 1.38 MPa oxygen pressure. Magnification 500x, analysis area approximately 260x360 μm. Prior to analysis the sample was sputtered lightly (for 5 seconds) to reduce the carbon contamination.

Oxygen has one major peak, the $KL_{2,3}L_{2,3}$ transition at about 510 eV, barely discernible in this instance because of its low concentration. Samples were always found to be contaminated with carbon (the $KL_{2,3}L_{2,3}$ transition at 269 eV) due to its pervasive presence in most atmospheres and its tendency to strongly adsorb onto surfaces. The carbon contamination was quite superficial (perhaps only one monolayer) but it was a nuisance because it tended to reduce the intensities of the Cu and Fe peaks. Hence the sample surfaces were usually "cleaned" prior

to analysis by lightly sputtering the surface. The spectrum depicted in Figure 5-13 was obtained after sputtering the surface for 5 seconds. In this particular example, the carbon peak is still fairly prominent. An additional 5 seconds sputtering virtually eliminated the carbon peak (spectrum not shown).

5.3.1.2 Surface Composition Results

Table 5-10 summarizes the results of Auger analyses performed on a fracture surface of unleached chalcopyrite and $CuFeS_2$ fracture surfaces leached at 110°C, 155°C and 200°C. Prior to analysis the surfaces were sputtered lightly, for 5-10 seconds, to remove adsorbed carbon. The elemental analyses (Cu, Fe, S, O and C) were expressed in terms of atomic percentages, with the sum of the percentages normalized to 100%.

The unleached sample had a surface composition closely resembling pure chalcopyrite; this was taken to indicate that the Auger analysis procedure and the elemental sensitivity factors used (Appendix 3) were reasonably reliable. The surface contained a small amount of oxygen (1.3%), probably because the sample was exposed to air for about 1 minute during transfer to the instrument's sample chamber (refer to Section 4.3.1 for the sample preparation details).

The leached samples all had surface compositions deviating considerably from $CuFeS_2$. The most notable change was a significantly lowered iron concentration and a slightly elevated copper concentration, resulting in the surfaces having a Cu/Fe atomic ratio of 1.6/1-1.7/1. The leach temperature appeared to have little effect on the results as there were only slight differences in Cu, Fe and S concentrations regardless of the temperature employed. The S/(Cu+Fe) ratios were marginally elevated at 1.1/1-1.3/1. Oxygen concentrations were low (2.3-3.4 at.%), indicating that possible iron hydrolysis products such as ferric hydroxide, hematite or basic ferric sulfate were not present to a significant extent on any of the leached surfaces.

The Auger results demonstrated quite conclusively that an iron-deficient sulfide phase forms on the surface of chalcopyrite during oxygen pressure leaching. The presence of this phase indicates that iron leaches preferentially to copper. It seems reasonable to presume that this altered phase may be responsible for the passivation of chalcopyrite during leaching. Additional information regarding the composition of the surface layer was obtained by XPS (Section 5.3.2).

Table 5-10. Auger analysis of the surface compositions of chalcopyrite samples leached at different temperatures. Prior to analysis the surfaces were sputtered for 5-10 seconds to clean the surfaces of adsorbed carbon.

Parameters	Sample 1	Sample 2	Sample 3	Sample 4
Leach Conditions:				
Temperature (°C)	Unleached	110	155	200
Oxygen Pressure (MPa)		1.38	1.38	0.69
Residence Time (h)		3	3	0.25
Analysis Area, mm^2	0.01	0.09	0.09	0.09
Surface Composition: (Normalized Atomic %)				
Cu	24.9	27.2	29.1	26.3
Fe	24.8	16.9	16.9	16.7
S	49.0	53.6	51.4	53.6
O	1.3	2.3	2.6	3.4
Atomic Ratio:				
Cu/Fe	1.0	1.6	1.7	1.6
S/Cu	2.0	2.0	1.8	2.0
S/Fe	2.0	3.2	3.1	3.2
S/(Cu+Fe)	1.0	1.2	1.1	1.3
O/(Cu+Fe)	0.03	0.05	0.06	0.08

5.3.1.3 Sputter Depth Profiling Results

Figure 5-14 gives an example of a typical AES sputter depth profile obtained by sequentially sputtering and analyzing the sputtered surface. The sample in this case was a $CuFeS_2$ fracture surface that had previously been leached at 200°C and 0.69 MPa oxygen pressure for 15 minutes. The sputter time interval was 50 seconds. After each sputter interval, the surface was analyzed for S, Fe, Cu, C and O (Figure 5-14a) and the S/(Cu+Fe) and Cu/Fe atomic ratios were calculated (Figure 5-14b). The sputter rate was not calibrated in terms of penetration depth per unit time, therefore only the variation in composition with total sputter time is given.

The original unsputtered surface contained (in atomic percentages) 39.0% S, 15.7% Fe, 26.5% Cu, 16.7% C and 2.1% O; the S/(Cu+Fe) and Cu/Fe atomic ratios were 0.9/1 and 1.7/1 respectively. As the surface was sputtered, the S and Fe concentrations increased whereas the Cu, C and O concentrations decreased. With prolonged sputtering, it was expected that the surface layer would be removed entirely and that the composition would stabilize and approach that of the bulk $CuFeS_2$, i.e., 25% Cu, 25% Fe and 50% S, giving S/(Cu+Fe) and Cu/Fe atomic

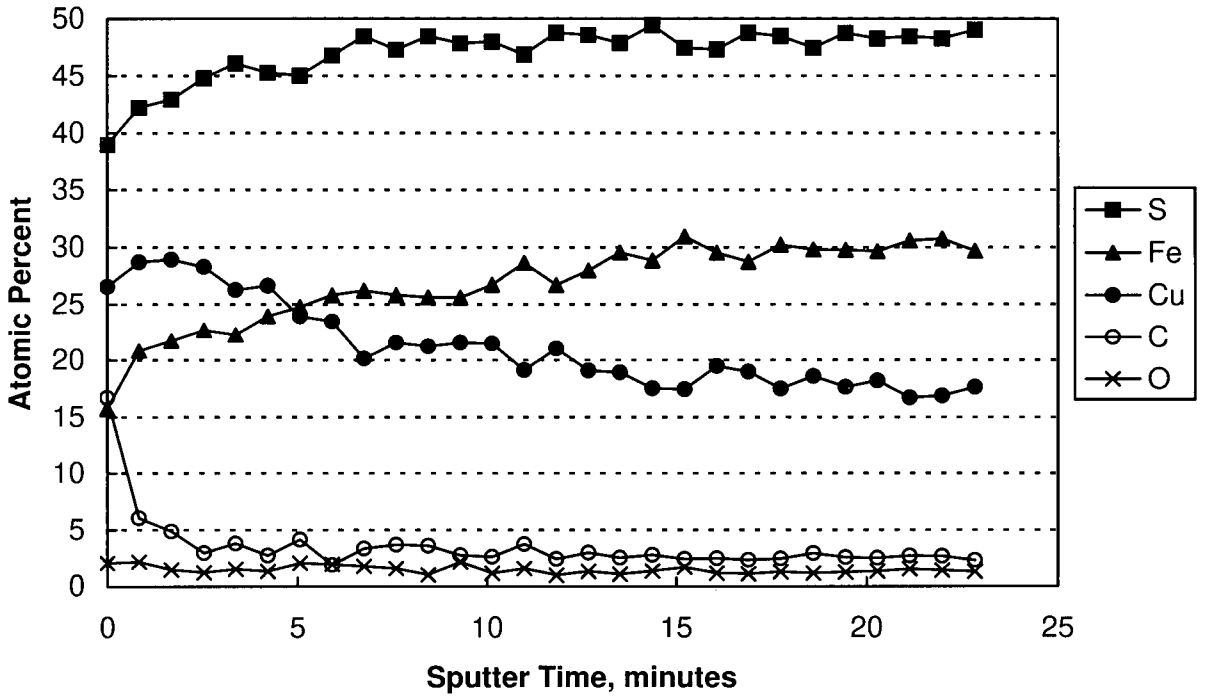

(a)

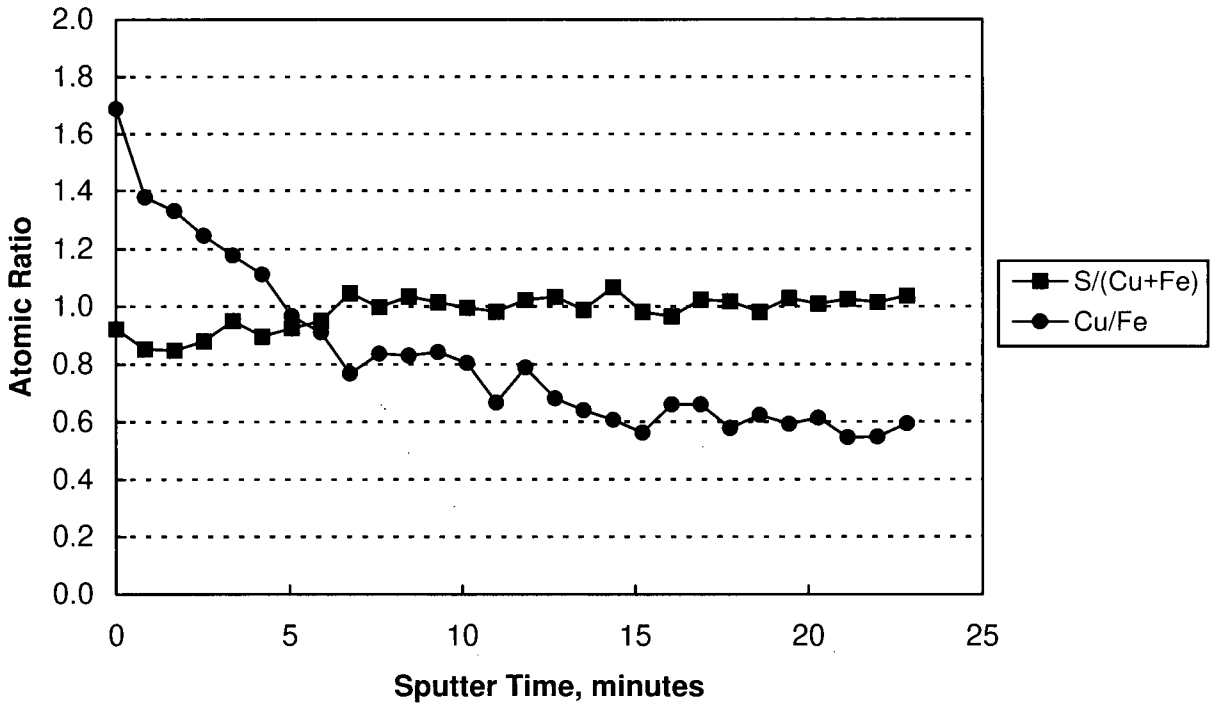

(b)

Figure 5-14. Compositional depth profile of a $CuFeS_2$ sample surface leached at 200°C and 0.69 MPa O_2 pressure for 15 minutes, showing: (a) relative atomic percentages of S, Fe, Cu, C, O and (b) S/(Cu+Fe) and Cu/Fe atomic ratios vs. sputter time. The sample was alternately sputtered for 50 seconds and analyzed.

ratios of 1/1. This was not the case. The copper concentration declined continuously to reach 17.6% after 23 minutes sputtering. The iron concentration increased steadily and reached 29.7%, giving a Cu/Fe atomic ratio of 0.6/1 rather than the expected 1/1, after 23 minutes sputtering. However, the sulfur concentration and the S/(Cu+Fe) atomic ratio did approach the expected values of 50% and 1/1 respectively. Figure 5-15 shows the Auger spectra obtained for the surfaces before and after sputtering respectively. The decline in copper peak intensities and the increase in iron peak intensities as a result of sputtering are readily apparent.

The decline in copper concentration to values well below those expected for $CuFeS_2$ is thought to be caused by a sputtering-induced artifact - preferential sputtering of the copper atoms. Preferential sputtering is a well known phenomenon frequently observed during the sputtering of multi-component surfaces [162], although it has not previously been reported for copper in chalcopyrite. The two main mechanisms which lead to preferential sputtering are mass difference effects and surface binding effects. An example of the former mechanism is the sputtering of metal oxides, where oxygen tends to sputter preferentially because of its lighter mass [190]. An example of the latter mechanism is the sputtering of copper-nickel alloys [191], where the preferential sputtering of copper has been ascribed to its lower surface binding energy [190]. Seah has provided estimates of pure element sputtering yields for most of the metals in the periodic table [192]. With 1 keV argon ions the Cu and Fe sputtering yields are about 2.6 and 2.0 atoms/argon ion respectively. The preferential sputtering of copper over iron would lead to a progressive enrichment in surface iron concentration, which would explain why, on prolonged sputtering, the iron concentration exceeded the 25 atomic percent expected for pure $CuFeS_2$. Another possibility to consider is that sulfur may also sputter preferentially, given its much lower atomic mass (32.06) in relation to copper (63.54) and iron (55.85). Preferential sputtering of sulfur over iron has been observed for pyrite [193], but not for pyrrhotite [194].

Preferential copper sputtering was observed time and again during the sputtering of unleached and leached $CuFeS_2$ samples. Therefore, it was concluded that sputtering was not a practical means of obtaining depth profile information, nor was it suitable for estimating the thickness of the surface layer. However, electron probe microanalysis (EPMA) of leached samples revealed unaltered chalcopyrite, confirming that: (1) the compositional changes identified by AES are indeed a surface phenomenon and (2) the surface layers are probably less than ~1 μm thick (based on the assumption that the depth resolution limit of EPMA for $CuFeS_2$ is ~ 1μm).

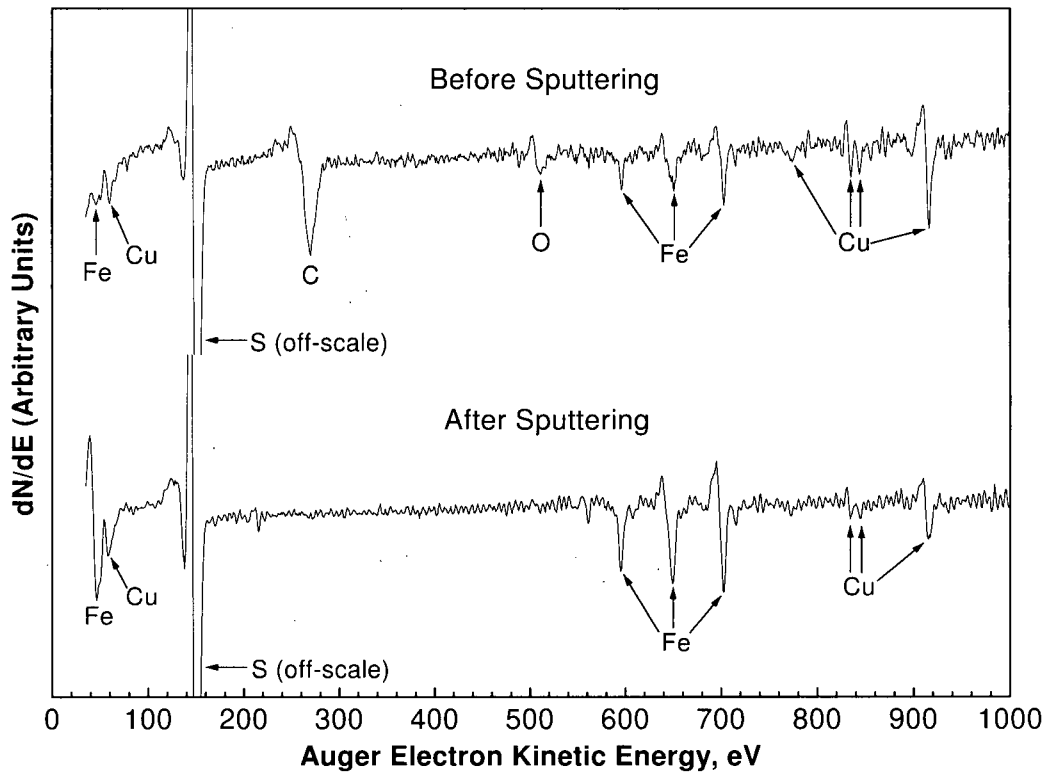

Figure 5-15. Auger electron spectra obtained for the leached chalcopyrite surface before and after sputtering for 23 minutes.

5.3.2 X-ray Photoelectron Spectroscopy Results

5.3.2.1 General Features of Broad-Scan Spectra

Broad-scan photoelectron spectra were used primarily to identify the major elements present on chalcopyrite surfaces. Figure 5-16 compares the broad-scan spectra obtained from the surfaces of unleached chalcopyrite and chalcopyrite leached at 110°C and 1.38 MPa oxygen pressure for 3 hours. By convention, the x-axis portrays the electron binding energy increasing from right to left, rather than the reverse. Assigning the major peaks to their respective elements proved to be relatively straightforward. As can be seen, most of the peaks were assigned to Cu, Fe, S, O and C. The spectra display photoelectron emission peaks as well as X-ray-excited Auger peaks for O, Cu and Fe (the multiple *KLL* and *LMM* transitions). Notable features include the spin-orbit splitting of the Cu *2p* peak, which produces a widely-spaced doublet (the $2p_{1/2}$ and $2p_{3/2}$ components). The splitting of the Fe *2p* peak is also evident in broad-scan spectra.

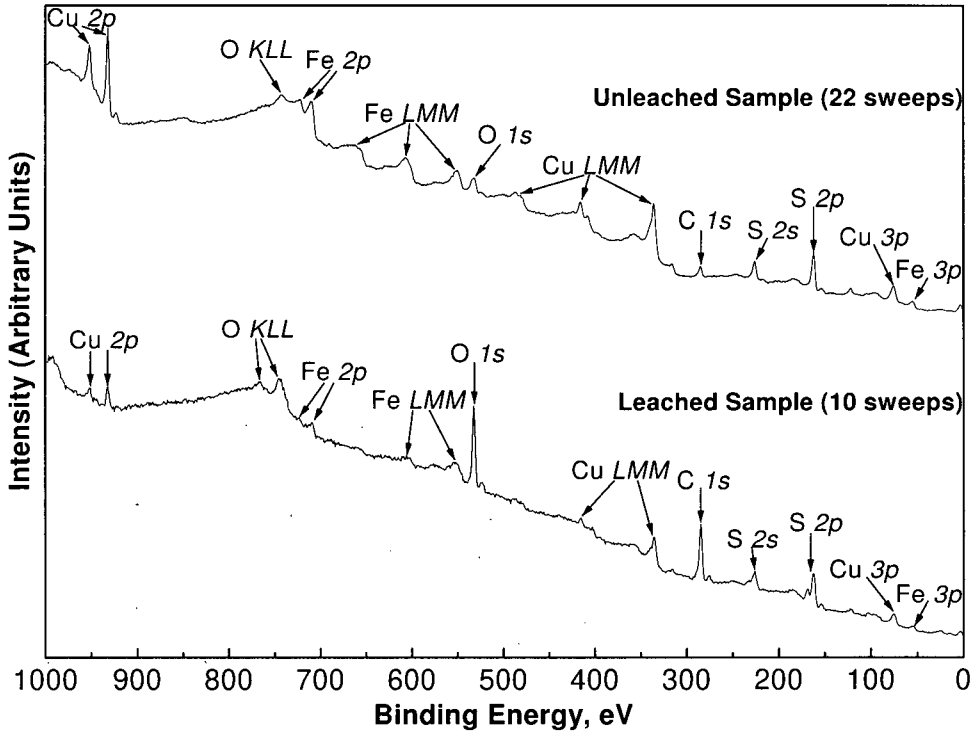

Figure 5-16. Comparison of broad-scan photoelectron spectra obtained from the surfaces of unleached chalcopyrite and chalcopyrite leached at 110°C and 1.38 MPa oxygen pressure for three hours. The unleached sample surface was exposed to air for approximately 1 minute and already shows evidence of contamination by atmospheric oxygen and carbon.

Some general qualitative observations can be made regarding the broad-scan spectra. The spectra for the unleached and leached sample surfaces appear to be virtually identical, with the following exceptions. First, the leached sample surface contained considerably more carbon and oxygen than the unleached sample surface. The unleached sample surface contained some oxygen and carbon, presumably as a result of having been exposed to air for about one minute during transfer to the spectrometer. The second major difference between the two spectra is that most of the peaks for the unleached sample surface are more intense than the peaks for the leached sample surface (except for the O *1s* and C *1s* peaks). There are two reasons for this: (1) the photoelectron collection time happened to be longer for the unleached sample (22 sweeps vs. 10 sweeps for the leached sample) and (2) the leached sample surface contained considerably more oxygen and carbon, which lowered the relative concentrations of the other elements, reducing their peak intensities.

Another notable difference between the two spectra is the S *2p* peak for the leached sample surface is broader and split into two, clearly indicating the presence of at least two, and possibly more, sulfur species. A detailed analysis of the chemical information that can be derived from the S *2p* peak is given in the next section.

5.3.2.2 Narrow-Scan Spectra

Narrow-scan photoelectron spectra of selected peaks were collected to provide chemical state information. In the following discussion the information derived from the Cu *2p*, Fe *2p*, S *2p* and O *1s* peaks are compared for the unleached chalcopyrite sample surface (1-minute air-exposed) and the $CuFeS_2$ surface leached at 110°C and 1.38 MPa oxygen for 3 hours. Peak assignments were made by consulting binding energy values for a number of reference compounds and species forming potential components of oxidized chalcopyrite surfaces (Appendix 4).

Cu *2p* Spectra

Figure 5-17 compares the Cu *2p* spectra for the unleached and leached $CuFeS_2$ sample surfaces. The spectra are virtually identical; each shows a sharply defined doublet separated by 20.0 eV with a Cu $2p_{3/2}$ binding energy of 932.0 eV. This value is characteristic for copper compounds containing univalent copper and indicates that copper remained bonded to sulfur as Cu (I). Peaks characteristic for Cu(II) species, which are identified by: (1) a Cu $2p_{3/2}$ binding energy 2-3 eV higher than the Cu(I) species, and (2) prominent shake-up satellite peaks [164], are clearly missing in both spectra. The lack of Cu(II) on the surface of the unleached sample shows that brief air exposure did not cause any detectable copper oxidation. The lack of Cu(II) on the surface of the leached sample indicates that the oxidized copper was completely soluble during leaching.

It is not possible to positively identify the surface Cu(I) species solely from the Cu *2p* peak positions, but at this point the possibilities can be narrowed down to include copper sulfides or mixed iron-copper sulfides containing univalent copper. An obvious possibility is unaltered chalcopyrite, which has the electronic structure $Cu^{+}Fe^{3+}(S^{2-})_2$ [22]. However, for the leached sample surface at least, this is inconsistent with the Auger evidence (Section 5.3.1.2), from which it was determined that the chalcopyrite surface is iron-deficient. Other possibilities include the sulfides that are thermodynamically predicted to form when chalcopyrite is oxidized, including bornite (Cu_5FeS_4), chalcocite (Cu_2S) and covellite (CuS). On the basis of their Cu *2p*

photoelectron spectra, Nakai *et al.* concluded these sulfides all contain univalent copper [23][2], and all have Cu $2p_{3/2}$ binding energy values (see Appendix 4) close to the value obtained here. However, these sulfides are all known to be much more reactive than chalcopyrite under the leach conditions used in this study [57]. This was experimentally confirmed to be the case with covellite (the results are discussed in Section 6.6). Thus it is hard to imagine how they could be present on the surface of leached chalcopyrite.

This leads us to consider the possibility that the surface sulfide phase is a metastable alteration product of chalcopyrite in which copper retains its univalent state. More definitive information on the composition of this phase was obtained from the S *2p* spectra, to be discussed subsequently.

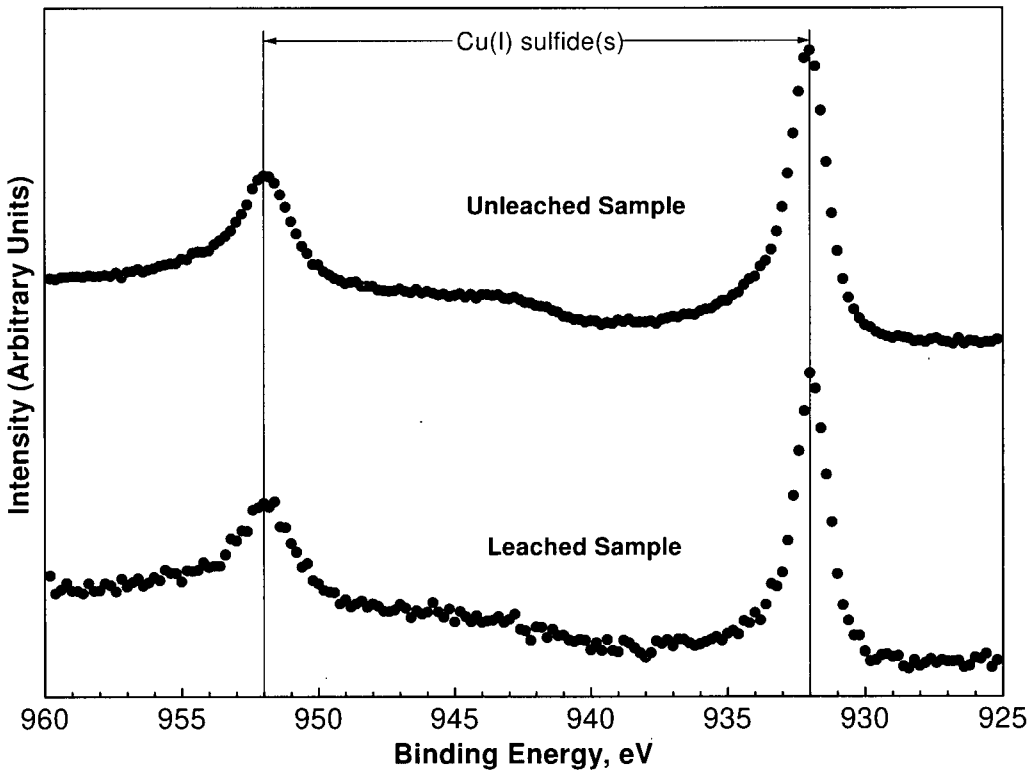

Figure 5-17. Comparison of the narrow-scan Cu *2p* photoelectron spectra for the unleached (1-minute air-exposed) and leached (110°C, 1.38 MPa O_2, 3 hours) chalcopyrite sample surfaces.

[2]Their assignment of Cu(I) to covellite is probably an over-simplification. Formal oxidation states do not appear to be assignable to the copper and sulfur atoms in covellite due to its complex structure and properties.

Fe *2p* Spectra

Figure 5-18 compares the Fe *2p* spectra for the unleached and leached samples and shows the binding energy values for several iron-containing compounds that are possible oxidation products. Interpretation of the spectra is complicated by multiplet splitting (see Section 3.4.3.3 for a discussion of multiplet splitting), which tends to broaden the peaks, hence their deconvolution was not attempted.

The Fe $2p_{3/2}$ peak for the unleached sample surface is considerably broader than for the leached sample surface. This was interpreted as indicating that more than one iron species was present on the unleached surface. In addition to unaltered $CuFeS_2$ it appears that Fe_3O_4 is the most likely species present. Note that Fe_3O_4 has two peaks, one at 708.3 eV due to the Fe^{2+} component and one at 710.6 eV due to the Fe^{3+} component. Thus, even brief exposure of fresh chalcopyrite to air caused some oxidation of the iron component.

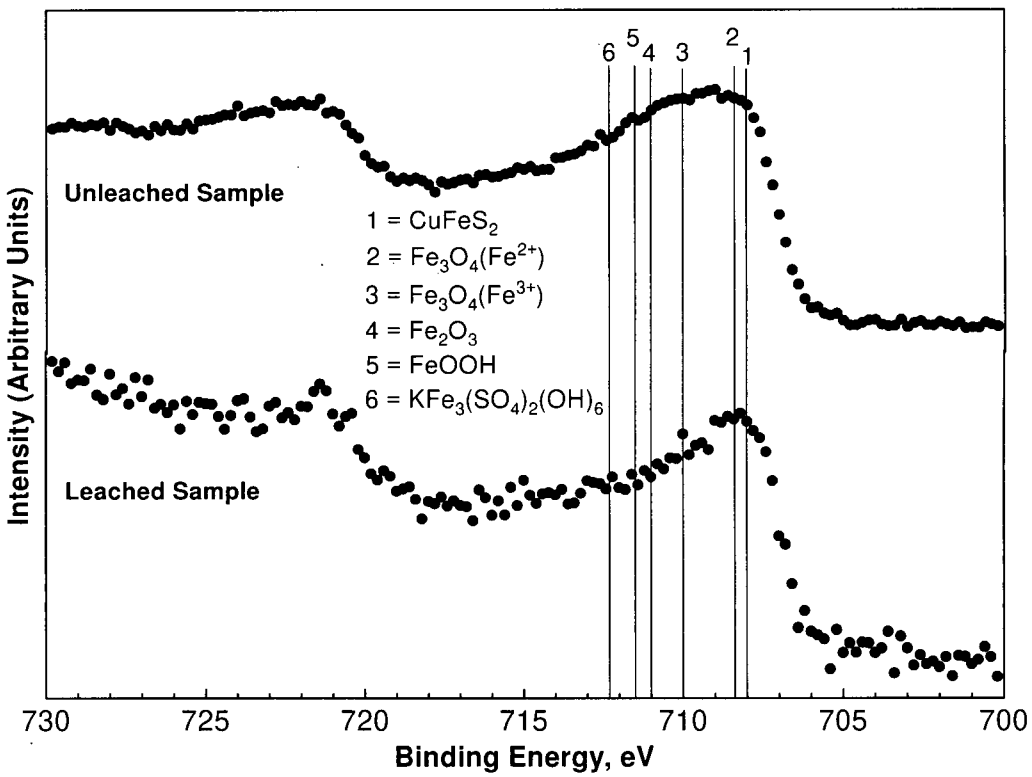

Figure 5-18. Comparison of the narrow-scan Fe *2p* photoelectron spectra for the unleached (1-minute air-exposed) and leached (110°C, 1.38 MPa O_2, 3 hours) chalcopyrite sample surfaces.

The Fe $2p_{3/2}$ peak for the leached sample surface is narrower and the $CuFeS_2$ component is clearly more intense than the oxide component. This indicates that the leached sample surface has less iron oxide than the unleached sample, probably because the leached iron remained soluble in the acidic medium used.

S *2p* Spectra

The most important chemical state information was derived from the S *2p* spectra. Figure 5-19 compares the S *2p* spectra for the unleached and leached sample surfaces and shows the expected binding energy ranges for the different sulfur valence states. As the sulfur becomes more electro-positive, the binding energy increases, as expected.

Comparison of the two spectra indicates one major difference - the leached sample surface displays a prominent peak assigned to sulfate, whereas the unleached sample surface contained no detectable sulfate. The sulfate cannot be attributed to a basic ferric sulfate-type compound, as such a compound would have been clearly evident in the Fe *2p* spectrum. Similarly the sulfate is not a copper-containing sulfate or the Cu *2p* spectrum would have

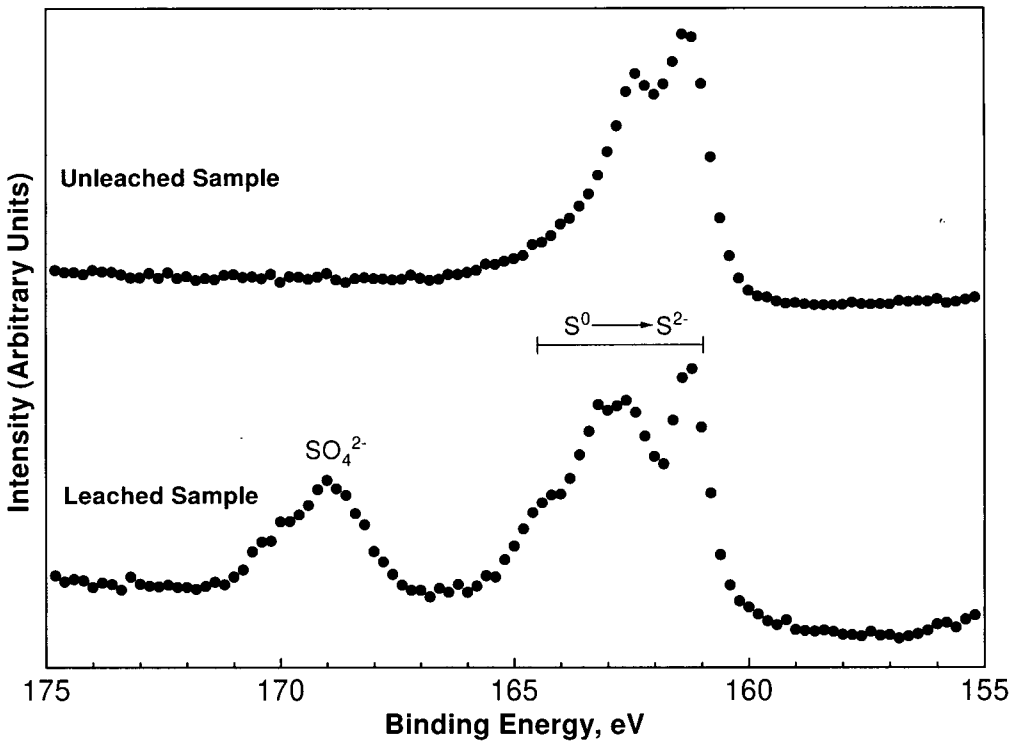

Figure 5-19. Comparison of the S *2p* photoelectron spectra for the unleached (1-minute air-exposed) and leached (110°C, 1.38 MPa O_2, 3 hours) chalcopyrite sample surfaces.

showed evidence of Cu^{2+} (a Cu(I) sulfate is not considered likely as Cu^{+} is not stable in sulfate media). As no other cationic counter-ions were present during leaching which could precipitate sulfate on the surface of chalcopyrite, it was concluded that the leached sample surface likely contained physically adsorbed sulfate ions.

The S *2p* peak in the 160-165 eV range is extremely broad for both the unleached and leached sample surfaces, indicating the presence of several different sulfur species with oxidation states varying from 0 to -2. The peaks were fitted using the following fit parameters:

Doublet spacing: S $2p_{3/2}$ - S $2p_{1/2}$ = 1.18 eV

Doublet area ratio: S $2p_{3/2}$/S $2p_{1/2}$ = 2.0

Peak full width at half maximum height (FWHM) = 1.1 eV

Figure 5-20 compares the fitted S *2p* peaks for the unleached and leached sample surfaces. It can be seen that excellent fits were obtained with four doublets which fall within the binding energy ranges expected for monosulfide (S^{2-}), disulfide (S_2^{2-}), polysulfide (S_n^{2-}, n > 2) and elemental sulfur (S°) species (see Appendix 4 for the reference values). The peaks for disulfide could also be attributable to an iron-deficient sulfide, as proposed by Buckley and Woods [97]. Table 5-11 lists the estimated relative amounts of the sulfur species for the two samples, determined from the doublet peak areas. The unleached sample surface contained primarily monosulfide (68%), with lesser amounts of disulfide (18%) and polysulfide (10%) and a small amount of S° (4%). The leached sample surface had less monosulfide (54%) and disulfide (8%) but much more polysulfide (35%) and minimal S° (3%). The monosulfide is assigned to unaltered $CuFeS_2$. The disulfide and the polysulfide are thought to be chalcopyrite oxidation products. The significance of these results is discussed in detail in Section 5.3.3.

The amount of elemental sulfur on the leached sample surface was unexpectedly low, suggesting that either: (1) the sulfur detached from the mineral surface during leaching or (2) the sulfur was volatilized in the ultra-high vacuum sample chamber. The latter possibility is considered to be more likely because sulfur is known to rapidly volatilize under ultra-high vacuum at room temperature [96].

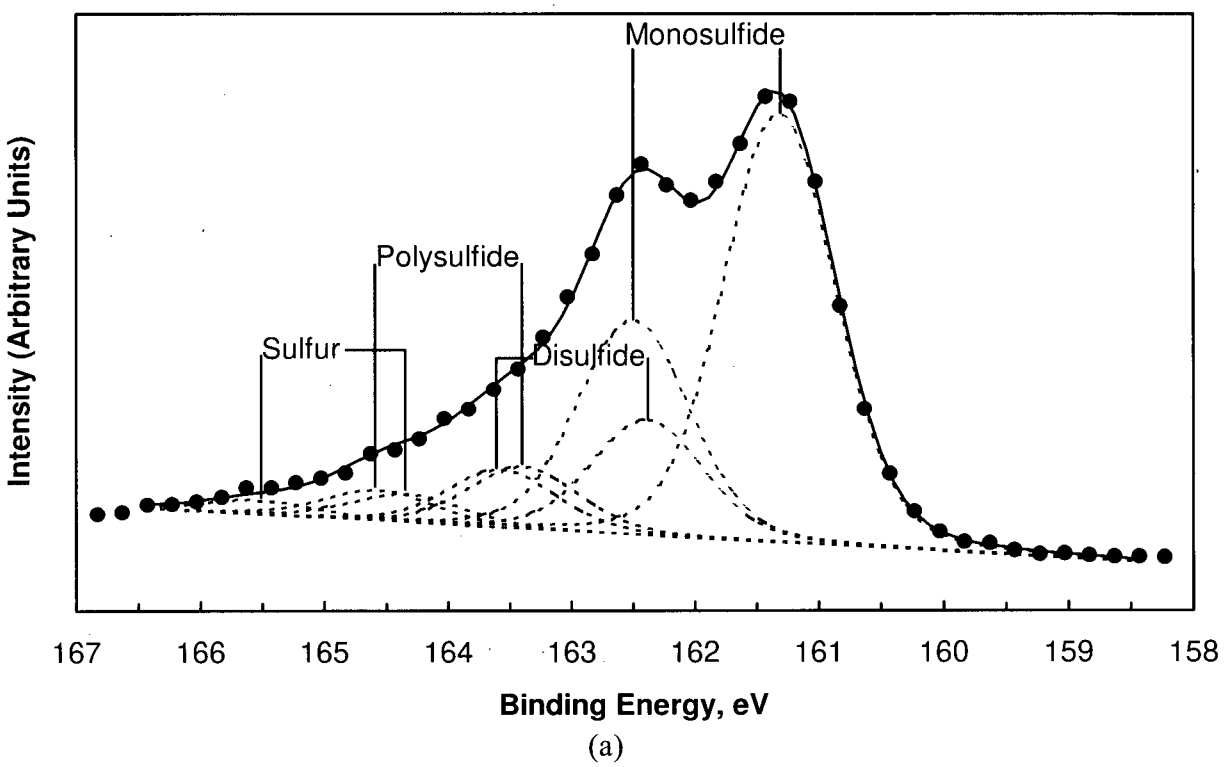

(a)

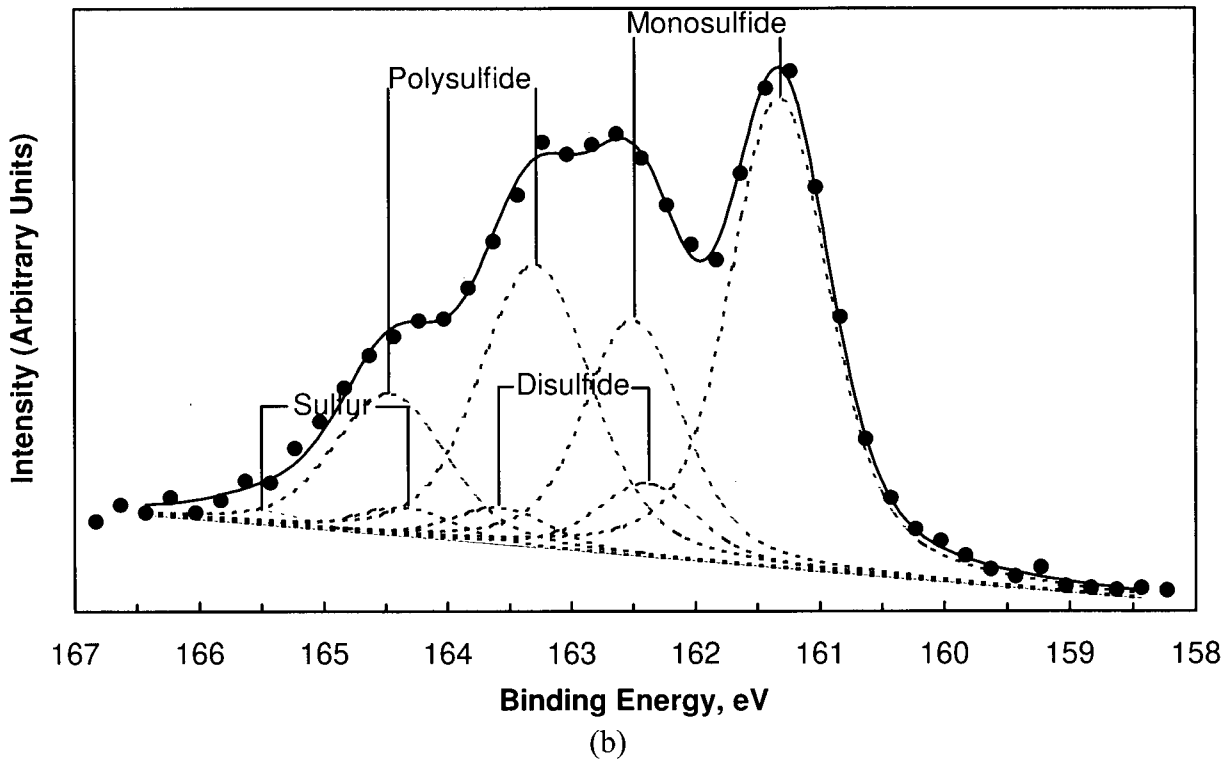

(b)

Figure 5-20. Comparison of the fitted S *2p* photoelectron spectra for: (a) the unleached (1-minute air-exposed) and (b) the leached (110°C, 1.38 MPa O_2, 3 hours) chalcopyrite sample surfaces. The solid symbols are the actual data, the dotted lines are the fitted components and the solid line represents the sum of the fitted components.

Table 5-11. Summary of the relative proportions of the different sulfur species present on the surfaces of the unleached (1-minute air-exposed) and leached (110°C, 1.38 MPa O_2, 3 hours) chalcopyrite sample surfaces.

Sulfur Species	Unleached Sample Surface	Leached Sample Surface
Monosulfide		
S $2p_{3/2}$ peak centre, eV	161.3	161.3
Relative amount present, %	68	54
Disulfide		
S $2p_{3/2}$ peak centre, eV	162.4	162.4
Relative amount present, %	18	8
Polysulfide		
S $2p_{3/2}$ peak centre, eV	163.4	163.3
Relative amount present, %	10	35
Elemental sulfur		
S $2p_{3/2}$ peak centre, eV	164.3	164.3
Relative amount present, %	4	3

O *1s* Spectrum

Figure 5-21 shows the fitted O *1s* spectrum for the leached chalcopyrite sample surface. (The O *1s* peak for the unleached sample surface is not shown as it was too weak to interpret). The spectrum was fitted with two peaks, assigned to SO_4^{2-} (531.9 eV) and H_2O (533.2 eV). As mentioned previously, sulfate was concluded to be physically adsorbed on the surface due to the lack of evidence for any metallic sulfate compounds (from the Cu *2p* and Fe *2p* spectra). Similarly, the H_2O is believed to be physically adsorbed water. The relative proportions of oxygen associated with SO_4^{2-} and H_2O were 65% and 35% respectively. Notably absent from the O *1s* spectrum are peaks for any iron precipitates such as basic ferric sulfate or iron oxide. This is consistent with the Fe *2p* spectrum which also indicated a lack of these types of compounds.

The presence of a significant amount of oxygen, the majority of which is associated with sulfate, is in contrast to the Auger results, which indicated minimal oxygen on the surface of leached chalcopyrite. This apparent contradiction can be explained by recalling that the Auger samples were all sputtered for 5-10 seconds prior to analysis, whereas the XPS samples were not. The sputtering may have removed most of the sulfate if it was only superficially adsorbed on the surface, just as brief sputtering is quite efficient at removing adsorbed carbon and oxygen. Evidence in support of this possibility was obtained when a leached sample surface that had previously been subjected to AES analysis was subsequently analyzed by XPS. In this

case the S 2p spectrum showed only a slight trace of sulfate (spectrum not shown). The brief sputtering may also have removed much of the adsorbed H_2O.

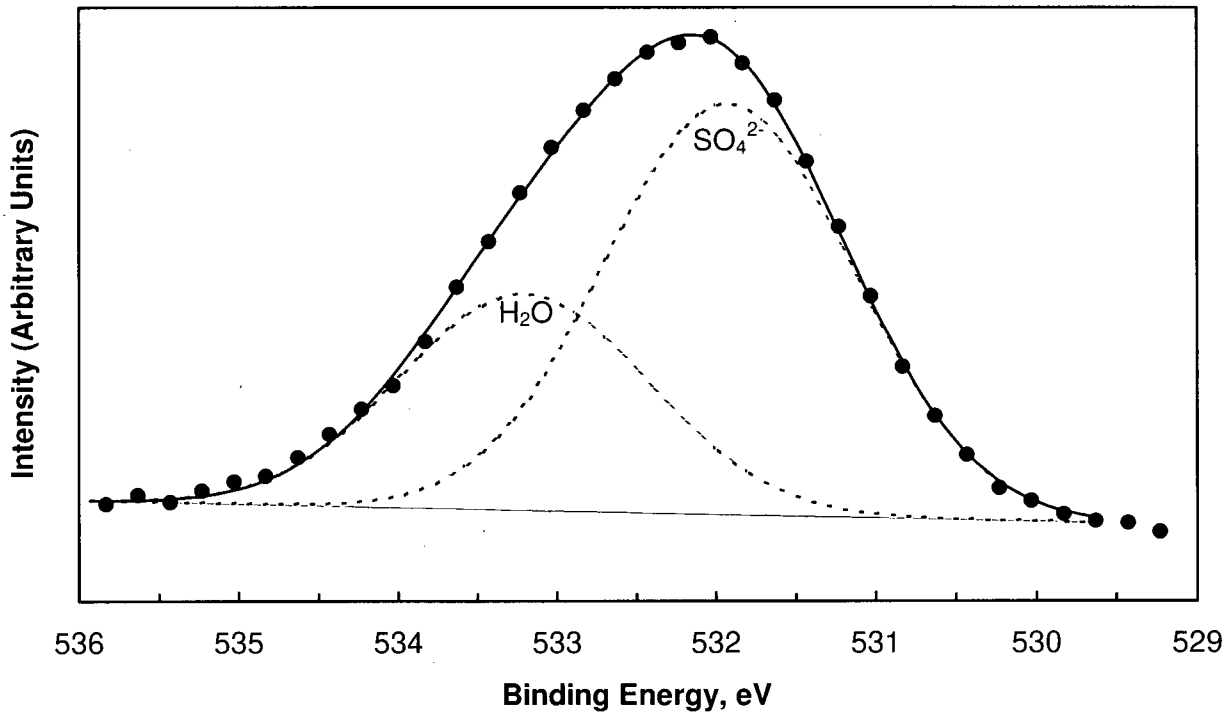

Figure 5-21. The fitted O 1s photoelectron spectrum for the leached (110°C, 1.38 MPa O_2, 3 hours) chalcopyrite sample surface.

5.3.3 Discussion

The AES and XPS studies have shown that oxidized chalcopyrite has a surface composition considerably different from that of the bulk. AES was used to provide quantitative information with respect to the relative proportions of the major elements (Cu, Fe, S, O) present on the surface. XPS complemented AES in that the former was used to provide chemical state information on the surface phases.

5.3.3.1 Significance of the AES Results

The AES results indicated that oxygen pressure leached chalcopyrite had a surface Cu/Fe atomic ratio of 1.6-1.7/1. This showed that the surface was severely depleted in iron compared to the bulk. The leached surface contained minimal oxygen, therefore the surface was relatively free of potential iron oxidation products such as basic ferric sulfate or iron oxide. From this it was inferred that iron dissolved preferentially to copper to form an iron-deficient

sulfide layer on the chalcopyrite mineral surface. This conclusion is in general agreement with the results of previous surface studies conducted on chalcopyrite subjected to other oxidative treatments (see Section 2.4.2).

The surface Cu/Fe atomic ratio was fairly constant regardless of the leach temperature (110°C, 155°C, 200°C) employed. To conclude that the surface composition is insensitive to leach temperature may be erroneous, however, as the surfaces were not analyzed *in situ*. The leach tests were terminated by cooling the autoclave contents to 25-35°C, a procedure that took approximately 5 minutes. It is possible that the surface composition changed on cooling or during the 24-hour period before the surface was analyzed. If so, the surface analyses may not accurately reflect the actual surface composition during leaching. On the other hand, if a passive surface layer forms during leaching, it is considerably less reactive than the underlying chalcopyrite, and a reduction in temperature (on cooling) should only enhance its stability. Thus it seems more likely that cooling would "freeze" the surface composition. Ideally, an *in situ* method of surface analysis is necessary to provide definitive information on the effect of leach temperature on the chalcopyrite surface composition.

5.3.3.2 Significance of the XPS Results

The most important chemical information from the XPS studies was derived from the S *2p* spectra. The S *2p* peaks were extremely broad, indicating the presence of multiple sulfur species. The spectra were fitted with four doublets representing four different sulfur species with valencies ranging from (-II) to (0). These sulfur species were assigned to monosulfide (S^{2-}), disulfide (S_2^{2-}) or an iron-deficient sulfide, polysulfide (S_n^{2-}, n > 2) and elemental sulfur (S°). The monosulfide was assigned to chalcopyrite. The other three species are oxidation products overlying the bulk chalcopyrite. The logical oxidation sequence is therefore:

$$CuFeS_2 \rightarrow Disulfide \rightarrow Polysulfide \rightarrow Sulfur \qquad (5\text{-}10)$$

These three oxididation products were found on both the unleached and the leached chalcopyrite surfaces. Considering that copper remained bonded to sulfur as Cu(I), the disulfide (or iron-deficient sulfide) and polysulfide must be Cu(I) sulfides. The fact that significant amounts of $CuFeS_2$ were still detected on the surface (actually the near surface) of the leached sample suggests that the polysulfide layer is quite thin, in the order of 10 nm or less.

The presence of detectable amounts of disulfide, polysulfide and sulfur on the surface of the unleached sample indicates that even minimal air exposure caused a measurable oxidation of the chalcopyrite surface. The more heavily oxidized, leached sample surface contained less chalcopyrite, less disulfide and more polysulfide than the unleached sample surface. Based on the finding that the leached sample surface had much more polysulfide than disulfide, the passivating layer is envisioned to be the polysulfide. These reactions are considered in more detail in Section 5.3.4. A kinetic model to explain the leaching and passivation of chalcopyrite is developed in Chapter 6.

It should be noted that the formation of polysulfide species on oxidized sulfide surfaces has been reported recently by other researchers. Using XPS and Raman spectroscopy, Mycroft *et al.* observed iron polysulfide on electrochemically oxidized pyrite surfaces [195]. This was confirmed by Li *et al.* who used Raman spectroscopy to identify polysulfide on electrochemically oxidized pyrite, as well as on electrochemically oxidized covellite surfaces [196]. Also, XPS studies by Pratt *et al.* revealed polysulfide on the surfaces of air-oxidized pyrrhotite [194]. Thus it appears that polysulfide formation is not restricted to chalcopyrite alone. In these studies, XPS and Raman spectroscopy were capable of detecting polysulfide species but they were incapable of determining their exact composition.

The leached sample surface also showed prominent S *2p* and O *1s* peaks for sulfate (SO_4^{2-}). The unleached sample surface had no sulfate peak and only a weak oxygen peak. The sulfate was attributed to superficially adsorbed sulfate ions rather than a metal-sulfate compound.

The unleached sample surface contained a small amount of iron oxide, tentatively thought to be Fe_3O_4. The leached sample surface contained little if any iron oxide or basic ferric sulfate. This essentially rules out the possibility (considered in Section 5.2.7) that Fe_xO_y, or a basic ferric sulfate-type phase, $Fe(SO_4)_x(OH)_y$, may be passivating chalcopyrite.

5.3.4 Proposed Reaction Sequence for Chalcopyrite

Based on the results of the leaching and surface characterization studies the following reactions are proposed to describe the oxidative leaching and passivation of chalcopyrite in sulfate media.

Anodic Reactions:

$$CuFeS_2 \rightarrow Cu_{1-x}Fe_{1-y}S_2 + xCu^{2+} + yFe^{2+} + 2(x+y)e^- \quad \text{(fastest, } y >> x\text{)} \quad (5\text{-}11a)$$

$$Cu_{1-x}Fe_{1-y}S_2 \rightarrow Cu_{1-x-z}S_2 + zCu^{2+} + (1-y)Fe^{2+} + 2(z+1-y)e^- \quad \text{(slower)} \quad (5\text{-}11b)$$

$$Cu_{1-x-z}S_2 \rightarrow (1-x-z)Cu^{2+} + 2S^\circ + 2(1-x-z)e^- \quad \text{(slowest)} \quad (5\text{-}11c)$$

$$CuFeS_2 \rightarrow Cu^{2+} + Fe^{2+} + 2S^\circ + 4e^- \quad \text{(overall)} \quad (5\text{-}11)$$

Cathodic Reactions:

$$Fe^{3+} + e^- \rightarrow Fe^{2+} \quad (5\text{-}12)$$

$$O_2 + 4H^+ + 4e^- \rightarrow 2H_2O \quad (5\text{-}13)$$

In the initial reaction, which is fast, iron leaches preferentially to copper to form an intermediate iron-deficient sulfide phase, $Cu_{1-x}Fe_{1-y}S_2$ ($y >> x$), where the sulfur component is possibly a disulfide (S_2^{2-}). The initial, preferential leaching of iron over copper has been observed by others (Section 2.4.1) and is consistent with thermodynamic prediction (see the Cu-Fe-S-H_2O Eh-pH diagram, Figure 2-5, page 12). In a second, slower reaction the remaining iron and additional copper leaches out of the iron-deficient sulfide phase to form a second intermediate; copper polysulfide, $Cu_{1-x-z}S_2$, more simply expressed as CuS_n where $n = 2/(1-x-z)$. The observed formation of two intermediate products (by XPS) is in agreement with Warren *et al.*'s findings with respect to the anodic behaviour of chalcopyrite (Section 2.4.1).

The slowest step is believed to be the decomposition of the copper polysulfide to cupric ions and elemental sulfur, with the polysulfide chains restructuring to form S_8 rings. Therefore, the copper polysulfide passivates chalcopyrite. Increasing the leach temperature increases the CuS_n decomposition rate until at 200°C CuS_n no longer passivates chalcopyrite. As the temperature increases, the elemental sulfur yield declines, probably because the S_n chains begin to fragment and oxidize to sulfate before they can form S_8 rings. Similarly, increasing the redox potential to a value not accessible in oxygen pressure leaching (say to 1 V or higher) through use of a stronger oxidant would be expected to facilitate the decomposition of CuS_n.

CHAPTER 6

FORMULATION OF A KINETIC MODEL FOR THE LEACHING AND PASSIVATION OF CHALCOPYRITE (AT 110°C)

6.1 Introduction

In this chapter a kinetic model is developed that attempts to explain the leaching and passivation of chalcopyrite at temperatures below the sulfur melting point. A shrinking spherical particle model is derived and tested using the low pulp density leaching data obtained for the $CuFeS_2$ concentrate at 110°C. The model is based on the particle leaching theory presented originally by Levenspiel [197] and later refined by Peters [198] and Dixon [199].

6.2 Initial Assumptions

In deriving the shrinking sphere model the following assumptions were made:

1. The particles leach at a rate dependent on the surface area of the mineral in contact with the solution;

2. The leach rate is not affected by the slight changes in solution composition that occur during leaching;

3. The mineral particles are spherically shaped and leach isotropically at a linear rate, i.e. they remain spherical during leaching;

4. The rate at which the particles leach is independent of particle size, i.e. large particles have the same "reactivity" as small particles.

6.3 Macromodel and Micromodel Rate Equations

The approach taken was to incorporate the initial assumptions into a model combining macromodel and micromodel particle leaching theory [198, 199].

Macromodels of leaching processes are concerned with the macroproperties of the leaching system. In pressure leaching processes these include such parameters as solution composition changes, temperature changes and pressure changes. Macromodels treat the solids

as if they were a homogeneous reactant with a given solid-liquid interfacial area. The macromodel rate equation for the present system is:

$$\frac{dC_i}{dt} = k_r A_{s/l} \tag{6-1}$$

where: C_i = the concentration of the product species (Cu^{2+}) in solution (units of mol m^{-3});

t = the leach time (minutes);

$A_{s/l}$ = the $CuFeS_2$ mineral surface area (m^2 mineral/m^3 leach solution, or m^{-1}) at time t;

k_r = the macromodel rate constant (mol m^{-2} min^{-1}).

Equation (6-1) says that the leaching rate is dependent only on the mineral surface area in contact with the leach solution. This rate equation incorporates the initial assumptions (1) and (2) but it does not deal with assumptions (3) and (4). To include the latter assumptions we need to also introduce a micromodel.

Micromodels deal with microscale changes, in this case the changes taking place in particle sizes and shapes. The micromodel rate equation for the present system is:

$$-\frac{dD}{dt} = 2k_l \tag{6-2}$$

where: D = the particle size (i.e. diameter, μm);

t = the leach time (min);

k_l = the micromodel linear rate constant or the rate of particle penetration (μm min^{-1}).

Equation (6-2) says that the mineral particles shrink at a constant, linear rate during leaching.

Thus the macromodel describes what is happening to the solution and the micromodel describes what is happening to the solids. The micromodel rate constant is related to the macromodel rate constant by the expression:

$$k_l = k_r V_m \left(10^6\right) \tag{6-3}$$

where: V_m = the molar volume of Cu in $CuFeS_2$ (m^3 mol^{-1}) ≡ the molar volume of $CuFeS_2$;

10^6 converts from m to μm.

The micromodel was used to develop a relationship between the surface area and the fraction of chalcopyrite reacted (surface area function). The surface area function was then incorporated into the macromodel in order to calculate k_r via:

$$k_r = \frac{dC_i}{dt}\left(\frac{1}{A_{s/l}}\right) \tag{6-4}$$

Support for the shrinking sphere model would be indicated by values of k_r (and k_l) that are constant with time.

6.4 Derivation of the Surface Area Function

The shrinking sphere micromodel was used to derive the surface area function for the $CuFeS_2$ feed used in this study. A pictorial representation of the model is depicted in Figure 6-1. For particles of initial size (diameter) D_i, the size at time t is:

$$D_t = D_i - 2k_l t \tag{6-5}$$

Here $k_l t = \delta_l$, the particle penetration depth.

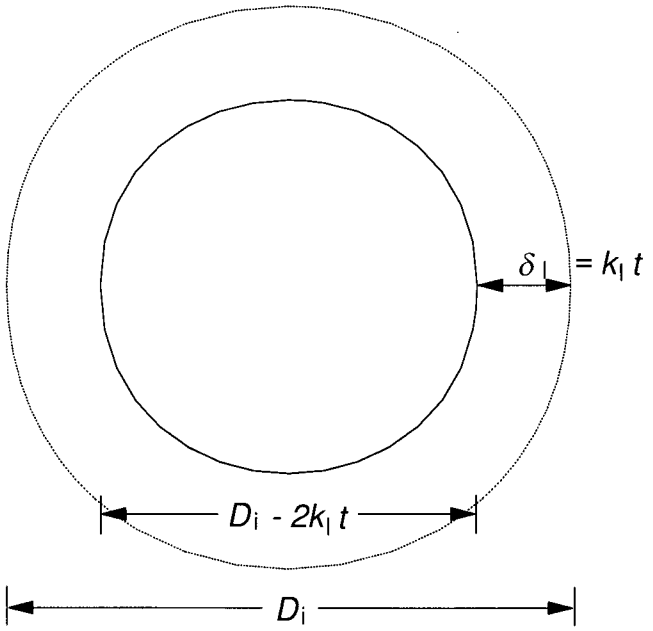

Figure 6-1. Pictorial representation of the shrinking sphere micromodel. Here δ_l is the particle penetration depth in μm.

Let $A(D_i)$ represent the fractional surface area lost to leaching and $X(D_i)$ the fraction leached. Then, the fractional surface area remaining at time t is:

$$1 - A(D_i) = \left(\frac{D_t}{D_i}\right)^2 = \left(1 - \frac{2k_1 t}{D_i}\right)^2 \tag{6-6}$$

and the fraction unleached at time t is:

$$1 - X(D_i) = \left(\frac{D_t}{D_i}\right)^3 = \left(1 - \frac{2k_1 t}{D_i}\right)^3 \tag{6-7}$$

where $2k_1 t \leq D_i$ to avoid negative values of $(1 - 2k_1 t/D_i)$.

For feeds with varying particle sizes equations (6-6) and (6-7) can be integrated over all particle sizes, provided the continuous particle size distribution function is known. Alternatively, the integrals can be solved by a simple numerical method using the experimentally determined discrete cumulative particle size distribution. The latter approach was adopted here. Let $F(D)$ represent the cumulative distribution function, such that $F(D_i)$ is the fraction of $CuFeS_2$ feed particles smaller than size D_i. $F(D)$ can be transformed into a discrete probability density function, $f(\overline{D_i})$, using the mean value theorem [199]:

$$f(\overline{D_i}) \approx \frac{F(D_{i+1}) - F(D_i)}{D_{i+1} - D_i} = \frac{\Delta F_i}{\Delta D_i} \tag{6-8}$$

where: $F(D_{i+1})$ and $F(D_i)$ are the cumulative fractions of particles smaller than size D_{i+1} and D_i respectively;

$\overline{D_i} = \dfrac{D_i + D_{i+1}}{2}$ = the arithmetic mean size of particles between size D_i and D_{i+1};

$\Delta F_i = f(\overline{D_i})\Delta D_i$ = the weight fraction of particles of size $\overline{D_i}$.

Note that the discrete probability density function is normalized, such that:

$$\sum_{i=0}^{n} f(\overline{D_i})\Delta D_i = 1 \tag{6-9}$$

At any size D, the discrete cumulative distribution function is related to the discrete probability density function by:

$$F(D) \approx \sum_{i=0}^{n} f\left(\overline{D_i}\right)\Delta D_i \tag{6-10}$$

The particle size distribution data generated by the Elzone and Horiba instruments for the $CuFeS_2$ feed were used to produce discrete cumulative distribution function and probability density function plots (Figure 6-2a and Figure 6-2b respectively). The Elzone and Horiba particle size results are compared in the plots. The Horiba instrument was capable of measuring particle sizes down to about 0.1 μm whereas the Elzone instrument was not able to measure particle sizes finer than about 1 μm. For the Horiba data, ΔD was set to 0.1 μm for $0 < D \leq 1$ μm and ΔD was increased to 1 μm for $D > 1$μm. For the Elzone data, ΔD was set to 1 μm for all D. In comparing the particle size distributions generated by the two instruments, it can be seen that the major difference is the larger proportion of fine particles indicated by the Horiba results. This leads to a large difference in the surface area calculated from the two size distributions. Assuming the particles are all spherical and smooth (i.e. non-porous), the specific surface area of the feed, S_o (units of $m^2\ kg^{-1}$), can be computed by summing the surface area-to-volume fractions for each $\overline{D_i}$ (units of m) and dividing by the feed density, ρ (units of $kg\ m^{-3}$) as follows:

$$S_o = \sum_{i=0}^{n}\left[\frac{\pi \overline{D_i}^2}{\frac{1}{6}\pi \overline{D_i}^3 \rho}\right]\Delta F_i = \frac{6}{\rho}\sum_{i=0}^{n}\frac{\Delta F_i}{\overline{D_i}} \tag{6-11}$$

Table 6-1 compares the experimentally determined surface area (determined by the BET gas adsorption method [200]) to the surface areas calculated by applying equation (6-11) to the Elzone and Horiba size distribution data. The surface area calculated from the Horiba data is a factor of two higher than the surface area calculated from the Elzone data, and the former is in much better agreement with the experimentally determined surface area. The BET surface area is still about 25% higher than the calculated Horiba surface, probably because of the error introduced by assuming the particles are spherical and totally non-porous.

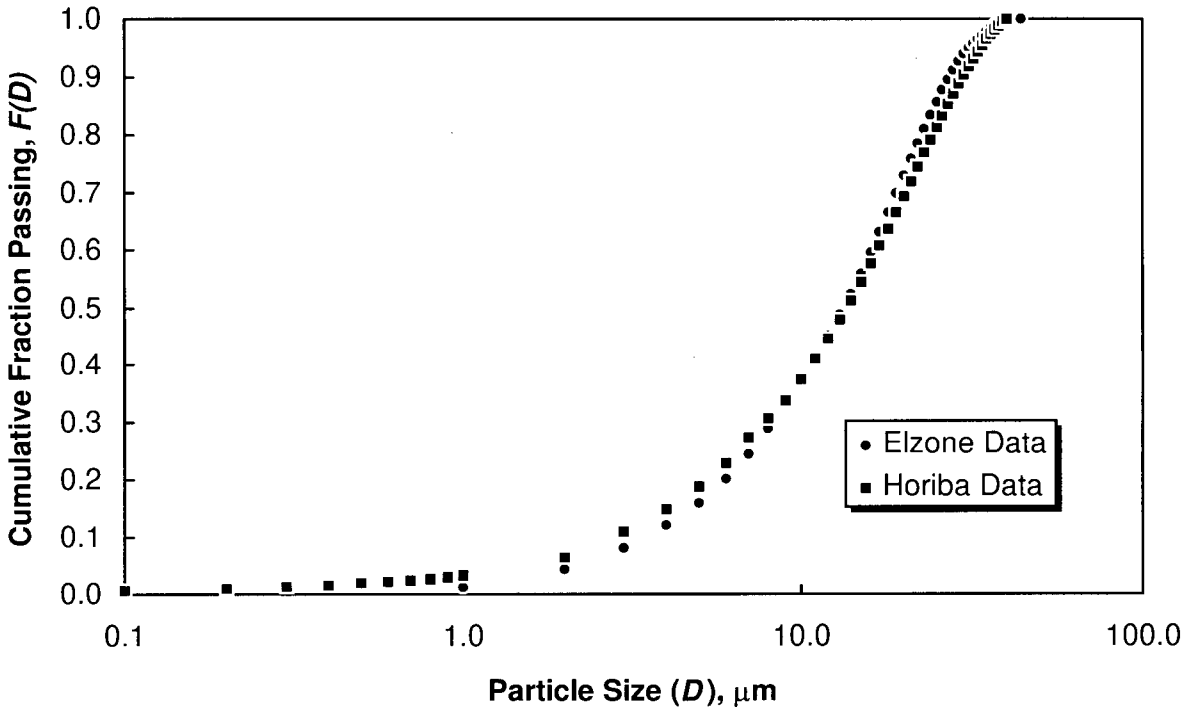

(a)

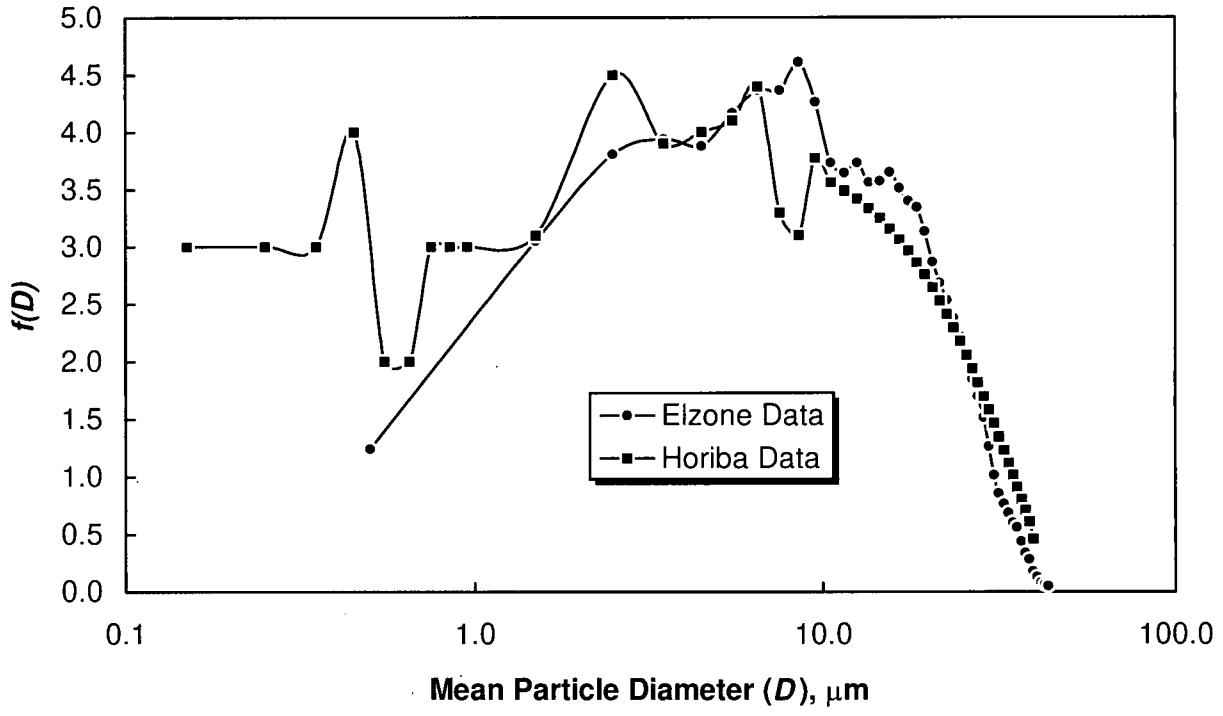

(b)

Figure 6-2. Plots of: (a) the discrete cumulative distribution function and (b) the discrete probability density function for the $CuFeS_2$ feed, in which the Elzone and Horiba particle size results are compared.

Table 6-1. Comparison of the experimentally determined and calculated specific surface area (S_o) values for the $CuFeS_2$ feed.

Method	Specific Surface Area S_o ($m^2\ kg^{-1}$)
BET analysis	600
Calculated from the Elzone data	210
Calculated from the Horiba data	480

Now that the discrete particle size distribution of the feed is known, the fraction unleached for each mean particle size (equation (6-7)) at any time t is multiplied by its respective weight fraction ΔF_i and summed over all particle sizes to obtain the total fraction unreacted $(1-\overline{X_t})$ at t:

$$1-\overline{X_t} = \sum_{\overline{D}(t=\tau)}^{\overline{D}_{max}} \left[1-X\left(\overline{D_i}\right)\right]\Delta F_i = \sum_{\overline{D}(t=\tau)}^{\overline{D}_{max}} \left[1-\frac{2k_1 t}{\overline{D_i}}\right]^3 \Delta F_i \qquad (6\text{-}12)$$

The lower limit of $\overline{D_i}$, $\overline{D}(t=\tau)$, is the size of the largest particle completely converted in time t. This is a necessary condition imposed by the fact that particles smaller than $\overline{D}(t=\tau)$ have disappeared and hence do not contribute to the fraction unconverted.

The fractional surface area remaining at any time t, $(1-\overline{A_t})$, can be calculated in a similar fashion:

$$1-\overline{A_t} = \sum_{\overline{D}(t=\tau)}^{\overline{D}_{max}} \left[1-A\left(\overline{D_i}\right)\right]\Delta S_i = \sum_{\overline{D}(t=\tau)}^{\overline{D}_{max}} \left[1-\frac{2k_1 t}{\overline{D_i}}\right]^2 \Delta S_i \qquad (6\text{-}13)$$

where ΔS_i is the surface area fraction of particles of size $\overline{D_i}$, calculated from the weight fraction as follows:

$$\Delta S_i = \frac{\Delta F_i / \overline{D_i}}{\sum_{i=0}^{n} \Delta F_i / \overline{D_i}} \qquad (6\text{-}14)$$

Using a spreadsheet program (Appendix 5) equations (6-12) and (6-13) were solved for varying values of particle penetration depth, δ_1 $(=k_1 t)$, to determine the relationship between

surface area and fraction reacted for the $CuFeS_2$ feed, based on the shrinking sphere micromodel. Figure 6-3a shows how the fraction of surface area remaining, $1-\overline{A}$, is predicted to vary with the fraction reacted, $\overline{X}$, when using either the Elzone or the Horiba data. The surface area declines more quickly in the initial stages of leaching due to the early disappearance of the high surface area fines fraction. The initial decline is particularly sharp with the Horiba data because a large proportion of the surface area is associated with the ultra-fine (< 1μm) fractions, which were measurable with the Horiba but not with the Elzone.

Figure 6-3b shows how the surface area, $A_{s/l}$, varies with the fraction reacted, $\overline{X}$. $A_{s/l}$ was calculated from $1-\overline{A}$ as follows:

$$A_{s/l} = \frac{S_o W_o}{V}\left(1-\overline{A}\right) \tag{6-15}$$

where S_o is the specific surface area of the feed ($m^2\ kg^{-1}$), W_o is the original feed weight (kg) and V is the solution volume (m^3). After about 10% conversion, the $A_{s/l}$ vs. $\overline{X}$ relationship is virtually identical regardless of whether the Elzone or Horiba data is used. Thus it was concluded that the ultra-fine, high surface area fraction has a very minor influence on extent of conversion because it disappears very quickly during leaching. This conclusion is further reinforced by examination of Figure 6-4, which shows how the fraction reacted, $\overline{X}$ is predicted to increase with increasing particle penetration depth, δ_l. It can be seen that the Elzone and Horiba data gave very similar results despite the differing surface areas determined by the two methods.

6.5 Calculation of the Rate Constants k_r and k_l

The surface area vs. fraction reacted relationship developed from the micromodel was then used to calculate the macromodel rate constant k_r from equation (6-4). First, the instantaneous copper leach rate at any time was determined by fitting the copper extraction vs. time data for $CuFeS_2$ at 110°C to a hyperbolic function with a non-linear least-squares curve fitting technique, using commercially available software (Microcal's Origin™). The details of the function fitting procedure are given in Appendix 5. The function was then differentiated to obtain the copper leach rate, dC_i/dt, as a function of residence time, t. The fitted copper extraction and copper leach rate plots are shown in Figure 6-5. As can be seen, the function fitted the extraction data quite well.

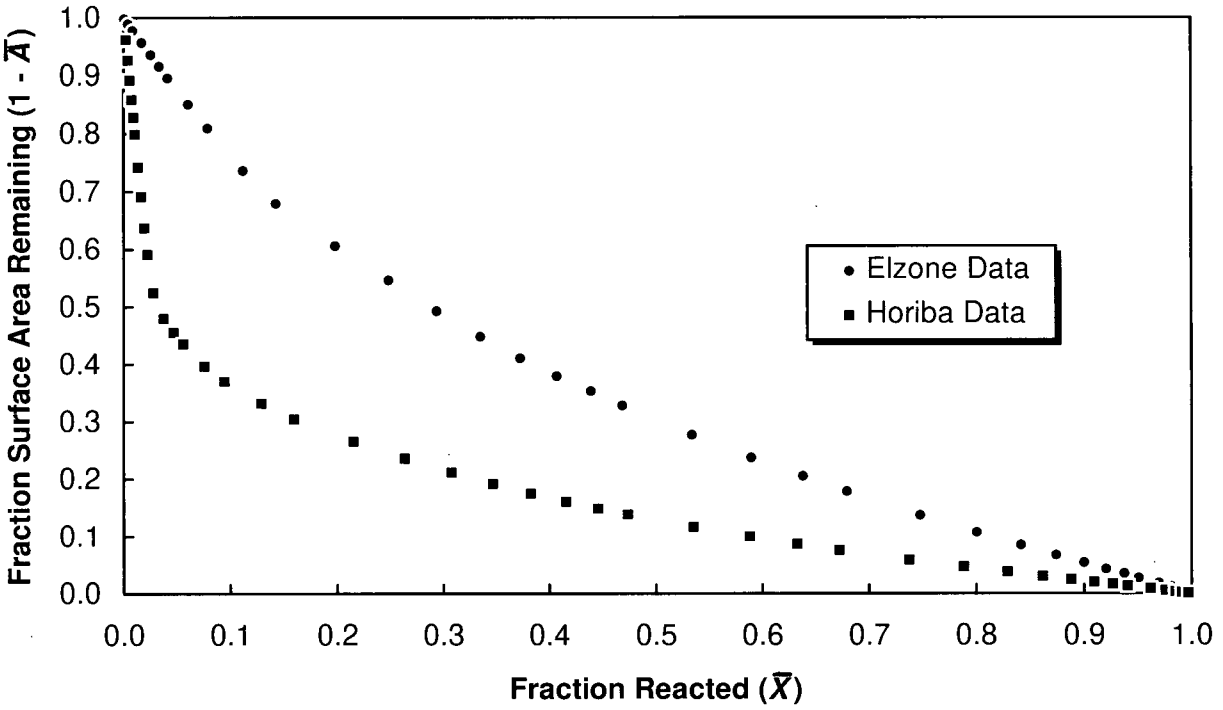

(a)

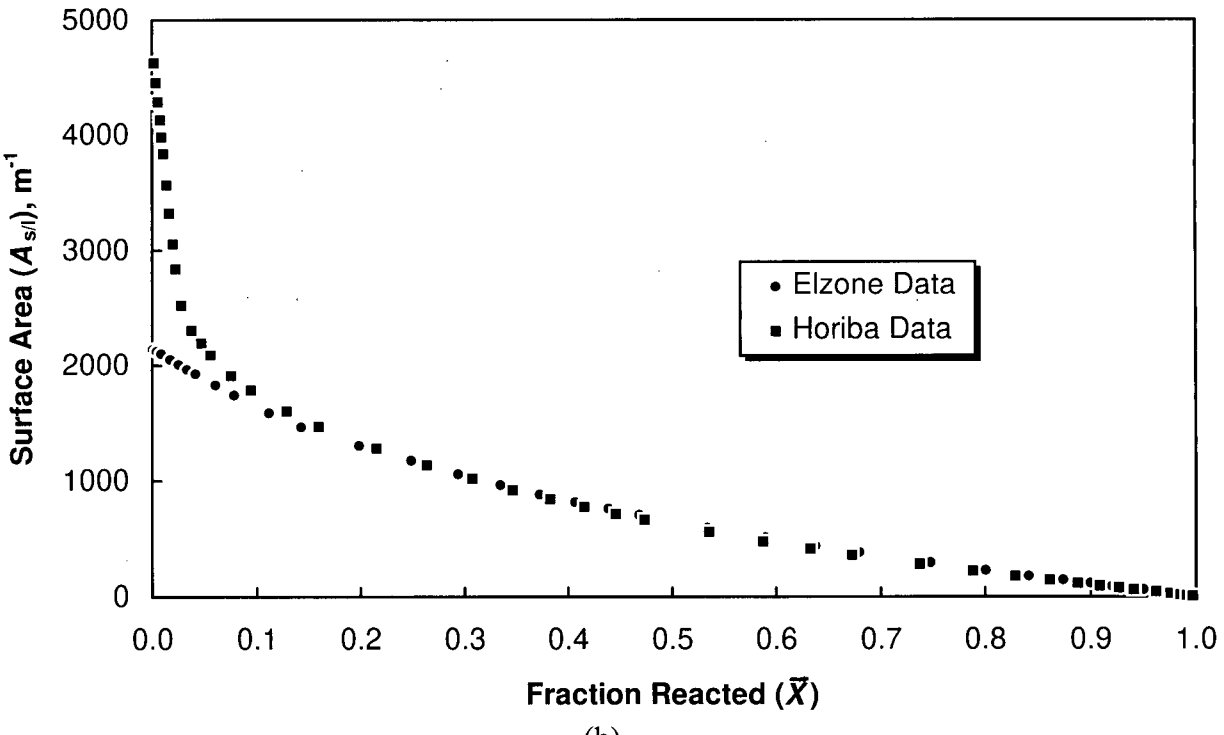

(b)

Figure 6-3. Plots of: (a) fraction surface area remaining ($1-\overline{A}$) vs. fraction reacted ($\overline{X}$) and (b) surface area, $A_{s/l}$, vs. fraction reacted ($\overline{X}$) for the $CuFeS_2$ concentrate, as predicted by the shrinking sphere micromodel.

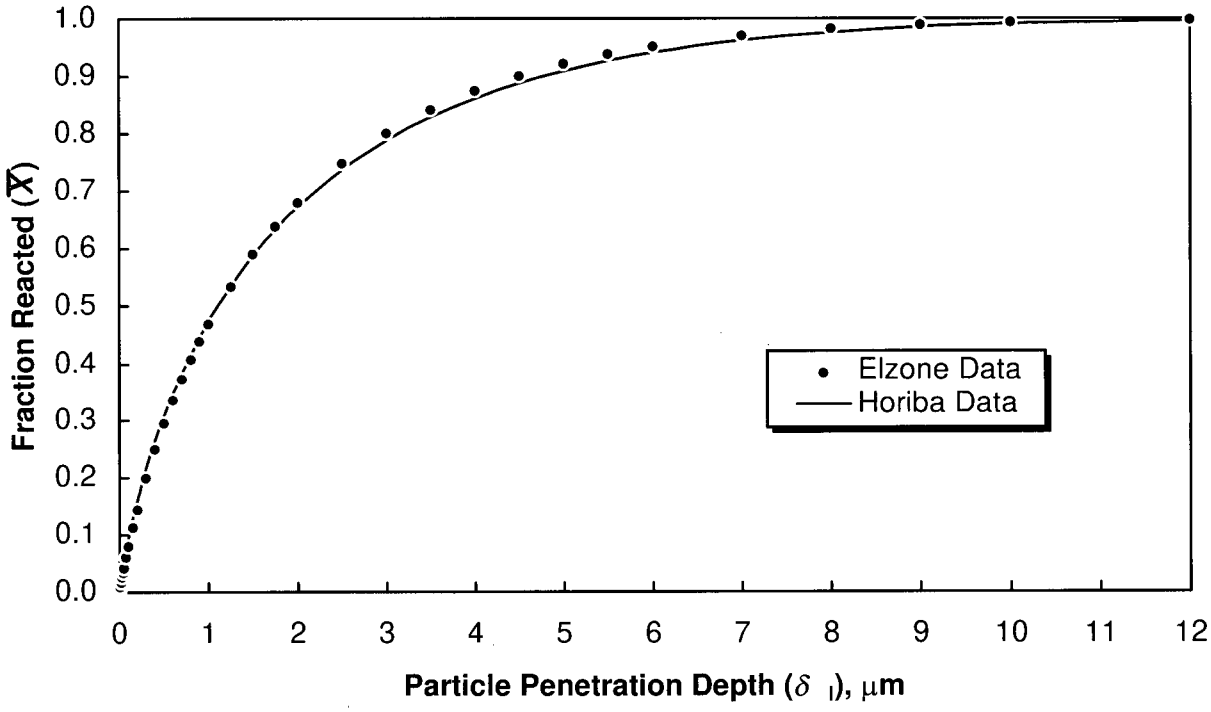

Figure 6-4. Fraction reacted ($\overline{X}$) vs. particle penetration depth (δ_l)for the $CuFeS_2$ concentrate, as predicted by the shrinking sphere micromodel.

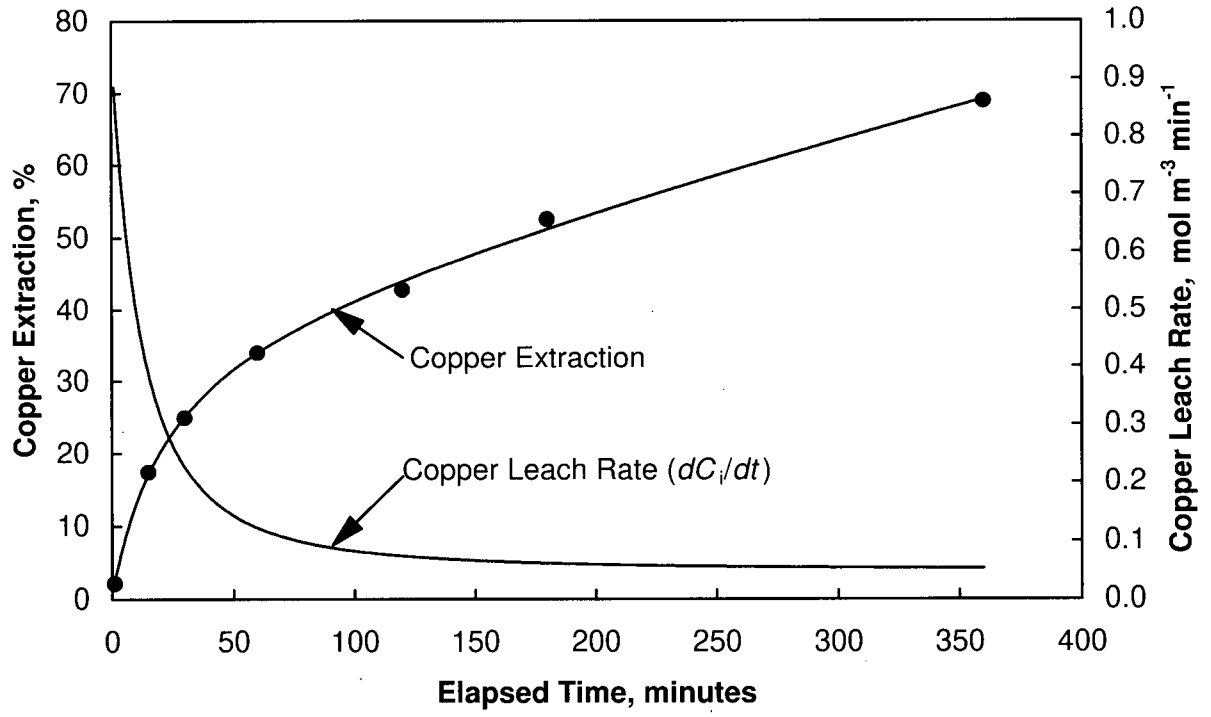

Figure 6-5. Copper extraction (%) and copper leach rate (dC_i/dt, mol m^{-3} min^{-1}) vs. time plots for the oxygen pressure leaching of the $CuFeS_2$ concentrate at 110°C. Copper extraction data (solid circles) were fitted to a hyperbolic function (solid line). The function was differentiated to obtain the leach rate vs. time relationship.

Next, the macromodel rate constant k_r was calculated from equation (6-4). Figure 6-6 shows how k_r varies with (a) residence time, (b) copper extraction and (c) particle penetration depth (δ_l). The k_r values obtained by using the surface area functions determined from both the Elzone and Horiba size data (Figure 6-3) are compared. For leaching to conform to the shrinking sphere model, k_r should be constant with time, extent of conversion and penetration depth. It can be seen that this was not the case in the early stages of leaching - k_r actually declined sharply, by a factor of 4 during the first 2 hours. This decline is more characteristic of a mechanism in which reactant/product diffusion through a product layer is rate controlling, i.e. shrinking core kinetics. However, after about 2 hours leaching, equivalent to ~40% copper extraction and a particle penetration depth of ~0.9 μm, k_r essentially levelled off, consistent with the shrinking sphere model. The behaviour of k_r can be explained in terms of a mixed mechanism in which the leaching kinetics are initially controlled by diffusion through a thickening passivating layer. Eventually, the passivating layer reaches a steady state thickness and the kinetics revert to chemical reaction control in which the rate is controlled by the rate at which the passivating layer decomposes. This mixed mechanism is discussed in further detail in Section 6.7.

After 3-4 hours, k_r appeared to increase slightly. One possible explanation for this increase is that the model may have underestimated the surface area, particularly after prolonged leaching times. The actual surface area may be higher than predicted due to agitation-induced particle breakage. If so, the magnitude of the deviation might be expected to become more pronounced with increasing residence times. To test this theory, the 6-hour leached residue was treated with toluene in a Soxhlet extractor to remove the elemental sulfur, and the particle size distribution of the remaining unreacted chalcopyrite was measured with the Elzone analyzer. The fractional residual surface area ($1-\overline{A}$) calculated from the particle size distribution (again assuming spherical particles) was 0.21 vs. 0.17 predicted by the model. Thus it appears that the model slightly underestimates the residual surface area. This may explain the upward trend in k_r observed after 3-4 hours.

The 6-hour leached residue particles were also examined by SEM to determine if leaching had caused any major changes in particle morphology, such as fissuring or pitting, that might invalidate the assumption that the particles leached isotropically. No changes in morphology were evident.

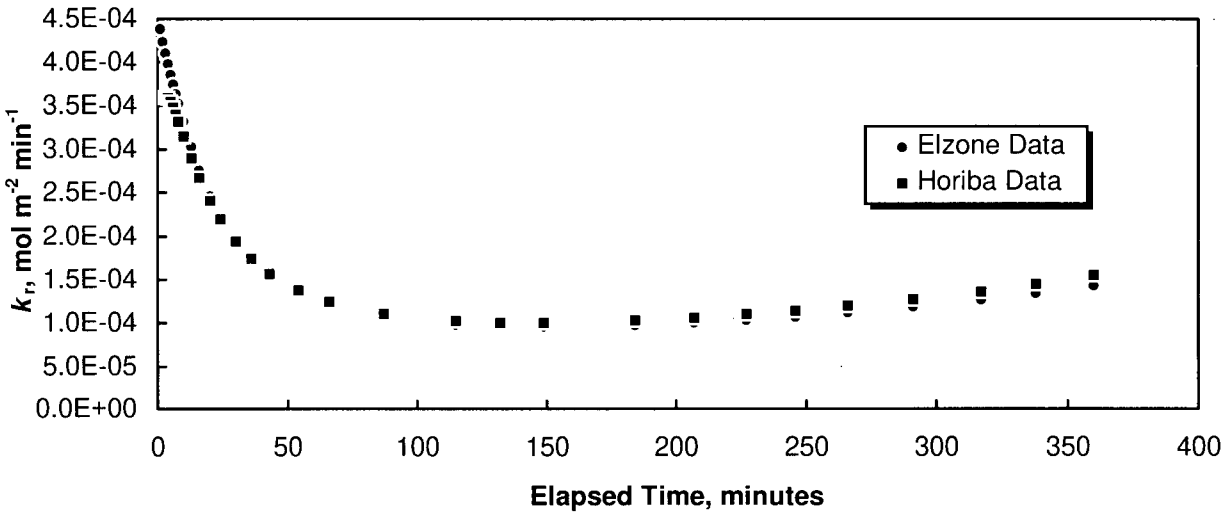

(a)

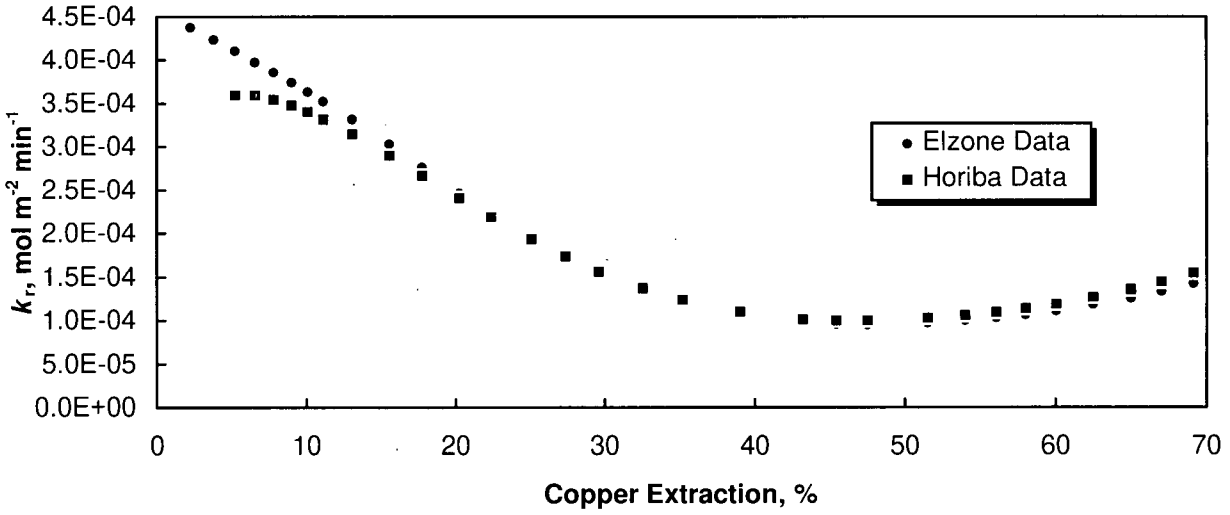

(b)

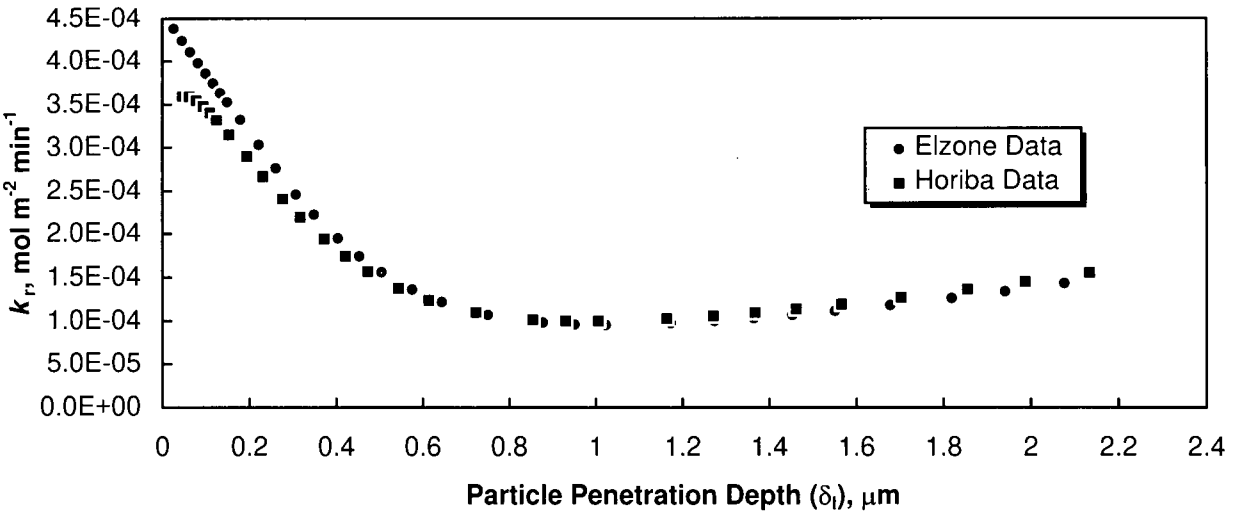

(c)

Figure 6-6. Plots of the macromodel rate constant k_r (mol m^{-2} min^{-1}) vs. (a) residence time, (b) copper extraction and (c) particle penetration depth, for the oxygen pressure leaching of the $CuFeS_2$ concentrate at 110°C.

Knowing k_r, the micromodel linear rate constant k_l can be calculated from equation (6-3), which simply involves multiplying k_r by a constant. Thus, it is evident that plots of k_l vs. time, extraction or penetration depth would show the same trends as seen in Figure 6-6.

Figure 6-7 depicts a plot of particle penetration depth, δ_l (= $k_l t$) as a function of residence time as predicted by the shrinking sphere model, using (a) the Elzone particle size data and (b) the Horiba particle size data. After about 2 hours δ_l increased at an essentially linear rate, in accordance with the shrinking sphere model. A linear regression of the data after 2 hours gave slopes equal to the rate constant, $k_l = 4.82 \times 10^{-3}$ and 5.14×10^{-3} $\mu m\ min^{-1}$ for the Elzone and Horiba data respectively. Table 6-2 gives examples of the copper extractions predicted by the model at various extended residence times, assuming the particle penetration rate (k_l) remains constant after the first two hours of leaching. The extractions were found to be almost identical (±0.3%) regardless of whether the Elzone or Horiba size data and their respective k_l's (see Figure 6-7) were used. It can be seen that due to the low value of k_l, an inordinately long residence time (30 hours) is predicted for 99% copper extraction.

6.6 Comparison of Chalcopyrite and Covellite Leaching Kinetics at 110°C

On the basis of electrochemistry and surface characterization studies performed on chalcopyrite (reviewed in Sections 2.4.1 and 2.4.2 respectively), some researchers have proposed that chalcopyrite is passivated by a layer of covellite (CuS). Covellite is thought to form as an intermediate species as chalcopyrite oxidizes. If a covellite reaction product is responsible for the passivation of chalcopyrite, it would seem reasonable to assume that covellite should leach at a much slower rate than chalcopyrite under identical leaching conditions. A search of the literature revealed that information comparing the leaching behaviour of chalcopyrite and covellite in sulfate media is quite scanty. Therefore, the relative reactivity of chalcopyrite and covellite under oxygen pressure leaching conditions was compared here to support or discount the covellite passivation theory. The same shrinking sphere model developed for $CuFeS_2$ was tested on leaching data obtained for CuS.

The ground covellite mineral sample was leached under the same conditions previously employed for the $CuFeS_2$ concentrate (see Section 5.2.2), i.e. low pulp density (10 g/L), 110°C and 1.38 MPa oxygen pressure. A temperature below the sulfur melting point was chosen to ensure that the kinetics would not be adversely affected by liquid sulfur. The starting leach solution contained 1 g/L Cu^{2+}, 0.5 g/L Fe^{3+} and 98 g/L H_2SO_4.

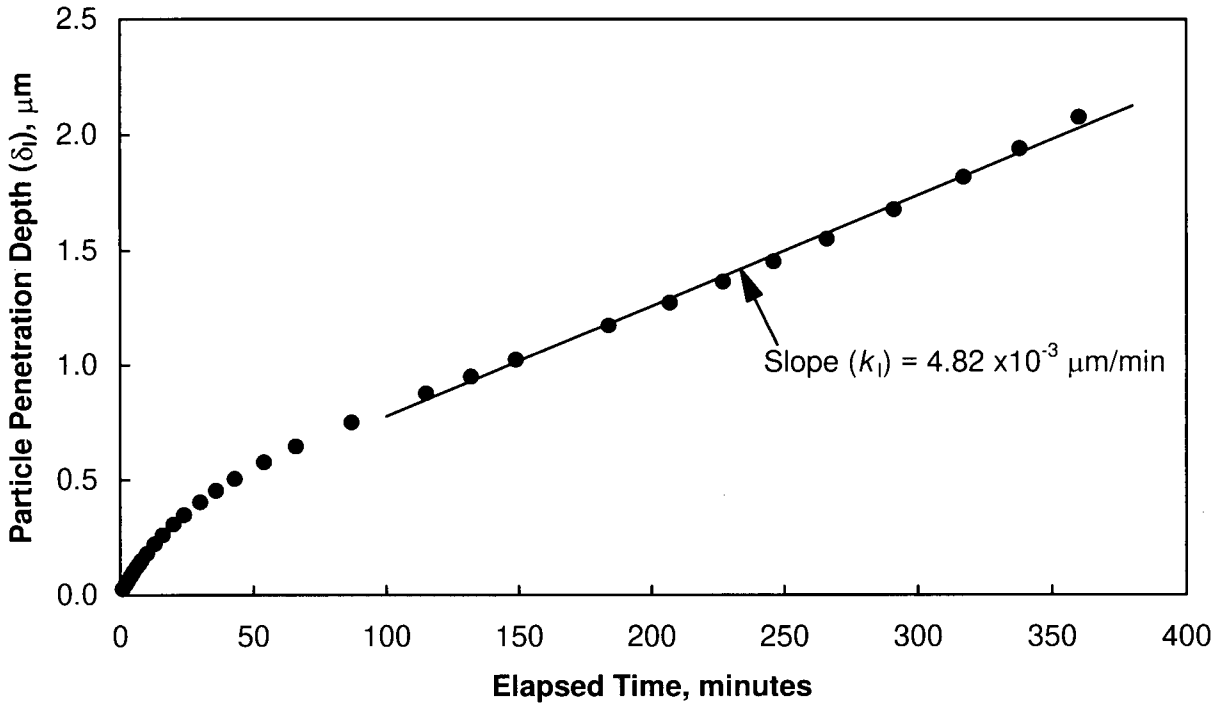

(a)

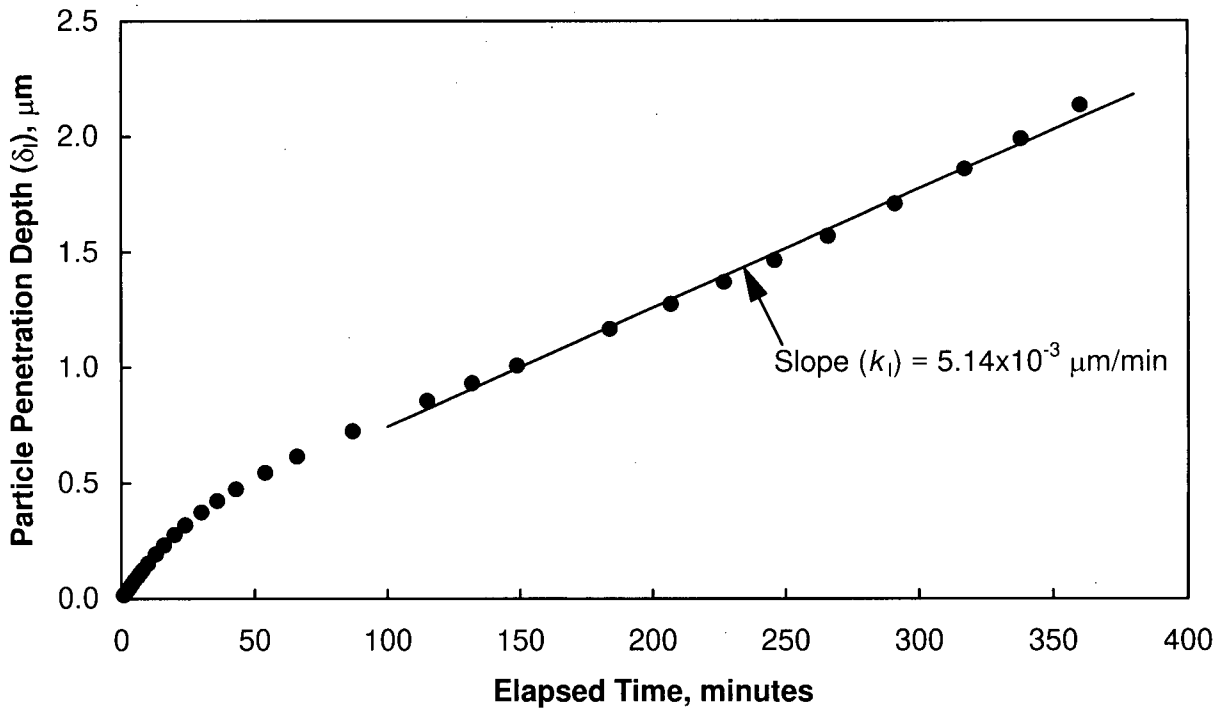

(b)

Figure 6-7. Particle penetration depth (δ_l) vs. time as predicted by the shrinking sphere model, using: (a) the Elzone particle size data and (b) the Horiba particle size data. The slope of the linear portion of the curve is equal to k_l, the micromodel linear rate constant.

Table 6-2. Examples of the model-predicted copper extractions at extended residence times for the oxygen pressure leaching of the $CuFeS_2$ concentrate at 110°C. The particle penetration rate (k_l) was assumed to remain constant after the first 2 hours of leaching.

Residence Time (hours)	Copper Extraction* (%)
6	68.8
8	76.3
10	81.8
15	90.6
20	95.2
25	97.6
30	98.9

*The copper extractions were calculated two ways: (1) using the Elzone size data and k_l and (2) using the Horiba size data and k_l. The extractions were found to be almost identical (±0.3%) regardless of whether the Elzone or Horiba data were used, hence the average extraction is reported.

A size analysis of the CuS feed was performed using the Elzone analyzer. The results showed that the CuS was considerably coarser than the $CuFeS_2$ feed (Table 6-3).

Table 6-3. Comparison of the $CuFeS_2$ and CuS feed particle sizes (Elzone data)

Feed	Arith. Mean Size (μm)	Median Size (μm)	P_{90}* (μm)
$CuFeS_2$	14.5	13.3	27.3
CuS	26.3	22.2	53.4

*P_{90} = 90% percent passing size.

Figure 6-8a compares the copper extraction profiles obtained for the $CuFeS_2$ and CuS feeds and Figure 6-8b compares their respective k_r values as a function of residence time. The results show that the covellite leached at a faster rate than the chalcopyrite over the entire residence time tested. After 6 hours leaching, the copper extraction from covellite was 88% vs. 69% for chalcopyrite despite the fact the covellite feed was significantly coarser. The k_r values for covellite were always about 6-9 times higher than for chalcopyrite. Thus it was concluded that covellite is considerably more reactive than chalcopyrite, and that the latter is unlikely to be passivated by the former.

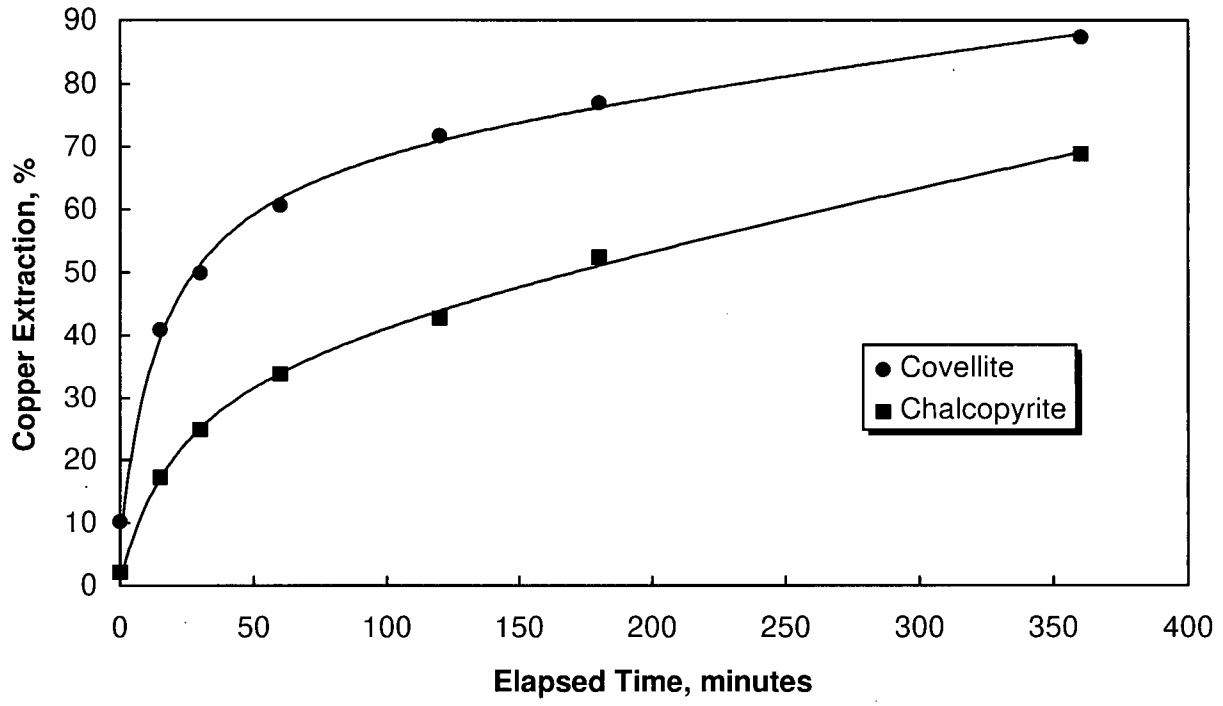

(a)

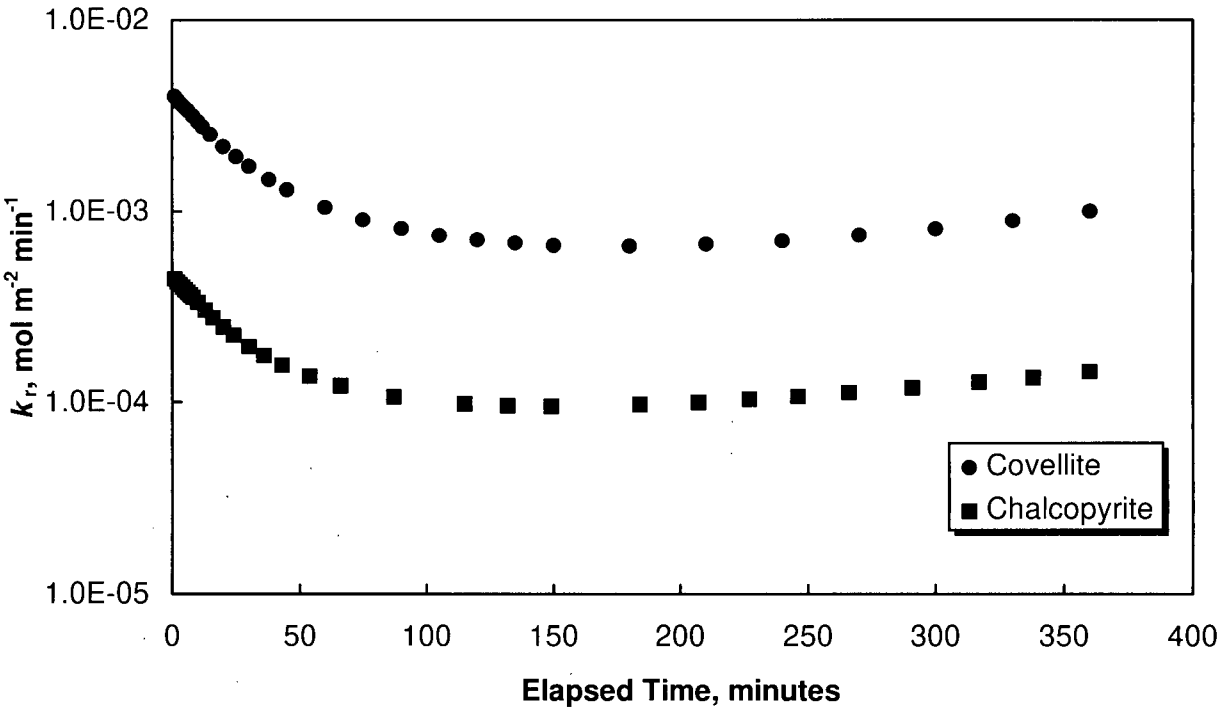

(b)

Figure 6-8. Comparison of: (a) copper extraction profiles and (b) k_r vs. residence time, for the oxygen pressure leaching of CuS and $CuFeS_2$ at 110°C. Test conditions: 10 g/L pulp density and 1.38 MPa oxygen overpressure. The initial leach solution contained 1 g/L Cu^{2+}, 0.5 g/L Fe^{3+} and 98 g/L H_2SO_4.

Interestingly, the variation in the CuS k_r value with time showed the same trends as the $CuFeS_2$ k_r value, in that it decreased in the initial stages of leaching then levelled off. The results suggest that CuS leaches by a mechanism similar to that for $CuFeS_2$. Figure 6-9 shows how k_r varies according to particle penetration depth, δ_l. The penetration depth reached about 4 μm before k_r levelled off, in contrast to $CuFeS_2$ where δ_l reached only 0.9 μm before k_r levelled off. As with $CuFeS_2$, δ_l increased at a linear rate in the latter stages of leaching CuS (Figure 6-10) with the slope equal to the linear rate constant k_l. However, the k_l value for CuS ($1.6x10^{-2}$ μm/min) is about three times larger than the k_l value for $CuFeS_2$ ($5.0x10^{-3}$ μm/min). Thus, when CuS is leached the particles are penetrated to a greater depth before passivation is complete. Moreover, the passivating layer is more reactive than the passivating layer for $CuFeS_2$. The leaching and passivation mechanism for both minerals is discussed in the next section.

6.7 Discussion

6.7.1 $CuFeS_2$ Leaching Kinetics

For the $CuFeS_2$ leaching kinetics to conform to the shrinking spherical particle model, the rate constant k_r (or k_l) should be constant with time, extent of conversion or particle penetration depth. This was not the case in the early stages of leaching; k_r actually declined rapidly, by a factor of 4 over the first 2 hours. However, after about 2 hours leaching k_r levelled off to a constant value, consistent with the shrinking sphere model. The kinetics are obviously too complex to be interpreted by a simple shrinking sphere model.

The kinetics can be explained in terms of a mixed diffusion/chemical reaction model, as follows. Initially, leaching is controlled by the rate at which ions diffuse through a thickening passive layer. As the thickness of the passive layer increases, k_r declines sharply. If the passive layer was completely unreactive, leaching would essentially obey shrinking core (parabolic) kinetics. However, the passive layer is not entirely inert and decomposes, but at a much slower rate than the original chalcopyrite. Eventually, the passive layer reaches a steady stage thickness and leaching is then controlled by the rate at which the passive layer decomposes. The kinetics in the latter stages of leaching conform approximately to the shrinking sphere model developed above and k_r reaches a constant value.

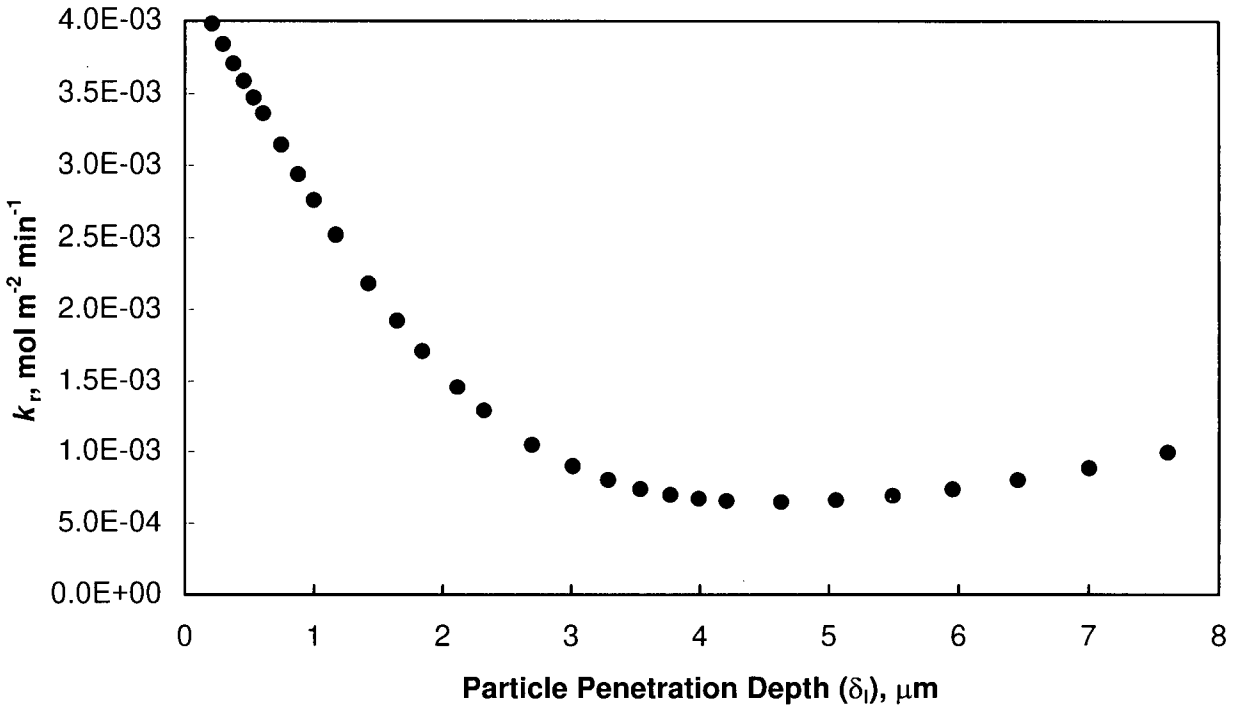

Figure 6-9. The variation in k_r with particle penetration depth, δ_l, for the oxygen pressure leaching of CuS at 110°C, as predicted by the shrinking sphere model.

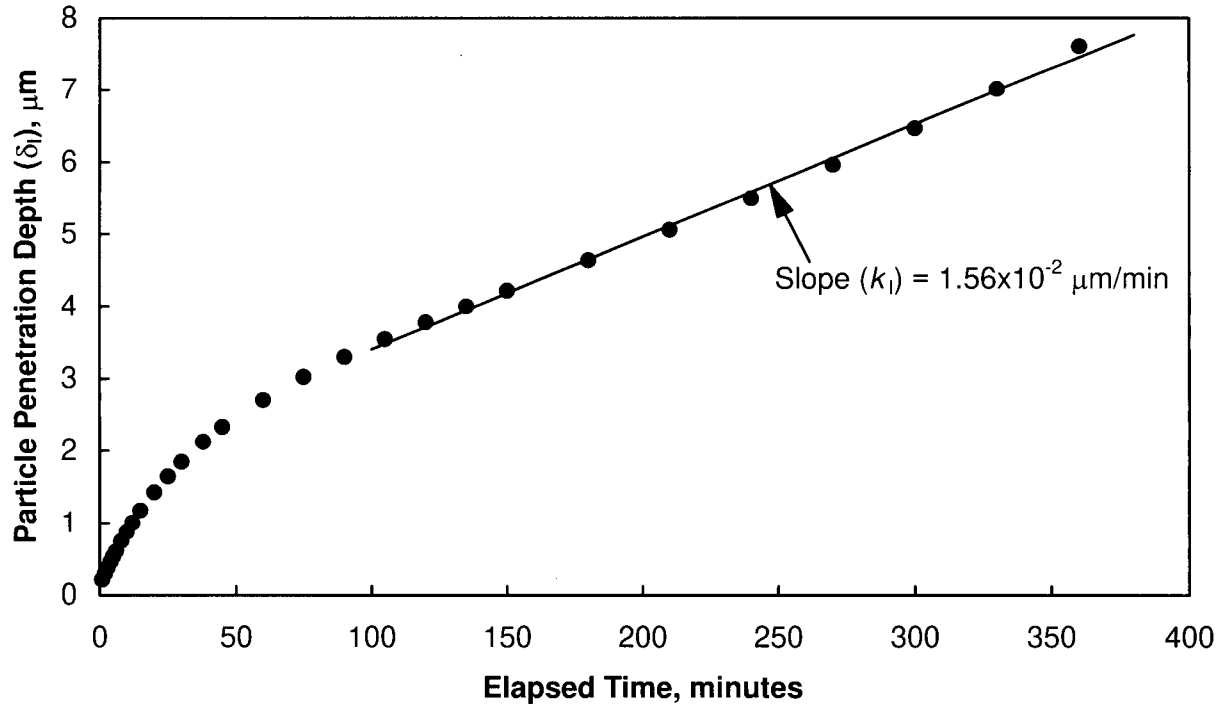

Figure 6-10. Particle penetration depth, δ_l, vs. residence time for the oxygen pressure leaching of CuS at 110°C, as predicted by the shrinking sphere model. The slope of the linear portion of the curve is equal to k_l.

The mixed diffusion/chemical reaction model is depicted pictorially in Figure 6-11. The diagram shows three interfaces:

Interface I - the chalcopyrite-passive layer (CuS_n) interface;

Interface II - the CuS_n-S° interface;

Interface III - the S°-aqueous solution interface.

As a chalcopyrite particle leaches, iron diffuses out of the mineral at a faster rate than copper, leading to the formation of a passivating copper polysulfide layer. This is depicted in the diagram by the receding interface I. However, the copper polysulfide is not completely inert and also reacts (shown by the receding interface II in Figure 6-11), albeit at a slower rate than the chalcopyrite. Thus in the early stages of leaching the rate at which interface I recedes is faster than the rate at which interface II recedes, and the thickness of the passive layer increases. Under these conditions leaching should obey shrinking core (parabolic) kinetics in which the reaction rate is inversely proportional to the thickness of the passive layer. For spherical particles, the micromodel rate equation for shrinking core kinetics is:

$$-\frac{dD}{dt} = 2\frac{k_p}{\delta_p} \tag{6-16}$$

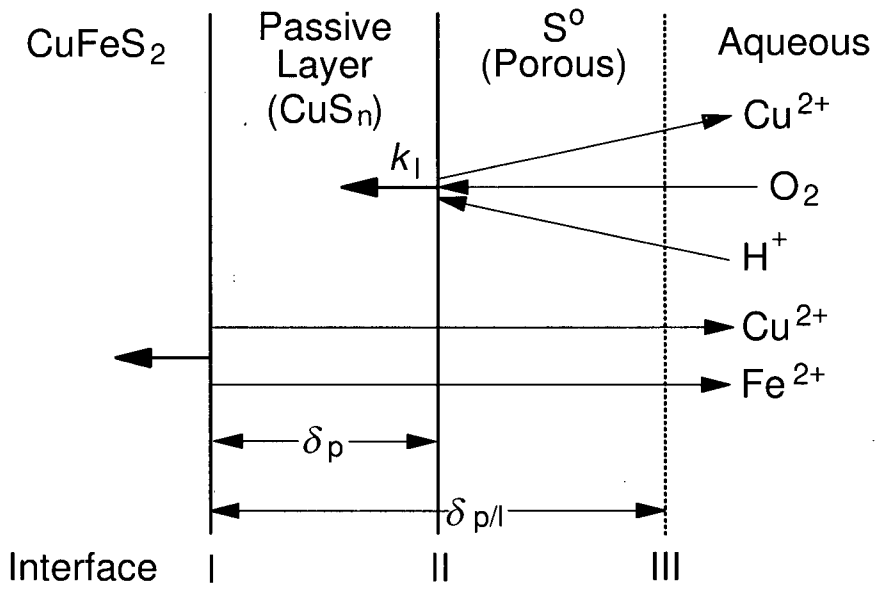

Figure 6-11. Pictorial representation of the mixed diffusion/chemical reaction model for the leaching and passivation of $CuFeS_2$.

where: D = the particle diameter (μm);

t = the leach time (min);

k_p = the parabolic micromodel rate constant (μm^2 min^{-1});

δ_p = the thickness of the passivating layer (μm).

Since:

$$-\frac{dD}{dt} = 2\frac{d\delta_p}{dt} \tag{6-17}$$

and substituting equation (6-17) into equation (6-16), we get:

$$\frac{d\delta_p}{dt} = \frac{k_p}{\delta_p} \tag{6-18}$$

Rearranging and integrating equation (6-18) leads to:

$$\delta_p = \sqrt{2k_p t} \tag{6-19}$$

It should be emphasized the copper polysulfide (CuS_n) layer must be quite thin and/or enriched in sulfur (n>2) to explain the near-congruent dissolution of copper and iron observed over the entire course of leaching (actually, at 110°C the amount of iron extracted from the $CuFeS_2$ concentrate was always 1.5-2% higher than the copper extraction). Otherwise, the leach solution would have contained significantly more dissolved iron than copper. Referring back to Figure 6-11, it can be seen that if k_l is assumed to be constant over all t, the passive layer thickness δ_p at any time t is:

$$\delta_p = \delta_{p/l} - k_l t \tag{6-20}$$

where $\delta_{p/l}$ is the mixed model (parabolic/linear) penetration depth. If an additional assumption is made that δ_p is small compared to $\delta_{p/l}$, then δ_l, the particle penetration depth for the shrinking spherical particle model, is approximately equal to $\delta_{p/l}$, so that:

$$\delta_p \approx \delta_l - k_l t \tag{6-21}$$

Equation (6-21) can be used to obtain a rough estimate of δ_p at any t. Figure 6-12 shows a plot of δ_p vs. t using both the Elzone and Horiba particle size data. According to this method of estimating δ_p, the passive layer thickness increases over the first 60 minutes then reaches a near-steady state value of about 0.3 μm. To determine if this value is realistic the micromodel spreadsheet program (Appendix 5) was used to calculate the expected copper and iron extractions at different retention times in excess of 60 minutes, assuming that the steady state δ_p thickness is 0.3 μm and equation (6-21) is reasonably valid. If the passive layer were this thick and consisted of CuS_2, the iron extractions after 60, 180 and 360 minutes would be approximately 13%, 8% and 4.5% greater than the respective copper extractions. Even if the passive layer was CuS_4, the above differences in iron and copper extractions would only be halved. Thus it appears that δ_p must be much less than 0.3 μm thick for this model to hold. This is consistent with the XPS results for the leached $CuFeS_2$ surface (Section 5.3.3.2), from which it was inferred that the polysulfide layer thickness is probably very thin, on the order of 10 nm or less. Equation (6-21) likely overestimates the passive layer thickness, meaning that the assumptions used in deriving the equation are faulty. One possibility is that k_l may initially be larger than the value determined from the shrinking particle δ_l vs. t plots (Figure 6-7). This would have the effect of reducing the passive layer thickness.

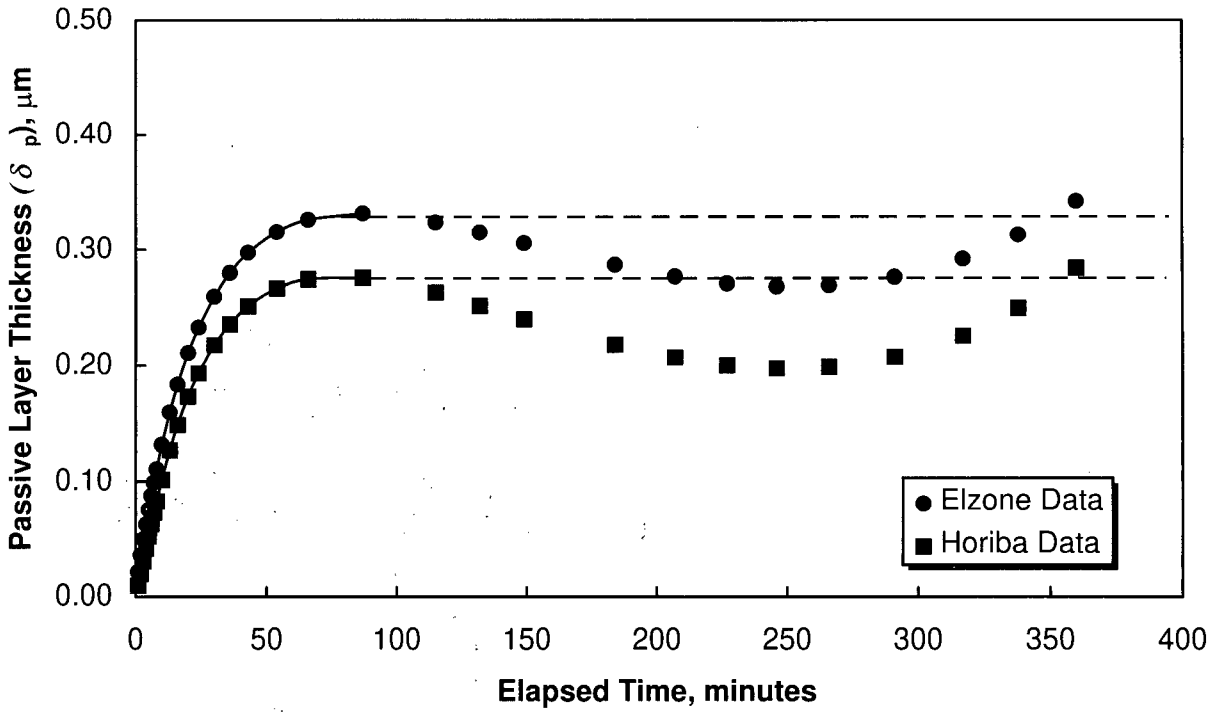

Figure 6-12. Plots of δ_p vs. t as calculated from equation (6-21).

After about 2 hours leaching, when the copper extraction reached about 40%, k_r had essentially levelled off to a constant value, which is consistent with the shrinking spherical particle model. This was interpreted as indicating a switch in reaction mechanism from diffusion control to chemical reaction control, in which the leach rate is now controlled by the rate at which the passivating layer decomposes. The reaction is thought to be:

$$CuS_n + \tfrac{1}{2}O_2 + 2H^+ \rightarrow Cu^{2+} + nS^o + H_2O \qquad (6\text{-}22)$$

The low value of the linear rate constant k_l (~$5x10^{-3}$ μm/min) for this reaction explains the inordinately long residence times required to achieve a high copper extraction at 110°C. The reason for the low reactivity of the copper polysulfide is not known but it may be related to the difficulty in exsolving elemental sulfur from the mineral. That is, the rearrangement of polysulfide chains into S_8 rings may be a kinetically slow process. The elemental sulfur is thought to be sufficiently porous that diffusional processes through the sulfur layer are not rate limiting. If diffusion through a thickening sulfur layer were rate limiting, the kinetics would be purely shrinking core (parabolic) for the entire leach.

There are precedents in the hydrometallurgical literature for the mixed diffusion/chemical reaction model developed here. Ahn and Wadsworth proposed a similar, "paralinear" model to explain the electrochemical reaction kinetics of molybdenite in acid media [201]. Zhu *et al.* found that the electrochemical oxidation of pyrite at pH 9.2 obeyed mixed parabolic/linear kinetics [202]. They suggested a protective surface film comprised of sulfur, polysulfides and/or metal-deficient sulfides formed which was subsequently oxidized to sulfate.

To conclude this discussion it should be mentioned that the modelling results alone do not prove conclusively that a passivating layer forms on chalcopyrite during leaching. Another possible explanation for the sharp initial decline in k_r is the near surface regions of the mineral particles may be more reactive than the bulk mineral as a result of lattice defects and deformations produced on the former by grinding. The mechanical activation of chalcopyrite by impact or vibration milling to effect a reactivity increase under oxidative leaching conditions was discussed in Section 2.5.2. However, when the modelling results are considered along with the surface characterization results (Section 5.3), which demonstrated the existence of a surface layer markedly different in composition to $CuFeS_2$, the passivation theory would seem to offer the most reasonable explanation for the observed kinetics.

6.7.2 CuS Leaching Kinetics

In Section 6.6 covellite was shown to be much more reactive than chalcopyrite under identical leaching conditions. On this basis the possibility of chalcopyrite becoming passivated by a covellite reaction product was ruled out. When the shrinking particle micromodel was applied to the covellite copper extraction data, the behaviour of k_r was observed to be quite similar to that of chalcopyrite (Figure 6-8b, Figure 6-9 and Figure 6-10). This raises the intriguing possibility that covellite leaching can also be explained by a mixed diffusion/chemical reaction model in which the terminal leach rate is dependent on the rate at which a passive layer decomposes. As no surface characterization studies were performed on covellite, the existence of a passive layer is speculation at this point. Possibly, a copper polysulfide layer also forms on covellite according to the following reaction:

$$nCuS \rightarrow CuS_n + (1-n)Cu^{2+} + 2(1-n)e^- \qquad (6\text{-}23)$$

However, it is not clear why copper extractions from covellite were higher than from chalcopyrite. Moreover, the passivating layer on covellite appears to be more reactive than the passivating layer on chalcopyrite as the k_l for CuS was about 3 times greater than the k_l for $CuFeS_2$.

CHAPTER 7

CONCLUSIONS

Following are the principal conclusions reached from this study of the leaching and passivation of chalcopyrite.

1. The oxygen pressure leaching behaviour of chalcopyrite was found to be very temperature dependent. At low temperatures, 110-120°C, the reaction rate was slow. At moderate temperatures, 130-170°C, the reaction extent was relatively temperature insensitive because leaching was stifled by the formation of liquid sulfur, which wetted and agglomerated the partially reacted sulfide particles. At high temperatures, 180-220°C, the reaction rate increased sharply with increasing temperature and total oxidation was achieved at 200°C or higher within 3 hours. The proportion of sulfide sulfur oxidized to elemental sulfur instead of sulfate (the sulfur yield) declined with increasing temperature. At 200°C or higher the sulfur yield was nil, i.e. sulfide was oxidized entirely to sulfate.

2. The interfacial properties of the surfactants orthophenylenediamine (OPD) and lignosulfonate in the chalcopyrite-liquid sulfur-cupric/ferric sulfate system were studied at elevated temperature and pressure. Both surfactants were found to lower significantly the liquid sulfur-aqueous solution interfacial tension as well as increase the chalcopyrite-sulfur contact angle. The net result is a dramatic reduction in the work of adhesion for liquid sulfur on chalcopyrite, meaning that the surfactants lower the work required to displace sulfur from chalcopyrite. On this basis the surfactants were predicted to be effective sulfur dispersants under copper pressure leaching conditions, provided they were sufficiently stable to retain their interfacial activity.

3. The application of sulfur-dispersing surfactants to the oxygen pressure leaching of chalcopyrite in the temperature range 125-155°C was found to be largely ineffective in enhancing copper extraction. Most of the surfactants tested decomposed too rapidly to be beneficial. The decomposition was hypothesized to be copper catalyzed. The best

results were obtained with OPD when it was added continuously at a low temperature (125°C) and a high dosage (50 kg/t). Under these conditions the surfactant was successful in dispersing liquid sulfur and it effected a modest increase in copper extraction over that obtained at 110°C, but only after prolonged retention times (6 hours). Lower surfactant dosages (5 kg/t) added either batchwise or continuously, had little effect. It was found that chalcopyrite leached slowly even if molten sulfur was prevented from wetting the mineral surfaces. This led to the conclusion that the reaction rate is ultimately controlled by a passivating mechanism unrelated to elemental sulfur formation.

4. Examination of oxidized chalcopyrite mineral surfaces by Auger electron spectroscopy and X-ray photoelectron spectroscopy indicated that an iron-deficient, copper-rich sulfide layer forms on the surface of chalcopyrite as a result of solid state changes that occur in the mineral during leaching. This layer is thought to be a copper polysulfide, CuS_n, where $n > 2$. The layer is quite thin (~10-100 nm) and hence is not detectable by conventional electron microscopy. The copper polysulfide is believed to passivate the chalcopyrite.

5. The addition of silver ions at a temperature below the sulfur melting point (110°C) was found to catalyze the leach, resulting in the copper extraction increasing from 53% to 96% after 3 hours leaching. Silver alone was ineffective at 125°C and 155°C because the leach was stifled by liquid sulfur. However, when silver was used in conjunction with OPD at 125°C the copper extraction was again enhanced significantly, to 91%. The OPD prevented the sulfur from wetting the mineral surfaces, allowing the catalytic effect of the silver ions to be maintained.

6. The kinetics of leaching chalcopyrite under oxygen pressure in sulfate media at 110°C have been explained in terms of a mixed diffusion/chemical reaction model. Initially, the kinetics are parabolic and the rate is controlled by ion diffusion through a thickening passivating layer. However, the passivating layer also decomposes, but at a slower rate than $CuFeS_2$, so it eventually reaches a steady state thickness. The mechanism then reverts to chemical reaction control where the rate is controlled by the rate at which the passivating layer decomposes. For the $CuFeS_2$ concentrate tested in this study, the

transition from diffusion to chemical reaction rate control was complete after about 2 hours leaching at 110°C, when the copper extraction had reached about 40%. The passivating layer leached at an extremely slow, near-linear rate with a rate constant, k_l = $5.0x10^{-3}$ μm/min. The low value of k_l explains why inordinately long residence times are required to obtain a high copper extraction from chalcopyrite at 110°C. Conformity of the kinetics to this type of mixed model would seem to rule out the commonly held notion that solid elemental sulfur passivates chalcopyrite. If the kinetics were controlled by diffusion through a thickening sulfur layer, the kinetics would be parabolic over the entire course of leaching.

7. Covellite was clearly demonstrated to be much more reactive than chalcopyrite under identical leaching conditions. This finding discounts the theory held by some researchers that chalcopyrite is passivated by a covellite reaction product.

CHAPTER 8

RECOMMENDATIONS FOR FURTHER WORK

These studies have shed new light on the reasons for the low reactivity of chalcopyrite under oxidizing conditions in acid sulfate media. The surface studies have identified the presence of a surface layer believed to be copper polysulfide, CuS_n, where n>2. Further leaching and characterization studies are desirable in order to more accurately define the composition of the polysulfide as well as determine the conditions affecting its formation and stability. A more thorough knowledge of the passivation phenomenon will assist in the development of leaching conditions and procedures designed to prevent or overcome passivation.

The focus of this thesis was a fundamental investigation of the passivation phenomenon. Due to time constraints it was not possible to mount a serious study into ways to overcome the passivation problem. However, the work has suggested some promising approaches to pursue in the future.

1. Catalyzed Leaching

The addition of silver ions has been shown to prevent the passivation of chalcopyrite. This would seem to be worth pursuing, both from a fundamental and a practical perspective. The role of silver may be to prevent formation of the copper polysulfide entirely. Alternatively, the silver ions may react with the copper polysulfide via:

$$CuS_n + 2Ag^+ \rightarrow Cu^{2+} + Ag_2S + (n-1)S^o \qquad (8\text{-}1)$$

Of course, the drawback to using silver is its cost. Any process employing silver will likely require a silver recovery and recycle step in order to be economic.

The use of silver in conjunction with OPD was shown to be an effective combination at temperatures above the sulfur melting point, provided the OPD did not decompose too quickly. The potential benefits of this approach should be investigated further.

It is also recommended that the use of potential catalysts that are less expensive than silver be considered.

2. Use of Cuprous-Stabilizing Ligands

It is well documented that chalcopyrite leaches much faster in chloride media than in sulfate media. The increased reactivity may be related to the fact that the chloride ion is a strong cuprous-stabilizing ligand. It can be speculated that the chloride ion accelerates the decomposition of the copper polysulfide according to the following reaction:

$$CuS_n + 2Cl^- \rightarrow CuCl_2^- + nS^\circ \qquad (8\text{-}2)$$

The addition of chloride ions to sulfate media in copper heap/dump leaching is under active investigation as a possible way to enhance copper dissolution. In addition to chloride, there may be other cuprous-stabilizing ligands that enhance the dissolution of chalcopyrite in sulfate media. These should be identified and tested.

3. Oxygen Pressure Leaching at Alkaline pH

The copper polysulfide layer identified in this study is surprisingly stable under oxygen pressure leaching conditions. Polysulfide species are known to be readily soluble at alkaline pH's. This suggests that oxygen pressure leaching of chalcopyrite at alkaline pH's may lead to enhanced copper dissolution, if conditions were found that also maintained a high copper solubility.

REFERENCES

1. Berezowsky, R.M.G.S., Collins, M.J., Kerfoot, D.G.E. and Torres, N., The commercial status of pressure leaching technology, *Journal of Metals, 43 (2)*, pp. 9-15, 1991.

2. Vizsolyi, A., Veltman, H., Warren, I.H. and Mackiw, V.N., Copper and elemental sulphur from chalcopyrite by pressure leaching, *Journal of Metals, 19 (11)*, pp. 52-59, 1967.

3. Braithwaite, J.W. and Wadsworth, M.E., Oxidation of chalcopyrite under simulated conditions of deep solution mining, *Extractive Metallurgy of Copper - Vol. 2*, J.C. Yannopoulos and J.C. Agarwal, Eds., The Metallurgical Society of AIME, New York, NY, USA, pp. 752-775, 1976.

4. Stanczyk, M.H. and Rampacek, C., Oxidation leaching of copper sulfides in acidic pulps at elevated temperatures and pressures, *U.S. Bureau of Mines Report of Investigations 6193*, 15 pp., 1963.

5. King, J.A., Dreisinger, D.B. and Knight, D.A., The total pressure oxidation of copper concentrates. In: *Extractive Metallurgy of Copper, Nickel and Cobalt, Volume 1: Fundamental Aspects*, R.G. Reddy and R.N. Weizenbach, Eds., The Minerals, Metals & Materials Society of AIME, Warrendale, PA, USA, pp. 735-756, 1993.

6. Kawulka, P., Haffenden, W.J. and Mackiw, V.N., Recovery of zinc from zinc sulphides by direct pressure leaching, U.S. Patent No. 3,867,268, February 18, 1975.

7. Meyer, B., Preparation and properties of sulfur allotropes, *Elemental Sulfur, Chemistry and Physics, Chapter 4*, B. Meyer, Ed., John Wiley & Sons Inc., New York, NY, USA, pp. 71-93, 1965.

8. Donohue, J., The structures of the allotropes of solid sulfur, *Elemental Sulfur, Chemistry and Physics, Chapter 2*, B. Meyer, Ed., John Wiley & Sons Inc., New York, NY, USA. pp. 13-44, 1965.

9. Bacon, R.F. and Fanelli, R., *Journal of the American Chemical Society, 65*, p. 539, 1943.

10. Tobolski, A.V. and Eisenberg, A., *Journal of the American Chemical Society, 81*, p. 780, 1959.

11. MacKnight, W.J. and Tobolski, A.V., Properties of polymeric sulfur, *Elemental Sulfur, Chemistry and Physics,* B. Meyer, Ed., Interscience Publishers, New York, NY, USA, p. 95, 1965.

12. Tobolski, A.V. and MacKnight, W.J., *Polymeric Sulfur and Related Polymers*, Interscience Publishers, New York, NY, USA, p. 91, 1965.

13. Steudel, V.R. and Mäusle, H.J., Molecular composition of liquid sulfur, part 2: qualitative analysis and preparation of S_7 S_{12}, α-S_{18} and S_{20} from S_8, *Z. anorg. allg. Chem.*, 478, pp. 156-176, 1981.

14. Steudel, V.R. and Mäusle, H.J., Molecular composition of liquid sulfur, part 3: quantitative analysis in the temperature region 115-350°C, *Z. anorg. allg. Chem.*, 478, pp. 177-190, 1981.

15. Bixby, D.W., Fike, H.L., Shelton, J.E. and Wiewiorowski, T.K., Sulfur, *Kirk-Othmer Encyclopedia of Chemical Technology, Volume 22, 3rd Edition*, pp. 78-106, 1983.

16. Tuller, W.N., *The Sulphur Data Book*, McGraw-Hill Book Company, New York, NY, USA, 1954.

17. Peters, E., Leaching of sulfides, *Advances in Mineral Processing*, P. Somasundaran, Ed., The Society for Mining, Metallurgy, and Exploration, Inc., of AIME, Littleton, CO, USA, pp. 445-462, 1986.

18. Habashi, F. and Bauer, E.L., Aqueous oxidation of elemental sulfur, *Industrial and Engineering Chemistry Fundamentals, 5 (4)*, pp. 469-471, 1966.

19. Jones, W.E. and Krause E., Leaching of nickeliferous pyrrhotite concentrate at temperatures above the melting point of sulfur. Paper presented at *15th Annual Conference of Metallurgists of the CIM*, Ottawa, Canada, August 25, 27 pp., 1976.

20. Corriou, J.P. and Kikindai, T., The aqueous oxidation of elemental sulfur and different chemical properties of the allotropic forms S_λ and S_μ, *Journal of Inorganic and Nuclear Chemistry, 43*, pp. 9-15, 1981.

21. Hall, S.R. and Stewart, J.M., The crystal structure refinement of chalcopyrite, $CuFeS_2$, *Acta Crystallographica, B29*, pp. 579-585, 1973.

22. Greenwood, N.N. and Whitfield, H.J., Mössbauer effect studies on cubanite ($CuFe_2S_3$) and related iron sulfides, *J. Chem. Soc. A. London, 7*, pp. 1697-1699, 1968.

23. Nakai, I., Sugitani, Y. and Nagashima, K., X-ray photoelectron spectroscopic study of copper minerals, *J. Inorg. Nucl. Chem., 40*, pp. 789-791, 1978.

24. Hiskey, J.B., Chalcopyrite semiconductor electrochemistry and dissolution, *Extractive Metallurgy of Copper, Nickel and Cobalt, Volume I: Fundamental Aspects*, R.G. Reddy and R.N. Weizenbach, Eds., The Minerals, Metals and Materials Society of AIME, Warrendale, PA, USA, pp. 949-969, 1993.

25. Jones, D.L., The leaching of chalcopyrite, Ph.D. Thesis, Department of Metals and Materials Engineering, University of B.C., Vancouver, Canada, 1974.

26. Warren, G.W., Electrochemical oxidation of chalcopyrite, Ph.D. Thesis, Department of Metallurgy and Metallurgical Engineering, University of Utah, Salt Lake City, USA, 1978.

27. Peters, E., The physical chemistry of hydrometallurgy, *International Symposium on Hydrometallurgy*, D.J.I. Evans and R.S. Shoemaker, Eds., AIME, New York, USA, pp. 205-228, 1973.

28. McGauley, P.J, Cove, G. and Roberts, E.S., Process for the recovery of copper from its ores and minerals, U.S. Patent No. 2,568,963, September 25, 1951.

29. Peters, E., Hydrometallurgical process innovation, *Hydrometallurgy*, 29, pp. 431-459, 1992.

30. Peters, E., Direct leaching of sulfides: chemistry and applications, *Metallurgical Transactions, 7B*, pp. 505-517, 1976.

31. Antonijevic, M.M., Jankovic, Z. and Dimitrijevic, M., Investigation of the kinetics of chalcopyrite oxidation by potassium dichromate, *Hydrometallurgy, 35*, pp. 187-201, 1994.

32. Havlik, T. and Skrobian, M., Acid leaching of chalcopyrite in the presence of ozone, *Canadian Metallurgical Quarterly, 29 (2)*, pp. 133-139, 1990.

33. Hackl, R.P., Peters, E. and Dreisinger, D.B., Reverse leaching of chalcopyrite, *Copper 87 Volume 3, Hydrometallurgy and Electrometallurgy of Copper*, W.C. Cooper, G.E. Lagos and G. Ugarte, Eds., University of Chile, Chile, pp. 181-199, 1987.

34. Jang, J.H. and Wadsworth, M.E., Hydrothermal conversion of chalcopyrite under controlled Eh and pH, *Extractive Metallurgy of Copper, Nickel and Cobalt, Volume I: Fundamental Aspects*, R.G. Reddy and R.N. Weizenbach, Eds., The Minerals, Metals and Materials Society of AIME, Warrendale, PA, USA, pp. 689-707, 1993.

35. Sullivan, J.D., Chemical and physical features of copper leaching, *Transactions of the American Institute of Mining and Metallurgy, 106*, pp. 515-546, 1933.

36. Wadsworth, M.E., Advances in the leaching of sulfide minerals, *Minerals Science and Engineering, 4 (4)*, pp. 36-47, 1972.

37. Roman, R.J. and Benner, B.R., The dissolution of copper concentrates, *Minerals Science and Engineering, 5 (1)*, pp. 3-24, 1973.

38. Dutrizac, J.E. and MacDonald, R.J.C., Ferric ion as a leaching medium, *Minerals Science and Engineering, 6 (2)*, pp. 59-100, 1974.

39. Habashi, F., *Chalcopyrite: Its Chemistry and Metallurgy*, McGraw-Hill, New York, NY, USA., 1978.

40. Dutrizac, J.E., The kinetics of dissolution of chalcopyrite in ferric ion media, *Metallurgical Transactions 9B*, pp. 431-439, 1978.

41. Dutrizac, J.E., The dissolution of chalcopyrite in ferric sulfate and ferric chloride media, *Metallurgical Transactions 12B*, pp. 371-378, 1981.

42. Dutrizac, J.E., Ferric ion leaching of chalcopyrites from different localities, *Metallurgical Transactions 13B*, pp. 303-309, 1982.

43. Dutrizac, J.E., Elemental sulfur formation during the ferric sulfate leaching of chalcopyrite, *Canadian Metallurgical Quarterly, 28 (4)*, pp. 337-344, 1989.

44. Jones, D.L. and Peters, E., The leaching of chalcopyrite with ferric sulfate and ferric chloride, *Extractive Metallurgy of Copper, Volume 2*, J.C. Yannopoulos and J.C. Agarwal, Eds., The Metallurgical Society of AIME, Warrendale, PA., USA, pp. 633-653, 1976.

45. Munoz, P.B., Miller, J.D. and Wadsworth, M.E., Reaction mechanism for the acid ferric sulfate leaching of chalcopyrite, *Metallurgical Transactions 10B*, pp. 149-158, 1979.

46. Beckstead, L.W., Munoz, P.B., Sepulveda, J.L., Herbst, J.A., Miller, J.D., Olson, F.A. and Wadsworth, M.E., Acid ferric sulfate leaching of attritor-ground chalcopyrite concentrates, *Extractive Metallurgy of Copper, Volume 2*, J.C. Yannopoulos and J.C. Agarwal, Eds., The Metallurgical Society of AIME, Warrendale, PA, USA, pp. 611-632, 1976.

47. Majima, H., Awakura, Y., Hirato, T., and Tanaka, T., The leaching of chalcopyrite in ferric chloride and ferric sulfate solutions, *Canadian Metallurgical Quarterly, 24 (4)*, pp. 283-291, 1985.

48. Hirato, T., Majima, H. and Awakura, Y., The leaching of chalcopyrite with ferric sulfate, *Metallurgical Transactions 18B*, pp. 489-496, 1987.

49. Dutrizac, J.E., MacDonald, R.J.C. and Ingraham, T.R., The kinetics of dissolution of synthetic chalcopyrite in aqueous acidic ferric sulfate solutions, *Transactions of the Metallurgical Society of the AIME, 245*, pp. 955-959, 1969.

50. Wan, R.Y., Miller, J.D. and Simkovich, G., Enhanced ferric sulphate leaching of copper from $CuFeS_2$ and C particulate aggregates, *Mintek 50 - International Conference on Mineral Science and Technology*, L.F. Haughton, Ed., The Council for Mineral Technology, Randburg, South Africa, pp. 575-588, 1984.

51. Buttinelli, D., Lavecchia, R., Pochetti, F., Geveci, A., Guresin, N. and Topkaya, Y., Leaching by ferric sulphate of raw and concentrated copper-zinc complex sulphide ores, *International Journal of Mineral Processing, 36*, pp. 245-257, 1992.

52. Linge, H.G., A study of chalcopyrite dissolution in acidic ferric nitrate by potentiometric titration, *Hydrometallurgy, 2*, pp. 51-64, 1976.

53. Lowe, D.F., The kinetics of the dissolution reaction of copper and copper-iron sulfide minerals using ferric sulfate solutions, Ph.D. Thesis, University of Arizona, Arizona, USA, 1970.

54. Dutrizac, J.E. and MacDonald, R.J.C., The effect of some impurities on the rate of chalcopyrite dissolution, *Canadian Metallurgical Quarterly, 12 (4)*, pp. 409-420, 1973.

55. Warren, I.H., A study of the acid pressure leaching of chalcopyrite, chalcocite and covellite, *Australian Journal of Applied Science, 9 (1)*, pp. 36-51, 1957.

56. Mackiw, V.N., Veltman, H. and Vizsolyi, A.I., Direct pressure leaching of copper-iron sulfides, U.S. Patent No. 3,637,371, January 25, 1972.

57. Peters, E. and Loewen, F., Pressure leaching of copper minerals in perchloric acid solutions, *Metallurgical Transactions, 4*, pp. 5-14, 1973.

58. Dysinger, D.K., Murphy, J.E. and Clark, A.E., Leaching of pure chalcopyrite with sulfuric acid-oxygen under in-situ temperatures and pressures, *Hydrometallurgy - Fundamentals, Technology and Innovations*, J.B. Hiskey and G.W. Warren, Eds., Society for Mining, Metallurgy, and Exploration, Inc. of AIME, Littleton, CO, USA, pp. 1029-1043, 1993.

59. Yu, P.H., Hansen, C.K. and Wadsworth, M.E., A kinetic study of the leaching of chalcopyrite at elevated temperatures, *Metallurgical Transactions, 4*, pp. 2137-2144, 1973.

60. Le Houillier, R. and Ghali, E., Contribution to the study of the leaching of chalcopyrite, *Hydrometallurgy, 9*, pp. 169-194, 1982.

61. Duncan, D.W. and Trussel, P.C., Advances in the microbiological leaching of sulfide ores, *Canadian Metallurgical Quarterly, 3 (1)*, pp. 43-55, 1964.

62. Bruynesteyn, A. and Duncan, D.W., Microbiological leaching of sulfide concentrates, *Canadian Metallurgical Quarterly, 10 (1)*, pp. 57-63, 1971.

63. Chen, C.S., Huddleston, R.L. and Johnson, M.A., Bioleaching of chalcopyrite concentrate. Presented at Joint A.I.Ch.Eng.-C.S.Ch.Eng. Meeting held in Vancouver, September, 1973, 26 pp.

64 Torma, A.E. and Itzkovitch, I.J., Influence of organic solvents on chalcopyrite oxidation ability of Thiobacillus ferrooxidans, *Applied and Environmental Microbiology*, July 1976, pp. 102-107.

65. Pinches, A., Al-Jaid, F.O. and Williams, D.J.A., Leaching of chalcopyrite concentrates with Thiobacillus ferrooxidans in batch culture, *Hydrometallurgy, 2*, pp. 87-103, 1976.

66. McElroy, R. and Bruynesteyn, A., Continuous biological leaching of chalcopyrite concentrates: demonstration and economic analysis, *Metallurgical Applications of Bacterial Leaching and Related Microbiological Phenomena*, L.E. Murr, A.E. Torma and J.A. Brierley, Eds., Academic Press, New York, USA, pp. 441-462, 1978.

67. Torma, A.E., Ashman, P.R., Olsen, T.M. and Bosecker, K., Microbiological leaching of a chalcopyrite concentrate and recovery of copper by solvent extraction and electrowinning, *Metall., 33*, pp. 479-484, 1979.

68. Babij, T. and Madgwick, J.C., High yield bacterial leaching of copper concentrates, *Proceedings of the Australasian Institute of Mining and Metallurgy, 287*, pp. 61-64, 1983.

69. Briceno, H. and Rossi, M.C., Bacterial leaching of chalcopyrite concentrates: a preliminary feasibility study, *Copper 87 Volume 3, Hydrometallurgy and Electrometallurgy of Copper*, W.C. Cooper, G.E. Lagos and G. Ugarte, Eds., University of Chile, Chile, pp. 131-147, 1987.

70. Trudinger, P.A., The metabolism of inorganic sulfur compounds by Thiobacilli, *Rev. Pure Appl. Chem., 17*, pp. 1-24, 1967.

71. Liu, M.S., Branion, R.M.R. and Duncan, D.W., Oxygen transfer to *Thiobacillus* cultures, *Biohydrometallurgy, Proceedings of the International Symposium, Warwick, 1987*, P.R. Norris and D.P. Kelly, Eds., pp. 375-384, 1988.

72. Hackl, R.P., Operation of a commercial scale bioleach reactor at the Congress gold property, *Advances in Gold and Silver Processing, Proceedings of the Symposium at GOLDTech 4*, Reno, Nevada, September 10-12, 1990, pp. 131-141, 1990.

73. Gentina, J.C., Rivera, R., Acevedo, F., Retamal, J. and Schaffeld, G., Influence of organic agents on the kinetics of bacterial leaching of copper ores, *Copper 87 Volume 3, Hydrometallurgy and Electrometallurgy of Copper*, W.C. Cooper, G.E. Lagos and G. Ugarte, Eds., University of Chile, Chile, pp. 107-117, 1987.

74. Hiskey, J.B., Chalcopyrite semiconductor electrochemistry and dissolution, *Extractive Metallurgy of Copper, Nickel and Cobalt, Volume 1: Fundamental Aspects*, R.G. Reddy and R.N. Weizenbach, Eds., The Minerals, Metals and Materials Society of AIME, Warrendale, PA, USA, pp. 949-969, 1993.

75. Warren, G.W., Wadsworth, M.E. and El-Raghy, S.M., Passive and transpassive anodic behaviour of chalcopyrite in acid solutions, *Metallurgical Transactions 13B*, December 1982, pp. 571-579.

76. Warren, G.W., Wadsworth, M.E. and El-Raghy, Anodic behaviour of chalcopyrite in sulfuric acid, *Hydrometallurgy, Research, Development and Plant Practice*, K. Osseo-Asare and J.D. Miller, Eds., The Metallurgical Society of AIME, Warrendale, PA, USA, pp. 261-275, 1983.

77. Baur, J.P., Gibbs, H.L. and Wadsworth, M.E., Initial-stage sulfuric acid leaching kinetics of chalcopyrite using radiochemical techniques, *U.S. Bureau of Mines Report of Investigations 7823*, 37pp., 1974.

78. Ammou-Chokroum, Sen, P.K. and Fouques, F., Electrooxidation of chalcopyrite in acid chloride medium; kinetics, stoichiometry and reaction mechanism, *Thirteenth International Mineral Processing Congress, Proceedings Part A*, J. Laskowski, Ed., Elsevier/Polish Scientific Publishers, pp. 759-809, 1979.

79. Linge, H.G., A study of chalcopyrite dissolution in acidic ferric nitrate by potentiometric titration, *Hydrometallurgy, 2*, pp. 51-64, 1976.

80. Parker, A.J., Paul, R.L. and Power, G.P., Electrochemical aspects of leaching copper from chalcopyrite in ferric and cupric salt solutions, *Australian Journal of Chemistry, 34*, pp. 13-34, 1981.

81. Parker, A.J., Paul, R.L. and Power, G.P., Electrochemistry of the oxidative leaching of copper from chalcopyrite, *Journal of Electroanalytical Chemistry 118*, pp. 305-316, 1981.

82. Biegler, T. and Swift, D.A., Anodic electrochemistry of chalcopyrite, *Journal of Applied Electrochemistry, 9*, pp. 545-554, 1979.

83. Biegler, T. and Horne, M.D., The electrochemistry of surface oxidation of chalcopyrite, *Electrochemistry in Mineral and Metal Processing*, P.E. Richardson, S. Srinivasan and R. Woods, Eds., The Electrochemical Society, Inc., Pennington, NJ, USA, pp. 321-339, 1984.

84. Holliday, R.J. and Richmond, W.R., An electrochemical study of the oxidation of chalcopyrite in acidic solution, *Journal of Electroanalytical Chemistry, 288*, pp. 83-98, 1990.

85. Gardner, J.R. and Woods, R., An electrochemical investigation of the natural flotability of chalcopyrite, *International Journal of Mineral Processing, 6*, pp. 1-16, 1979.

86. Hamilton, I.C. and Woods, R., A voltammetric study of the surface oxidation of sulfide minerals, *Electrochemistry in Mineral and Metal Processing*, P.E. Richardson, S. Srinivasan and R. Woods, Eds., The Electrochemical Society, Inc., Pennington, NJ, USA, pp. 259-285, 1984.

87. Jones, D.L. and Peters, E., Electrochemical experiments with chalcopyrite electrodes in aqueous solutions up to 200°C, *High Temperature High Pressure Electrochemistry in Aqueous Solutions, NACE-4*, pp. 443-458, 1976.

88. Peters, E., The electrochemistry of sulfide minerals, *Trends in Electrochemistry*, J.O'M. Bockris, D.A.J. Rand and B.J. Welch, Eds., Plenum Publishing Corp., New York, USA, pp. 267-290, 1977.

89. Clifford, R.K., Purdy, K.L. and Miller, J.D., Characterization of sulfide mineral surfaces in froth flotation systems using electron spectroscopy for chemical analysis, *Advances in Interfacial Phenomena*, A.I.Ch.E. Symposium Series 71 (150), pp. 138-147, 1975.

90. Smart, R.St.C., Surface layers in base metal sulfide flotation, *Minerals Engineering, 4 (7-11)*, pp. 891-909, 1991.

91. Eadington, P., Study of oxidation layers on surfaces of chalcopyrite by use of Auger electron spectroscopy, *Transactions of the Institution of Mining and Metallurgy, 86*, pp. C186-C189, 1977.

92. Brion, D., Etude par spectroscopie de photoelectrons de la degradation superficielle de FeS_2, $CuFeS_2$, ZnS et PbS a l'air et dans l'eau, *Applications of Surface Science, 5*, pp. 133-152, 1980.

93. Holloway, P.H., Remond, G. and Swartz, W.E., Jr., Surface composition and reflectance of polished $CuFeS_2$, *Interfacial Phenomena in Mineral Processing*, B. Yarar and D.J. Spottiswood, Eds., Engineering Foundation, New York, USA, pp. 93-117, 1981.

94. Ruzakowski, P.H., Holloway, P.H. and Remond, G., Complementary surface characterization of chalcopyrite by electron microscopy, electron spectroscopy, and optical reflectance, *Scanning Microscopy, 3 (1)*, pp. 71-82, 1989.

95. Luttrell, G.H. and Yoon, R.H., Surface studies of the collectorless flotation of chalcopyrite, *Colloids and Surfaces, 12*, pp. 239-254, 1984.

96. Buckley, A.N. and Woods, R., An x-ray photoelectron spectroscopic study of the oxidation of galena, *Applications of Surface Science, 17*, pp. 401-414, 1984.

97. Buckley, A.N. and Woods, R., An x-ray photoelectron spectroscopic study of the oxidation of chalcopyrite, *Australian Journal of Chemistry, 37*, pp. 2403-2413, 1984.

98. Buckley, A.N. and Woods, R., An x-ray photoelectron spectroscopic investigation of the surface oxidation of sulfide minerals, *Electrochemistry in Mineral and Metal Processing*, P.E. Richardson, S. Srinivasan and R. Woods, Eds., The Electrochemical Society, Inc., Pennington, NJ, USA, pp. 286-302, 1984.

99. Folmer, J.C.W. and Jellinek, F., The valence of copper in sulfides and selenides: an x-ray photoelectron spectroscopy study, *Journal of the Less-Common Metals, 76*, pp. 153-162, 1980.

100. Folmer, J.C.W., Jellinek, F. and Calis, G.H.M., The electronic structure of pyrites, particularly CuS_2 and $Fe_{1-x}Cu_xSe_2$: an XPS and Mössbauer study, *Journal of Solid State Chemistry, 72*, pp. 137-144, 1988.

101. Burkin, A.R., Composition and phase changes during oxidative acid leaching reactions, *Hydrometallurgical Process Fundamentals*, R.G. Bautista, Ed., Plenum Press, New York, USA pp. 113-123, 1984.

102. Warren, I.H., Vizsolyi, A. and Forward, F.A., The pretreatment and leaching of chalcopyrite, *CIM Bulletin, 61 (673)*, pp. 637-640, 1968.

103. Subramanian, K.N. and Kanduth, H., Activation and leaching of chalcopyrite concentrate, *CIM Bulletin, 66 (734)*, pp. 88-91, 1973.

104. Parker, A.J., Muir, D.M., Giles, D.E. and Alexander, R., The leaching of copper from sulfur activated chalcopyrite with cupric sulfate in nitrile-water mixtures, *Hydrometallurgy, 1*, pp. 169-181, 1975.

105. Adam, M.J. and Neumeier, L.A., Partitioning of chalcopyrite by sulfidation, *Process Mineralogy VII: Applications to Mineral Beneficiation Technology and Mineral Exploration, With Special Emphasis on Disseminated Carbonaceous Gold Ores*, A.H. Vassiliou, D.M Hausen and D.J.T. Carson, Eds., The Metallurgical Society of AIME, Warrendale, PA, USA, pp. 511-523, 1987.

106. Jolly, A.F. and Neumeier, L.A., Leaching sulfidation-partitioned chalcopyrite to selectively recover copper, *U.S. Bureau of Mines Report of Investigations 9343*, 12 pp, 1991.

107. Swinkels, G.M., and Berezowski, R.M.G.S., The Sherritt - Cominco copper process - part I: the process, *CIM Bulletin, 71 (790)*, pp. 105-121, 1978.

108. Kawulka, P., Kirby, C. R. and Bolton, G.L., The Sherritt - Cominco copper process - part II: pilot-plant operation, *CIM Bulletin, 71 (790)*, pp. 122-130, 1978.

109. Maschmeyer, D.E.G., Milner, E.F.G. and Parekh, B.M, The Sherritt - Cominco copper process - part III: commercial implications, *CIM Bulletin, 71 (790)*, pp. 131-139, 1978.

110. Gerlach, J.K., Gock, E.D. and Ghosh, S.K., Activation and leaching of chalcopyrite concentrates with dilute sulfuric acid, *International Symposium on Hydrometallurgy*, D.J.I. Evans and R.S. Shoemaker, Eds., AIME, New York, USA, pp. 403-416, 1973.

111. Wadsworth, M.E., Miller, J.D., Herbst, J.A., Kolbe, J.L. and Hayden, H.W., Acid ferric sulfate leaching of copper sulfide concentrates, U.S. Patent 4,115,221, September 19, 1978.

112. Rice, D.A., Cobble, J.R. and Brooks, D.R., Effects of turbomilling parameters on the simultaneous grinding and ferric sulfate leaching of chalcopyrite, *U.S. Bureau of Mines Report of Investigations 9351*, 9 pp, 1991.

113. Cobble, J.R., Improved leaching kinetics of chalcopyrite with simultaneous grinding and leaching. *Paper 91-134 presented at the 1991 SME Annual Meeting*, Denver, USA, February 25-28, 1991, 10 pp.

114. Tkacova, K. and Balaz, P., Structural and temperature sensitivity of leaching of chalcopyrite with iron (III) sulfate, *Hydrometallurgy, 21*, pp. 103-112, 1988.

115. Tiwari, B.L., Kolbe, J. and Hayden, H.W., Leaching of high-solids, attritor-ground chalcopyrite concentrate by in-situ generated ferric sulfate solution, *Metallurgical Transactions 11B*, pp. 89-93, 1980.

116. Snell, G.J., Sulfate leaching of copper ores using silver catalyst, U.S. Patent 3,886,257, May 27, 1975.

117. Snell, G.J., New oxidative leaching process uses silver to enhance copper recovery, *Engineering and Mining Journal*, October 1977, pp. 100-105.

118. Pawlek, F.E., Hydrometallurgical process for extracting copper from chalcopyrite or bornite concentrates, U.S. Patent 3,949,051, April 6, 1976.

119. Pawlek, F.E., The influence of grain size and mineralogical composition on the leachability of copper concentrates, *Extractive Metallurgy of Copper, Volume 2*, J.C. Yannopoulos and J.C. Agarwal, Eds., The Metallurgical Society of AIME, Warrendale, PA, USA, pp. 690-705, 1976.

120. Miller, J.D. and Portillo, H.Q., Silver catalysis in ferric sulfate leaching of chalcopyrite, *Thirteenth International Mineral Processing Congress, Proceedings Part A*, J. Laskowski, Ed., Elsevier/Polish Scientific Publishers, pp. 851-901, 1979.

121. Miller, J.D., McDonough, P.J. and Portillo, H.Q., Electrochemistry in silver catalyzed ferric sulfate leaching of chalcopyrite, *Process and Fundamental Considerations of Selected Hydrometallurgical Systems*, M.C. Kuhn, Ed., Society for Mining, Metallurgy, and Exploration, Inc. of AIME, Littleton, CO, USA, pp. 327-338, 1981.

122. Mateos, F.B., Perez, I.P. and Mora, F.C., The passivation of chalcopyrite subjected to ferric sulfate leaching and its reactivation with metal sulfides, *Hydrometallurgy, 19*, pp. 159-167, 1987.

123. Peters, E. and Doyle, F.M., Leaching and decomposition of sulfide minerals, *Challenges in Mineral Processing*, K.V.S. Sastry and M.C. Fuerstenau, Eds., Society for Mining, Metallurgy, and Exploration, Inc. of AIME, Littleton, CO, USA, pp. 509-526, 1988.

124. McElroy, R.O. and Duncan, D.W., Copper extraction by a rapid bacteriological method, U.S. Patent 3,856,913, December, 1974.

125. Bruynesteyn, A., Hackl, R.P., Lawrence, R.W. and Vizsolyi, A.I., Biological-acid leach process, U.S. Patent 4,571,387, February 18, 1986.

126. Lawrence, R.W., Vizsolyi, A. and Vos, R.J., The silver catalyzed bioleach process for copper concentrate, *Microbiological Effects On Metallurgical Processes*, J.A. Clum and L.A. Haas, Eds., The Minerals, Metals and Materials Society of AIME, Warrendale, PA, USA, pp. 65-82, 1985.

127. Tuovinen, O.H., Puhakka, J., Hiltunen, P. and Dolan, K.M., Silver toxicity to ferrous iron and pyrite oxidation and its alleviation by yeast extract in cultures of *Thiobacillus ferrooxidans*, *Biotechnology Letters, 7*, pp. 389-394, 1985.

128. Sukla, L.B., Chaudhury, G.R. and Das, R.P., Effect of silver ion on kinetics of biochemical leaching of chalcopyrite concentrate, *Trans. Instn. Min. Metall. C, 99*, pp. C43-C46, 1990.

129. Ballester, A., Gonzalez, F., Blazquez, M.L., Gomez, C. and Mier, J.L., The use of catalytic ions in bioleaching, *Hydrometallurgy, 29*, pp. 145-160, 1992.

130. Myers, D., *Surfactant Science and Technology*, VCH Publishers Inc., New York, USA, p. 10, 1988.

131. Myers, D., *Surfactant Science and Technology*, VCH Publishers Inc., New York, USA, p. 42, 1988.

132. Osseo-Asare, K., Interfacial phenomena in leaching systems, *Hydrometallurgical Process Fundamentals*, R.G. Bautista, Ed., Plenum Press, New York, USA, pp. 227-268, 1984.

133. Owusu, G., The role of surfactants in the leaching of zinc sulphide minerals at temperatures above the melting point of sulphur, Ph.D. Thesis, Department of Metals & Materials Engineering, University of B.C., Vancouver, Canada, 1993, 208 pp.

134. Owusu, G., Dreisinger, D.B. and Peters, E., Interfacial effects of surface-active agents under zinc pressure leach conditions, *Metallurgical and Materials Transactions B, 26B*, pp. 5-12, 1995.

135. Young, T., *Miscellaneous Works, Vol. I*, G. Peacock, Ed., Murray, London, p. 418, 1855.

136. Forward, F.A. and Veltman, H., Direct leaching zinc sulfide concentrates by Sherritt Gordon, *Journal of Metals, 11*, pp. 836-840, 1959.

137. Morikawa, T., Shoji, K. and Wakamatsu, N., Acid pressure leaching of metal sulfide concentrates, Japan Patent, Showa 47-7965, March 7, 1972.

138. Salomon-De-Friedberg, H., personal communication, Cominco Ltd., Trail, B.C., December 7, 1992.

139. Boissoneault, M., personal communication, Falconbridge Ltd., Kidd Creek Division, Timmins, Ontario, December 17, 1992.

140. Krysa, B., personal communication, Hudson Bay Mining and Smelting Company, Flin Flon, Manitoba, January 6, 1993.

141. Dreisinger, D.B., personal communication, Department of Metals and Materials Engineering, University of B.C., Vancouver, B.C., December 1992.

142. Bolton, G.L., Zubryckyj, N. and Veltman, H., Pressure leaching process for complex zinc-lead concentrates. Paper presented at the *13th International Mineral Processsing Congress*, Warsaw, Poland, June 1979.

143. Kunda, W., Rudyk, B. and Mackiw, V.N., Iron and sulphur from sulphidic iron ores, *CIM Bulletin, 61 (675)*, pp. 819-835, 1968.

144. Thornhill, P.G., Autoclave treatment of pyrrhotite for sulfur recovery, *Canadian Metallurgical Quarterly, 8 (2)*, pp. 219-225, 1969.

145. Ryan, P.J.M., Leaching sulfide concentrates, Canadian Patent 964,867, May 8, 1972.

146. Jones, W.E., Krause, E. and O'Neill, C.E., High temperature leaching of sulfide ores, Canadian Patent 1,024,355, January 17, 1978.

147. Krause, E., personal communication, INCO Ltd., J. Roy Gordon Research Centre, Mississauga, Ontario, December 8, 1992.

148. Shneerson, Y.M., Krasnov, A.L., Kukin, A.V., Vigdorchik, E.M., Filippov, G.F. and Sirkis, A.L., Kinetics of high-temperature leaching of pyrrhotite concentrates, *Tsvetnye Metally, 59 (1)*, pp. 17-19, 1986.

149. Yakovlev, V.V., Mantsevich, M.I. and Shcherbakov, V.A., Improving sulfur-sulfide flotation efficiency in autoclaving of pyrrhotite concentrates, *Tsvetnye Metally, 59 (2)*, pp. 90-91, 1986.

150. Berezowski, R.M.G.S., Haines, A.K. and Weir, D.R., The Sao Bento gold project - pressure oxidation process development, *Projects '88, Proceedings of the 18th Annual Hydrometallurgical Meeting of the CIM*, Edmonton, Canada, May 9-11, 1988.

151. Carvalho, T.M., Haines, A.K., da Silva, E.J., Doyle, B.N. and Stauffer, R.F., Startup of the Sherritt pressure oxidation process at Sao Bento, *Precious Metals '89, Proceedings of the 13th International Precious Metals Institute Conference*, Montreal, Canada, B. Harris, Ed., pp. 319-326, 1989.

152. L'amour, C., personal communication, Placer Dome Inc., Porgera Operations, December 17, 1992.

153. Suttill, K., Sao Bento plans bioox, *Engineering and Mining Journal*, June 1990, pp. 30-34.

154. Frostiak, J. and Haugrud, B., Start-up and operation of Placer Dome's Campbell Mine gold pressure oxidation plant, *Mining Engineering*, August 1992, pp. 991-993.

155. Frostiak, J., personal communication, Placer Dome Inc., Campbell Mine, Balmertown, Ontario, January 6, 1993.

156. Geldart, J., Williamson, R. and Maltby, P., Aqueous pressure oxidation as a waste treatment process - stabilizing roaster wastes, *Hydrometallurgy, Theory and Practice, Part B, Proceedings of the Ernest Peters International Symposium*, W.C. Cooper and D.B. Dreisinger, Eds., Elsevier, Amsterdam, The Netherlands, pp. 29-44, 1992.

157. Maltby, P., personal communication, Nerco Con Mine, Yellowknife, Northwest Territories, December 11, 1992.

158. Pieterse, H., personal communication, Barrick Goldstrike Mine, Carlin, Nevada, December 11, 1992.

159. Goldstein, J.I., Electron beam-specimen interaction, *Practical Scanning Electron Microscopy, Chapter III*, J.I. Goldstein and H. Yakowitz, Eds., Plenum Press, New York, NY, USA, pp. 49-94, 1975.

160. McIntyre, N.S. and Chan, T.C., Uses of Auger electron and photoelectron spectroscopies in corrosion science, *Practical Surface Analysis, 2nd Edition, Volume I: Auger and X-Ray Photoelectron Spectroscopy, Chapter 10*, D. Briggs and M.P. Seah, Eds., John Wiley & Sons, New York, NY, USA, pp. 485-529, 1990.

161. Smart, R.St.C., Surface layers in base metal sulfide flotation, *Minerals Engineering, 4 (7-11)*, pp. 891-909, 1991.

162. Hochella, M.F. Jr., Auger electron and X-ray photoelectron spectroscopies, *Reviews in Mineralogy, Volume 18, Spectroscopic Methods in Mineralogy and Geology, Chapter 13*, F.C. Hawthorne, Ed., Mineralogical Society of America, Washington, DC, USA, pp. 573-637, 1988.

163. Nesbitt, H.W. and Pratt, A.R., Applications of Auger-electron spectroscopy to geochemistry, *The Canadian Mineralogist, 33*, pp. 243-259, 1995.

164. Briggs, D. and Rivière, J.C., Spectral interpretation, *Practical Surface Analysis, 2nd Edition, Volume I: Auger and X-Ray Photoelectron Spectroscopy, Chapter 3*, D. Briggs and M.P. Seah, Eds., John Wiley & Sons, New York, NY, USA, pp. 85-141, 1990.

165. Davis, L.E., MacDonald, N.C., Palmberg, P.W., Riach, G.E. and Weber, R.E., *Handbook of Auger Electron Spectroscopy, 2nd Edition*, Perkin-Elmer Corporation, Eden Prairie, Minnesota, USA, 190 pp, 1976.

166. Browning, R., Auger spectroscopy and scanning Auger spectroscopy, *Surface Analysis Methods in Materials Science, Chapter 6*, D.J. O'Connor, B.A. Sexton and R.St.C. Smart, Eds., Springer-Verlag, New York, NY, USA, pp. 149-164, 1992.

167. Seah, M.P., Quantification of AES and XPS, *Practical Surface Analysis, 2nd Edition, Volume I: Auger and X-Ray Photoelectron Spectroscopy, Chapter 5*, D. Briggs and M.P. Seah, Eds., John Wiley & Sons, New York, NY, USA, pp. 201-255, 1990.

168. Hochella, M.F. Jr., Turner, A.M. and Harris, D.W., High resolution scanning Auger microscopy of mineral surfaces, *Scanning Electron Microscopy, II*, pp. 337-349, 1986.

169. Kibel, M.H., X-ray photoelectron spectroscopy, *Surface Analysis Methods in Materials Science, Chapter 7*, D.J. O'Connor, B.A. Sexton and R.St.C. Smart, Eds., Springer-Verlag, New York, NY, USA, pp. 165-186, 1992.

170. Muilenburg, G.E. (Ed.), *Handbook of X-ray Photoelectron Spectroscopy*, Perkin-Elmer Corporation, Eden Prairie, Minnesota, USA, 1979.

171. Sherwood, P.M.A., Data analysis in XPS and AES, *Practical Surface Analysis, 2nd Edition, Volume I: Auger and X-Ray Photoelectron Spectroscopy, Appendix 3*, D. Briggs and M.P. Seah, Eds., John Wiley & Sons, New York, NY, USA, pp. 555-586, 1990.

172. Waddington, S.D., Auger chemical shifts and the Auger parameter, *Practical Surface Analysis, 2nd Edition, Volume I: Auger and X-Ray Photoelectron Spectroscopy, Appendix 4*, D. Briggs and M.P. Seah, Eds., John Wiley & Sons, New York, NY, USA, pp. 587-594, 1990.

173. Watts, J.F., *An Introduction to Surface Analysis by Electron Spectroscopy*, Oxford University Press Oxford, UK, p. 23, 1990.

174. Hofmann, S., Depth profiling in AES and XPS, *Practical Surface Analysis, 2nd Edition, Volume I: Auger and X-Ray Photoelectron Spectroscopy, Chapter 4*, D. Briggs and M.P. Seah, Eds., John Wiley & Sons, New York, NY, USA, pp. 143-199, 1990.

175. Lignosite lignin products, Product Information Sheet, Georgia-Pacific Corporation, Bellingham, WA, USA, 5 pp., 1990.

176. Kina, K. and Tôei, K., Stability constants of Cu(II) chelates with o-phenylenediamine derivatives, *Bulletin of the Chemical Society of Japan, 44*, pp. 1289-1293, 1971.

177. Handbook of Chemistry and Physics, 63rd Edition, R.C. Weast and M.J. Astle, Eds., CRC Press, Inc., Boca Raton, Florida, USA, p. F-6, 1982-1983.

178. Ambwani, D.S. and Fort Jr., T., Pendant drop technique for measuring liquid boundary tensions, Surface and Colloid Science, Volume II, Experimental Methods, R.J. Good and R.R. Stromberg, Eds., Plenum Press, New York, NY, USA, pp. 93-119, 1979.

179. Rotenberg, Y., Boruvka, L. and Neumann, A.W., Determination of surface tension and contact angle from the shapes of axisymmetric fluid interfaces, *Journal of Colloid and Interface Science, 93 (1)*, pp. 169-183, 1983.

180. Cheng, P., Li, D., Boruvka, L., Rotenberg, Y. and Neumann, A.W., Automation of axisymmetric drop shape analysis for measurements of interfacial tensions and contact angles, *Colloids and Surfaces, 43*, pp. 151-167, 1990.

181. Adamson, A.W., *Physical Chemistry of Surfaces, Second Edition*, Interscience Publishers, New York, NY, USA, p. 353, 1967.

182. Berg, R.H., Electronic size analysis of subsieve particles by flowing through a small liquid resistor. In: *Symposium on Particle Size Measurement*, Special Technical Publication No. 234, American Society for Testing Materials, 6 pp., 1958.

183. Instruction Manual for Particle Size Distribution Analyzer: Model CAPA-700, Horiba Instruments Inc., Kyoto, Japan.

184. Devon, M.J., Provder, T. and Rudin, A., Measurement of particle size distributions with a disc centrifuge, *Particle Size Distribution II, Assessment and Characterization, Chapter 9,* T. Provder, Ed., ACS Symposium Series 472, American Chemical Society, Washington, DC, USA, pp. 134-153, 1991.

185. Grewal, I., Dreisinger, D.B., Krueger, D., Tyroler, P.M., Krause, E. and Nissen, N.C., Total oxidative leaching of Cu_2S-containing residue at INCO Ltd.'s copper refinery: laboratory studies on the reaction pathways, *Hydrometallurgy, 29*, pp. 319-333, 1992.

186. DOWFAX Anionic Surfactants, Dow Chemical Company Brochure No. 192-1108-1191, 1991.

187. Sierakowski, M.J., Personal Communication, 3M Company, 1993.

188. Davis, L.E., MacDonald, N.C., Palmberg, P.W., Riach, G.E. and Weber, R.E., *Handbook of Auger Electron Spectroscopy, 2nd Edition*, Physical Electronics Division, Eden Prairie, Minnesota, USA, 190 pp, 1976.

189. Bailey, L.K. and Peters, E., Decomposition of pyrite in acids by pressure leaching and anodization: the case for an electrochemical mechanism, *Canadian Metallurgical Quarterly, 15 (4)*, pp. 333-344, 1976.

190. Malherbe, J.B., Hofmann, S. and Sanz, J.M., Preferential sputtering of oxides: a comparison of model predictions with experimental data, *Applied Surface Science, 27*, pp. 355-365, 1986.

191. Saeki, N. and Shimuzu, R., Auger study of preferential sputtering for Cu-Ni alloy sample, *Japanese Journal of Applied Physics, 17 (1)*, pp. 59-68, 1978.

192. Seah, M.P., Pure element sputtering yields using 500-1000 eV argon ions, *Thin Solid Films, 81*, pp. 279-287, 1981.

193. Remond, G., Holloway, P.H. and Le Gressus, C., Electron spectroscopy and microscopy for studying surface changes of mechanically prepared pyrite and quartz, *Scanning Electron Microscopy, I*, pp. 483-492, 1981.

194. Pratt, A.R., Muir, I.J. and Nesbitt, H.W., X-ray photoelectron and Auger electron spectroscopic studies of pyrrhotite and mechanism of air oxidation, *Geochimica et Cosmochimica Acta, 58 (2)*, pp. 827-841, 1994.

195. Mycroft, J.R., Bancroft, G.M, McIntyre, N.S., Lorimer, J.W. and Hill, I.R., Detection of sulphur and polysulphides on electrochemically oxidized pyrite surfaces by X-ray photoelectron spectroscopy and Raman spectroscopy, *Journal of Electroanalytical Chemistry, 292*, pp. 139-152, 1990.

196. Li, J., Zhu, X. and Wadsworth, M.E., Raman spectroscopy of natural and oxidized metal sulfides, *EPD Congress 1993*, J.P. Hager, Ed., The Minerals, Metals and Materials Society of AIME, Warrendale, PA, USA, pp. 229-244, 1992.

197. Levenspiel, O., *Chemical Reaction Engineering, Second Edition, Chapter 12, Fluid-Particle Reactions*, John Wiley & Sons, New York, NY, USA, pp. 357-408, 1972.

198. Peters, E., The mathematical modeling of leaching systems, *Journal of Metals, 43 (2)*, pp. 20-26, 1991.

199. Dixon, D.G., *Hydrometallurgical Reactor Design and Analysis, Chapters 6 and 7*, Hydrometallurgy Short Course, Department of Metals and Materials Engineering, University of B.C. Vancouver, B.C., Canada, 1995.

200. Gregg, S.J. and Sing, K.S.W., *Adsorption, Surface Area and Porosity, Chapter 2*, Academic Press, New York, NY, USA, 1967.

201. Ahn, J.H. and Wadsworth, M.E., The electrochemical reaction kinetics of molybdenite in aqueous acid solution, *Electrochemistry in Mineral and Metal Processing II*, P.E. Richardson and R. Woods, Eds., The Electrochemical Society, Inc., Pennington, NJ, USA, pp. 280-302, 1988.

202. Zhu, X., Li, J. and Wadsworth, M.E., Kinetics of the transpassive oxidation of pyrite, *EPD Congress 1993*, J.P. Hager, Ed., The Minerals, Metals and Materials Society of the AIME, Warrendale, PA, USA, pp. 355-368, 1993.

APPENDIX 1

THEORY OF AXISYMMETRIC DROP SHAPE ANALYSIS

Sulfur-solution interfacial tensions and chalcopyrite-sulfur contact angles were determined using the Axisymmetric Drop Shape Analysis-Profile (ADSA-P) program developed by Rotenberg *et al.* [1]. The ADSA-P program automatically digitizes the drop profile from negative or positive photographic images, then fits the drop profile curve to a curve satisfying the Laplace equation of capillarity. The equation is solved numerically to obtain the interfacial tension and contact angle. An overview of the theory behind the method, summarized from ref. [1], is presented here.

The Laplace equation relates the pressure difference across a curved interface separating two bulk media to the interfacial tension and curvature of the interface [2]:

$$\gamma\left(\frac{1}{R_1}+\frac{1}{R_2}\right)=\Delta P \tag{A1-1}$$

where γ is the interfacial tension, R_1 and R_2 are the two principal radii of curvature, and ΔP is the pressure difference across the interface. In the absence of external forces other than gravity, the pressure difference is a linear function of the elevation:

$$\Delta P=\Delta P_o+(\Delta\rho)gz \tag{A1-2}$$

where ΔP_o is the pressure difference at a reference plane, $\Delta\rho$ is the density difference between the two bulk phases, g is the gravitational acceleration and z is the vertical height of the drop measured from the reference plane.

When the origin of the coordinate system is placed at the apex point of the drop and the x-axis is tangent to the origin and normal to the axis of symmetry (Figure A1-1), equation (A1-1) can be rewritten as:

$$\gamma\left(\frac{1}{R_1}+\frac{\sin\phi}{x}\right)=\frac{2\gamma}{R_o}+(\Delta\rho)gz \tag{A1-3}$$

where R_1 turns in the plane of the paper, $R_2 = x/\sin\phi$ rotates in the plane perpendicular to the paper and about the axis of symmetry, and R_o is the radius of curvature at the origin ($R_0 = R_1 = R_2$ at the origin). ϕ is the turning angle measured between the tangent of the interface at (x_1, z_1) and the plane of reference, and represents the contact angle at the point where the liquid touches the solid surface.

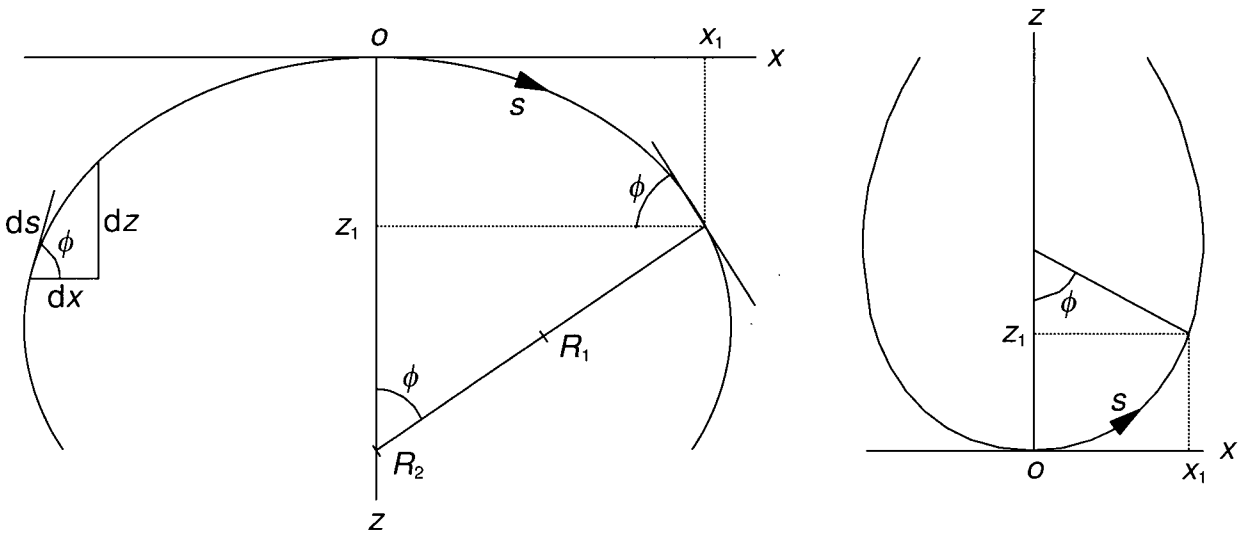

(a) (b)

Figure A1-1. Definition of the coordinate system for (a) a sessile drop and (b) a pendant drop [1]. At a point (x_1, z_1), the turning angle is ϕ and s is the arc length measured along the drop. R_1 and R_2 are the two principal radii of curvature; R_1 turns in the plane of the paper and R_2 rotates in the plane perpendicular to the paper.

Since the drop is axisymmetric, the interface can be described by the meridian section alone, shown in Figure A1-1. If the interface is given by:

$$u = u(x, y, z) \tag{A1-4}$$

the meridian curve can be represented by:

$$x = x(s),\ z = z(s) \tag{A1-5}$$

where s is the arc length measured from the origin, o. A geometrical consideration yields the differential identities:

$$\frac{dx}{ds} = \cos\phi \tag{A1-6}$$

and:

$$\frac{dz}{ds} = \sin\phi \tag{A1-7}$$

By definition:

$$\frac{1}{R_1} = \frac{d\phi}{ds} \tag{A1-8}$$

is the rate of change of the turning angle ϕ with respect to the arc-length s. Hence, combining equation (A1-8) with (A1-3) and rearranging yields:

$$\frac{d\phi}{ds} = \frac{2}{R_o} + \frac{(\Delta\rho)g}{\gamma} z - \frac{\sin\phi}{x} \tag{A1-9}$$

Equations (A1-6), (A1-7) and (A1-9) from a set of first-order differential equations with boundary conditions:

$$x(0) = z(0) = \phi(0) = 0 \tag{A1-10}$$

For a given R_o and $(\Delta\rho)g/\gamma$ the complete shape of the curve may be obtained by integrating these three equations simultaneously.

The ADSA-P program automatically digitizes the drop profile to provide measured profile points μ_n, $n = 1, \ldots N$. These points are compared to a calculated Laplace curve, $v = v(s)$, by computing the normal distance between u_n and v. The program defines an objective function, E:

$$E = \tfrac{1}{2}\sum_n \left[d(u_n, v)\right]^2 \tag{A1-11}$$

where $d(u_n, v)$ is the normal distance between μ_n and the curve v. This function is a measure of the discrepancy between the calculated Laplace curve and the measured curve. The value of E depends on the shape of the curve v, and on its position relative to the axis of symmetry of the

measured curve u. The position of the axis of symmetry of the calculated curve relative to the axis of symmetry of the measured curve is fixed by the location of the origin (X_o, Z_o) of the measured curve. The origins of the two curves must coincide if the function E is to assume a minimum value. Since (X_o, Z_o) cannot be determined accurately these coordinates are regarded as variables. As a result, the value of E is a function of four variables, q_1, q_2, q_3 and q_4, where:

$$q_1 = X_o \tag{A1-12}$$

$$q_2 = Z_o \tag{A1-13}$$

$$q_3 = R_o \tag{A1-14}$$

$$q_4 = \frac{(\Delta\rho)gR_o^2}{\gamma} \tag{A1-15}$$

The minimization of E leads to a system of nonlinear equations which are solved by using the Newton-Raphson method with incremental loading. The function values x, z ϕ and their derivatives, which are terms in the nonlinear equations, must be solved from equations (A1-6), (A1-7) and (A1-9). A second order implicit Euler method is used to perform the numerical integration. Refer to ref. [1] for further details.

The ADSA-P program requires as input: (1) coordinate points along the drop profile, (2) the value of the density difference, $\Delta\rho$, between the bulk phases, (3) the value of the local gravitational acceleration, g (g is assigned positive for sessile drops and negative for pendant drops), and (4) the unmagnified and magnified capillary tip diameters. The program starts with $q_4 = 0$, i.e., γ = infinity, and the parameters X_o, Z_o and R_o are then determined within the program. The solution of the ADSA-P program yields interfacial tension, contact angle, volume, surface area, radius of curvature at the origin, and contact radius of the drop.

Appendix 1 References

1. Rotenberg, Y., Boruvka, L. and Neumann, A.W., Determination of surface tension and contact angle from the shapes of axisymmetric fluid interfaces, *Journal of Colloid and Interface Science, 93 (1)*, pp. 169-183, 1983.

2. de Laplace, P.S., *Mechanique Celeste, Supplement to Book 10*, J.B.M. Duprat, Paris, 1806.

APPENDIX 2

FUNCTION FITTING OF COPPER EXTRACTION DATA AND DETERMINATION OF INSTANTANEOUS COPPER LEACH RATES

The procedure used for determining instantaneous copper leach rates from copper extraction data is outlined here. First, the copper extraction plots were mathematically fitted to a hyperbolic function using Microcal Origin™'s nonlinear least-squares curve fitting software [1]. The hyperbolic function is of the following general form:

$$y = \frac{P_1 x}{P_2 + x} + \frac{P_3 x}{P_4 + x} + P_5 x \qquad \text{(A2-1)}$$

where in this case y = percent Cu extraction, x = leach residence time in minutes and $P_1,...P_5$ are constants.

Then, equation (A2-1) was differentiated to obtain the rate equation:

$$\frac{dy}{dx} = \frac{P_1}{P_2 + x} - \frac{P_1 x}{(P_2 + x)^2} + \frac{P_3}{P_4 + x} - \frac{P_3 x}{(P_4 + x)^2} + P_5 \qquad \text{(A2-2)}$$

where dy/dx is the instantaneous copper leach rate at any x, in units of %Cu/min.

The copper extraction data obtained for the low pulp density runs on the $CuFeS_2$ concentrate at 110°C and 125°C (discussed in Sections 5.2.2 and 6.5) and the CuS sample at 110°C (Section 6.6) were fitted in this fashion. Table A2-1 lists the values of the coefficients $P_1,...P_5$ obtained for each set of runs. Figure A2-1 portrays the copper extraction and copper leach rate plots vs. time. It can be seen that the function fits are quite good.

Table A2-1. Coefficient values obtained for function fitted copper extraction data.

Sample	Leach Temp. (°C)	P_1	P_2	P_3	P_4	P_5
$CuFeS_2$	110	39.19	23.73	0.5473	0	0.0884
$CuFeS_2$	125	46.36	31.68	0	0	0
CuS	110	65.94	15.69	6.451	0	0.0506

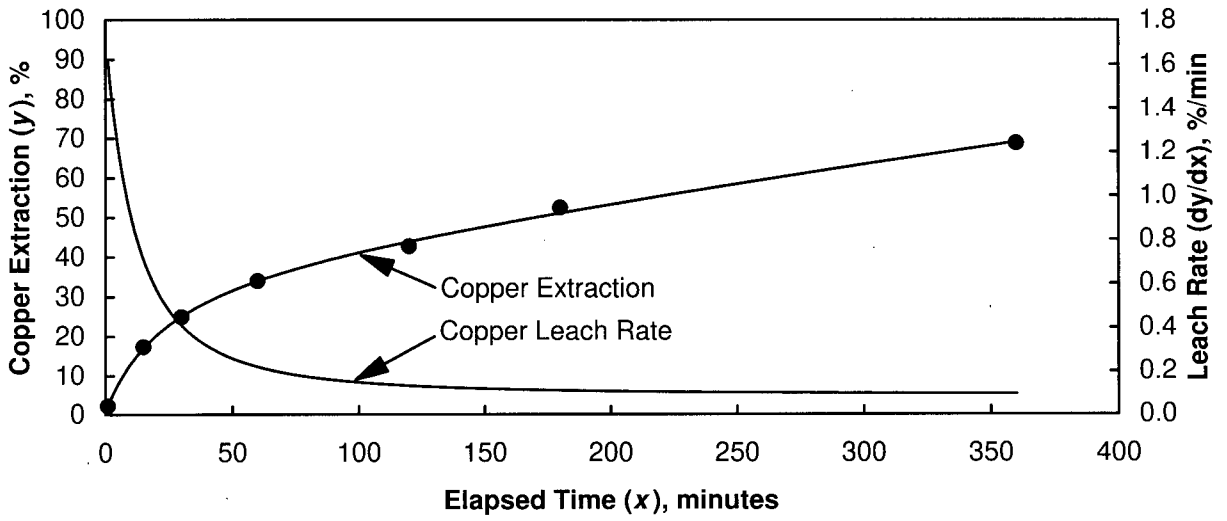

(a)

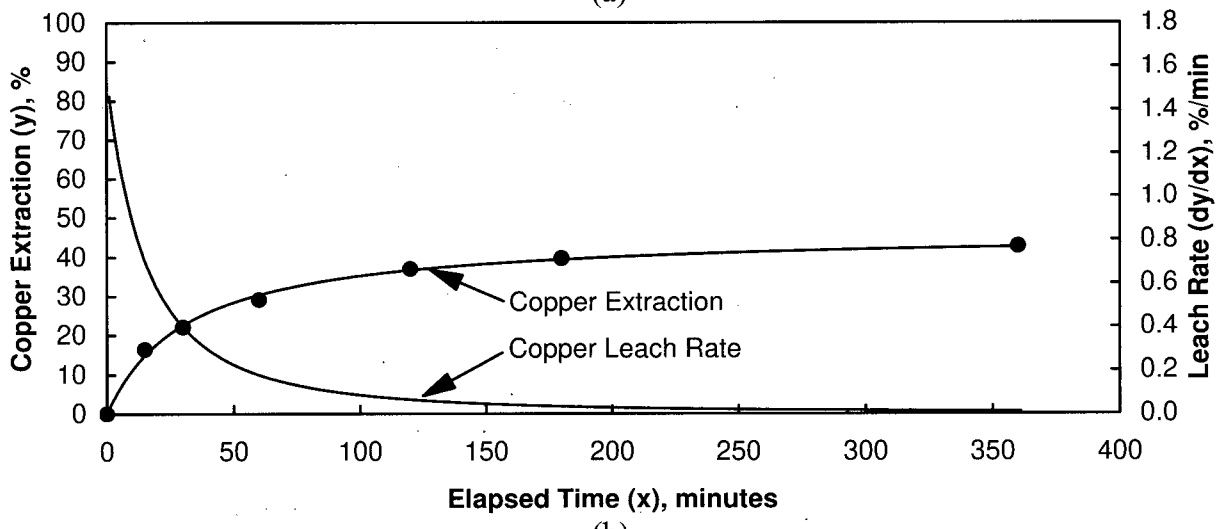

(b)

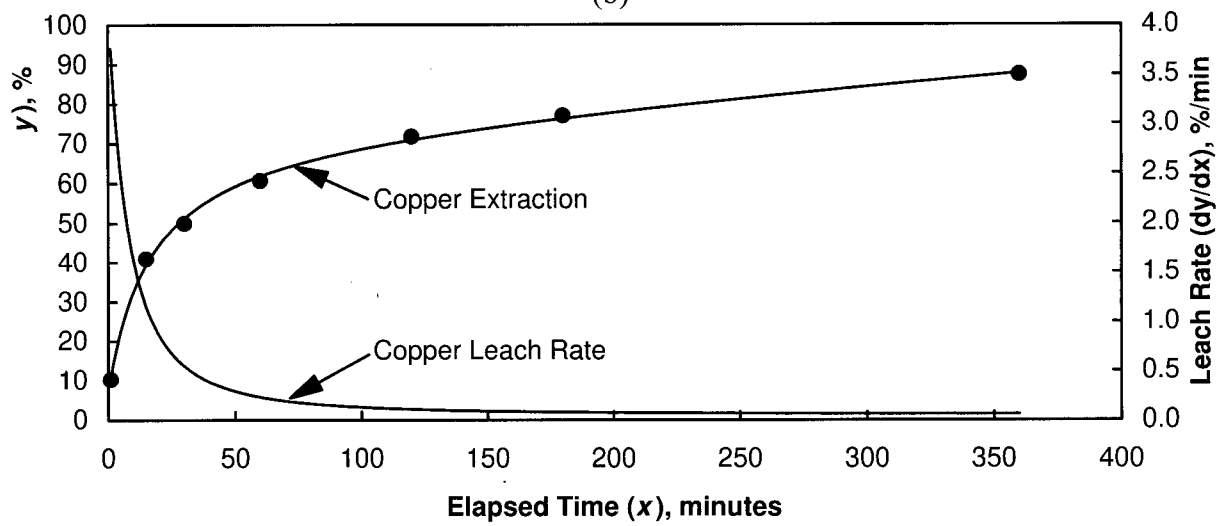

(c)

Figure A2-1. Plots of copper extraction (y) and copper leach rate (dy/dx) vs. time (x) for the oxygen pressure leaching of: (a) $CuFeS_2$ at 110°C, (b) $CuFeS_2$ at 125°C and (c) CuS at 110°C. The solid symbols represent the actual data and the solid lines represent the function fitted data.

Appendix 2 Reference

1. Microcal Origin Version 3.5 Reference Manual, Microcal Software, Inc., Northampton, MA, USA, pp. 157-212, 1994.

APPENDIX 3

AUGER REFERENCE DATA AND COMPOSITION CALCULATION PROCEDURE

Table A3-1. Major Auger transitions, peak positions and relative sensitivity factors (for the most intense peaks) for the elements of interest in this study [1].

Element	Auger Transition	Peak Position (eV)	Sensitivity Factor
Sulfur	$L_3M_{2,3}M_{2,3}$	152	0.87
Carbon	$KL_{2,3}L_{2,3}$	272	0.20
Oxygen	$KL_{2,3}L_{2,3}$	503	0.52
Iron	$M_{2,3}VV$	47	
Iron	$L_3M_{2,3}M_{2,3}$	598	
Iron	$L_3M_{2,3}V$	651	
Iron	L_3VV	703	0.21
Copper	$M_{2,3}VV$	60	
Copper	$L_3M_{2,3}M_{2,3}$	776	
Copper	$L_3M_{2,3}V$	849	
Copper	L_3VV	917	0.22

To determine surface compositions, the relative atomic percentages C_i of the above elements were calculated by using the following formula:

$$C_i = \frac{I_i/S_i}{\sum_j (I_j/S_j)} \cdot 100\% \qquad \text{(A3-1)}$$

where I_i is the Auger intensity (peak-to-peak amplitude of the strongest peak) of element i, S_i is the sensitivity factor for i, and j runs from 1 to the number of elements of interest. The summation was carried out for the elements Cu, Fe, S and O. The element C, if present, was excluded from the composition calculations. Thus the analyses were considered only in terms of the four elements of interest, i.e. $C_{Cu}+C_{Fe}+C_S+C_O = 100\%$.

Appendix 3 Reference

1. Davis, L.E., MacDonald, N.C., Palmberg, P.W., Riach, G.E. and Weber, R.E., *Handbook of Auger Electron Spectroscopy, 2nd Edition*, Perkin-Elmer Corportation, Eden Prairie, Minnesota, USA, 190 pp, 1976.

APPENDIX 4

X-RAY PHOTOELECTRON REFERENCE DATA

Table A4-1. Compilation of photoelectron binding energies for species forming potential components of oxidized chalcopyrite surfaces.

Emission	Mineral or Species		Binding Energy (eV)	Reference Binding Energy (eV)	Ref.
S $2p_{3/2}$	$CuFeS_2$		161.3	Au $4f_{7/2}$ = 84.0	[1]
	$CuFeS_2$		160.8	Au $4f_{7/2}$ = 83.8	[2]
	$CuFeS_2$		161.1	Au $4f_{7/2}$ = 83.9	[3]
	CuS_2		161.5	not given	[4]
	CuS		161.8	not given	[4]
	CuS		161.9	C *1s* = 285.0	[5]
	Cu_2S		161.8	not given	[4]
	Monosulfide ($Fe_{1-x}S$):	S^{2-}	161.1	C *1s* = 284.8	[6]
	Monosulfide ($Fe_{1-x}S$):	S^{2-}	161.25	Au $4f_{7/2}$ = 84.00	[7]
	Disulfide (FeS_2):	S_2^{2-}	162.5	Au $4f_{7/2}$ = 83.9	[8]
	Disulfide (on $Fe_{1-x}S$):	S_2^{2-}	162.21	Au $4f_{7/2}$ = 84.00	[7]
	Polysulfide (on FeS_2):	S_n^{2-}	163.3	Au $4f_{7/2}$ = 83.9	[8]
	Polysulfide (on $Fe_{1-x}S$):	S_n^{2-}	163.25	Au $4f_{7/2}$ = 84.00	[7]
	Sulfur (on $Fe_{1-x}S$)	S°	164.35	Au $4f_{7/2}$ = 84.00	[7]
	Sulfur	S°	164.3	C *1s* = 285	[9]
	Sulfur	S°	164.0	Au $4f_{7/2}$ = 83.9	[8]
	Sulfur	S°	164.2	Au $4f_{7/2}$ = 84.0	[10]
	Sulfite (on $Fe_{1-x}S$)	SO_3^{2-}	166.45	Au $4f_{7/2}$ = 84.00	[7]
	$KFe_3(SO_4)_2(OH)_6$		168.8	C *1s* = 285	[9]
	$Fe_2(SO_4)_3$		169.5	C *1s* = 285	[9]
	Sulfate (on $Fe_{1-x}S$)	SO_4^{2-}	168.25	Au $4f_{7/2}$ = 84.00	[7]
O *1s*	Cu_2O		530.5	Au $4f_{7/2}$ = 84.0	[11]
	CuO		529.6	Au $4f_{7/2}$ = 84.0	[11]
	Fe_3O_4		530.2	Au $4f_{7/2}$ = 84.0	[12]
	Fe_2O_3		529.9	Au $4f_{7/2}$ = 84.0	[12]
	FeOOH (O)		530.3	Au $4f_{7/2}$ = 84.0	[12]
	FeOOH (OH)		531.4	Au $4f_{7/2}$ = 84.0	[12]
	$CaSO_4$		531.8	Au $4f_{7/2}$ = 83.8	[13]
	$KFe_3(SO_4)_2(OH)_6$		532.5	C *1s* = 285	[9]
	$Fe_2(SO_4)_3$		532.4	C *1s* = 285	[9]
	H_2O		532.9	Au $4f_{7/2}$ = 83.8	[13]
	adsorbed H_2O on Fe_2O_3		532.3	Au $4f_{7/2}$ = 83.8	[14]
	adsorbed H_2O on $Fe_{1-x}S$		533.9	C *1s* = 284.8	[6]

Table A4-1. Compilation of photoelectron binding energies for species forming potential components of oxidized chalcopyrite surfaces (cont'd).

Emission	Mineral or Species	Binding Energy (eV)	Reference Binding Energy (eV)	Source
Cu $2p_{3/2}$	$CuFeS_2$	932.3	Au $4f_{7/2}$ = 84.0	[1]
	$CuFeS_2$	932.4	C *1s* = 285.0	[5]
	$CuFeS_2$	932.2	C *1s* = 285	[9]
	Cu_5FeS_4	932.5	C *1s* = 285.0	[5]
	Cu_7S_4	932.3	C *1s* = 285.0	[5]
	CuS_2	931.3	not given	[4]
	CuS	931.4	not given	[4]
	CuS	932.0	C *1s* = 285.0	[5]
	CuS	932.5	C *1s* = 285	[9]
	Cu_2S	932.0	not given	[4]
	Cu_2S	932.6	C *1s* = 285.0	[5]
	Cu_2S	932.8	C *1s* = 285	[9]
	Cu_2O	932.4	C *1s* = 285.0	[5]
	Cu_2O	932.5	Au $4f_{7/2}$ = 84.0	[11]
	CuO	933.8	Au $4f_{7/2}$ = 84.0	[11]
	$CuSO_4$	935.3	C *1s* = 285	[9]
	$Cu_3(SO_4)(OH)_4$	935.2	C *1s* = 285.0	[5]
Fe $2p_{3/2}$	$CuFeS_2$	708.0	Au $4f_{7/2}$ = 84.0	[1]
	$CuFeS_2$	708.0	Au $4f_{7/2}$ = 83.8	[2]
	$CuFeS_2$	708.5	C *1s* = 285	[9]
	Fe_3O_4 (Fe^{2+})	708.3	Au $4f_{7/2}$ = 84.0	[12]
	Fe_3O_4 (Fe^{3+})	710.6	Au $4f_{7/2}$ = 84.0	[12]
	Fe_2O_3	711.0	C *1s* = 285	[9]
	Fe_2O_3	711.0	Au $4f_{7/2}$ = 84.0	[12]
	FeOOH	711.5	C *1s* = 285	[9]
	FeOOH	711.9	Au $4f_{7/2}$ = 84.0	[12]
	$KFe_3(SO_4)_2(OH)_6$	712.2	C *1s* = 285	[9]
	$Fe_2(SO_4)_3$	713.5	C *1s* = 285	[9]

Appendix 4 References

1. Laajalehto, K., Kartio, I. and Nowak, P., XPS study of clean metal sulfide surfaces, *Applied Surface Science, 81*, pp. 11-15, 1994.

2. Buckley, A.N. and Woods, R., An X-ray photoelectron spectroscopic study of the oxidation of chalcopyrite, *Australian Journal of Chemistry*, pp. 2403-2413, 1984.

3. McCarron, J.J., Walker, G.W. and Buckley, A.N., An X-ray photoelectron spectroscopic investigation of chalcopyrite and pyrite surfaces after conditioning in sodium sulfide solutions, *International Journal of Mineral Processing, 30*, pp. 1-16, 1990.

4. Folmer, J.C.W. and Jellinek, F., The valence of copper in sulphides and selenides: an X-ray photoelectron spectroscopic study, *Journal of the Less-Common Metals, 76*, pp. 153-162, 1980.

5. Nakai, I., Sugitani, Y. and Nagashima, K., X-ray photoelectron spectroscopic study of copper minerals, *J. Inorg. Nucl. Chem., 40*, pp. 789-791, 1978.

6. Jones, C.F., LeCount, S., Smart, R.St.C. and White, T.J., Compositional and structural alteration of pyrrhotite surfaces in solution: XPS and XRD studies, *Applied Surface Science, 55*, pp. 65-85, 1992.

7. Pratt, A.R., Muir, I.J. and Nesbitt, H.W., X-ray photoelectron and Auger electron spectroscopic studies of pyrrhotite and mechanism of air oxidation, *Geochimica et Cosmochimica Acta, 58 (2)*, pp. 827-841, 1994.

8. Mycroft, J.R., Bancroft, G.M., McIntyre, N.S., Lorimer, J.W. and Hill, I.R., Detection of sulphur and polysulphides on electrochemically oxidized pyrite surfaces by X-ray photoelectron spectroscopy and Raman spectroscopy, *J. Electroanal. Chem., 292*, pp. 139-152, 1990.

9. Brion, D., Etude par spectroscopie de photoélectrons de la degradation superficielle de FeS_2, $CuFeS_2$, ZnS et PbS à l'air et dans l'eau, *Applications of Surface Science, 5*, pp. 133-152, 1980.

10. Karthe, S., Szargan, R. and Suoninen, E., Oxidation of pyrite surface: a photoelectron spectroscopic study, *Applied Surface Science, 72*, pp. 157-170, 1993.

11. McIntyre, N.S. and Cook, M.G., X-ray photoelectron studies on some oxides and hydroxides of cobalt, nickel, and copper, *Analytical Chemistry, 47 (13)*, pp. 2208-2213, 1975.

12. McIntyre, N.S. and Zetaruk, D.G., X-ray photoelectron spectroscopic studies of iron oxides, *Analytical Chemistry, 49 (11)*, pp. 1521-1529, 1977.

13. Wagner, C.D., Zatko, D.A. and Raymond, R.H., Use of the oxygen KLL Auger lines in identification of surface chemical states by electron spectroscopy for chemical analysis, *Analytical Chemistry, 52 (9)*, pp. 1445-1451, 1980.

14. Harvey, D.T. and Linton, R.W., Chemical characterization of hydrous ferric oxides by X-ray photoelectron spectroscopy, *Analytical Chemistry, 53 (11)*, pp. 1684-1688, 1981.

APPENDIX 5

CALCULATION OF THE SURFACE AREA FUNCTION FROM THE SHRINKING SPHERICAL PARTICLE MODEL

In Chapter 6 the following equations were derived to calculate the residual surface area vs. fraction reacted relationship for a discrete particle size distribution, based on the shrinking sphere model. The total fraction unreacted ($1-\overline{X_t}$) at t is:

$$1-\overline{X_t} = \sum_{\overline{D}(t=\tau)}^{\overline{D}_{max}} \left[1-X\left(\overline{D_i}\right)\right]\Delta F_i = \sum_{\overline{D}(t=\tau)}^{\overline{D}_{max}} \left[1-\frac{2k_l t}{\overline{D_i}}\right]^3 \Delta F_i \qquad \text{(A5-1)}$$

and the total fractional surface area remaining ($1-\overline{A_t}$), is:

$$1-\overline{A_t} = \sum_{\overline{D}(t=\tau)}^{\overline{D}_{max}} \left[1-A\left(\overline{D_i}\right)\right]\Delta S_i = \sum_{\overline{D}(t=\tau)}^{\overline{D}_{max}} \left[1-\frac{2k_l t}{\overline{D_i}}\right]^2 \Delta S_i \qquad \text{(A5-2)}$$

where: $\overline{D_i} = \dfrac{D_i + D_{i+1}}{2}$ = the arithmetic mean size (μm) of particles between size D_i and D_{i+1};

$X\left(\overline{D_i}\right)$ = the mass fraction leached of particles of size $\overline{D_i}$;

$A\left(\overline{D_i}\right)$ = the surface area fraction leached of particles of size $\overline{D_i}$;

k_l = the linear rate constant (μm/min);

$k_l t = \delta_l$, the particle penetration depth (μm);

ΔF_i = the mass fraction of particles of size $\overline{D_i}$;

$\Delta S_i = \dfrac{\Delta F_i / \overline{D_i}}{\sum_{i=0}^{n} \Delta F_i / \overline{D_i}}$ = the surface area fraction of particles of size $\overline{D_i}$;

$\overline{D}(t=\tau)$, is the size of the largest particle completely converted in time t.

A spreadsheet program was set up to solve equations (A5-1) and (A5-2) for arbitrarily chosen values of particle penetration depth, $\delta_l = k_l t$. Table A5-1 gives an example of the output obtained for the $CuFeS_2$ concentrate using the Elzone particle size distribution data. For each δ,

the spreadsheet calculates the residual mass and surface area fraction for each $\overline{D_i}$ and sums up the respective values to determine the total mass and surface area fractions remaining. If $2k_l t$ happens to be greater than $\overline{D_i}$, the values of $[1 - X(\overline{D_i})]\Delta F_i$ and $[1 - A(\overline{D_i})]\Delta S_i$ are set to zero to avoid negative values of these parameters. Thus, in the example depicted in Table A5-1, a δ_l value of 0.9 μm was input, and the spreadsheet output values of 0.4389 for the total fraction reacted, $\overline{X_t}$, and 0.3526 for the total residual surface area, $1 - \overline{A_t}$.

The spreadsheet also calculates the specific surface area of the feed, S_o (units of m^2 kg^{-1}), by summing the surface area-to-volume fractions for each $\overline{D_i}$ (units of m) and dividing by the feed density, ρ (units of kg m^{-3}) as follows:

$$S_o = \sum_{i=0}^{n} \left[\frac{\pi \overline{D_i}^2}{\frac{1}{6}\pi \overline{D_i}^3 \rho} \right] \Delta F_i = \frac{6}{\rho} \sum_{i=0}^{n} \frac{\Delta F_i}{\overline{D_i}} \qquad \text{(A5-3)}$$

Table A5-1. Spreadsheet for calculating surface area vs. fraction reacted for the shrinking sphere model.

$CuFeS_2$ feed					δ_l (μm)=	0.9
Elzone particle size data					Total fraction reacted =	0.4389
					Total fraction surface area remaining =	0.3526
Particle Diameter D_i (μm)	Mean Particle Diameter $\overline{D_i}$ (μm)	Cumulative Mass Fraction	Incremental Mass Fraction ΔF_i	Area/ Volume Ratio $6\Delta F_i/\overline{D_i}$ (μm^{-1})	Mass Fraction Remaining $[1-X(\overline{D_i})]\Delta F_i$	Area Fraction Remaining $[1-A(\overline{D_i})]\Delta S_i$
0	0.0	0.0000	0.0000			
1	0.5	0.0124	0.0124	0.1488	0.0000	0.0000
2	1.5	0.0429	0.0305	0.1220	0.0000	0.0000
3	2.5	0.0810	0.0381	0.0914	0.0008	0.0082
4	3.5	0.1204	0.0394	0.0675	0.0045	0.0183
5	4.5	0.1592	0.0388	0.0517	0.0084	0.0213
6	5.5	0.2009	0.0417	0.0455	0.0127	0.0236
7	6.5	0.2446	0.0437	0.0403	0.0165	0.0242
8	7.5	0.2883	0.0437	0.0350	0.0192	0.0231
9	8.5	0.3344	0.0461	0.0325	0.0226	0.0232
10	9.5	0.3770	0.0426	0.0269	0.0227	0.0203
11	10.5	0.4143	0.0373	0.0213	0.0212	0.0168
12	11.5	0.4507	0.0364	0.0190	0.0218	0.0155
13	12.5	0.4880	0.0373	0.0179	0.0234	0.0150
14	13.5	0.5236	0.0356	0.0158	0.0232	0.0136
15	14.5	0.5593	0.0357	0.0148	0.0240	0.0130
16	15.5	0.5958	0.0365	0.0141	0.0252	0.0126
17	16.5	0.6309	0.0351	0.0128	0.0248	0.0116

Table A5-1. Spreadsheet for calculating surface area vs. fraction reacted for the shrinking sphere model (cont'd).

Particle Diameter D_i (μm)	Mean Particle Diameter $\overline{D_i}$ (μm)	Cumulative Mass Fraction	Incremental Mass Fraction ΔF_i	Area/ Volume Ratio $6\Delta F_i/\overline{D_i}$ (μm^{-1})	Mass Fraction Remaining $[1-X(\overline{D_i})]\Delta F_i$	Area Fraction Remaining $[1-A(\overline{D_i})]\Delta S_i$
18	17.5	0.6649	0.0340	0.0117	0.0246	0.0108
19	18.5	0.6983	0.0334	0.0108	0.0246	0.0101
20	19.5	0.7296	0.0313	0.0096	0.0234	0.0091
21	20.5	0.7582	0.0286	0.0084	0.0217	0.0080
22	21.5	0.7850	0.0268	0.0075	0.0206	0.0072
23	22.5	0.8103	0.0253	0.0067	0.0197	0.0065
24	23.5	0.8340	0.0237	0.0061	0.0187	0.0059
25	24.5	0.8561	0.0221	0.0054	0.0176	0.0053
26	25.5	0.8768	0.0207	0.0049	0.0166	0.0048
27	26.5	0.8952	0.0184	0.0042	0.0149	0.0041
28	27.5	0.9121	0.0169	0.0037	0.0138	0.0037
29	28.5	0.9272	0.0151	0.0032	0.0124	0.0032
30	29.5	0.9398	0.0126	0.0026	0.0104	0.0026
31	30.5	0.9499	0.0101	0.0020	0.0084	0.0020
32	31.5	0.9584	0.0085	0.0016	0.0071	0.0016
33	32.5	0.9660	0.0076	0.0014	0.0064	0.0014
34	33.5	0.9728	0.0068	0.0012	0.0058	0.0012
35	34.5	0.9788	0.0060	0.0010	0.0051	0.0011
36	35.5	0.9844	0.0056	0.0009	0.0048	0.0010
37	36.5	0.9888	0.0044	0.0007	0.0038	0.0007
38	37.5	0.9922	0.0034	0.0005	0.0029	0.0006
39	38.5	0.9950	0.0028	0.0004	0.0024	0.0005
40	39.5	0.9968	0.0018	0.0003	0.0016	0.0003
41	40.5	0.9981	0.0013	0.0002	0.0011	0.0002
42	41.5	0.9989	0.0008	0.0001	0.0007	0.0001
43	42.5	0.9995	0.0006	0.0001	0.0005	0.0001
44	43.5	1.0000	0.0005	0.0001	0.0004	0.0001
Total			1.0000	0.8728	0.5611	0.3526

Calculated feed specific surface area (S_o) = 214 m^2/kg